THE UNIVERSITY
of EDINBURGH

This thesis has been submitted in fulfilment of the requirements for a postgraduate degree (e.g. PhD, MPhil, DClinPsychol) at the University of Edinburgh. Please note the following terms and conditions of use:

This work is protected by copyright and other intellectual property rights, which are retained by the thesis author, unless otherwise stated.
A copy can be downloaded for personal non-commercial research or study, without prior permission or charge.
This thesis cannot be reproduced or quoted extensively from without first obtaining permission in writing from the author.
The content must not be changed in any way or sold commercially in any format or medium without the formal permission of the author.
When referring to this work, full bibliographic details including the author, title, awarding institution and date of the thesis must be given.

First Investigation of Electromagnetic Coupling of the d*(2380) Hexaquark

Stephen John Donald Kay

A thesis submitted for the degree of
Doctor of Philosophy
The University of Edinburgh
June 2018

For Don and Geoff

Acknowledgements

I would like to begin by thanking my excellent supervisors on this project, Dan Watts and Mikhail Bashkanov. Without their expertise and guidance none of this would have been possible. It has been an absolute pleasure to work with them both. I would also like to thank all of the other members of the Hadron Physics group at Edinburgh, Lorenzo Zana was invaluable for his assistance in getting software up and running quickly. Thanks to Nick Zachariou and Gary Smith too for their insight and assistance at various stages of the PhD.

Of course the experimental work in this thesis is all made possible by the hard work of all the members of the A2 collaboration. In particular I'd like to thank my colleagues at the University of Glasgow. Chris Mullen for getting the calibration up and running (and for his unwavering support of the worlds greatest football team, Newcastle United), Derek Glazier for all his insight into the challenging world of recoil polarimetry experiments and Ken Livingston for working his magic with the Goniometer. At Mainz I'd like to thank Phillipe Martel and Cristina Collicott for all their hard work and for helping me get my head around GoAT. Thanks to Andreas Thomas too for the work he puts into managing the collaboration. Indeed thanks to everyone I haven't mentioned in the collaboration, I've got to cut this one short before it ends up being the whole thesis!

Back in Edinburgh I'd like to thank our truly excellent research technician Peter Black, both for his assistance in all things engineering related and for all the interesting discussions on all manner of topics! Whilst on the topic of making things I have to give a special thanks to the staff in the mechanical workshop at the University of Edinburgh, without them the PID wouldn't be much more than a sheet of plastic scintillator! Thanks as well to all of the other staff at the University that have supported me in various ways during my time as a PhD student.

I've thoroughly enjoyed my past four years in Edinburgh. A big part of this is down to all my excellent friends in Edinburgh (and elsewhere!) and my wonderful partner Frances. She has kept me going and believed in my ability to get this all done when I've doubted it myself. Thank you Frances. The Nuclear Physics PhD office at Edinburgh has also been a big part of making my time here so enjoyable, I think anyone would be hard pressed to find a nicer bunch of Physicists anywhere! Thanks to all of you, past and present, for the office chat and for the coding/physics discussions and help. It has been a blast. That being said the current occupants of the office do hold some dubious opinions on a certain series of popular science fiction movies...

Last but not least, thank you to my wonderful family for supporting and believing in me, for as long as I can remember you've always been there to encourage me in following my interests. Finally I would like to dedicate this thesis to the memory of my grandfather, Donald Kay (Don), and my uncle, Geoffrey Ian Stone (Geoff). Both Don and Geoff sadly passed away during my time at Edinburgh.

Declaration

The data presented in this thesis was obtained in an experiment carried out by the A2 Collaboration at the Mainz Microtron (MAMI) facility located in the Johannes Gutenberg Universität in Mainz, Germany. I played a major role in the preparation and execution of the experiment including the design and construction of the Phase-II Nucleon Polarimeter. The data analysis and interpretation are entirely my own work. Any contributions from colleagues in the collaboration, such as diagrams or calibrations, are explicitly referenced in the text. This thesis was written by myself and the work presented in it has not been submitted in support of another degree or qualification from this or any other university or institute of learning.

(*Stephen John Donald Kay, June 2018*)

Abstract

This thesis presents the first measurement of the d*(2380) (hexaquark) electromagnetic coupling, extracted from the deuteron photodisintegration ($\vec{\gamma}d \rightarrow d^{*} \rightarrow \vec{n}p$) reaction. The experiment was carried out at the Mainzer Microtron (MAMI) facility in the Institut für Kernphysik in Mainz, Germany. A racetrack microtron at the MAMI facility provided a 1557 MeV longitudinally polarised electron beam. This electron beam was directed onto a thin radiator to produce a bremsstrahlung photon beam. Diamond and amorphous (metallic) radiators were used to produce linearly and circularly polarised photons respectively. The produced bremsstrahlung photon beam was energy ‘tagged’ with a resolution of ∼4 MeV over the photon-energy range of 150–1400 MeV using the Glasgow Photon Tagger. The tagged photons were incident on a 10 cm long liquid deuterium target. This target was surrounded by a new nucleon recoil polarimeter apparatus and placed within the Crystal Ball calorimeter at MAMI. An array of $PbWO_4$ and BaF_2 detectors (TAPS) was used to provide calorimetry at forward angles.

The newly constructed large acceptance recoil polarimeter measures the polarisation of the nucleons in the final state. The combination of this new apparatus with the polarised photon beam facility gives access to a number of single and double polarisation observables. The photon beam asymmetry, Σ, and the double polarisation observable, $C_{x'}$, were examined in measurements of the reaction d($\vec{\gamma}$,$\vec{n}\vec{p}$) over a large range of energies with a close to full angular coverage. The observable $C_{x'}$ is determined for the neutron produced in deuteron photodisintegration for the first time. The new data constrains mechanisms of deuteron photodisintegration and assesses the existence and contribution of the d*(2380) resonance.

Lay Summary

Understanding the matter that makes up the universe around us has been a subject of research throughout human history. It is only within the last century that we have begun to develop a true understanding of this subject. We have discovered that the world around us is comprised of atoms. Atoms themselves consists of a dense, compact, positively charged nucleus that is surrounded by negatively charged electrons. The atomic nucleus consists of two types of particles, positively charged protons and electrically neutral neutrons. Protons and neutrons are not fundamental particles, i.e. they are themselves formed of other particles. We refer to the particles that make up protons and neutrons as *quarks*.

Quarks are fundamental particles. Quarks interact with each other via the strong nuclear force, one of the four fundamental forces of nature. The strong nuclear force is difficult to understand and model theoretically. Our understanding of this force primarily comes from experimentally measuring particle interactions and examining the particles that are formed in these interactions.

Particles formed of quarks are referred to as *hadrons*. All of the well known and measured hadrons discovered so far are formed of two quarks (referred to as *mesons*) or three quarks (referred to as *baryons*). However, hadrons formed of differing numbers of quarks are not forbidden by our theoretical models. In recent years there have been a number of experiments that have claimed observation of states formed of four quarks (tetraquarks), five quarks (pentaquarks) or six quarks (hexaquarks).

One of these hexaquark states is known as the d*(2380). This state has been observed and produced in various experiments utilising hadronic beams (i.e. proton beams). Such experiments have revealed some of the properties of this state such as its mass and how it decays into other particles. These measurements do not provide any information on the *size* of this state or its *structure* (how the quarks are arranged inside the object). Such properties can only be determined from experiments that utilise beams of electromagnetic particles (electrons, photons) to produce the state.

This thesis outlines the first dedicated experiment that utilises a photon beam to produce the d*(2380). This experiment was carried out in August 2016 at the Mainz Microtron (MAMI) facility in Mainz, Germany. At this facility a high energy electron beam is utilised to produce a beam of photons. These photons are incident upon a target of liquid deuterium (a hydrogen atom with a proton and a neutron in the nucleus). The particles produced when the photon beam interacts with the target are measured by a detector array that surrounds the target. These reaction particles are examined and experimental observables are extracted.

Contents

List of Figures

List of Tables

Chapter 1

Introduction

The family of particles known as hadrons includes the protons and neutrons that make up the visible matter in the universe around us. Hadrons are complicated objects formed of fundamental particles called quarks. Quarks experience all four of the fundamental forces in the Standard Model. However, within hadrons it is the strong nuclear force that plays by far the most important role. Quarks within hadrons interact with each other through the strong nuclear force in interactions that are mediated by gauge bosons known as gluons. Our best theoretical model of the strong interaction postulates that the strong force interacts between objects with "colour" charge. This theory is known as Quantum Chromodynamics (QCD).

In QCD, quarks carry one of three colour charges and gluons carry one of these three colours and one of three anti-colours. Under this theory only objects that are 'colour neutral' can be observed. The meson, formed of a quark and an anti-quark, and the baryon, formed of three quarks, are two such colour neutral configurations of hadrons. QCD can be used to describe and make predictions for strong-force interactions at high energy (perturbative regime) very successfully. However, at low energies, where perturbative calculations cannot be performed, theoretical predictions are hard to obtain. This is particularly problematic as this low-energy regime contains the interactions that occur within nucleons. These interactions are responsible for the vast majority of the overall mass of nucleons (and consequently, the visible universe)[1, 2].

Recent advances in computing power and the development of theoretical techniques such as Lattice QCD (LQCD) have improved the theoretical picture in the low-energy regime however. Predictions of certain hadronic properties can now be made to within a few % of the values observed in experiments. The excitation spectra for hadrons can also be predicted. Such spectra can include new classifications of hadrons with properties and configurations beyond those which are currently known, the meson and the baryon.

QCD, as it is currently understood, does not forbid the existence of hadronic states other than the meson and baryon. The requirement for a state to be colour neutral can be achieved in numerous other ways. Combinations of any number of quarks (other than 1) and anti-quarks can be made to be colour neutral. A combination of gluons (a "glueball") could also potentially form a colour neutral object. Experimental searches for such objects are ongoing and recent observations have discovered several interesting possibilities for new hadronic states.

Recent experiments at LHCb, WASA-at-COSY, BELLE and elsewhere have observed resonance structures with properties (e.g. spin-parity combinations) that cannot be described by normal mesons or baryons. The interpretation of the observed states is that they are states formed of four quarks (two of which are anti-quarks), five quarks (one anti-quark) or six quarks. Such combinations are often referred to as tetraquarks, pentaquarks and hexaquarks respectively. Whether these observed states are truly single compact objects or are more like 'molecular' states is a subject of much debate. To answer this question these states must be studied in more detail.

Of the observed states so far, the d*(2380) dibaryon state is perhaps the state with the most well-defined properties. The mass, width and spin parity of this state, as well as its branching ratio, have been determined from measurements of numerous hadron induced reaction channels by the WASA-at-COSY collaboration. However, these measurements do not provide information on the size or structure of this state. Such properties can be determined using electromagnetic probes. This thesis provides the first steps in this process.

The deuteron photodisintegration reaction $\gamma d \rightarrow np$ is the simplest photon induced reaction that may show sensitivity to the d*(2380). Previous spin polarimetry measurements of the final state proton in this reaction have produced intriguing hints of a resonance structure in a mass range very similar to that of the d*(2380) observed at WASA. The d*(2380) could potentially be produced in this reaction via an intermediate step, $\vec{\gamma} d \rightarrow d^* \rightarrow \vec{n}\vec{p}$.

This thesis outlines new measurements of the deuteron photodisintegration reaction ($\vec{\gamma}d \rightarrow \vec{n}\vec{p}$) over a wide photon-energy range of 150–1400 MeV. The polarisation observable Σ is extracted in the photon-energy range 410–620 MeV ($\sqrt{s} \approx$ 2249–2417 MeV) of interest to the d*(2380) dibaryon resonance. The polarisation transfer observable, $C_{x'}$, is also studied in the photon-energy range 200–1000 MeV. This observable is determined for the neutron produced in deuteron photodisintegration for the first time. These measurements constitute the first dedicated study of the d*(2380) in a photon induced reaction. Studies of observables for this reaction have been carried out on the proton but the neutron has never been examined [3].

The measurements were carried out in August 2016 at the Mainzer Microtron (MAMI) facility in Mainz, Germany [4]. The experiment utilised a new nucleon polarimeter within the existing detector setup in the A2 hall at MAMI, which comprises the Crystal Ball and TAPS detector arrays [5–7]. The setup provides acceptance for charged and uncharged reaction products with close to a 4-π coverage in solid angle.

The structure of this thesis is as follows; hadronic states in QCD are introduced in Chapter 2, the formalism for the deuteron photodisintegration reaction examined in this thesis is introduced in Chapter 3. Possibilities for new "exotic" hadron states are reviewed in Chapter 4. Chapter 5 discusses the MAMI experimental facility and Chapter 6 provides an overview of the design and construction of the new polarimeter utilised in the experiment. Chapter 7 summarises the calibration procedure for the detectors used in the experiment. The event selection and analysis procedure is outlined in Chapter 8, along with a discussion of systematic errors. Results are presented in Chapter 9. An initial attempt at interpreting the results along with the conclusions of this body of work are contained in Chapter 10.

Chapter 2

Hadrons in QCD

This chapter outlines our current understanding of the family of particles known as hadrons. Hadrons are composite particles formed of quarks. The properties and varieties of quarks, as well as how they combine to form hadrons, are discussed in this chapter. There are two well known sub groupings of hadronic states: mesons and baryons. This chapter will detail how to build, interpret and group these states based upon their properties and quantum numbers. The theoretical model used to understand strong-force interactions between quarks, Quantum Chromodynamics (QCD), will also be outlined. Our models and theories do not forbid hadronic states other than mesons and baryons; indeed many models predict a plethora of other possibilities. These “exotic” states and the various searches for them are discussed in Chapter 4.

2.1 Building Hadrons

Although hadrons are formed of quarks, free quarks have never been observed. Their existence has been inferred from deep inelastic scattering measurements [8, 9] and from hadron spectroscopy [10]. The existence of quarks and their flavour is supported by the fact that measurements of hadronic states carried out so far generally match quark-model predictions quite well [11]. This section discusses the quantum numbers and properties of quarks and how they are arranged to form meson and baryon states.

2.1.1 Quarks

The quark model was introduced in 1964 by Gell-Mann [12] and by Zweig independently [13, 14](although Zweig refers to them as "aces"). The model was formulated in order to group the hadrons observed up to that point and to understand their properties. Today the quark model consists of six flavours of quark. These flavours are the down, up, strange, charm, bottom and top. The properties of these six quarks are summarised in Table 2.1.

The properties of hadrons are related to their internal quark content. In the case of many of the quantities (electrical charge Q, baryon number $B\#$, isospin I_3 (discussed in Section 2.1.3), strangeness S, charm C, bottomness - or "beauty", B and topness - or "truth", T) the properties of hadrons are simply a linear combination of the values of their constituent quarks. The spin, J, of the hadron is more complicated as it depends upon the orientation (up or down) of each quark. However, for a state of three quarks it is easy to infer that the magnitude of the total spin in the ground state can be either $\frac{1}{2}$ (two up one down or vice versa) or $\frac{3}{2}$ (all up or down). The mass of a hadronic state however is far more complicated; (discussed further in Section 2.2) it is *not* simply a linear combination of its constituent quark masses. The listed quark masses are only the inferred masses of the lone quarks (sometimes referred to as the "valence" quark mass). Hadronic states are typically characterised by their mass and spin-parity, J^P (or J^π). J is the overall value of the spin and P is the parity of the hadron wave function. This quantity is either positive (+1) or negative (-1). For hadrons that are eigenstates of C-Parity (charge conjugation) the state may be listed with its spin, parity and charge conjugation as J^{PC}.

2.1.2 Grouping States

Hadrons are generally classified as mesons or baryons. Mesons are states formed of a quark and an anti-quark, as baryon number is inverted for anti-quarks this leads to a hadron with $B\# = 0$. Baryons are formed of three quarks (or three anti-quarks for anti-baryons) and as such have $B\# = 1$ (-1 for anti-baryons). Sets of hadrons with the same baryon number, spin and parity can be arranged into multiplets. This is relatively straightforward for states consisting only of u, d and s quarks but rapidly becomes more complicated when systems that include c or b quarks are also considered. Example multiplets (formed from only u, d or

Table 2.1 *Quark Properties*

Flavour	Mass (MeV/c^2)	J	$B\#$	Q	I_3	S	C	B	T
u	1.5-3.3	$\frac{1}{2}$	$\frac{1}{3}$	$\frac{2}{3}$	$\frac{1}{2}$	0	0	0	0
d	4.1-5.7	$\frac{1}{2}$	$\frac{1}{3}$	-$\frac{1}{3}$	-$\frac{1}{2}$	0	0	0	0
s	100	$\frac{1}{2}$	$\frac{1}{3}$	-$\frac{1}{3}$	0	-1	0	0	0
c	1290	$\frac{1}{2}$	$\frac{1}{3}$	$\frac{2}{3}$	0	0	1	0	0
b	4200	$\frac{1}{2}$	$\frac{1}{3}$	-$\frac{1}{3}$	0	0	0	-1	0
t	172900	$\frac{1}{2}$	$\frac{1}{3}$	$\frac{2}{3}$	0	0	0	0	1

s quarks) for spin $\frac{1}{2}$ and spin $\frac{3}{2}$ baryons are shown in Figures 2.1 and 2.2. The three "axes" of the multiplets are the strangeness, charge and I_3 values of the state.

2.1.3 Isospin

Within groups of hadrons with the same J, P, S, C and B quantum numbers but differing values of Q the masses of the hadrons tend to be very similar. For example, the proton and the neutron both have $J^{\pi} = \frac{1}{2}^{+}$ and masses of $\mathrm{m_p} \sim$ 938 MeV/c^2 and $\mathrm{m_n} \sim$ 939.6 MeV/c^2 but differing charges (+1 and 0). The quark content of the proton is *uud* and the neutron is *udd*. The similar mass but differing quark content leads to the assumption of a "symmetry" between the u and d quarks. This symmetry is referred to as "isospin" symmetry and has a new associated quantum number, I. Using this new quantum number the proton and the neutron can be treated as being the same particle but in different states of isospin.

This isospin symmetry requires the introduction of more quantum numbers beyond I. Isospin is a vector quantity, the third component of the isospin, I_3 can take values in the range

$$I_3 = I, I-1, ... - I. \tag{2.1}$$

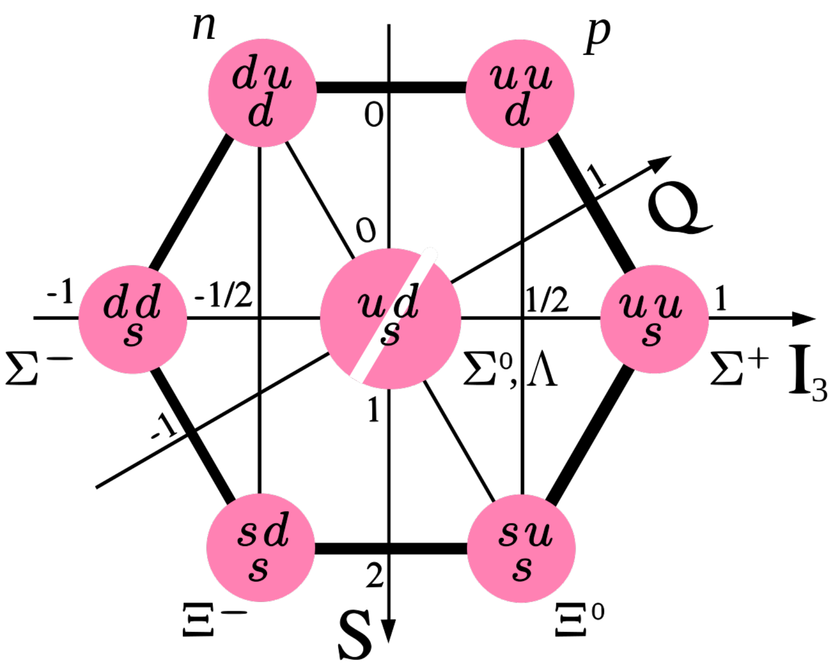

Figure 2.1 *The octet of* $J = \frac{1}{2}$ *baryons formed of* u*,* d *and* s *quarks [15].*

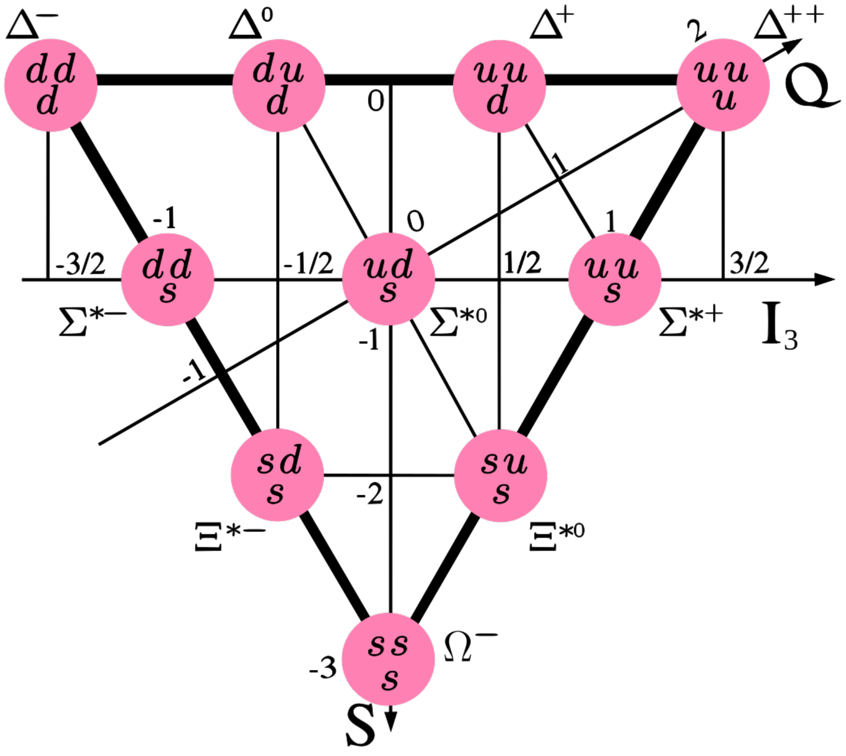

Figure 2.2 *The decuplet of* $J = \frac{3}{2}$ *baryons formed of* u*,* d *and* s *quarks [16].*

In analogy to angular momentum in quantum mechanics I_3 is similar to m_l, the value of I_3 can be calculated from the electrical charge, Q, of the state and a new quantity, the hypercharge Y, via

$$Y = B\# + S + C + B + T \tag{2.2}$$

$$I_3 \equiv Q - \frac{Y}{2} \tag{2.3}$$

The quantities I, I_3 and Y are all conserved in strong force interactions. The hypercharge, Y, for the proton and neutron is 1 and $I_3 = \frac{1}{2}$ for the proton and $I_3 = -\frac{1}{2}$ for the neutron, with $I = \frac{1}{2}$ in both cases.

2.1.4 Issues

The quark model as introduced in 1964 was successful in explaining observed patterns in states from the early period of experiments. It was also successfully used to predict the existence of states such as the Ω^- baryon [17]. However, this baryon, formed of three strange quarks with all their spins aligned, highlights an issue with the quark model. As quarks are fermions, a state of three identical quarks with spins aligned would violate the Pauli exclusion principle. The observation of the Ω^- (sss), Δ^{++} (uuu) and Δ^- (ddd), $J^\pi = \frac{3}{2}^+$, states implied that something was missing from the model.

Greenberg rectified this issue by proposing that quarks are parafermions of order three [18]. This implies that quarks can exist in one of three different states, later referred to as colour states. The implication is that in a baryon, each quark has one of three colour states (red, green or blue) and combine together to form an overall colour-neutral object. Similarly, for mesons the quark carries one colour and the anti-quark carries the corresponding anti-colour; again forming a colour-neutral object. The idea that only colour-neutral objects can be observed is known as confinement. Confinement implies that colour-charged objects cannot be observed, as such individual free quarks are not observable. This phenomenon is one of the key properties of the theoretical model that dictates the strong-force interaction between colour-charged objects, Quantum Chromodynamics (QCD).

2.2 Quantum Chromodynamics

Quantum Chromodynamics (QCD) is a theory of the strong nuclear force that governs interactions between colour-charged objects, such as quarks. These interactions are mediated by the gluon, a massless spin-1 boson with no electrical charge. However, gluons carry a colour charge and an anti-colour charge. This property has significant consequences for the strong interaction. As gluons carry colour charge they can interact with themselves via the strong force. This is in stark contrast to the uncharged photons that mediate electromagnetic (EM) interactions between electrically charged objects. It is actually this property of self interaction and the strength of QCD itself that leads to the vast majority of the mass of hadrons, and as such the majority of visible mass in the universe [1, 2]. This is why the mass of hadrons is not simply the sum of the masses of the individual valence quarks. For example the free (or valence) quarks within the proton add up to only ~1% of its total mass. The rest stems from the energy of the strong-force interactions.

In addition to this, there are two key features of QCD. One of these features, confinement, has already been discussed. The second feature is known as asymptotic freedom. The strong coupling constant, α_s, is a measure of the strength of the strong nuclear force. The value of α_s is not constant and varies depending upon the energy scale of the interaction. As seen in Figure 2.3, the coupling constant reduces in strength with increasing energy. In the high-energy region the coupling constant is relatively small and shows a much weaker dependence on energy. This is the region of "asymptotic freedom". Quarks behave as though they are free in this region.

The trend seen in Figure 2.3 can also be considered in terms of distance scales if the graph is reflected, i.e. the coupling constant is strong (and increases in strength) at long distances but is weaker over short distances. When considering the variation this way, the property of confinement becomes clear; if a pair of quarks was to be separated, the binding energy between them would increase as the distance between them increases. Eventually it will become energetically favourable to produce a new quark anti-quark pair from the vacuum rather than isolate one of the quarks in the initial pair.

Due to the variation of α_s, QCD calculations fall into two distinct regimes. At high energy (short distances), in the asymptotic freedom regime, the coupling

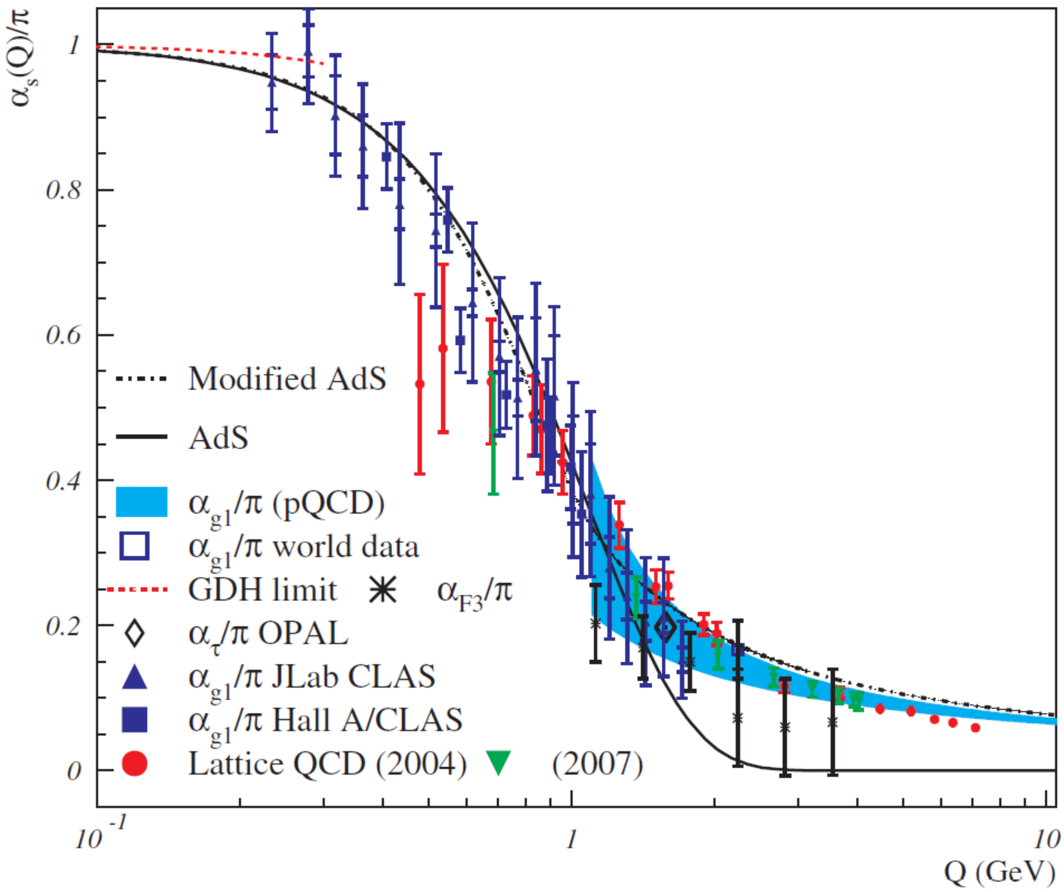

Figure 2.3 *The strong coupling constant (divided by π), $\frac{\alpha_s}{\pi}$ as a function of the energy scale Q [19].*

is sufficiently weak to allow perturbative calculations to be performed. At low energies (long distances) such calculations are not possible. This non-perturbative regime requires the application of novel computational methods, simplifications to the model or a combination of both. It is somewhat unfortunate that it is within this non-perturbative regime that the majority of the interactions that influence the world (and universe) around us occur.

2.2.1 Non-Perturbative QCD Methods

In the non-perturbative regime at low energies (Q $<$ 1 GeV) a full analytical QCD solution is not possible. Instead approximate solutions must be applied. One potential approach is Chiral Perturbation Theory (ChPT) [2, 20]. In ChPT an effective Lagrangian is formulated based on symmetries and symmetry breaking patterns in QCD. Taylor series can be extracted from this Lagrangian and solved perturbatively to produce matrix elements and scattering amplitudes. This effective Lagrangian is made to be chirally symmetric by treating the quarks involved as being massless and splitting them into two helicities, parallel and anti-parallel to the momentum. The expansion at low energies is generally done in terms of $\frac{p}{m_\pi}$, for calculations at high energy the expansion is in terms of α_s. In the region between the high and low energy regimes this expansion is very difficult. Nonetheless ChPT is a useful theoretical approach for describing some interactions such as $\pi\pi$ and πN [20].

Another technique for solving problems in the non-perturbative regime is Lattice QCD (LQCD). This technique was first introduced by Wilson in 1974 [21]. In LQCD, problems are formulated on a lattice of points in space and time. The points are separated by a fixed finite distance, a, in an overall volume, V. Quarks are positioned at the points of the lattice and gluons propagate as the “links” between these lattice points. QCD interactions in this model can be numerically solved via Monte Carlo computing methods to make predictions. Such computations are very intensive however and require the use of supercomputing resources. Due to the intensity of these computations, they are also typically carried out using unrealistically large quark masses that simplify the calculation. Nevertheless, such calculations are a very useful and have been used to accurately predict the masses of light hadrons to within a few % [22]. LQCD can also be used to make predictions of meson and baryon excitation spectra [23, 24]. With the ongoing increase in computing power available, predictions from LQCD will only become more and more accurate in the future. Also, such advances may be expected to enable larger lattice sizes to be simulated that will allow more extended reaction processes and particles to be studied.

2.3 Studying Hadronic States

Hadronic states are often studied by carrying out scattering experiments. In such experiments a beam (electrons, photons, other nucleons) is incident upon a target. The incident wave (particle in beam) can be treated as being a plane wave. Once scattered by the potential, the outgoing wave is represented as a spherical wave front. The incoming plane wave can be re-expressed as a superposition of spherical waves given by

$$\psi_{\mathrm{inc}} = Ae^{ikz} = A\sum_{l=0}^{\infty} i^l(2l+1)j_l(kr)P_l(\cos(\theta)), \tag{2.4}$$

where $j_l(kr)$ are spherical Bessel functions and $P_l(\cos(\theta))$ are Legendre Polynomials. This expression of the plane wave is the "partial wave expansion". The resulting set of partial waves, each corresponding to a specific value of the angular momentum, l, are each weighted by $(2l+1)$ with a phase factor i^l. At large distances from the scattering potential the Bessel functions simplify, such that Equation (2.4) can be expressed as

$$e^{ikz} = e^{ikr.\cos(\theta)} = \sum_{l=0}^{\infty} i^l(2l+1)P_l(\cos(\theta))\left[\frac{e^{i(kr-l\frac{\pi}{2})} - e^{-i(kr-l\frac{\pi}{2})}}{kr}\right]. \tag{2.5}$$

With such an expression, each partial wave can be considered as the superposition of two partial waves, $e^{i(kr-l\frac{\pi}{2})}$ representing the outgoing wave and $e^{-i(kr-l\frac{\pi}{2})}$ representing the incoming wave. A scattering process can be modelled by introducing a phase to multiply the outgoing part of the wave. For purely elastic scattering this phase has the form

$$S_l(k) = e^{2i\delta_l}, \tag{2.6}$$

where δ_l is the phase shift. For purely elastic scattering the flux of incident and scattered particles is conserved. To extend this result to inelastic scattering a complex "elasticity" term, $\eta_l(k)$ must be introduced and utilised rather than the expression given in Equation (2.6). For elastic scattering the phase shifts are real whereas in inelastic scattering the phase shifts are complex with the real part corresponding to elastic scattering and the imaginary component corresponding to absorption/inelastic processes. The scattering amplitude for the inelastic process can be expressed as

$$f(\theta) = \frac{1}{k}\sum_{l=0}^{\infty}(2l+1)\left(\frac{\eta_l e^{2i\delta_l}[l-1]}{2i}\right)P_l(\cos(\theta)), \tag{2.7}$$

where the amplitude of a given partial wave is given by

$$T_l = \left(\frac{\eta_l e^{2i\delta_l}[l-1]}{2i}\right). \tag{2.8}$$

This partial wave amplitude, T_l, is a complex quantity. In an interaction, it is this component that should be measured as it provides information about the mass and width of any resonance states decaying with this given partial wave. The presence of a resonance in a given partial wave channel can most easily be seen by examining the motion of this partial wave amplitude on an argand diagram (plotting the real vs imaginary part of the amplitude) as the energy of the reaction is altered. If a resonance is present such a plot should follow a close to circular path [25].

Chapter 3

Observables in Deuteron Photodisintegration

3.1 Definition of Frames

The deuteron photodisintegration reaction, $\gamma d \rightarrow pn$, can be depicted in the lab and centre of mass frames as shown in Figure 3.1. Deuteron photodisintegration reactions, where one of the nucleons subsequently undergoes a scattering interaction in some analysing material, may consider polarisation components in a new scattered frame defined by the axes x', y' and z'. When considering, for example, a neutron undergoing a secondary scattering interaction the axes of this frame are defined by

$$\hat{\underline{z'}} = \hat{\underline{n}}, \tag{3.1}$$

$$\hat{\underline{y'}} = \hat{\underline{\gamma}} \times \hat{\underline{p}}, \tag{3.2}$$

$$\hat{\underline{x'}} = \hat{\underline{y'}} \times \hat{\underline{z'}}, \tag{3.3}$$

where $\hat{\underline{n}}$, $\hat{\underline{\gamma}}$ and $\hat{\underline{p}}$ are the neutron, photon and proton (the proton from the initial reaction that is assumed to be unscattered) three-vectors respectively [26]. The polar and azimuthal angles in the (x', y', z') frame, θ_{Sc} and ϕ_{Sc}, of the recoil particle, p', can be determined as in Figure 3.2. These angles are utilised to form

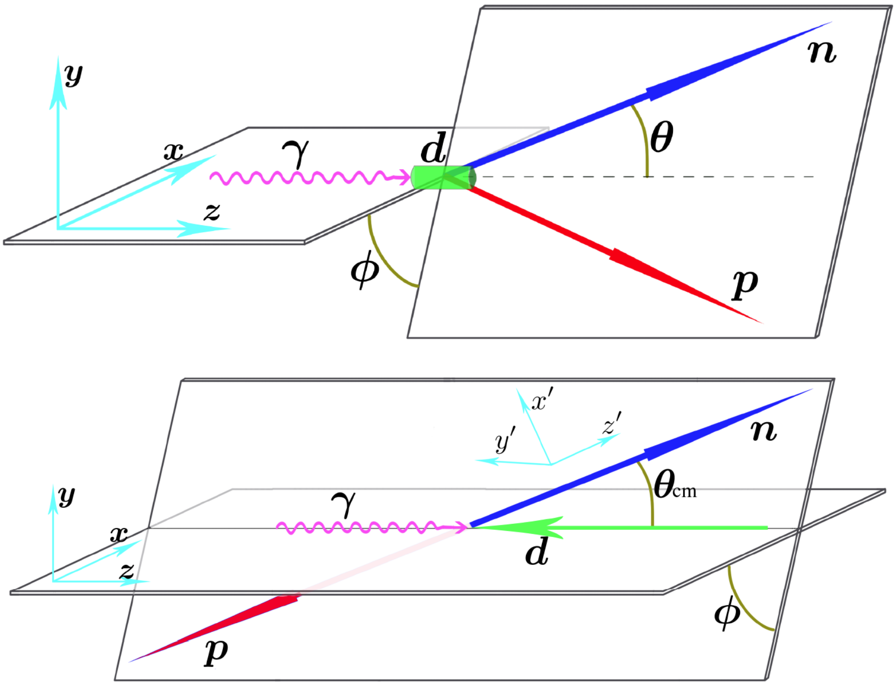

Figure 3.1 *The kinematics of the reaction $\gamma d \to pn$ as depicted in the lab (top) and centre of mass (bottom) frames [27]. The unprimed axes, x, y and z are defined such that the z axis is along the photon beam line and the x axis is parallel to the laboratory floor.*

asymmetries through which some polarisation observables can be determined.

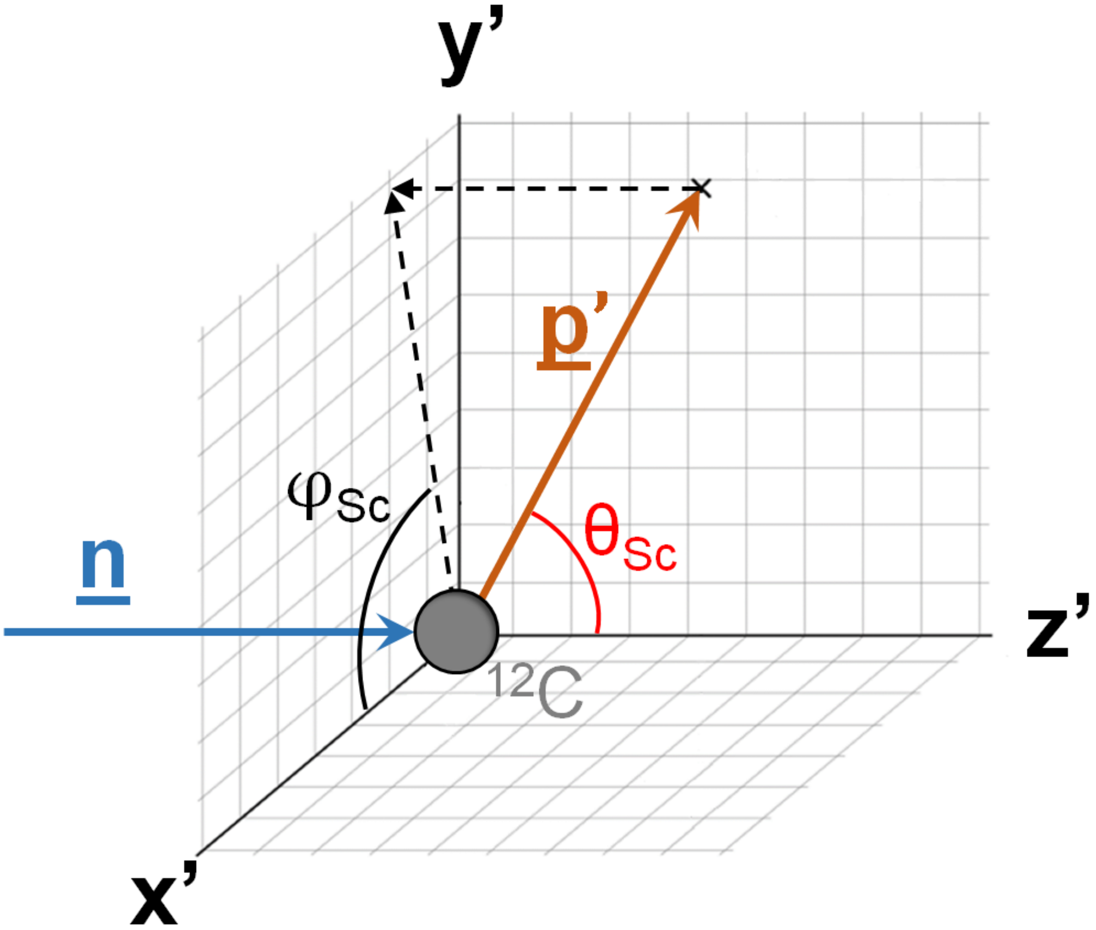

Figure 3.2 *Neutron, n, undergoing a charge exchange interaction with a carbon nucleus in the (x', y', z') frame as defined by Equations (3.1–3.3). The angles* θ_{Sc} *and* ϕ_{Sc} *for the recoiling proton,* p'*, are shown (modified version of [28]).*

Table 3.1 *Formulae for polarisation observables in deuteron photodisintegration [3]. How the terms $F_{i\pm}$ relate to the helicity amplitudes are defined in Table 3.2.*

Observable	Helicity Amplitude Combination
p_y	$2\Im\sum_{i=1}^{3}[F^*_{i+}F_{(i+3)-} + F_{i-}F^*_{(i+3)+}]$
T	$2\Im\sum_{i=1}^{2}\sum_{j=0}^{1}[F^*_{(i+3j)+}F^*_{(i+3j+1)+} + F_{(i+3j)-}F^*_{(i+3j+1)-}]$
Σ	$2\Re\sum_{i=1}^{3}(-)^i[-F_{i+}F^*_{(4-i)-} + F_{(3+i)+}F^*_{(7-i)-}]$
T_1	$2\Im\sum_{i=1}^{3}(-)^i[-F_{i+}F^*_{(7-i)+} + F_{i-}F^*_{(7-i)-}]$
$\mathrm{C}_{x'}$	$2\Re\sum_{i=1}^{3}[F^*_{i+}F_{(i+3)-} + F_{i-}F^*_{(i+3)+}]$
$\mathrm{C}_{z'}$	$\sum_{i=1}^{6}\{\lvert F_{i+}\rvert^2 - \lvert F_{i-}\rvert^2\}$
$\mathrm{O}_{x'}$	$2\Im\sum_{i=1}^{3}(-)^{i+1}[F_{i+}F^*_{(7-i)+} + F_{i-}F^*_{(7-i)-}]$
$\mathrm{O}_{z'}$	$2\Im\sum_{i=1}^{3}(-)^{i+1}[F_{i+}F^*_{(4-i)-} + F_{(3+i)+}F^*_{(7-i)-}]$

3.2 Polarisation Observables in Deuteron Photodisintegration

Polarisation observables in deuteron photodisintegration differ from those in photon-nucleon (γN) interactions (see Appendix C). The differential cross section for the process $\gamma d \rightarrow pn$ can be expressed as [3]

$$\frac{d\sigma}{d\Omega} = \frac{1}{2}\left(\frac{d\sigma}{d\Omega}\right)_0 [1 + p^N_y p_y + p^d_y T - p^{\mathrm{lin}}_\gamma(\Sigma + p_y T_1)\cos(2\phi) + p^{\mathrm{lin}}_\gamma(O_{x'}p_{x'} + O_{z'}p_z)\sin(2\phi) + p^{\odot}_\gamma(C_{x'}p_{x'} + C_{z'}p_{z'})] \tag{3.4}$$

where $\left(\frac{d\sigma}{d\Omega}\right)_0$ is the differential cross section for unpolarised photons; p^d_y and p^N_y are the polarisations of the deuteron target and outgoing nucleon; p^{lin}_γ and $p^{\odot}_\gamma$ are the degrees of linear and circular polarisation of the photon beam and p_i is the direction of the polarisation of the outgoing particle with respect to the x', y' or z' axes. The other quantities in this equation are the polarisation observables, these observables are formulated in terms of their helicity amplitude components in Table 3.1.

The observables p_y, Σ and T are the single polarisation observables that correspond to the induced proton (or neutron if the neutron is considered)

Table 3.2 *Relation between terms $F_{i\pm}$ and the helicity amplitudes [3, 29]. The formalism is $\langle \lambda_p, \lambda_n | J \cdot \epsilon_+ | \lambda_d \rangle$ where λ_i is the helicity of particle i, J is the angular momentum operator and ϵ_+ is the photon spin.*

F Representation	Amplitude
$F_{1\pm}$	$\langle \pm\frac{1}{2}, \pm\frac{1}{2} | J \cdot \epsilon_+ | 1 \rangle$
$F_{2\pm}$	$\langle \pm\frac{1}{2}, \pm\frac{1}{2} | J \cdot \epsilon_+ | 0 \rangle$
$F_{3\pm}$	$\langle \pm\frac{1}{2}, \pm\frac{1}{2} | J \cdot \epsilon_+ | -1 \rangle$
$F_{4\pm}$	$\langle \pm\frac{1}{2}, \mp\frac{1}{2} | J \cdot \epsilon_+ | 1 \rangle$
$F_{5\pm}$	$\langle \pm\frac{1}{2}, \mp\frac{1}{2} | J \cdot \epsilon_+ | 0 \rangle$
$F_{6\pm}$	$\langle \pm\frac{1}{2}, \mp\frac{1}{2} | J \cdot \epsilon_+ | -1 \rangle$

polarisation, the linearly polarised photon beam asymmetry and the target asymmetry respectively. The quantities T_1, $O_{x',z'}$ and $C_{x',z'}$ are the double polarisation observables. T_1 is the asymmetry of the recoil proton polarisation from a linearly polarised photon beam. $O_{x',z'}$ and $C_{x',z'}$ are the components of the recoil proton polarisation (in the x' or z' plane depending upon subscript) from linear ($O_{x',z'}$) and circularly ($C_{x',z'}$) polarised beams.

3.3 Experimental Determination of Σ

Polarisation observables can be determined experimentally by examining asymmetries. The method by which the observable Σ can be determined in this manner is outlined in an analysis note for the CLAS collaboration at Jefferson Lab [30]. The polarized differential cross section for reactions initiated by a linearly polarised photon beam is given by

$$\frac{d\sigma}{d\Omega} = \left(\frac{d\sigma}{d\Omega}\right)_0 \left(1 + p_\gamma^{\text{lin}} \Sigma \cos(2\beta)\right) , \tag{3.5}$$

where $\left(\frac{d\sigma}{d\Omega}\right)_0$ is the unpolarised differential cross section, p_γ^{lin} is the degree of photon linear polarisation, Σ is the beam-spin asymmetry observable and β is the angle between the photon polarization vector and the reaction plane. β can be expressed in terms of the angle ϕ and an angular offset, ϕ_0, which corresponds to the offset of the photon polarisation from the x-axis, via the relation

$$\beta = \phi - \phi_0. \tag{3.6}$$

Σ could in theory be extracted directly from Equation (3.5) by fitting a $\cos(2\beta)$ function to the polarised differential cross section. However, doing so would require that the acceptance is accurately determined. By combining linearly polarised data with unpolarised data, the need to know the detector acceptance can be eliminated. Equation (3.5) is proportional to the yield given by

$$N(\phi) \sim F \left(1 + p_\gamma^{\text{lin}} \Sigma \cos(2\beta)\right) A(\phi), \tag{3.7}$$

where F is the incident photon flux and $A(\phi)$ is the detector acceptance as a function of phi. The $A(\phi)$ term can be eliminated by taking a ratio of the yield for the linearly polarised and unpolarised cases producing

$$\frac{N(\phi)}{N(\phi)^a} = \frac{F}{F^a} \left(1 + p_\gamma^{\text{lin}} \Sigma \cos(2\beta)\right). \tag{3.8}$$

In Equation (3.8) F and F^a are the photon fluxes for the linearly polarised case and the unpolarised case respectively. However, Equation (3.8) is only valid under the assumption that $A(\phi)$ is constant within each ϕ bin and that it does not vary in time. Σ can also be determined without measuring unpolarised data. By measuring two different photon linear polarisations orientated at 90° to each other Σ can also be determined through asymmetries. The two polarisations measured are typically referred to as parallel (para, $\|$) and perpendicular (perp, $\perp$). The “parallel” axis is at 45° from $\phi = 0°$ and the “perp” axis is at 135°. The yields for the para and perp cases are given by

$$N(\phi)^{\|,\perp} \sim F^{\|,\perp} \left(1 \pm p_\gamma^{\|,\perp} \Sigma \cos(2(\phi - \phi_0))\right) A(\phi), \tag{3.9}$$

where $F^{\parallel,\perp}$ is incident the incident photon flux and A(ϕ) is again the acceptance. In this case ϕ_0 is equal to 45°. By taking the ratio between linear combinations of the polarised yields, Σ can be determined. Specifically in the asymmetry:

$$R = \frac{N(\phi)^{\parallel} - N(\phi)^{\perp}}{N(\phi)^{\parallel} + N(\phi)^{\perp}}, \tag{3.10}$$

the acceptance terms cancel out (under the same assumptions outlined previously). If the total yields are scaled (using the photon fluxes) such that they are equal and under the assumption that the degree of linear polarisation in the para and perp case is equal ($p_{\gamma}^{\parallel} = p_{\gamma}^{\perp} = p_{\gamma}^{\mathrm{lin}}$) then the ratio given in Equation (3.10) is equivalent to

$$\frac{N(\phi)^{\parallel} - N(\phi)^{\perp}}{N(\phi)^{\parallel} + N(\phi)^{\perp}} = p_{\gamma}^{\mathrm{lin}} \Sigma \cos(2(\phi - \phi_0)). \tag{3.11}$$

This results implies that by measuring the experimental yield (as a function of ϕ) for the para and perp case and constructing the asymmetry defined by Equation (3.10) then the observable Σ can be determined. Fitting the asymmetry with a function of the form $P_0 cos(2(\phi - \phi_0))$, Σ can be calculated simply by dividing the fit parameter P_0 with the degree of linear photon polarisation, $p_{\gamma}^{\mathrm{lin}}$. Assuming that the uncertainties, $\sigma_{N^{\parallel}}$ and $\sigma_{N^{\perp}}$, follow a Poisson distribution they can be expressed as $\sigma_{N^{\parallel}} = \sqrt{N^{\parallel}}$ and $\sigma_{N^{\perp}} = \sqrt{N^{\perp}}$. From propagation of uncertainties the statistical uncertainty, σ_A, on the asymmetry value, A, can be shown to be given by

$$\sigma_A = \frac{2}{(N^{\parallel} + N^{\perp})^2} \sqrt{N^{\parallel} N^{\perp} (N^{\parallel} + N^{\perp})}. \tag{3.12}$$

Care must be taken to ensure that yields, $N^{\parallel}$ and $N^{\perp}$, are normalised correctly and that the degree of polarisation is equivalent for each orientation. If this is not the case the extraction of Σ will be much more complicated as discussed in [30]. The choice of the number of bins in ϕ is also important due to the crucial assumption that the acceptance is constant within ϕ bins. This may not be the case in reality but this can be examined. The potential effect of the choice of ϕ binning on the final results for Σ is discussed further in Section 8.3.

3.4 Experimental Determination of $C_{x'}$

In a similar manner to Σ, the recoil polarisation observable $C_{x'}$ can be determined by forming and fitting asymmetries. When considering secondary scattering of reaction products in some analysing material the azimuthal distribution of secondary scattered particles takes the form

$$N(\theta_{\text{Sc}}, \phi_{\text{Sc}}) \sim N_0(\theta_{\text{Sc}}) \left(1 + A(\theta_{\text{Sc}}) \left[p_y \cos(\phi_{\text{Sc}}) - p_x \sin(\phi_{\text{Sc}})\right]\right), \tag{3.13}$$

where $N_0(\theta_{\text{Sc}})$ is the number of detected particles that scattered with angle θ_{Sc} and $A(\theta_{\text{Sc}})$ is the analysing power at angle θ_{Sc} (see Section 3.4.1) [31, 32]. $N_0(\theta_{\text{Sc}})$ depends upon the polarimeter acceptance, $\Omega(\theta_{\text{Sc}}, \phi_{\text{Sc}})$, the total number of scattered particles in the analysing material, N_{Sc} and the acceptance of the unscattered particles, $K(\theta_{\text{p}}, \phi_{\text{p}})$. This formalism is implying that the neutron, n, from deuteron photodisintegration undergoes a charge exchange interaction to p' and the proton, p, is not scattered. The relation between these terms is given by

$$N_0(\theta_{\text{Sc}}) = \Omega(\theta_{\text{Sc}}, \phi_{\text{Sc}}) K(\theta_{\text{p}}, \phi_{\text{p}}) N_{\text{Sc}}. \tag{3.14}$$

By measuring the yield across a range of θ_{Sc} and θ_{p} the dependence upon the polar angle can be integrated out. Combining Equations (3.13) and (3.14) yields

$$N(\phi_{\text{Sc}}) = N_{\text{Sc}} \left(1 + A_{\text{Eff}} \left[p_y \cos(\phi_{\text{Sc}}) - p_x \sin(\phi_{\text{Sc}})\right]\right) \Omega\phi_{\text{Sc}} K(\phi_{\text{p}}), \tag{3.15}$$

where A_{Eff} is the effective analysing power of the reaction (see Section 3.4.1). As in the determination of Σ, the acceptance can be removed from the determination of $C_{x'}$ by forming asymmetries. In the case of $C_{x'}$ the asymmetry is in terms of the beam helicity. The yield for a given helicity state (+ or −) is

$$N^{\pm}(\phi_{\mathrm{Sc}}) = N_{\mathrm{Sc}}\left(1 + A_{\mathrm{Eff}}\left[p_y \cos(\phi_{\mathrm{Sc}}) \mp p_x \sin(\phi_{\mathrm{Sc}})\right]\right)\Omega\phi_{\mathrm{Sc}}K(\phi_{\mathrm{p}}), \tag{3.16}$$

where for recoil particles produced with a circularly polarised photon beam (of polarisation degree $P_\gamma^{\odot}$), $p_x = P_\gamma^{\odot}C_{x'}$ and $p = p_y$. Forming the asymmetry $\frac{N^- - N^+}{N^- + N^+}$ yields the relation

$$\frac{N^- - N^+}{N^- + N^+} = \frac{A_{\mathrm{Eff}}P_\gamma^{\odot}C_{x'}\sin(\phi_{\mathrm{Sc}})}{1 + A_{\mathrm{Eff}}p_y\cos(\phi_{\mathrm{Sc}})}. \tag{3.17}$$

Thus by forming asymmetries of the yield as a function of ϕ_{Sc}, the observable $C_{x'}$ can be determined by fitting the asymmetries with a function of the form

$$f(\phi_{\mathrm{Sc}}) = \frac{P_1 \sin\phi_{\mathrm{Sc}}}{1 + P_2\cos\phi_{\mathrm{Sc}}}. \tag{3.18}$$

To extract values of $C_{x'}$ from such a fit the effective analysing power, A_{Eff}, must be determined.

3.4.1 Analysing Power

Interactions between pairs of nucleons (N-N interactions) are complex interactions. The force between nucleons is a residual of the QCD colour force. These interactions can be considered in analogy to van der Waals forces except between quarks in the nucleons as they approach each other. The nuclear force is strongly spin dependent [33]. In interactions where a polarised nucleon interacts with another nucleon (polarised scattering interactions) the spin-orbit coupling component of the nuclear force is particularly important. This terms couples the angular momentum l with the total spin of the nucleons, s. The potential

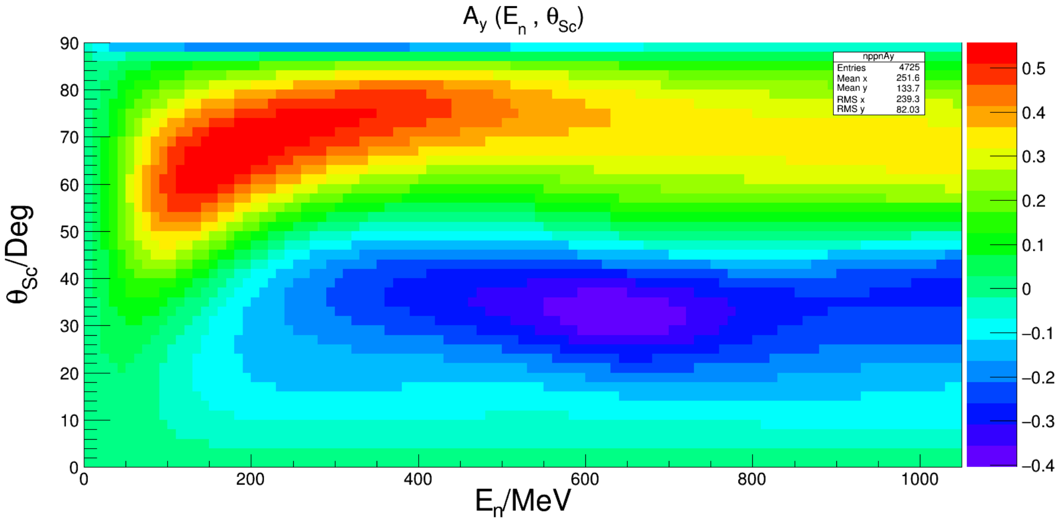

Figure 3.3 *A_y for the elastic scattering reaction $np \rightarrow pn$ as a function of θ_{Sc} and E_n. A colour scale for the value of A_y is included.*

between the nucleons in such an interaction can be written as $V_{so}(r)(l \cdot s)$ where $V_{so}(r)$ is a position dependent scalar. This spin-orbit term produces an angular distribution of the scattered particles that is dependent upon their spin. By examining the azimuthal distributions of the scattered particles information about the polarisation of the incident nucleon can be inferred. This azimuthal distribution can be shown to be the product of the initial polarisation and a quantity, A_y, referred to as the analysing power of the interaction [34].

This thesis considers interactions where polarised neutrons scatter from some carbon analysing material. In this reaction the effective analysing power, A_{Eff}, can be approximated from the determined values of the analysing power, A_y, from elastic np data [35]. $A_y(E_{\mathrm{n}}, \theta_{\mathrm{Sc}})$ from a PWA solution is depicted in Figure 3.3.

The analysing power for elastic neutron scattering from a quasi-free proton is typically larger than for quasi-elastic charge exchange interactions. The analysing power for the quasi-elastic case is approximately 70% of that for the elastic case [36]. In this first analysis of $C_{x'}$ the elastic scattering values of A_y have been assumed. The difference between the quasi-elastic and elastic values will need to be further assessed and accounted for a systematic error in the resulting values of $C_{x'}$. A_{Eff} is approximated from the distribution of A_y by plotting θ_{Sc} as a function of E_{n} for each angular and energy bin examined. The mean E_{n} and θ_{Sc} point from each plot is determined and the value of A_y from this point is taken by comparison with Figure 3.3. This value is used as the value of A_{Eff} to subsequently calculate $C_{x'}$.

Chapter 4

Current Searches for Exotic QCD States

Hadrons beyond the well known meson ($q\overline{q}$) and baryon (qqq) states were proposed by Gell-Mann [12] with the introduction of the quark model. A wide range of other colour-neutral states formed of quarks and gluons have been predicted since then. These include $q\overline{q}q\overline{q}$ [37, 38], $qqqq\overline{q}$ [38, 39] and $qqqqqq$ states [40–42]. Other possibilities for new states include objects formed only of gluons, glueballs [43, 44], as well as "hybrid" mesons [45], which contain one or more gluonic degrees of freedom in addition to $q\overline{q}$.

There is a long history of claimed observations for various exotic states, these are states with quantum numbers combinations that would be forbidden with a standard meson or baryon quark content. Following the prediction of the H-dibaryon (a state with $B\# = 2$ and S = -2) [41], there was a rush of experimental claims of observations [46]. However, as discussed by Clement [46], none of these observations stood up to further scrutiny. States of five quarks, referred to as pentaquarks [47], have also been the subject of many historical experimental searches and claims [48]. In particular the Θ^+ state gathered a lot of attention in the early 2000's with numerous claims of an observation. Following initial optimism, subsequent experiments failed to reproduce the early results, leading to the conclusion that such a state had not been found [49].

More recently the field of exotic states has been reinvigorated by a string of exciting new possibilities from high quality, high statistics observations of tetraquarks ($q\bar{q}q\bar{q}$), pentaquarks ($qqqq\bar{q}$) and hexaquarks ($qqqqqq$). In particular claims of tetraquark and pentaquark states by the LHCb collaboration have reignited the search for such exotic states with incredibly high statistical significance on their observations. A dibaryon state, the d*(2380), has also been observed by the WASA-at-COSY collaboration and studied in great detail in various reaction channels [50, 51].

This chapter will briefly discuss the tetraquark and pentaquark states recently observed by the LHCb collaboration. This is followed by a more in-depth review of the observations of the d*(2380) state. Future experimental prospects for the d*(2380) are discussed and the measurements presented in this thesis are put into context.

4.1 LHCb Tetraquark States

Measurements of $B \to K\pi^{\pm}\psi'$ decays at Belle observed a resonance-like structure in the invariant-mass spectrum of the $\pi^{\pm}\psi'$ component of the decay [52]. More recent work by the LHCb collaboration also observed a structure in this decay that was consistent with the results observed at Belle [53]. A clear bump at ∼4500 MeV, that is inconsistent with background predictions, can be seen in the $\pi^{\pm}\psi'$ invariant mass spectrum from this decay (see Figure 4.1). Additionally, the complex amplitudes of the resonance-fit exhibit clear resonance behaviour when plotted on an argand diagram (see Figure 4.2). The spin parity of the observed state was determined to be 1^{+}. This determination led the authors to rule out other possible interpretations of the state and conclude that the observed state is a bound four quark state with quark content $c\bar{c}d\bar{u}$ [53].

More recently, further results have indicated the presence of an additional four states that are potential tetraquark candidates. A narrow structure was observed in the $J/\psi\phi$ mass spectrum for $B^{+} \to J/\psi\phi K^{+}$ decays by the CDF collaboration [54]. Further investigation of these decays by the LHCb collaboration [55, 56] observed four structures in the decay of this state, the lightest of which had a mass consistent with the results from the CDF collaboration, albeit with a larger width. The four observed states can be seen in Figure 4.3. The four observed states are referred to as X(4140), X(4274), X(4500) and X(4700). It is particularly interesting that a tetraquark model [57] ,not only predicts the correct J^{PC} assignment of the observed X(4140), but also predicts a further state with the same J^{PC} at a slightly higher mass in the region of the observed X(4274) state.

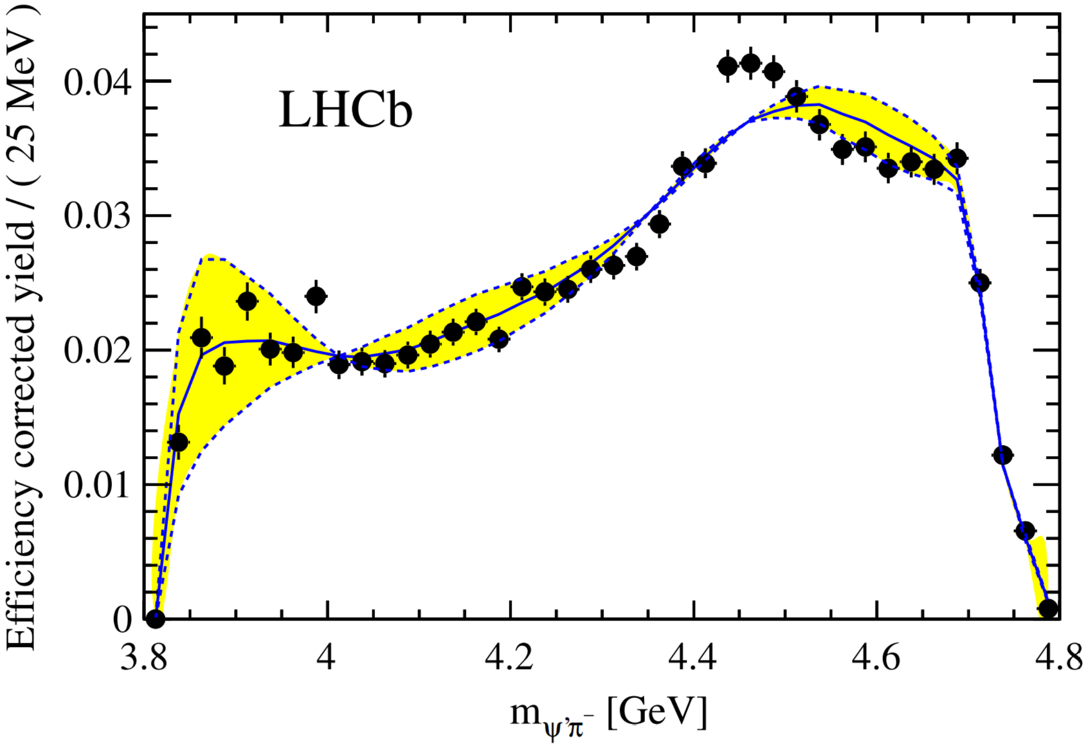

Figure 4.1 *Background subtracted* $m_{\psi'\pi^-}$ *distribution from the decay of* $B^0 \to \psi'\pi^- K^+$ *[53]. Data points are superimposed with reflections of* $\cos\theta_{K'}$ *moments (blue solid line) and their correlated statistical uncertainties (yellow band).*

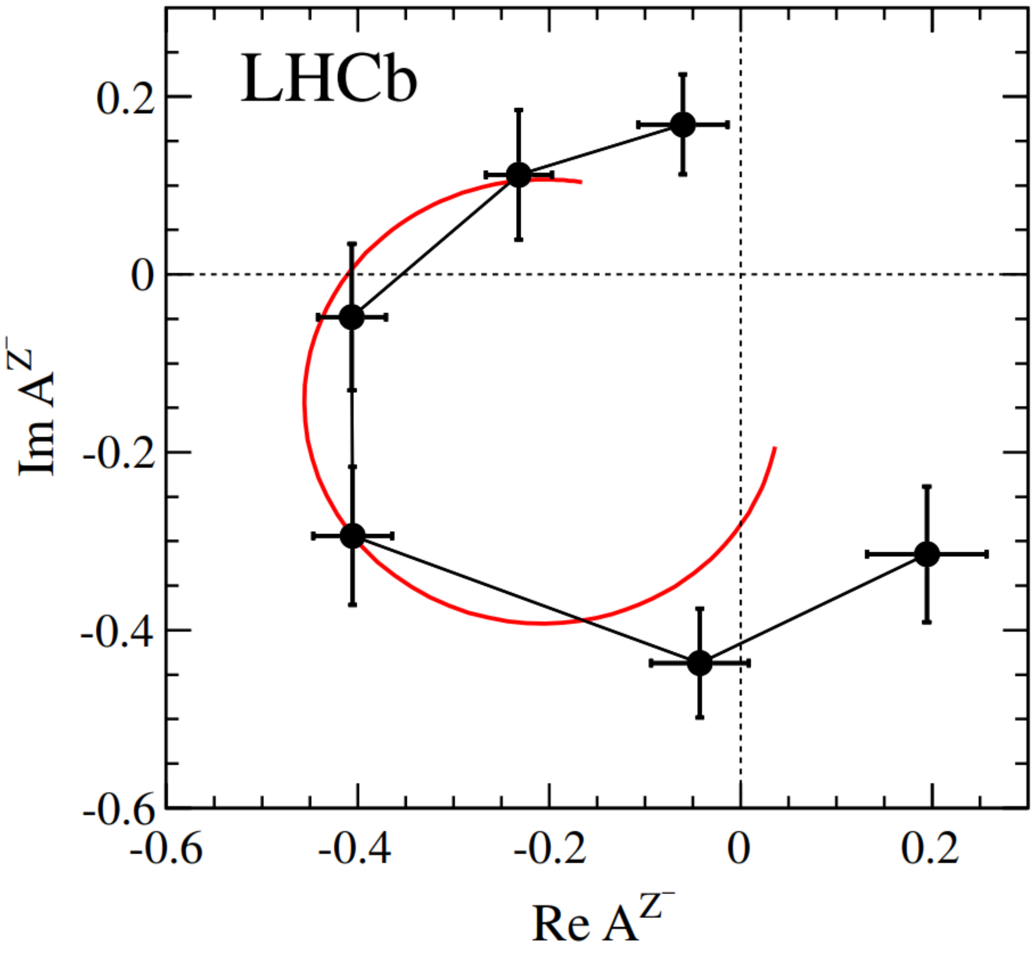

Figure 4.2 *Values of the Z_1^- amplitude for six bins in $m^2_{\psi'\pi^-}$ (points increase in value counterclockwise) with predictions from a Breit-Wigner formula shown in red [53].*

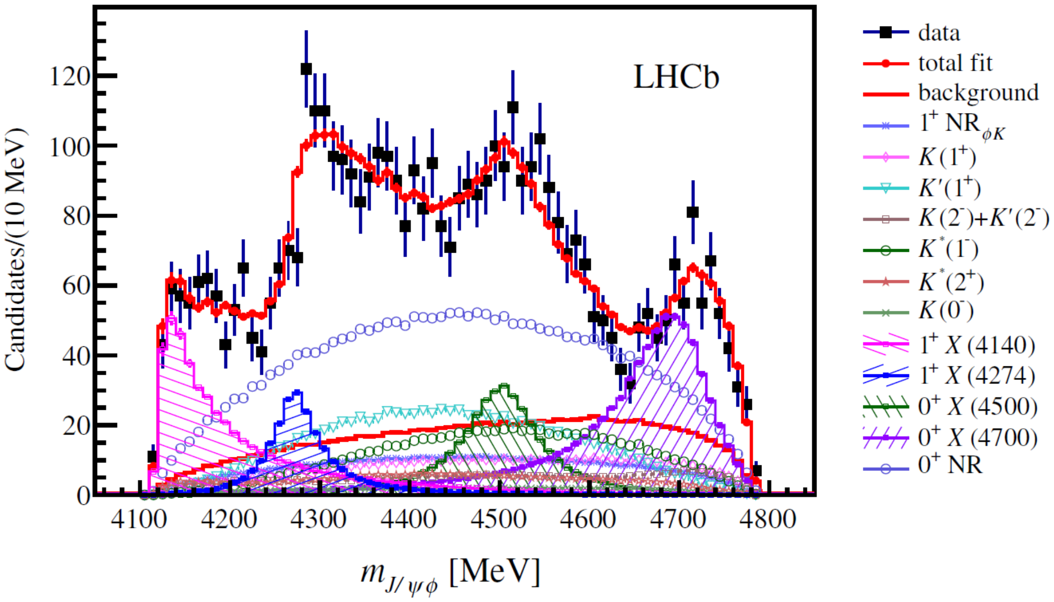

Figure 4.3 *Distributions of $J/\psi\phi$ invariant mass from the decay $B^+ \to J/\psi\phi K^+$ [55]. Components of the fit are included with a key on the right.*

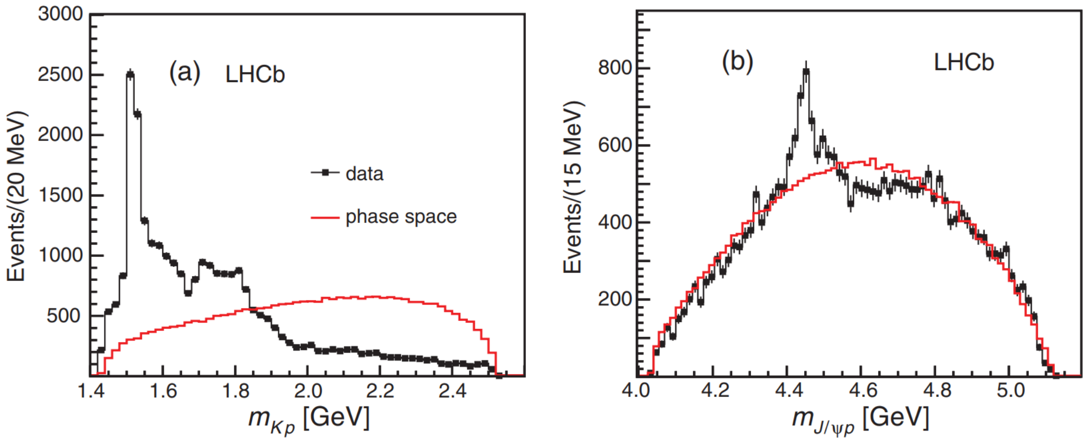

Figure 4.4 *Background substracted invariant mass distributions for K^-p (left, (a)) and $J/\psi p$ (right, (b)) combinations from $\Lambda_b^0 \to J/\psi K^- p$ decays [58]. The red curve shows expectations from phase space. A clear peak is observed in the distributions for $J/\psi p$.*

4.2 LCHb Pentaquark States

Recent measurements by the LHCb collaboration at CERN observed resonance-like structures in the $J/\psi p$ channel of $\Lambda_b^0 \to J/\psi K^- p$ decays [58]. A clear peak (see Figure 4.4, panel (b)) in the invariant-mass spectrum of the $J/\psi p$ combinations from this decay can be seen. The observed data cannot adequately be described without the inclusion of two Breit-Wigner resonances in the distribution. These resonances are attributed to two pentaquark states (of quark content $uudc\bar{c}$), $\mathrm{P_c}(4380)^+$ and $\mathrm{P_c}(4450)^+$. The resonance behaviour of the $\mathrm{P_c}(4450)^+$ state is particularly clear in the argand diagram (see Figure 4.5, panel (a)) of the complex amplitudes of the resonance fits. Further analysis of these observations also reached the conclusion that the data was consistent with the resonances proposed [59, 60].

Following the announcement of the observed $\mathrm{P_c}(4380)^+$ and $\mathrm{P_c}(4450)^+$ states, there were a wide range of theoretical interpretations of the results. Some of these interpretations attributed the states to anti-charmed meson-hyperon ($\overline{\mathrm{D}}$ or $\overline{\mathrm{D}}^*$ with Σ or Σ^*) molecular configurations [61, 62]. Other interpretations using diquark models predict a compact five quark system [63, 64]. A definitive theoretical description of the observations requires further study of the states observed at LHCb in addition to other potential pentaquark states. One such route for further study of the LHCb states would be to attempt to observe them

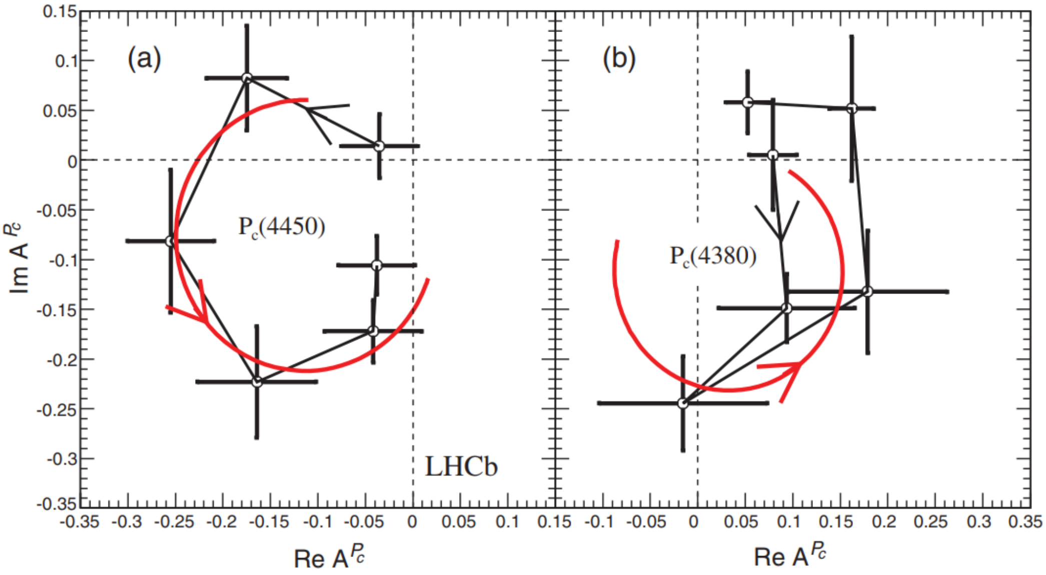

Figure 4.5 *Values of the complex amplitudes for the fits to the* $P_c(4450)^+$ *(left, (a)) and* $P_c(4380)^+$ *(right, (b)) states [58]. Values are plotted for six bins in* $m_{J/\psi p}$ *for each plot with values increasing counterclockwise. Solid red lines are the predictions from the Breit-Wigner formula over the same mass ranges with fixed* Γ_0 *and* M_0 *values.*

in photoproduction reactions as discussed by Wang, Kubarovsky and Karliner [65–67].

4.3 d*(2380) Dibaryon State

In measurements of double-pionic fusion of $p + d \rightarrow {}^3\text{He}\pi\pi$ in 1960 [68], an unexpected enhancement in the invariant-mass spectrum was observed close to the $\pi\pi$ production threshold. Subsequent measurements in 1961 [69] by the same researchers implied that this enhancement was isoscalar ($I_{\pi\pi} = 0$) in nature. This anomalous result was observed by other groups and evidence for the isoscalar nature of the state mounted [70, 71]. This enhancement is often referred to as the "ABC" effect after the authors of the initial research [68].

The impact of this effect is particularly pronounced at beam energies corresponding to the excitation of two Δ particles in the nuclear system. This observation led to the subsequent interpretation of the ABC effect as a t-channel $\Delta\Delta$ excitation [72, 73] (see Appendix B for explanation of t-channel process). Further theoretical studies discussed the potential of this excitation as a "dibaryon" resonance [74–76]. Recently this resonance was the subject of a large body of work by the WASA collaboration that carried out numerous measurements across different reaction channels. The measured resonance would come to be known as the d*(2380) dibaryon in reference to a state predicted from theoretical work [42, 77] and to follow the convention of resonance states (N* denoting $I = \frac{1}{2}$ resonances for example). The measurements at WASA and the properties of the d*(2380) inferred from them are discussed in the next subsection.

4.3.1 WASA Collaboration Measurements

Early measurements [50] of the $pd \rightarrow {}^3\text{He}\pi^+\pi^-$ and $pd \rightarrow {}^3\text{He}\pi^0\pi^0$ reactions using the WASA detector setup at the CELSIUS storage ring, once again observed the expected enhancement of the ABC effect. It was noted that the effect was particularly strong in the isoscalar $\pi^0\pi^0$ channel. These measurements were followed up by further exclusive and kinematically complete measurements of the double-pionic fusion reaction, $pn \rightarrow d\pi^0\pi^0$, at CELSIUS [51]. These measurements provided the first hints of a resonance-like structure as seen in Figure 4.6; however, due to limited statistics no firm conclusions could be drawn from these measurements. It was noted that the data is described very well by an s-channel resonance with a mass of 2.36 GeV/c^2 and a width of 80 MeV.

Following an upgrade of the WASA detector setup, further measurements of the

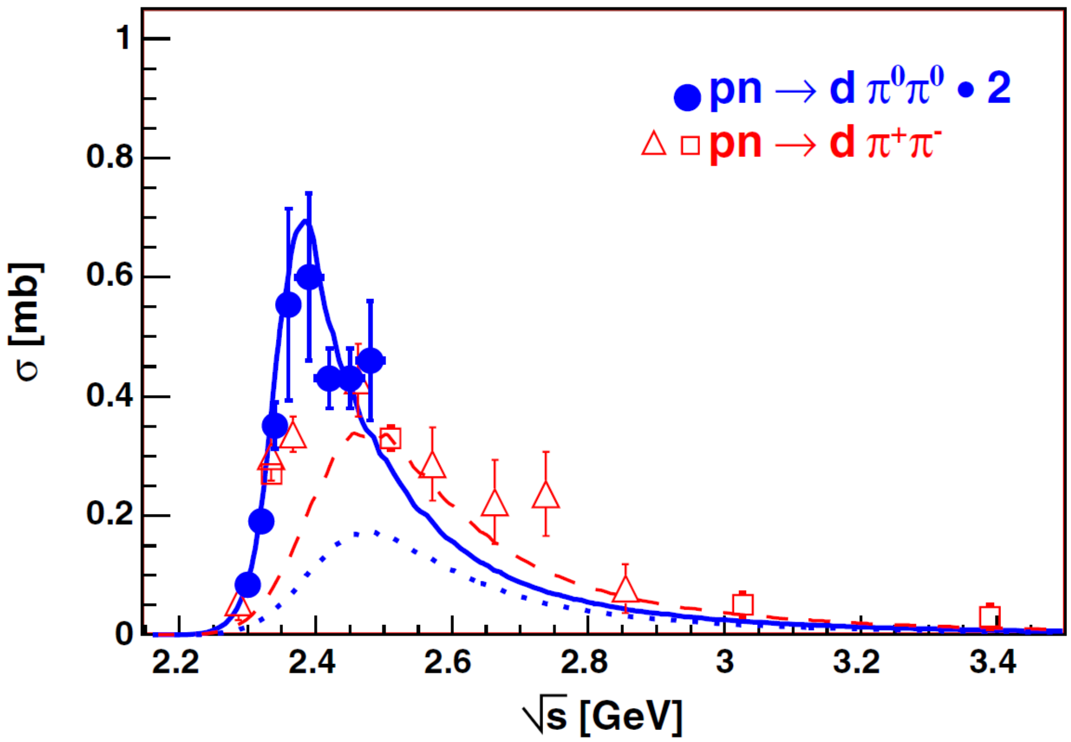

Figure 4.6 *A plot of the energy dependence of the cross section for the reactions* $pn \to d\pi^+\pi^-$ *and* $pn \to d\pi^0\pi^0$ *showing hints of an enhancement at around* $\sqrt{s}$ *= 2.4 GeV [51].*

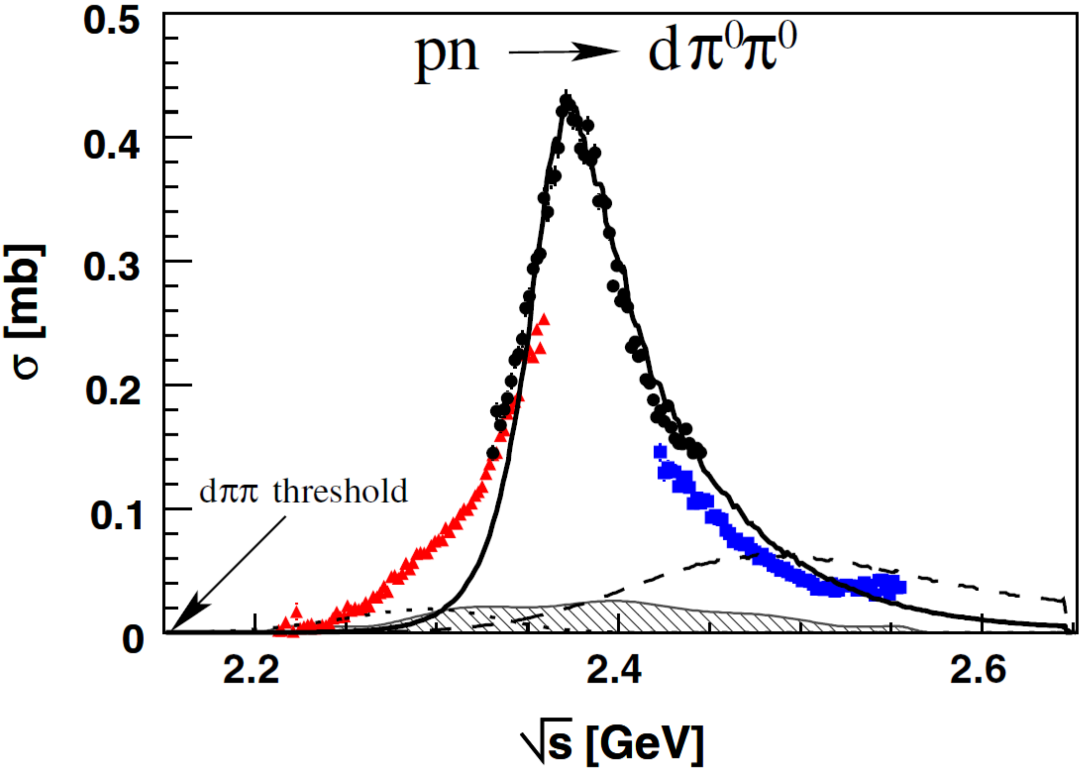

Figure 4.7 *The total cross section for the reaction* $pd \to d\pi^0\pi^0 + p_{\text{spectator}}$ *as a function of* $\sqrt{s}$ *showing a clear enhancement at* $\sqrt{s} \approx 2.4$ *GeV [78].*

$pn \to d\pi^0\pi^0$ reaction were taken at COSY [78]. These new measurements were again exclusive and kinematically complete but with far higher statistics than the previous measurement. These measurements concluded that the observed results (see Figure 4.7) were consistent with an s-channel resonance with $I(J^\pi) = 0(3^+)$ (determined from angular distributions), m ≈ 2.37 GeV and Γ = 70 MeV. As a caveat to this it was noted that for further confirmation elastic pn scattering should be measured as the observed resonance should also be prominent in this process; particularly in the $^3D_3$ - $^3G_3$ partial waves.

Further studies of double-pionic fusion processes were undertaken with the WASA detector setup at COSY [79]. In addition to the isoscalar $pn \to d\pi^0\pi^0$ channel these new studies also examined the isovector $pp \to d\pi^+\pi^0$ and isospin mixed (I = 0 and 1) $pn \to d\pi^+\pi^-$ channels with high statistics. The isovector channel (see Figure 4.8) appears to only have a broad structure which can be accounted for by a t-channel ΔΔ process. There is no evidence of a narrow resonance structure at $\sqrt{s} = 2.37$ GeV in this channel. For the isospin mixed channel (see Figure 4.9) there is a clear narrow resonance structure present in addition to a

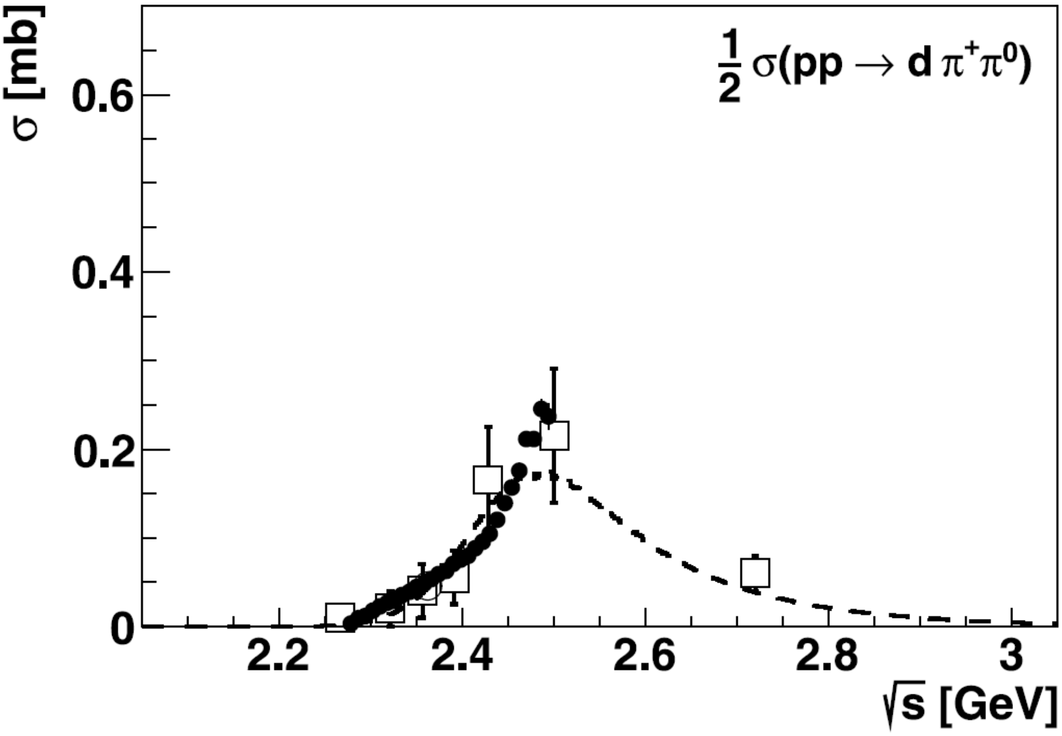

Figure 4.8 *The total cross section for the isovector reaction* $pp \rightarrow d\pi^+\pi^0$ *as a function of* $\sqrt{s}$ *showing a broad structure but no narrow resonance at* $\sqrt{s}$ *= 2.37 GeV [79].*

broader structure. The narrow structure observed in this channel is consistent with an s-channel resonance of m = 2.37 GeV and Γ = 70 MeV. This same structure is again observed in the isoscalar channel and is consistent with the previous measurements [78]. This work confirmed the purely isoscalar nature of the resonance. The need for further measurements, particularly on np scattering and non-fusion two pion production reactions (such as $np \rightarrow np\pi\pi$ and $np \rightarrow pp\pi^0\pi^-$), was also reiterated in this new work.

The $pn \rightarrow pp\pi^0\pi-$ [80], $np \rightarrow np\pi^0\pi^0$ [81] and $np \rightarrow np\pi^+\pi^-$ [82] channels were subsequently measured, again evidence of the contribution of the s-channel d* resonance was observed. More crucially measurements were also taken of polarised np scattering [83, 84]. To prove that the observed structure is indeed a true resonance it *must* be seen in this channel.

Exclusive and kinematically complete measurements of $\vec{n}p$ scattering were carried out using the WASA detector setup at COSY [84]. These measurements were carried out by utilising a polarised deuteron beam impinging upon a hydrogen

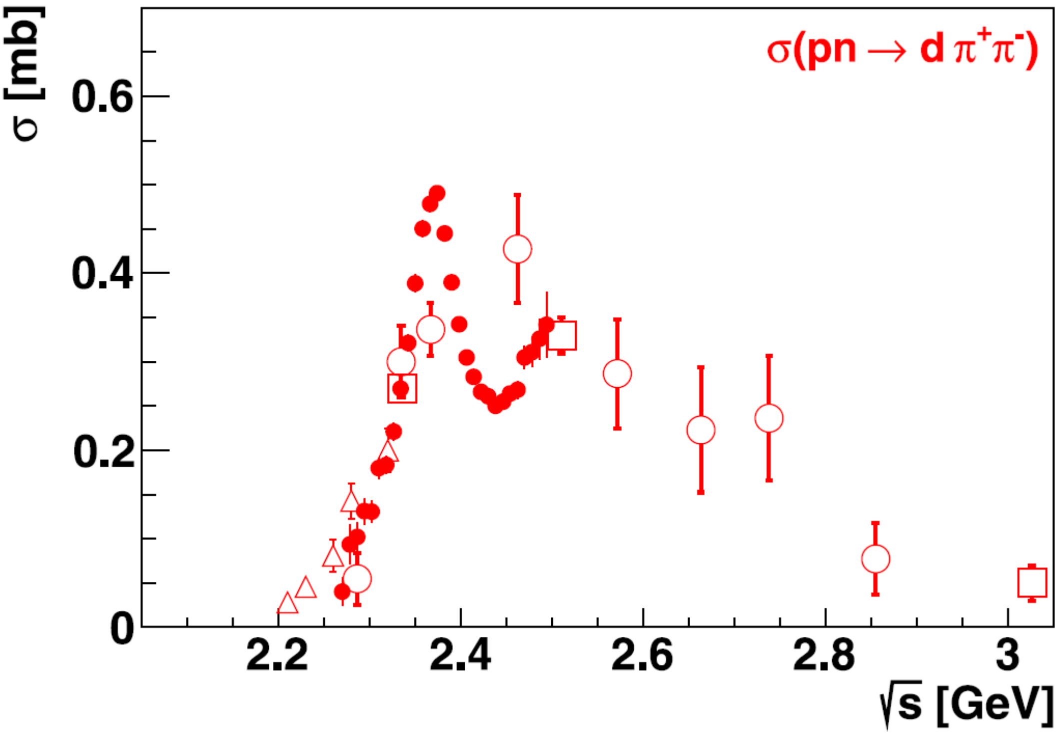

Figure 4.9 *The total cross section for the isospin mixed (I = 0 and 1) reaction* $pn \rightarrow d\pi^+\pi^-$ *as a function of* $\sqrt{s}$ *[79]. Previous data (open circles) did not have sufficient statistics to observe the narrow structure at* $\sqrt{s}$ *= 2.37 GeV seen with the new data (closed circles).*

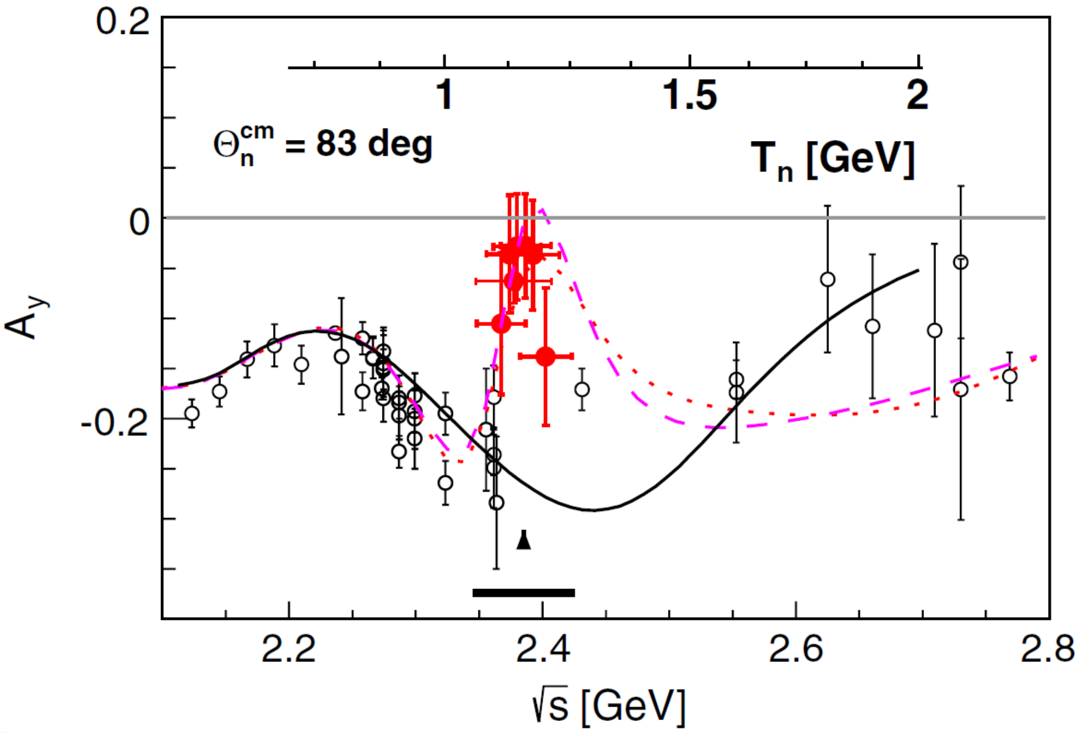

Figure 4.10 *The np analysing power, A_y, as a function of $\sqrt{s}$ [84]. The solid line is the unmodified SAID SP07 PWA solution [85], the dashed (dotted) lines show the modified weighted (unweighted) solution.*

target. This allows for the process $\vec{d}p \rightarrow np + p_{\mathrm{Spectator}}$ to be treated as a quasi free process so that $\vec{n}$p scattering can be studied. The analysing power, A_y, for this reaction was measured over a broad angular range. When these measurements were compared to the existing SAID SP07 [85] partial wave analysis (PWA) solution significant deviations were observed. However, when this PWA solution was revised by incorporating this new data set (now referred to as the AD14 fit [86]) clear poles were produced in the $^3D_3$ - $^3G_3$ partial waves. This revised solution is also a very good fit to the data as seen in Figures 4.10 and 4.11. As mentioned in [84] due to the proportionality of A_y to the P_3^1 Legendre polynomial the resonance behaviour is strongest at $\theta^{CM} = 90°$, hence the clear effect observed at 83° seen in Figure 4.10. Additionally pronounced looping behaviour can be seen in Figure 4.11; such behaviour is strongly indicative of a resonance.

Further evidence has been observed in other hadron production channels, such as the double-pionic fusion to ^{3}He and the double-pionic fusion to ^{4}He channels [87, 88]. The measurements detailed in this subsection support the existence of a narrow s-channel resonance of mass m = 2.37 GeV, $\Gamma = 70$ MeV and $I(J^\pi) = 0(3^+)$. It is particularly striking that these measurements agree very well with

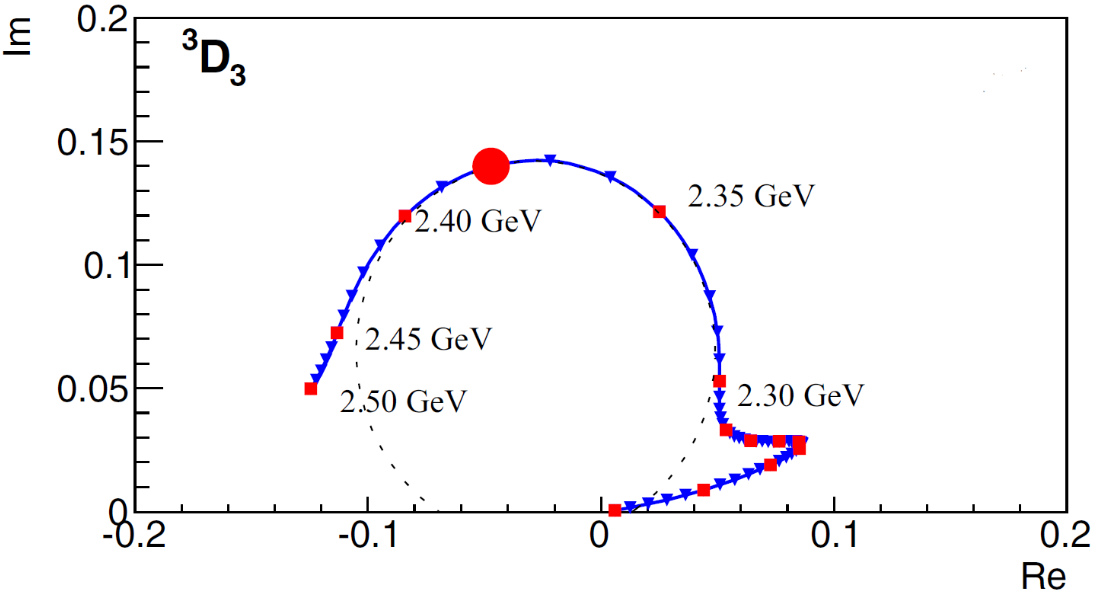

Figure 4.11 *Argand diagram of the* $^3D_3$ *partial wave in the modified SAID PWA solution showing looping behaviour [83]. The pole position is indicated by the large solid red circle.*

early theoretical predictions [40, 42] of such a state as discussed below.

Modern chiral quark model theory predictions ([89] and references therein) reproduce this state with roughly the correct mass and width. These model predictions are also able to predict the size of the state. Hadron production measurements such as those detailed in this subsection do not provide information on the size or the structure of the d*(2380). Measurements of the d*(2380) using electromagnetic probes will provide access to such properties however. By examining EM induced reactions the transition and electromagnetic form factors can be determined. The transition form factors give access to the size and structure of the state [46, 90]. Examination of the electric quadrupole and magnetic dipole (and other multipolarity) moments can also provide information about the structure of the resonance [91]. Previous relevant experiments using EM probes are discussed in the next subsection.

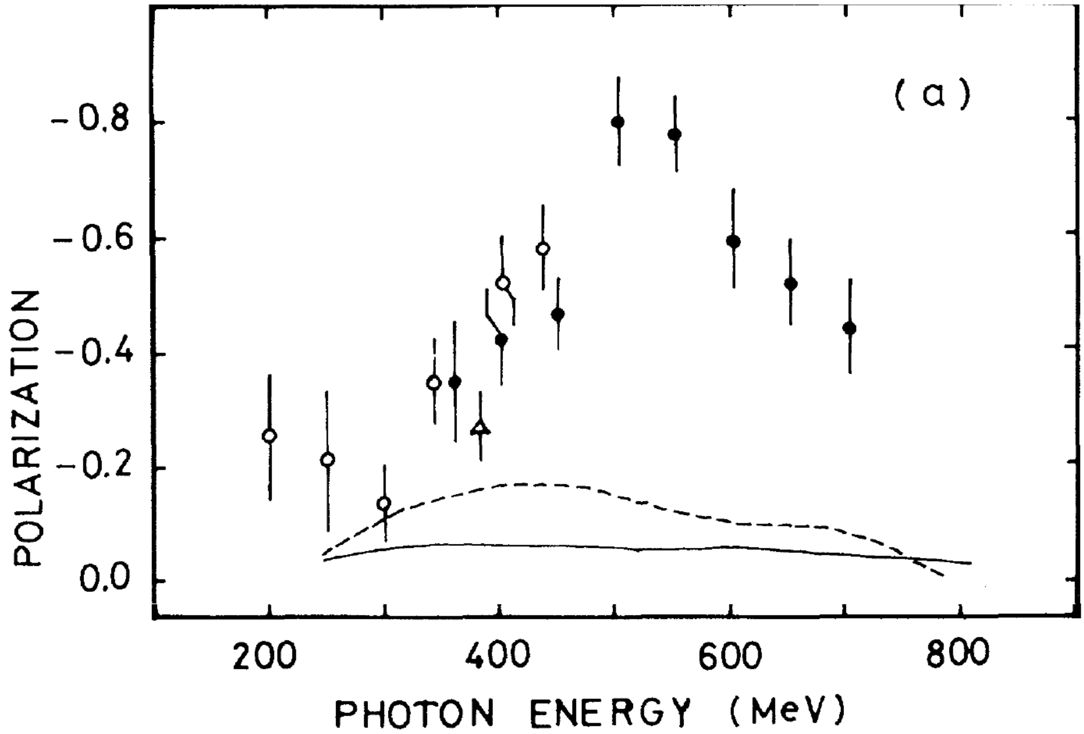

Figure 4.12 *The proton polarisation at 90° in the centre of mass system as a function of the photon energy [92]. Data points from other sources are shown as open circles [93] and triangles [94]. The lines show basic theoretical predictions.*

4.3.2 Photoproduction - Previous Hints

The interpretation by Kamae and Fujita [76] of the structure seen at $\sqrt{s} =$ 2380 MeV as being a potential dibaryon resonance was based upon work on deuteron photodisintegration [92]. In these measurements the final state proton polarisation from deuteron photodisintegration ($\gamma d \rightarrow \vec{p}n$) was determined and an anomalous peaking in the polarisation was observed at photon energies (E_γ) of $\approx$ 550 MeV (Figure 4.12). Note that in terms of $\sqrt{s}$, a photon energy of 550 MeV is roughly 2362 MeV in the γd system. This strange behaviour had been hinted at by previous measurements [93, 94], however, these earlier measurements were at lower energies and over a relatively limited range of energies. Nevertheless, these measurements disagreed with theoretical models available at the time [95] as can be seen in Figure 4.13.

A range of subsequent measurements [96–101] of the proton polarisation from this reaction were carried out. A review article on the subject [3] compiled the range of measurements as can be seen in Figure 4.14. Despite some disagreement

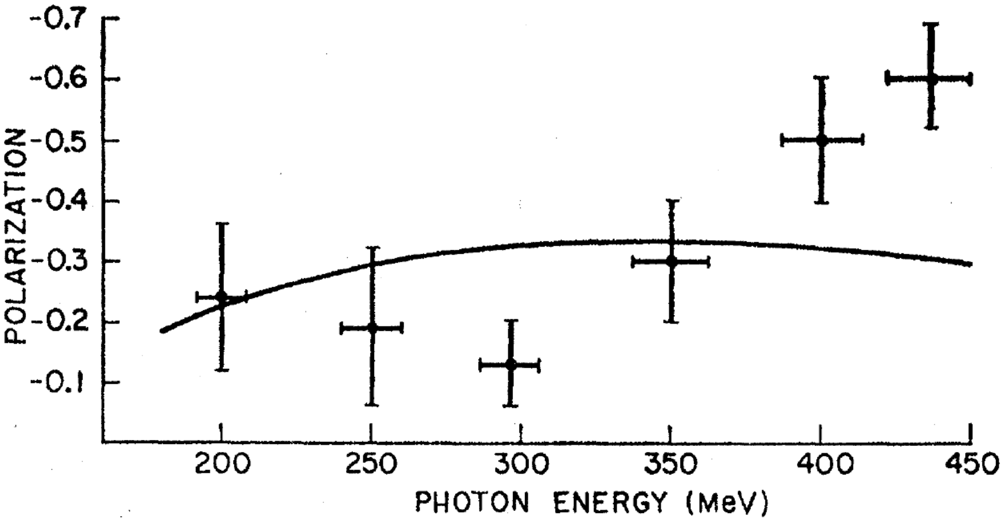

Figure 4.13 *The proton polarisation at 90° in the centre of mass system as a function of the photon energy [93]. An increase that is inconsistent with a theory prediction (Solid line, based on [95]) is seen as the photon energy increases.*

at energies above ∼ 600 MeV (reasons for this and for why the Kharkov measurements [98–100] are not generally particularly reliable, are discussed briefly in [3, 101]) the sharp increase in the proton polarisation at energies between 500 and 600 MeV is again observed. Note that the measurements of p_y are focused at 90°. As with A_y in np scattering, the polarisation of the outgoing nucleons from this reaction should be proportional to the P_3^1 Legendre polynomial [46], so should again have the largest effect at 90°.

Kamae [76] proposed a deeply bound $\Delta - \Delta$ system as an explanation for the observed behaviour and made tentative links to the ABC effect. They conclude that the anomaly observed is due to an $I(J^\pi) = 0(3^+)$ dibaryon resonance. Similar conclusions are also drawn by Ikeda [96], although this work also proposes an additional dibaryon resonance in the region. Further work by Ganenko [100] also attributes this behaviour to a dibaryon resonance. Whilst it is exciting to note that the observed behaviour coincides with the mass of the d*(2380) and that the proposed $I(J^\pi)$ values for the resonance match those observed in the WASA measurement it should be noted that there are some issues.

All conclusions drawn estimate a width for the state that is far broader than that observed for the d*(2380); this is likely due to the relatively limited number of data points (and statistics) available for the measurements across the crucial

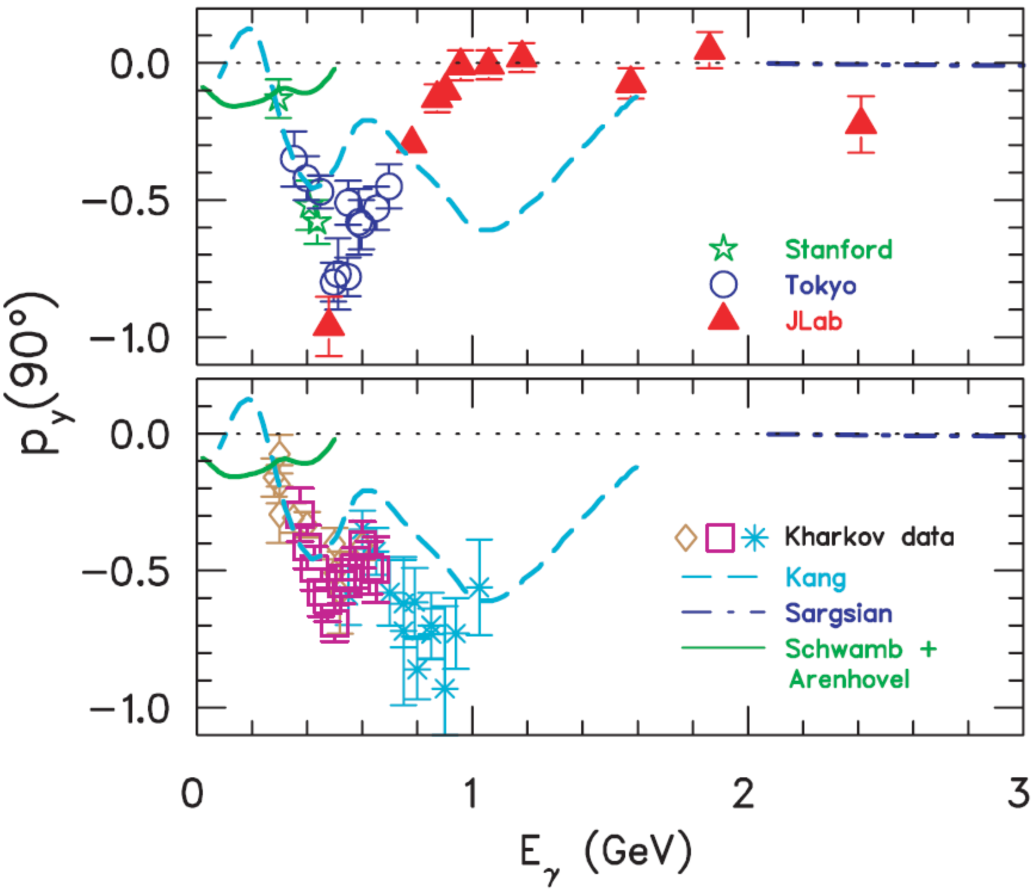

Figure 4.14 *The proton polarisation at 90° in the centre of mass system as a function of the photon energy [3]. Results from numerous measurements are plotted including Stanford [93], Tokyo [96, 97], Jeferson Lab (JLab) [101] and Kharkov [98–100]. Note that the Kharkov results are deliberately plotted separately due to issues with the data (discussed in [3]).*

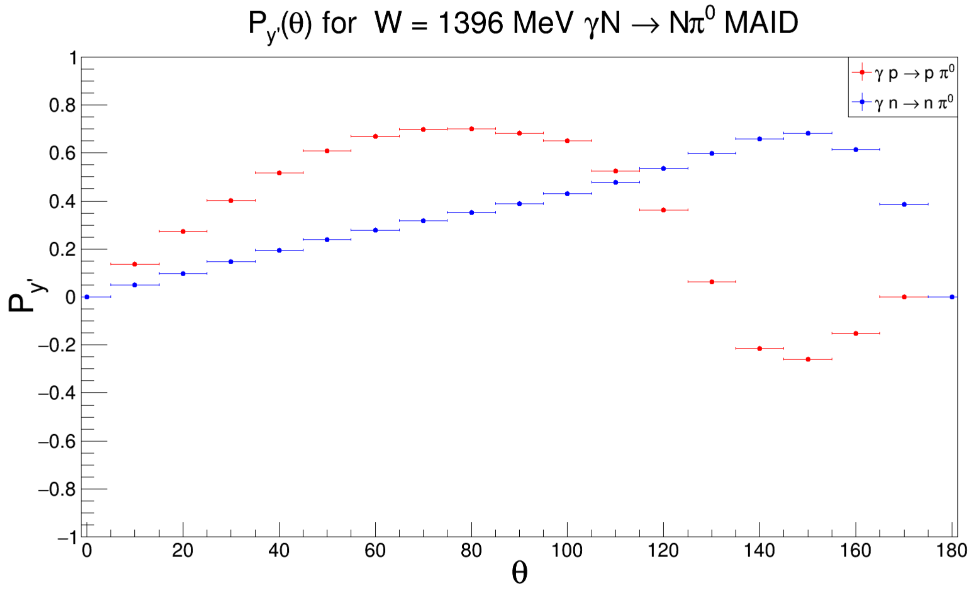

Figure 4.15 *MAID model predictions for $p_{y'}$ for $\gamma N \rightarrow \pi^0 N$ with photon polarisation = 1 and E_γ = 570 MeV ($W = \sqrt{s} \approx$ 1396 MeV for γN) [102].*

energy range of 400-600 MeV. It is also particularly problematic that all of the measurements carried out so far only the proton final state polarisation has been determined. If a similar enhancement of the polarisation of the final state neutron was also measured with the same characteristics this would be a strong indication of the formation of a high-spin resonance state from this reaction. Similarly to the *pn* scattering measurements [84] the strength and direction of the polarisation should be identical for the proton and the neutron for the $^3D_3$ - $^3G_3$ partial waves. This is unlike in meson production reactions on the nucleon where model predictions (MAID [102]) indicate that $p_{y'}$ will differ for the proton and neutron as seen in Figure 4.15. As such there is a clear need for further tests of nucleon polarisation from deuteron photodisintegration as a test of the d*(2380) hypothesis and as a potential key to unlocking further information about the size and structure of this state [46, 90]. This is the motivation behind the experimental work detailed in this thesis.

4.3.3 Structure of the d*(2380)

The size and structure of exotic hadrons is a subject of theoretical and experimental interest. Whether these objects are truly compact systems of six (or four/five) quarks or more like "molecular" systems of baryons and mesons is so far an unanswered question. As discussed for the LHCb pentaquark results, there are many theoretical models proposed to explain the results [61–64].

One property that is sensitive to the structure of the state is its size. An estimate for the radius of a system of two quark clusters can be estimated from the binding energy, ϵ, of the state via [46, 103].

$$r \approx \frac{\hbar c}{\sqrt{2m\epsilon}} \tag{4.1}$$

The states observed at LHCb are generally loosely bound near threshold states and as such the above relation predicts radii on the order of 10's of fm. This implies that they are extended molecular states. In contrast this relation predicts a radius of ∼0.5 fm for the d*(2380) implying a compact hexaquark system.

Although a rough estimate, this conclusion is also implied by theoretical calculations which predict that the observed d*(2380) is a hexaquark-dominated state [89], being roughly 66% hexaquark and 33% molecular. These calculations also predict a very small, compact state (see Figure 4.16) of roughly 0.8 fm. To examine the size of states such as this, the form factor of the state should be determined. The inverse Fourier transform of the form factor provides information on the radial charge distribution of the state. The d*(2380) is unique amongst the exotic states observed so far, in that testing these predictions via measurements of form factors from photoproduction reactions is currently achievable. For the tetraquark and pentaquark states currently observed it is unlikely that such measurements will be achievable in the near future with the possible exception of the $\mathrm{P_c}(4450)^+$ state.

4.3.4 Photoproduction - Future Prospects

New measurements of $\gamma d \rightarrow pn$ would need to cover the appropriate photon energy range and be able to measure the final state polarisation of both the proton and neutron with good statistics. As discussed by Bashkanov [90] such measurements should also utilise polarisation measurements to filter out resonance contributions from background. Such experimental conditions can be

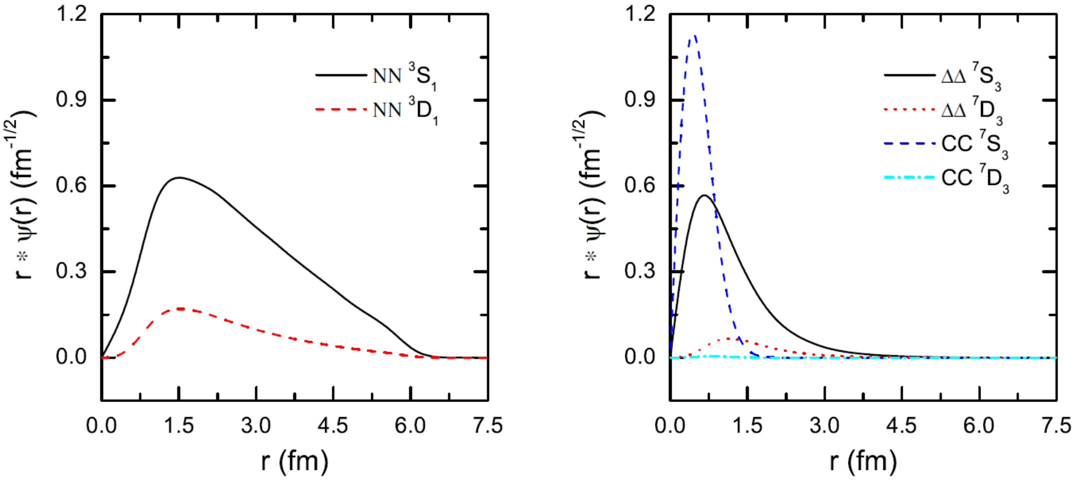

Figure 4.16 *Relative wave functions for the deuteron (left) and d* (right) [89].*

realised at the Mainzer Microtron (MAMI) [4] facility.

MAMI is capable of producing a high intensity (on the order of 10's of μA) polarised electron beam of up to 1.557 GeV in energy. In the A2 experimental hall at MAMI this electron beam is used to produce real photons via bremsstrahlung. Depending upon the choice of bremsstrahlung radiator used, the produced photons can be linearly or circularly polarised. By using a polarimeter setup, such a photon beam can be utilised to carry out recoil polarimetry measurements. A recoil polarimetry measurement of this type has already been successfully carried out by the A2 collaboration on the ^{1}H($\vec{\gamma}$, $\vec{p}\pi^0$) reaction [26]. As such the A2 hall at MAMI is the ideal place to undertake further study of the $\gamma d \to pn$ reaction by utilising a new polarimeter setup capable of simultaneously measuring the proton and neutron polarisation. The experimental setup in the A2 hall and the new polarimeter setup are discussed in Chapters 5 and 6 respectively; a summary of previous recoil polarimetry work at MAMI and elsewhere is discussed in the next section.

4.4 Previous Recoil Polarimetry Measurements

Previous experimental work at MAMI successfully extracted recoil polarisation observables for the reaction ^{1}H($\vec{\gamma}$, $\vec{p}\pi^0$) [26]. In this experiment the degree of polarisation transfer from the incident photon beam to the proton target was determined. This observable is referred to as $C_{x'}$ (see Appendix C for description of polarisation observables in photon-nucleon interactions). $C_{x'}$ is measured by fitting the angular distributions of the protons after they undergo a nuclear scattering interaction with some analysing material. In the case of the experiment at MAMI a graphite analyser was used as a polarimeter, the graphite was placed around the target. The setup used at MAMI for this experiment was not capable of measuring the recoil polarisation of neutrons.

There is a limited range of other recoil polarimetry measurements carried out at JLab [31, 101] and by the GEpIII and GEp2γ collaborations [104]. Of particular interest are the JLab measurements that examined the recoil observables C_x and C_z in deuteron photodisintegration [101]. As seen in Figure 4.17 these measurements cover a very limited energy range in the region relevant to the d*(2380) dibaryon. These observables were also only measured for the produced protons from the $\gamma d \to pn$ reaction.

4.5 Summary

There has been renewed interest in the field of exotic states in QCD in recent years. Particularly interesting is the d*(2380) dibaryon state. As discussed, this state has been observed across a wide range of hadron-production channels. However, as yet there has been no dedicated search for this state with electromagnetic probes. The motivation for a new, high-statistics measurement of deuteron photodisintegration utilising polarisation observables over the energy range relevant to the d*(2380) is therefore clear. Such a measurement would not only provide further evidence for the conclusions drawn about this state but could also be the key to unlocking some of the unknown properties of the state, such as its size and structure.

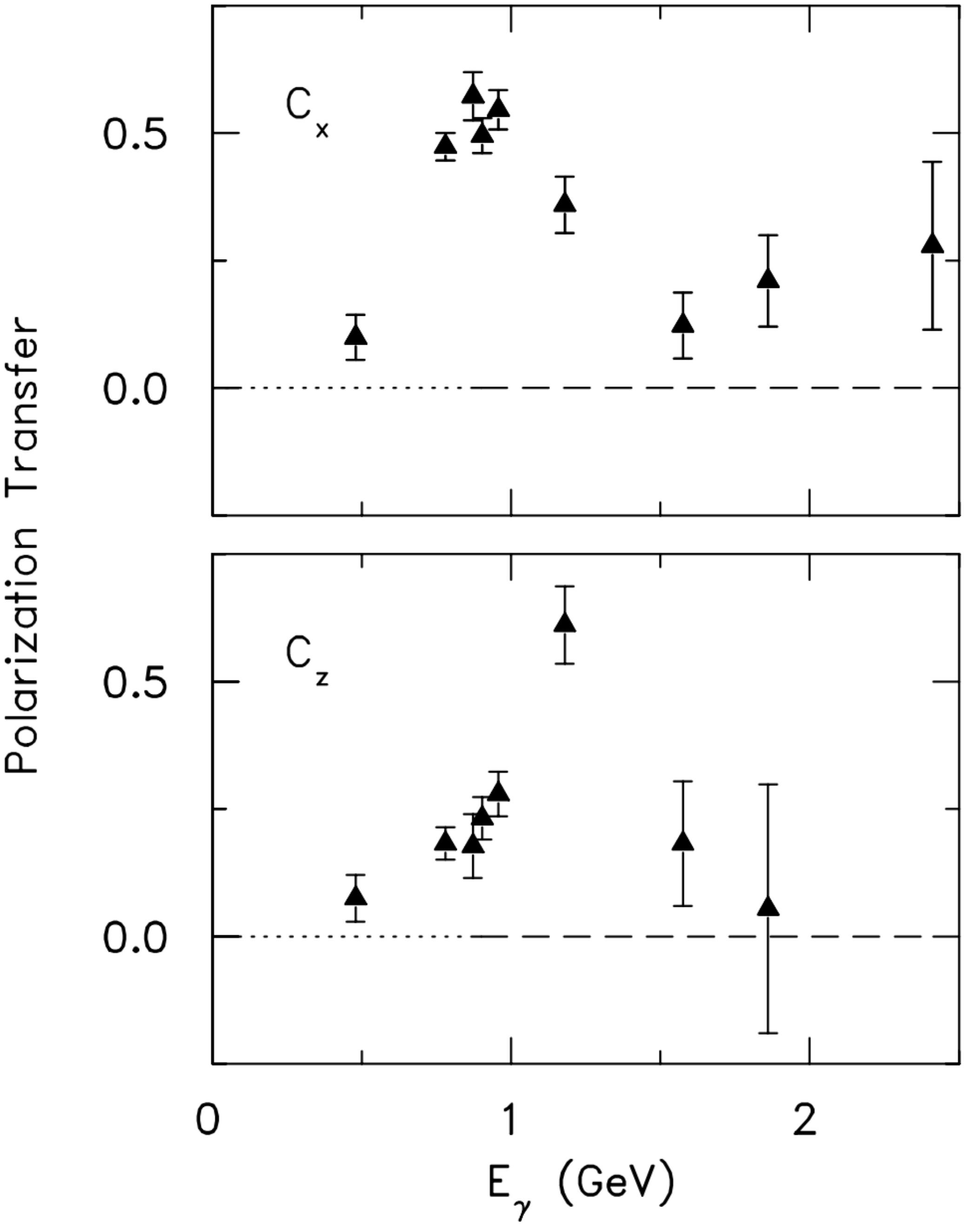

Figure 4.17 *Recoil proton polarisation transfer observables C_x (top) and C_z (bottom) for the reaction $\gamma d \rightarrow pn$ as a function of the incident photon energy, E_γ [101]. Note the lack of data points in the region below 1 GeV that is relevant to the d*(2380).*

Chapter 5

Experimental Apparatus

The experimental work outlined in this thesis was carried out in the A2 hall at the Mainz Microtron (MAMI) facility located in the Johannes Gutenberg Universität in Mainz, Germany (see Figure 5.1). This work was carried out in August 2016. MAMI is an electron beam facility capable of producing polarised electron beams with energies up to 1.557 GeV [4]. This electron beam is used to produce a real photon beam in the A2 hall. The polarised electron beam is impinged upon a radiator to produce a beam of bremsstrahlung photons. The energy of these photons is deduced via momentum analysis of the recoil electrons in the Glasgow Photon Tagger [105, 106]. The photon beam is incident upon a liquid deuterium target yielding various photoproduction reactions. The target is surrounded by the Particle Identification Detector (PID) which provides a ΔE signal for charged particles. This allows for the identification of protons, distinguishing them from any other particles (charged or neutral). Surrounding the PID, is the Edinburgh Phase-II Recoil polarimeter. Critical information on nucleon spin orientation can be extracted from the experimental data by measuring rescattering processes in the polarimeter. Encircling the polarimeter are two Multi Wire Proportional Chambers (MWPCs) that provide charged particle tracking information. The target, PID, polarimeter and MWPCs are all contained within the Crystal Ball calorimeter [5]. A further calorimetry array, the Two Arm Proton Spectrometer (TAPS), is situated upstream of the Crystal Ball to provide calorimetry information for forward polar angles [6, 7]. This chapter outlines the technical parameters of the various detector systems in use at MAMI; the data acquisition systems and the MAMI accelerator.

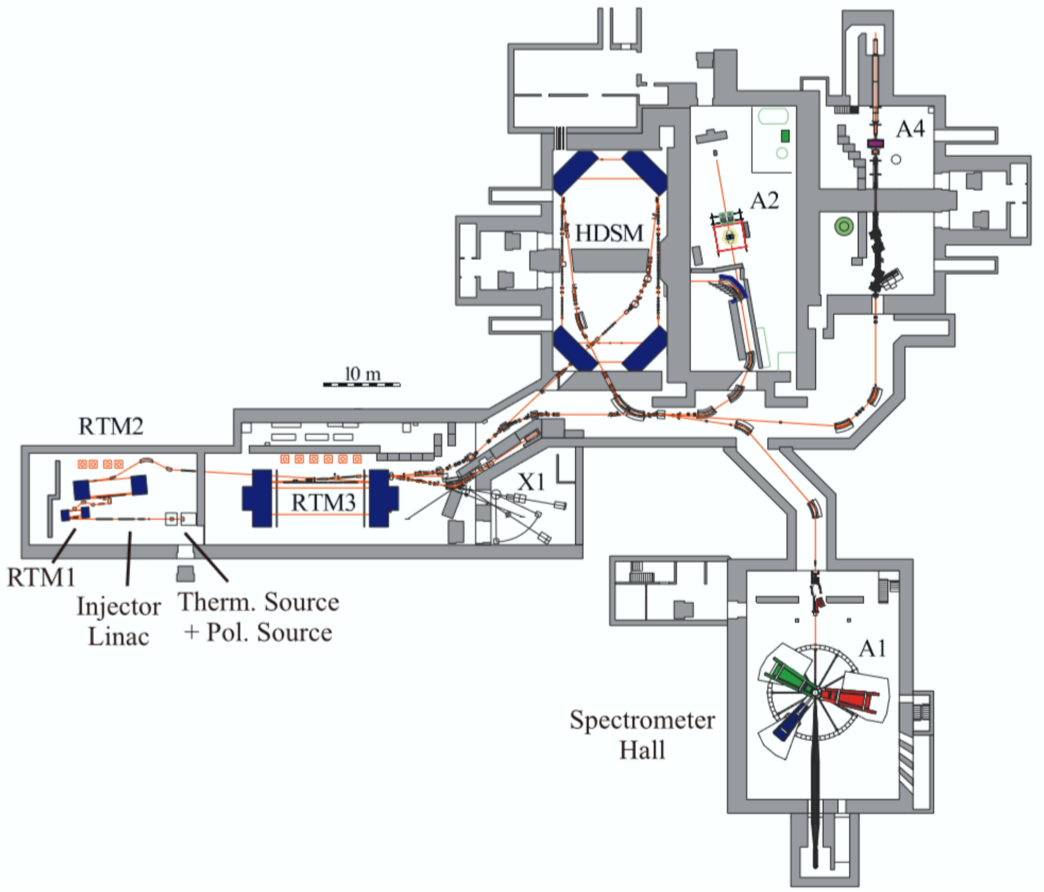

Figure 5.1 *Overview of the MAMI facility showing the various experimental halls [107]. The electron beam is produced in the far left hall and is accelerated through a series of microtrons (RTM1, RTM2, RTM3 and HDSM) before being delivered to one of the experimental halls. The narrow red line illustrates the* e^- *beamline.*

5.1 Particle Interactions in the Detector Systems

There are various particle detectors in use in the A2 hall. The purposes of these detector systems and the interactions particles have with these systems are outlined briefly in this section.

5.1.1 Calorimetry Detectors

Calorimetry detectors measure the energy of incident particles. Particles incident on calorimetry detectors will induce electromagnetic or hadronic showers (depending on the type of particle) in the detector volume. Calorimetry detectors convert the energy of these showers into a measurable quantity that can be used to infer the energy of the incident particle. The Crystal Ball (CB) and Two Arm Proton Spectrometer (TAPS) detector systems provide calorimetry information for charged and neutral particles in the A2 hall. Both detector systems utilise inorganic crystal scintillators to detect incident particles. Although the two detector systems use crystals of different materials (see Section 5.5), the basic principle of particle detection is the same for each. Incident particles produce scintillation light which is proportional to the initial energy of the incident particle. This light is collected by a photomultiplier tube to produce an electrical signal. The processes by which charged and neutral particles produce scintillation light differ slightly however, these processes are described briefly below.

Charged Particles

Charged particles (e^-, protons, charged pions) incident upon inorganic scintillator material will interact with nuclei in the crystal via coulomb interactions. These interactions cause excitation or ionisation of the atoms in the crystal. Ions produced from these events will in turn excite other atoms in the crystal. Excited atoms will rapidly de-excite by emitting photons.

Neutral Particles

Photons incident upon inorganic scintillator material can interact via the photoelectric effect, Compton scattering or by pair production. All of these interactions will result in the emission of a charged particle (or two in the case of pair production). These produced charged particles will in turn lose energy in the material as outlined above. Incident neutrons can interact in a variety of ways. They may interact by quasi-elastically scattering from a proton bound in a nucleus [108]. The outgoing proton will in turn lose energy in the same way as described above for charged particles. The efficiency of neutron detection in the Crystal ball is strongly energy dependent, the detection efficiency peaks at roughly 40% for neutrons of $\sim$250 MeV [109].

5.1.2 Tracking and Particle Identification Detectors

The Particle Identification Detector (PID) and Multi-Wire Proportional Chambers (MWPCs) provide particle identification and tracking for charged particles respectively. The PID is a segmented detector formed of thin strips of plastic scintillator material. When charged particles are incident upon the detector they will deposit a small fraction of their energy (ΔE) in one of the PID elements. The value of ΔE is dependent upon the velocity of the incident particle. For a given momentum a charged pion or a proton will have different velocities. As such they should produce a different ΔE signal. This allows different charged particles to be distinguished. This process is outlined further in Section 5.6.1.

The MWPCs operate slightly differently from the other detector systems in use. The MWPCs are gas ionisation based detectors. Charged particles passing through the chambers will ionise the gas inside. The negatively charged electrons will move towards the nearest anode wire inside the chamber. Positively charged ions will drift towards the cathode planes of the detector. As electrons approach the anode wires they will accelerate rapidly producing an “avalanche”. This avalanche induces a negative signal on the nearest anode wire and a positive signal in adjacent wires. This behaviour can be utilised to determine where the ionising event occurred. By utilising two wire chambers, two interaction points can be determined and as such a particle track can be reconstructed. Information from the wire chambers can also be utilised in conjunction with information from other detectors such as the CB or PID to further refine this track.

5.2 MAMI

5.2.1 Accelerators

The MAMI facility consists of a series of racetrack microtrons (RTMs) [110] that have been expanded upon over time. A racetrack microtron consists of a continuous wave linear accelerator (linac) situated between two large D-shaped magnets (see Figure 5.2). An initial electron beam is accelerated through the linac and is circulated back around into the linac via the two magnets. This process is repeated many times. The electron beam gains energy and traverses a larger path around the microtron on each pass around the device. This process carries on until a maximum energy is reached for this particular RTM, at this point the beam is ejected. MAMI was initially built with a single RTM and further, larger RTMs were added over time to increase the energy range the e^- beam can cover.

The longitudinally polarised electron beam that is injected into the first stage of the MAMI system is produced via photoemission from (III-V) semiconductors [111]. Either strained GaAsP or InGaP photocathodes are used in conjunction with a circularly polarised Ti:Sapphire laser beam. Following production, the photoelectrons are accelerated to 3.5 MeV by a linac and injected into the first RTM, RTM1. RTM1 accelerates the electrons up to 14 MeV before injecting them into RTM2, here the electrons go through 51 turns; further increasing the energy to 175 MeV. Once at 175 MeV the electron beam can be fed to RTM3 where it can be accelerated to 855 MeV.

In the mid 2000s an additional microtron was added to the MAMI facility to allow for the production of electron beams with energies of up to 1.5-1.6 GeV [107, 112]. A further standard RTM was simply not feasible due to the excessively large size of the magnets that would be needed to achieve such energies ($\sim$ 2200 tons of iron per magnet). As such, a new double sided microtron design utilising two linacs was used. With such a design four 90° magnets are used rather than two 180° magnets. The overall weight of the magnets in such a situation is comparable to that of the weight of those needed for RTM3. The two linacs used in the design operate at different frequencies (one at 2.45 GHz the other at 4.9 GHz) to reduce the degree of longitudinal defocusing caused by phase shifts in the linac frequencies. A schematic of the microtron, dubbed a “Harmonic Double Sided

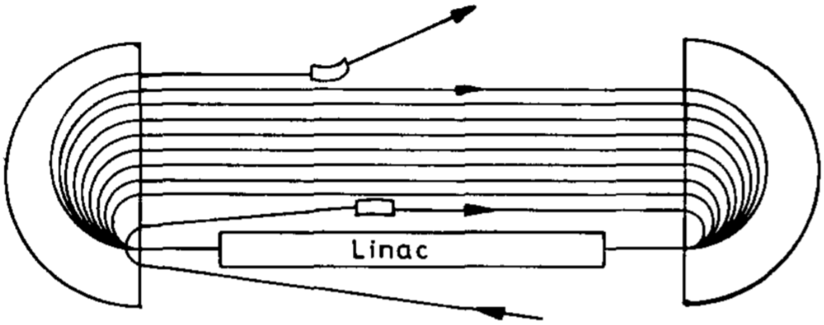

Figure 5.2 *A typical racetrack microtron design [110].*

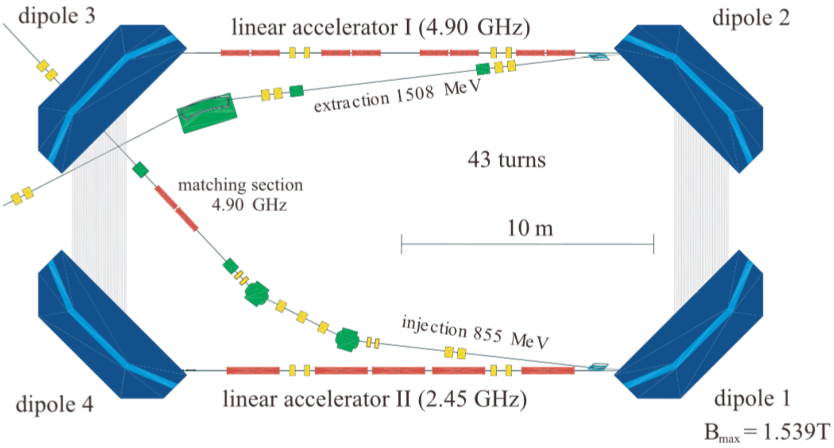

Figure 5.3 *Schematic of the MAMI-C harmonic double sided microtron, the four 90° dipole magnets are shown in blue [107].*

Microtron" (HDSM) and referred to as MAMI-C (see Figure 5.3). There are three possible configurations of the four accelerators available at MAMI that are summarised in Table 5.1. Using the MAMI-C configuration the produced electron beam can reach up to 1557 MeV in energy with a maxiumum beam current of 20 μA for a polarised electron beam (or up to 100 μA unpolarised).

Table 5.1 *Summary table of different MAMI configurations*

MAMI Configuration	Accelerators Used	Max e^- Energy/MeV
A	RTM1, RTM2	175
B	RTM1, RTM2, RTM3	855
C	RTM1, RTM2, RTM3, HDSM	1557

Table 5.2 *Mott measurements taken over the August 2016 production run. Errors on polarisation percentage are taken to be equivalent to percentage error in asymmetry measurements.*

Date	$p^{\odot}_{e^-}$ With $\frac{\lambda}{2}$ plate/%	$p^{\odot}_{e^-}$ Without $\frac{\lambda}{2}$ plate/%
2/8/16	74.77±0.05	75.53±0.05
4/8/16	75.81±0.05	76.79±0.05
6/8/16	75.85±0.05	76.64±0.05
8/8/16	76.20±0.05	77.06±0.05
10/8/16	76.49±0.05	77.30±0.05
12/8/16	77.01±0.06	77.72±0.05
19/8/16	77.50±0.06	77.68±0.06
22/8/16	77.53±0.07	77.20±0.08

5.2.2 Real Photon Beam - The A2 Hall

The experimental work detailed in this thesis was carried out in the A2 hall at MAMI. In the A2 hall the electron beam from MAMI is not used directly. Instead the electron beam is used to produce a beam of bremsstrahlung photons by impinging it upon a thin radiator. As the initial electron beam is polarised the resulting bremsstrahlung photon beam can either be linearly or circularly polarised depending upon the radiator that is used. If a radiator with an amorphous structure, such as the 12 μm thick copper radiator, is used then the resulting bremsstrahlung photons produced will be circularly polarised. The degree of circular polarisation, $p^{\odot}_{\gamma}$, for a given photon is defined by [113]

$$p^{\odot}_{\gamma} = \frac{p^{\odot}_{e^-} \times E_{\gamma} \times (E_{e^-} + \frac{1}{3}(E_{e^-} - E_{\gamma}))}{E^2_{e^-} + (E_{e^-} - E_{\gamma})^2 - \frac{2}{3}E_{e^-} \times (E_{e^-} - E_{\gamma})}, \tag{5.1}$$

where E_{γ} is the energy of the produced photon, E_{e^-} is the energy of the MAMI electron beam and $p^{\odot}_{e^-}$ is the degree of circular polarisation of the MAMI electron beam. This is typically ~75%. The degree of photon beam circular polarisation is illustrated in Figure 5.4 (for $E_{e^-} = 1.557$ GeV and $p^{\odot}_{e^-} = 76.6\%$). A Mott polarimeter is utilised to measure $p^{\odot}_{e^-}$ [114]. This polarimeter measures the asymmetry of elastically scattered electrons either side of the scattering plane for each helicity. From this asymmetry, $p^{\odot}_{e^-}$ can be determined. A Mott measurement is typically performed every few days during production running, the measured values during the August 2016 production run are tabulated in Table 5.2.

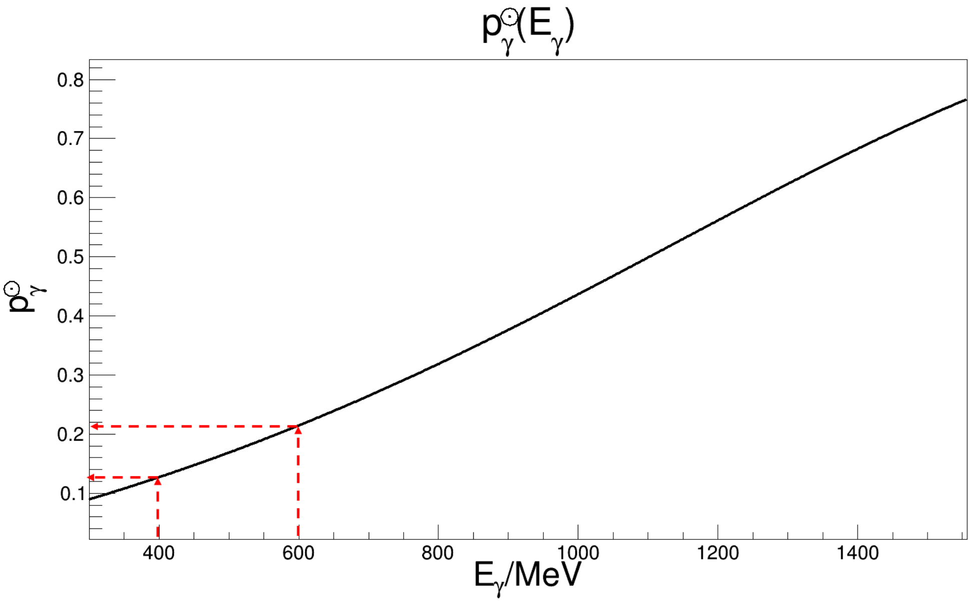

Figure 5.4 *The circular polarisation of the bremsstrahlung photon beam as a function of photon energy, the range relevant to the d*(2380)(400-600 MeV) is illustrated.*

The helicity of the produced electron beam is flipped with a frequency of 1 Hz during production running. This helicity flipping is achieved by changing the polarity of the voltage at the source of the polarised Ti:Sapphire laser beam that is used to produce the initial electron beam. This results in the produced bremsstrahlung photon beam also switching helicity with the same frequency.

To produce a linearly polarised photon beam a 30 μm thick diamond radiator is used. High-energy electrons incident upon a crystalline radiator (such as diamond) can produce linearly polarised photons via coherent bremsstrahlung. The lattice vector of the radiator must be carefully aligned with the direction of the electron beam to produce a high degree of linear polarisation. Alignment of the crystal with the electron beam is achieved via a process known as the Stonehenge technique [115]. The degree of linear polarisation (see Figure 5.5) due to the crystaline radiator shows distinct drops in the polarisation (referred to as a coherent edge). The peaks correspond to coherent bremsstrahlung production from different crystal planes in the radiator. The position of the first coherent edge was deliberately placed at 630 MeV to ensure a large degree of linear polarisation in the 400-600 MeV region of interest. During the August 2016 production run both the copper and diamond radiators were used to gather data with both linearly and circularly polarised photons.

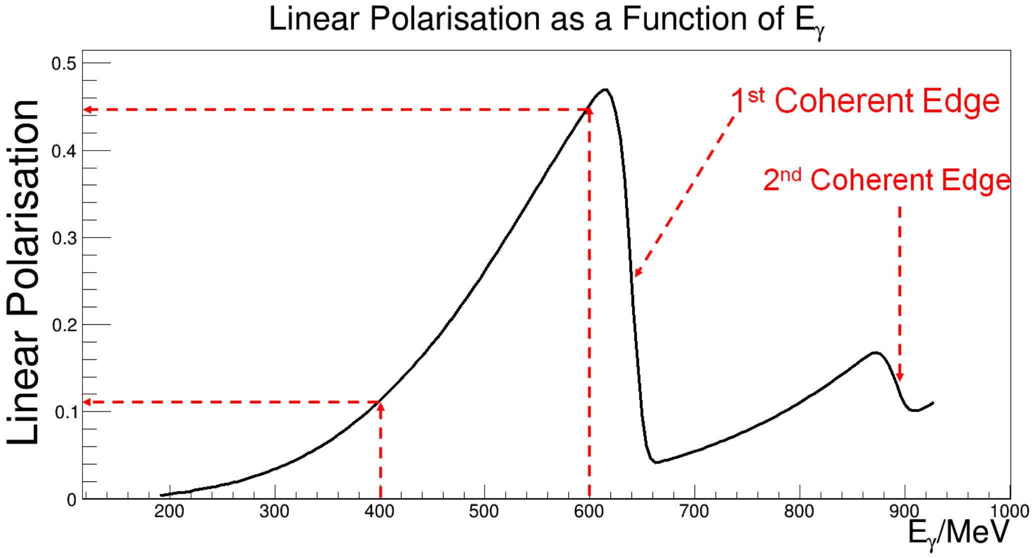

Figure 5.5 *The linear polarisation of the bremsstrahlung photon beam as a function of E_γ, the first two coherent peaks can be clearly seen. The two coherent edges mark the point where the second derivative of the polarisation as a function of the energy changes in sign.*

The degree of linear polarisation, p_γ^{lin}, is determined by examining the "enhancement" in the photon distribution due to the coherent bremsstrahlung. This enhancement is defined as being the ratio of the coherent and incoherent (amorphous) bremsstrahlung distributions. The degree of polarisation is determined using the analytic bremsstrahlung calculation, which is a function fitted on the enhancement distribution [27]. An example plot of how the enhancement and polarisation compare can be seen in Figure 5.6.

Photons produced from coherent bremsstrahlung interactions are more forward focused (i.e. are preferentially along the initial direction of the electron beam). As such coherent bremsstrahlung photons are less effected by collimation than incoherent bremsstrahlung photons. p_γ^{lin} can be increased by utilising a narrow collimator on the photon beam [116]. It should be noted that the photon beam needs to be collimated for other purposes. The beam is collimated to reduce background induced by photons interacting directly with detector components rather than the target. During the August 2016 experimental run a 3 mm diameter collimator situated 2.5 m downstream of the radiator was used.

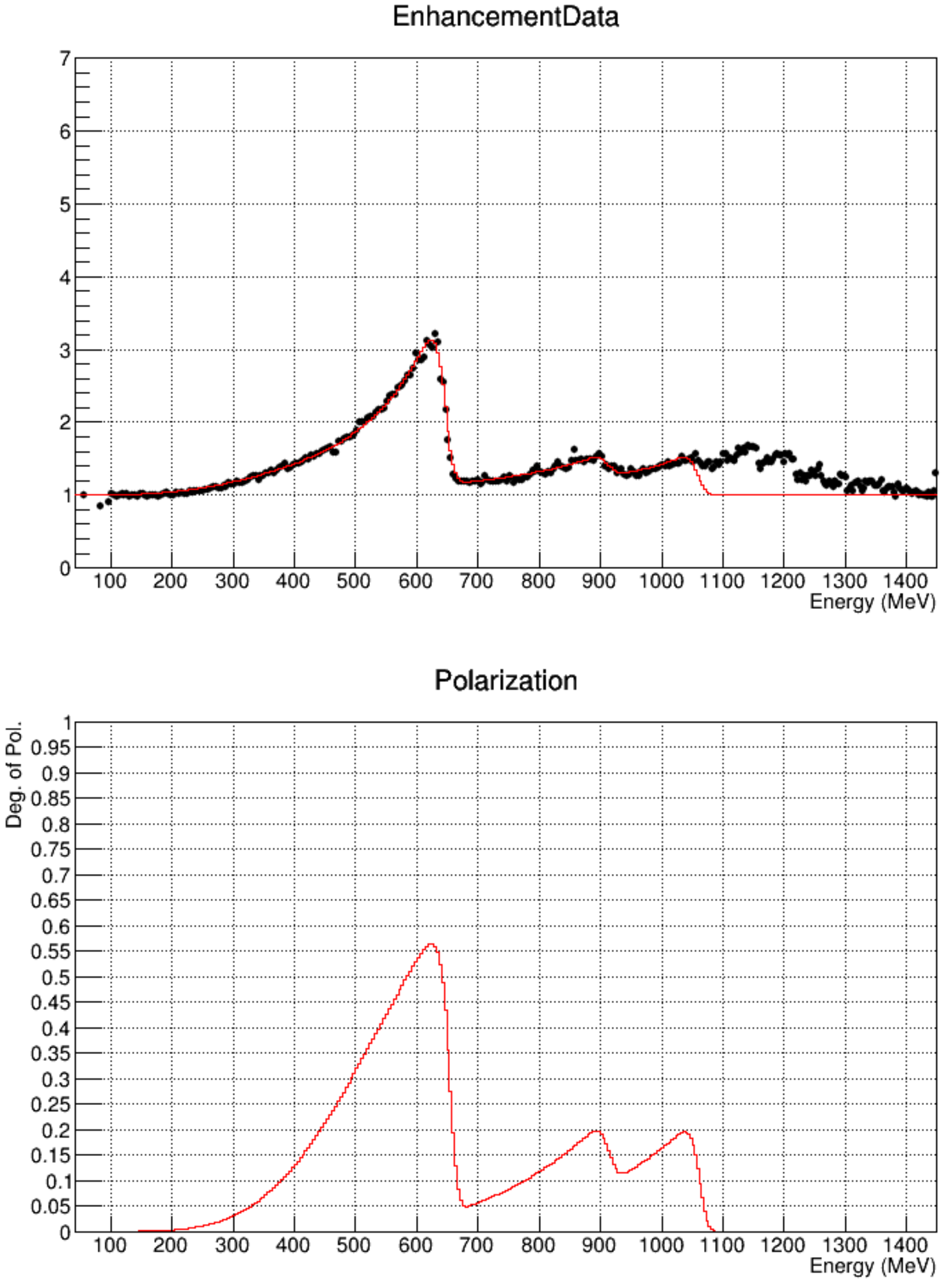

Figure 5.6 *The linear enhancement (top) and the resulting degree of linear polarisation (bottom) [117]. Note that this figure is for comparison only and is* not *from the August 2016 beamtime.*

5.3 Glasgow Photon Tagger

The Glasgow Photon Tagger [105, 106] is used to determine the energy of the bremsstrahlung photon beam. This is achieved via a series of 353 EJ200 plastic scintillator elements that form a focal plane detector (FPD) in combination with a magnetic spectrometer (see Figure 5.7). The 80 mm long and 2 mm thick scintillator elements vary in width from 9-32 mm. The widths of each element decrease along the focal plane to keep the tagged energy range covered by each element roughly constant.

An incoming electron of energy E_{Beam} undergoes a bremsstrahlung interaction with the radiator producing a photon of energy E_γ. The bremsstrahlung electron from this interaction is then momentum analysed by the 1.8 T magnetic spectrometer and is detected in the FPD. The energy of the electron, E_{fp}, is determined from the position of its hit along the focal plane. The energy of the resulting photon is therefore given by

$$E_\gamma = E_{\text{Beam}} - E_{\text{fp}}. \tag{5.2}$$

The scintillator strips in the FPD are individually wrapped in aluminised mylar to reduce cross talk between elements and to light proof the elements. The detector elements are read out by individual Hamamatsu R1635 photomultiplier tubes. Each PMT has a thin (0.7 mm) steel plate either side of it to shield it from magnetic fields. Each of the scintillator strips in the FPD overlaps with its neighbours by slightly more than half their width. This is so that an electron hit is defined by coincident signals in adjacent detector elements. This method reduces the rate of random coincidences caused by multiple scattered electrons. Overall the FPD array covers $\sim$ 5-93 % of the initial electron beam energy with a resolution of $\sim$ 4 MeV when tagging a 1500 MeV electron beam. An individual element can handle a maximum photon flux of roughly $10^6 \gamma s^{-1}$. Due to the roughly 1/E cross section for bremsstrahlung, it is effectively the highest energy electron FPD elements (lowest E_γ) that set an upper limit on the overall electron (and thus photon) beam intensity.

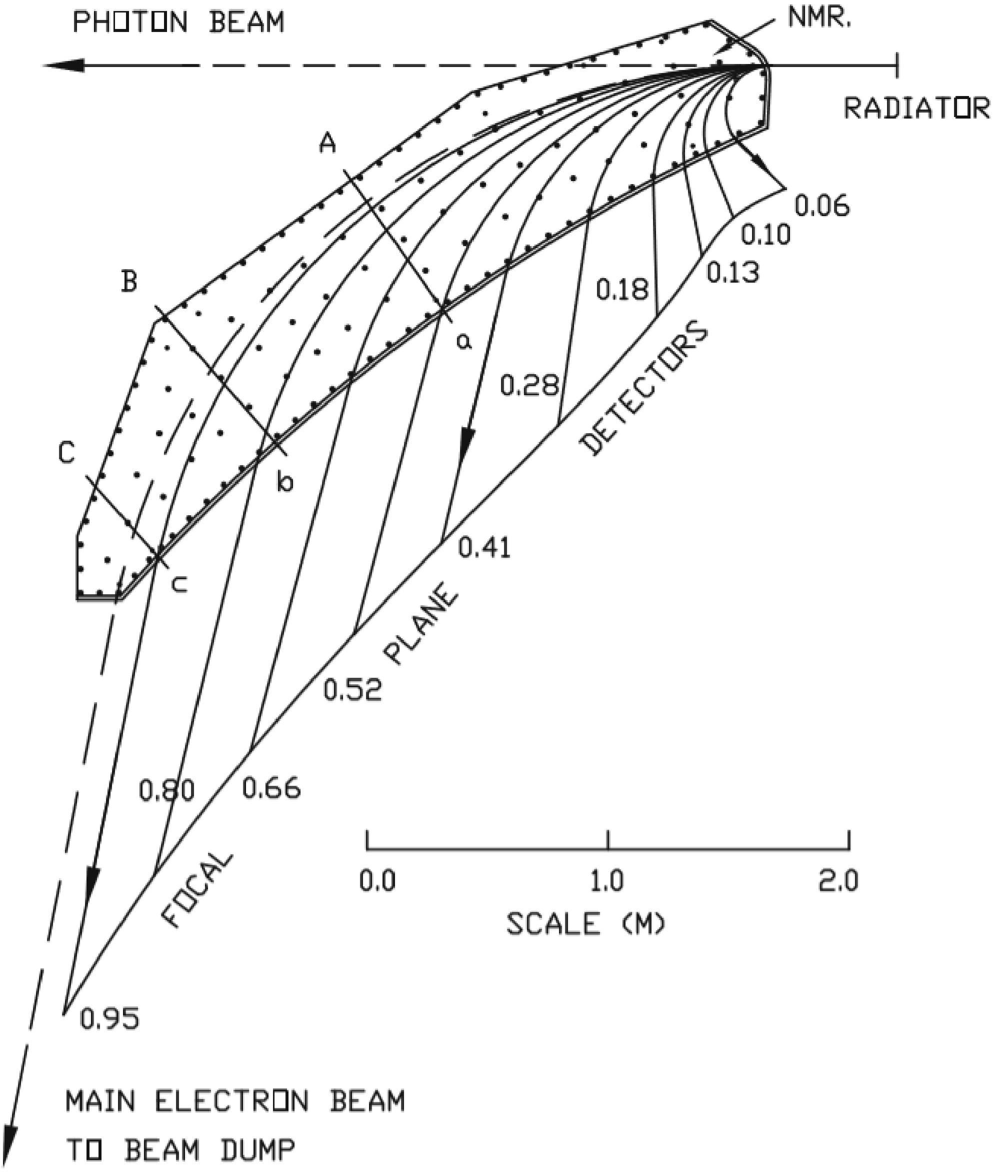

Figure 5.7 *The Glasgow Photon Tagger, trajectories of electrons with energies expressed as a fraction of the initial beam energy are shown [106].*

5.4 Target

The target cell is a 10 cm long cylinder with a 3 cm diameter contained in a 125 μm thick kapton housing at the centre of the Crystal Ball. Gaseous deuterium from a storage tank is compressed and liquefied before being supplied to the target. Hydrogen can also be supplied in this way if required. During the August 2016 experimental run the target was kept at a pressure of 1080 mBar and cooled to 21 K. In these conditions the liquid has a density of $\rho \approx 0.07$ gcm^{-3}. During operation these conditions are monitored and maintained by carefully heating the target with two 4 W heaters or by supplying more liquid deuterium.

5.5 Calorimetry

Calorimetry information in the A2 hall is provided by two detector systems; the Crystal Ball (CB) and the Two Arm Proton Spectrometer (TAPS). The Crystal Ball is a spherical detector that covers a wide angular range ($\sim 21° - 159°$ in polar angle, θ, and almost the whole range in azimuthal angle, ϕ) for charged and neutral particles. TAPS provides calorimetry information for forward polar angles between $\theta \sim 2 - 20°$.

5.5.1 The Crystal Ball

The Crystal Ball is a calorimeter that was constructed to study the J/ψ meson at SLAC [118, 119] in the 1970s. After its use at SLAC, the Crystal Ball was later used at other facilities around the world [120, 121]. The Crystal Ball was moved to the A2 hall at MAMI in 2002.

The Crystal Ball is constructed from 672 NaI(Tl) scintillator crystals. These crystals are arranged into a roughly spherical shape with two entry points on opposite sides of the ball. Even with these two entry points the detector has an angular coverage of $\sim 93\%$ of 4π. The spherical shape is achieved by sub-dividing the 20 triangular faces of an icosahedron (a regular 20 sided polygon, see Figure 5.8). Each face of the icosahedron forms a *major triangle*, each of these major triangles is further divided into 4 *minor triangles*. Each minor triangle comprises 9 individual NaI(Tl) crystals. Individual crystals are shaped as a truncated pyramid

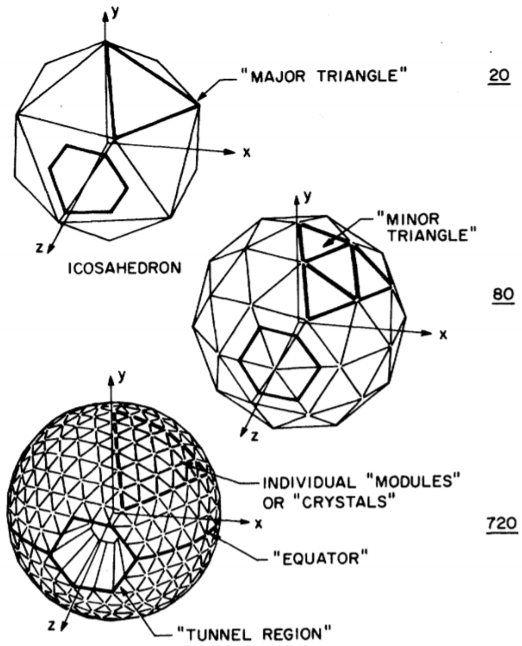

Figure 5.8 *Illustration of the Crystal ball geometry showing the major and minor triangles [118].*

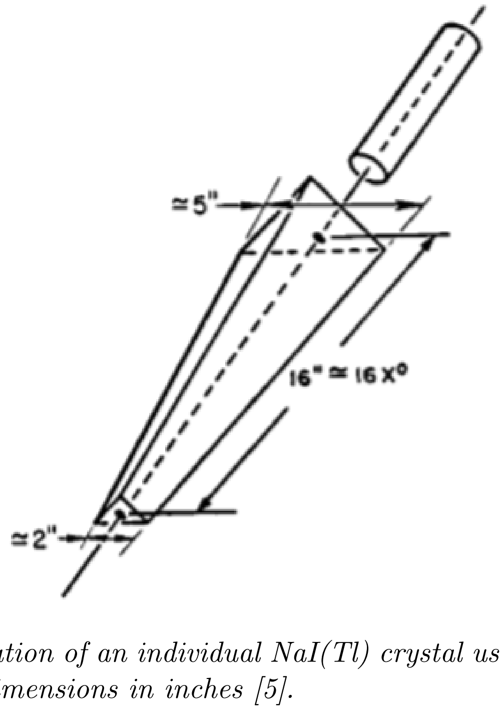

Figure 5.9 *Illustration of an individual NaI(Tl) crystal used in the Crystal Ball with dimensions in inches [5].*

(see Figure 5.9), with the "point" of the pyramid aimed toward the centre of the ball. Each element is 40.6 cm long (corresponding to 15.7 radiation lengths for photons). The base is an equilateral triangle with sides of length 5.1 cm whereas the apex is an equilateral triangle with sides of length 12.7 cm. Each crystal is wrapped in aluminised mylar to optically isolate it. Every crystal has its own SRC L50B01-4 Photomultiplier tube to measure light output.

The array of 672 crystals is arranged into two hermetically sealed hemispheres to protect the hygroscopic NaI(Tl) crystals. The two hemispheres have an inner radius of 25.3 cm and an outer radius of 66.0 cm; there is a small gap of 0.8 cm between the two hemispheres.

The full detector array achieves an energy resolution of $\frac{\Delta E}{E} = \frac{0.020}{E[GeV]^{0.36}}$ and an angular resolution of $\sigma_\theta = 2$ - 3° and $\sigma_\phi = \frac{\sigma_\theta}{\sin\theta}$ in polar and azimuthal angles respectively [122]. These quoted resolutions are for electromagnetic showers. Electromagnetic showers from events in the Crystal Ball will generally spread over a group of crystals. When an event triggers a crystal a clustering algorithm checks all adjacent crystals for an energy deposit. If any adjacent crystals have an energy deposit above a user defined threshold (typically 2 MeV) then they are included in the cluster. Any crystals adjacent to the included crystal are then checked in the same way. This process carries on until no further crystals are found to be above the threshold. The total measured energy for an event is the sum of the energies from all the crystals included in the cluster. The overall hit position, $\underline{r}$, is determined by calculating the centre of mass for the individual crystal energies via Equation (5.3). Proton and pion events generally hit fewer crystals whereas electron and photon events produce broader showers.

$$\underline{r} = \frac{\Sigma_N \underline{r}_i \sqrt{E_i}}{\Sigma_N \sqrt{E_i}} \tag{5.3}$$

5.5.2 TAPS Forward Wall

The Two Arm Proton Spectrometer (TAPS)[6, 7] forward wall provides calorimetry information for forward angles ($\theta = 2 - 20^{\circ}$) that are missed by the Crystal Ball due to the downstream exit point. The TAPS forward wall (see Figure 5.10) consists of 366 hexagonally shaped BaF_2 crystals and 72 $PbWO_4$ crystals. Each BaF_2 crystal is 25 cm in length (12 radiation lengths) and 59 mm in diameter. The $PbWO_4$ crystals are shaped such that four combine to form one BaF_2 crystal. Each $PbWO_4$ crystal is 20 cm (22 radiation lengths) long. The $PbWO_4$ crystals replaced 18 BaF_2 crystals in the region closest to the beam line. The faster timing of the $PbWO_4$ crystals reduces pileup and allows for higher detection rates; the larger number of crystals also helps to reduce the rate per crystal. Each crystal is read by a Hamamatsu R2059-01 photomultiplier tube.

The BaF_2 crystals cover the angular range of 4-20° in θ; the $PbWO_4$ crystals increase this angular range to $\sim 2-20^{\circ}$ in θ. The energy resolution for EM showers in the BaF_2 TAPS crystals is $\frac{\sigma_E}{E} = 0.018 + \frac{0.008}{E[GeV]^{0.5}}$. The energy resolution of the $PbWO_4$ crystals is comparable [123]. The angular resolution in θ is better than 1° and in ϕ the resolution improves with increasing θ. Each crystal also has a 5 mm layer of NE102A scintillator in front that is read out via two wavelength shifting fibres. This scintillator can be used as a veto for charged particles by using a ΔE-E method. This procedure is similar to that used for particles in the Crystal Ball and is explained in Section 5.6.1. Particle identification in TAPS can also be achieved by a Time of Flight (ToF) method. For the BaF_2 crystals pulse shape analysis (PSA) can also be used.

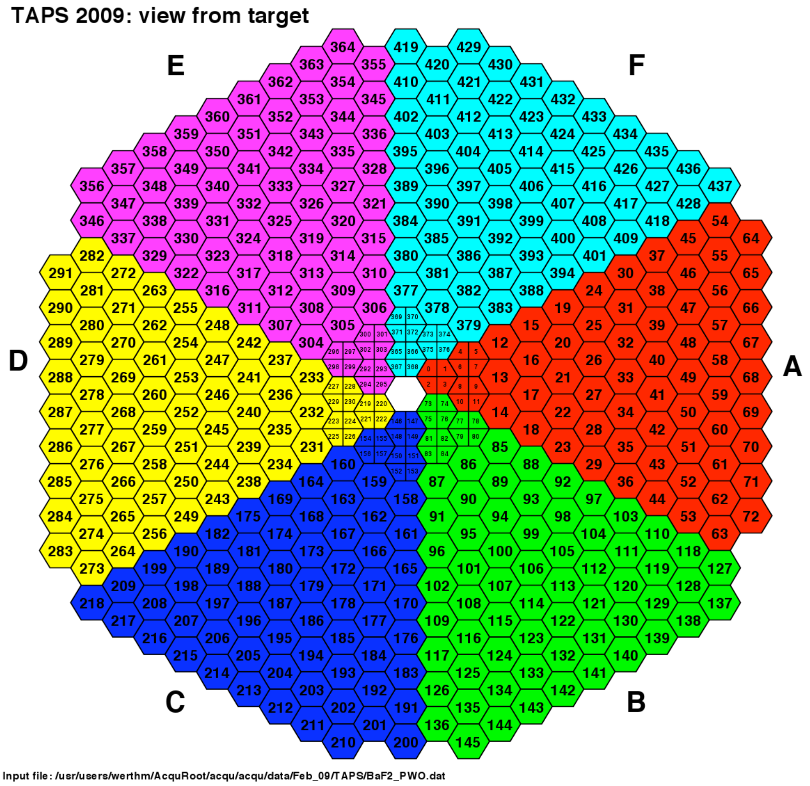

Figure 5.10 *Schematic of the TAPS crystal arrangement at MAMI, the smaller inner crystals are the* $PbWO_4$ *crystals [124].*

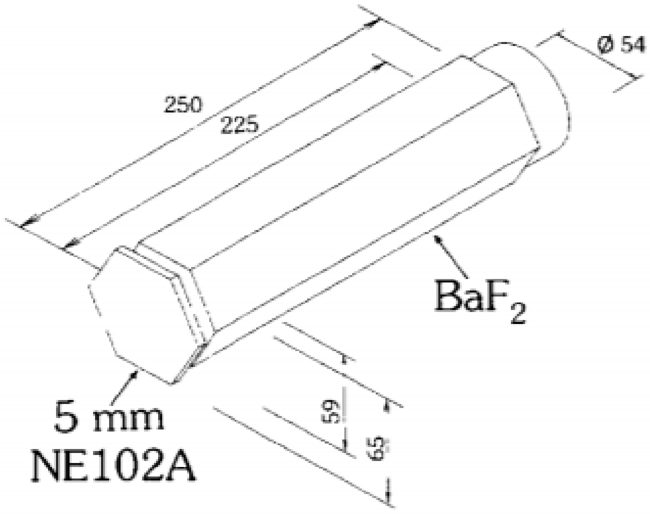

Figure 5.11 *Diagram of individual TAPS* BaF_2 *crystal with VETO [7].*

5.6 Particle Tracking and Identification

Charged particle tracking and identification in the Crystal Ball is achieved via the combination of two detector systems, the Particle Identification Detector (PID) and two Multi Wire Proportional Chambers (MWPCs). These two detector systems surround the cryogenic target within the Crystal Ball. These two systems are described in the following sections.

5.6.1 Particle Identification Detector

There have been numerous iterations of the PID used at MAMI [125, 126]. The current PID, PID-III, was specially designed and constructed for the August 2016 recoil polarimetry experimental run. PID-III is very similar in design to the previous iterations but is far more compact.

PID-III consists of 24 individually wrapped EJ204 scintillator elements. Each element is 30 cm long and 4 mm thick, and has a 45° cut at one end. A small piece of scintillator is attached beneath this to allow for detection of particles down to $\sim 7^\circ$ in θ. At the opposite end, each element is glued to a curved perspex lightguide which is then optically connected to a Hamamatsu H3164-10 PMT. On each element, one of the long edges has a side angled at 15° so that all 24 elements can be arranged into a barrel shape (see Figure 5.12). The barrel formed by the elements of PID-III has an inner radius of 3.3 cm and an outer radius of 3.7 cm. Further details of the design and construction process for PID-III are outlined in Chapter 6.

Charged particles that pass through the PID leave a small energy deposit, ΔE, in the detector. Hits in the PID are correlated to hits in the Crystal Ball if they are within a user defined angular range in ϕ (typically 15°). ΔE from the PID can be compared to the full energy deposition, E, in the Crystal Ball. When doing such a comparison (see Figure 5.13) protons and charged pions leave distinct bands in the data.

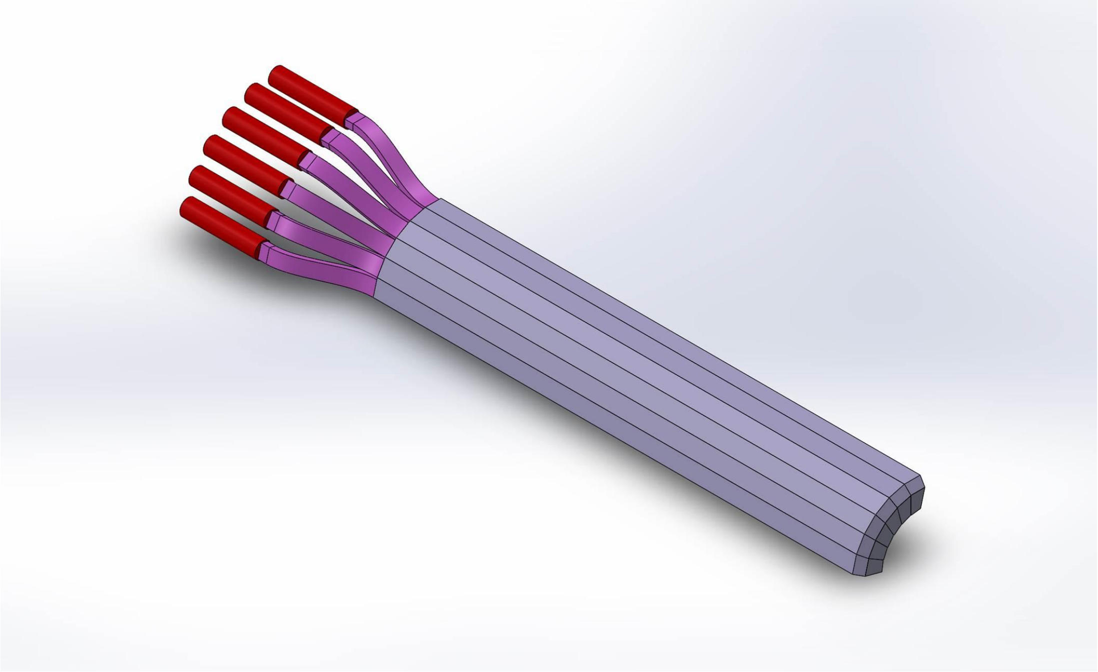

Figure 5.12 *CAD drawing of a quarter of the PID-III array showing how six elements fit together. The PMTs are displayed in red on the left, the lightguides in magenta and the plastic scintillator elements in lilac on the right.*

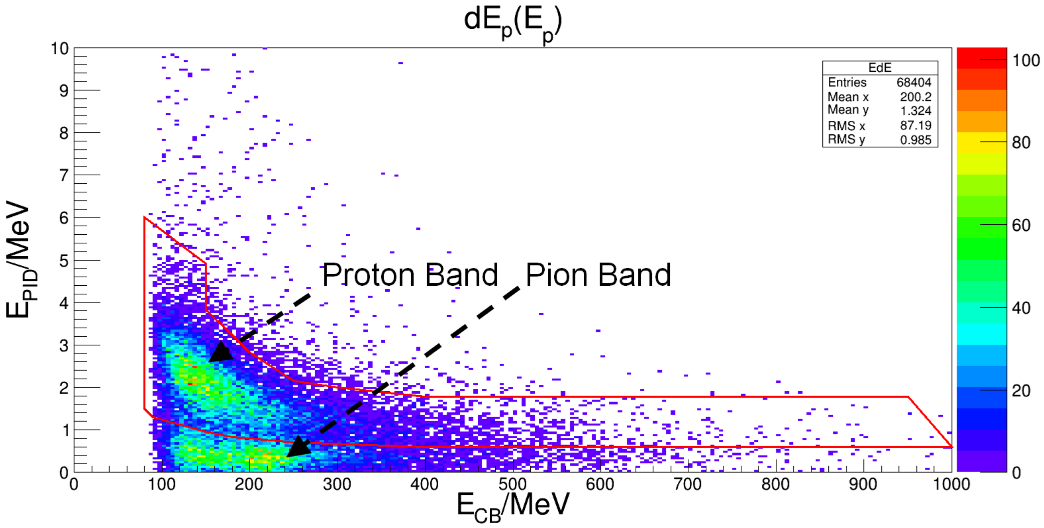

Figure 5.13 *An example $E-\Delta E$ plot showing distinct proton (uppper band) and pion (lower band) bands in the analysed data. The cut region used to select out protons is shown in red (discussed further in Chapter 8).*

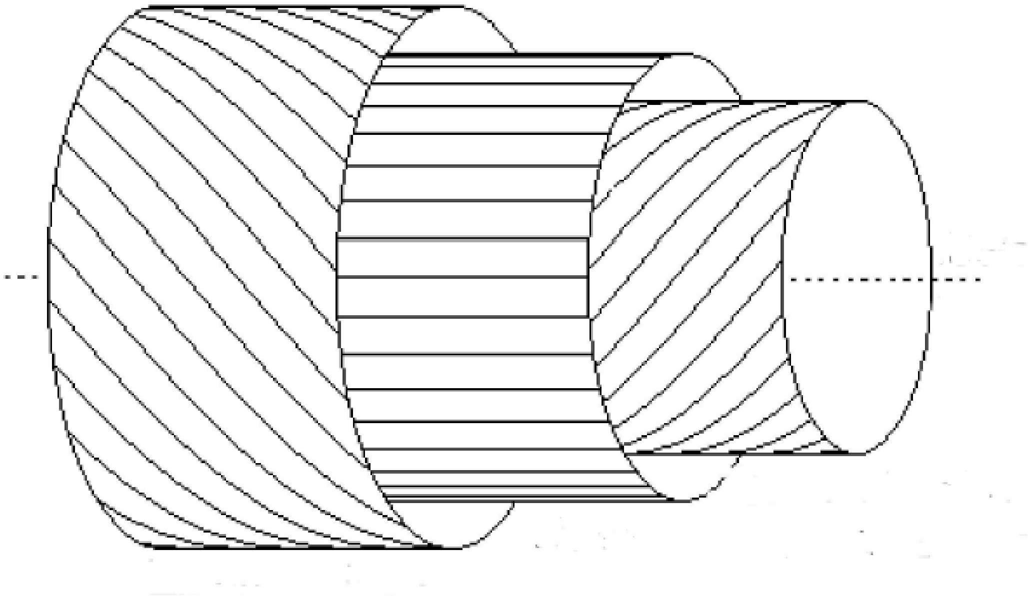

Figure 5.14 *Diagram of the one of the MWPCs illustrating the orientation of the strips and wires relative to each other [128].*

5.6.2 Multi Wire Proportional Chambers

Surrounding the PID there are also two Multi Wire Proportional Chambers (MWPCs), these are used to provide additional tracking and position information for charged particles. These MWPCs are based on a design originally used for the DAPHNE detector system [127]. The two coaxial MWPCs used surround the target, PID and polarimeter inside the Crystal Ball. Each chamber consists of three layers. The middle layer consists of wire running parallel to the beam axis that acts as an anode. The inner and outer layers, that act as the cathode, are strips wound at ±45° with respect to the central layer (and therefore are at 90° to each other, see Figure 5.14). The wire chambers are filled with an ionising gas mixture of argon, ethane, ethanol and freon in various quantities (ordered in concentration from high to low). During operation in August 2016 a voltage of 2500 V was applied to the first chamber and 2550 V was applied to the second chamber. The efficiency of the wire chambers is strongly dependent upon the operating voltage. The MWPCs cover the full angular range in ϕ and 21° to 159° in θ.

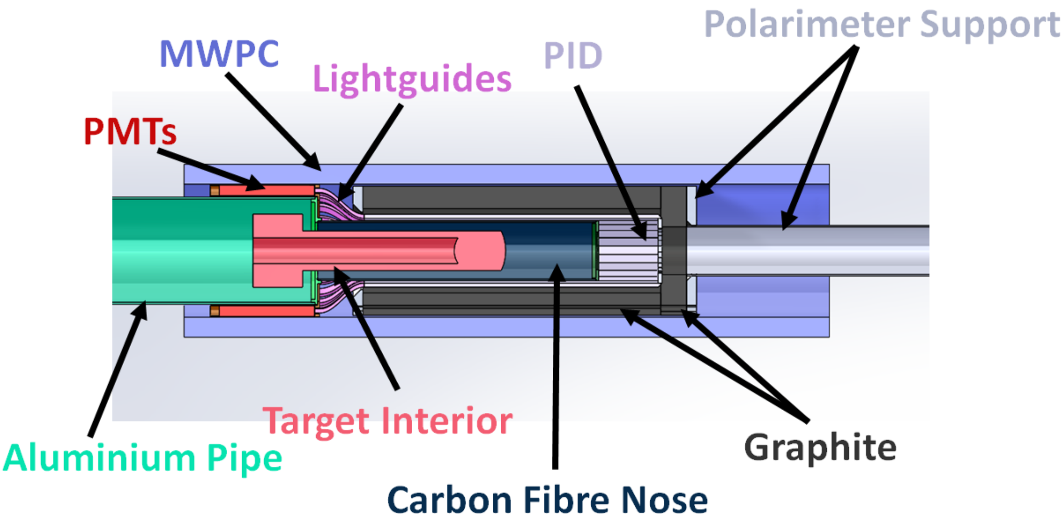

Figure 5.15 *An annotated CAD drawing of the experimental setup used in the August 2016 production run.*

5.7 Full Detector Array

The components of the detector setup contained within the Crystal Ball are illustrated in Figures 5.15 & 5.16. The target is enveloped by the PID, polarimeter and MWPCs in turn. This arrangement allows for the easy distinction of $\vec{\gamma}d \rightarrow \vec{n}p$ events (see Figure 5.17) where the neutron then undergoes a charge exchange interaction in the polarimeter. Event selection details are outlined in Section 8.1. The inner detectors are then surrounded by the Crystal Ball. For forward angles TAPS was present (not shown in figures) at 1.75 m downstream to provide calorimetry for forward going particles. The polarimeter support cradle is fixed (via three adjustable legs) to the CB tunnel region at the downstream end.

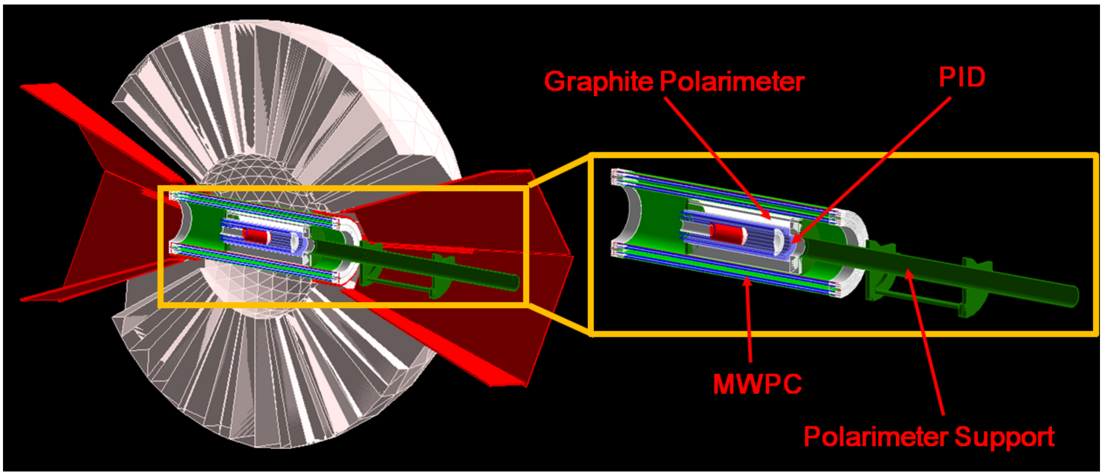

Figure 5.16 *Annotated Geant4 simulation of the August 2016 experimental setup showing the polarimeter support cradle.*

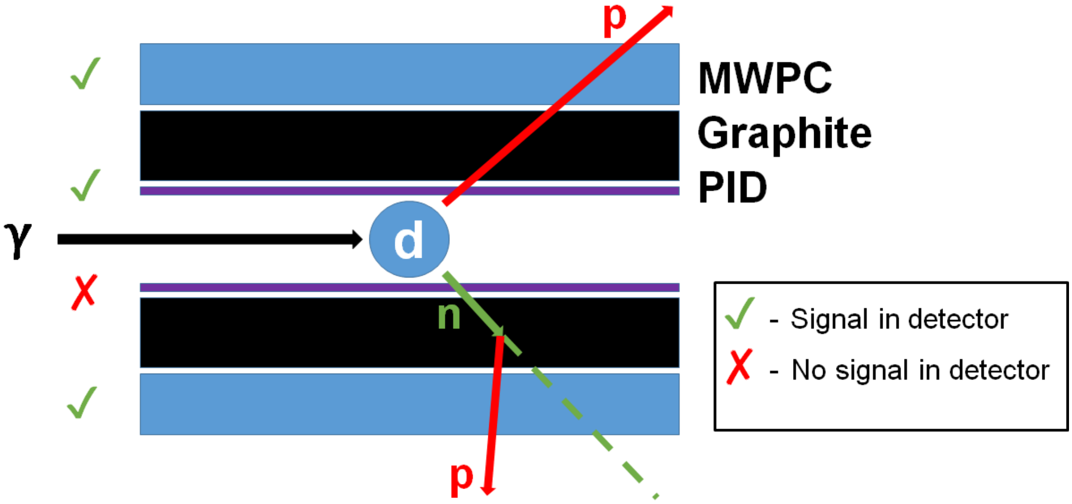

Figure 5.17 *A cartoon showing a* $\vec{\gamma}d \rightarrow \vec{n}p$ *reaction where the neutron then undergoes a charge exchange interaction in the polarimeter.*

5.8 DAQ System

Photomultiplier tubes (PMTs) are used to collect the scintillation light output from many of the detector elements. A PMT produces an electrical signal with an output proportional to the light incident upon it. The light input is in turn proportional to the initial energy deposited in the detector element. The electrical signal from the PMT is then digitised. Digitisation is done via an Analogue to Digital Converter (ADC), a Charge to Digital Converter (QDC) or a Time to Digital Converter (TDC) depending upon the particular detector system. These digital signals are then read by the data acquisition system (DAQ). The electrical signals produced by a detector must be converted into the desired physical measurement from the detector (e.g. energy deposited in a CB element). The conversion constants are determined through calibration procedures. These procedures undertaken for the various detector systems are described in Chapter 7.

5.8.1 Tagger

As discussed in Section 5.3, the energy measurement of bremsstrahlung electrons incident upon the tagger is determined by the hit position on the focal plane detector. The output from the individual tagger PMTs is amplified by a factor of 10 and then passed to a constant fraction discriminator. If the pulse passes the discriminator threshold it is read by a multi-hit CATCH TDC. The CATCH TDC is based upon the design used for the COMPASS experiment [129]. The logic pulse from the discriminator is also fed to a FASTBUS scaler unit. Scalers are not gated by the trigger and can be used to obtain a measurement of the electron event rate in the tagger. This event rate can be used to calculate the overall photon flux.

5.8.2 Crystal Ball

The output signal from each CB PMT is fed into an active splitter, this splitter accepts inputs from groupings of 16 crystals. The active splitter produces three matched outputs for every input signal (see Figure 5.18). The three signals are sent to a Flash ADC, a CATCH TDC and the other is used as an analogue signal

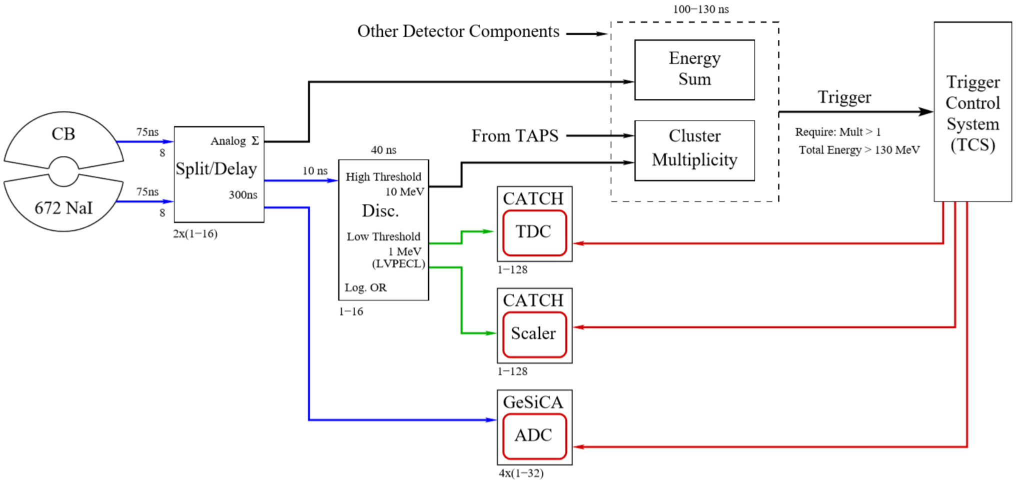

Figure 5.18 *Schematic diagram of the CB electronics system [125].*

for triggering. The signal sent to the CATCH TDC is first passed through a discriminator. The CATCH TDCs give a timing signal that is based upon the timing of the pulse. The signal sent to the Flash ADC is sent via a delay, the ADC samples the signal with a frequency of 40 MHz and calculates three integral values. These values are the integral over 1 μs (signal), over 100 ns before the main pulse (pedestal) and the integral over the first 300 ns (tail) of the pulse.

5.8.3 TAPS

The signals from the TAPS BaF_2 elements are analysed in such a way that the fast and slow timing scintillation components of the crystal can be used for pulse shape analysis [130]. The signals from these elements are passed through a splitter that produces three outputs (see Figure 5.19). The first of these outputs is sent to a leading edge discriminator (LED), this signal is used for triggering. The second output is sent with a delay to two QDCs. The QDCs have different integration times (200 ps and 40 ps) to allow for pulse shape analysis. The third output is processed with a constant fraction discriminator (CFD) and TDC, this output gives timing information for the pulse.

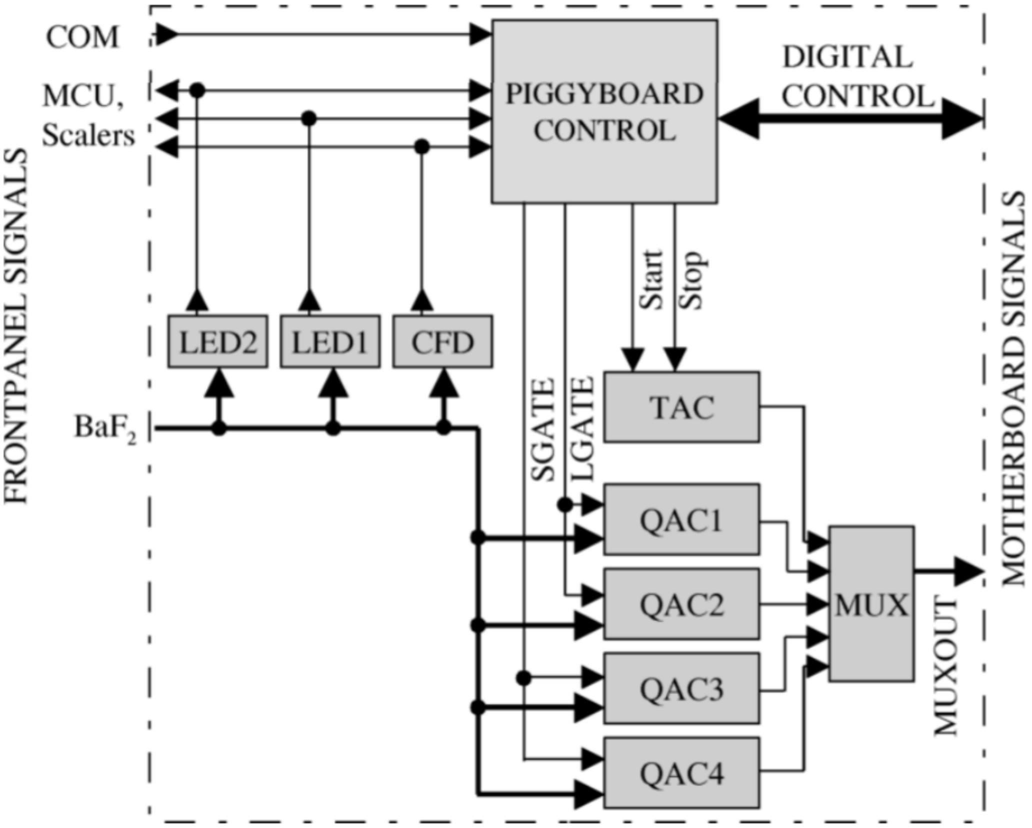

Figure 5.19 *Schematic diagram of the TAPS electronics system [130].*

5.8.4 Trigger

During the August 2016 experimental run the trigger was set to save an event from the DAQ only if the total energy sum in the CB of over 100 MeV and the event multiplicity was 2+. The energy sum amount is based upon the analogue sum of all output signals from the Crystal Ball.

5.9 Geant4 Simulation

The energy of particles detected in the Crystal Ball (CB) must be corrected for energy losses. This energy loss correction is a function of the path length through the detector array and the energy of the particle, E. The path length is a function of $\sin(\theta)$. The energy loss correction function is therefore a function of E and θ. To parametrise this function a simulation of the detector system was used. This simulation is also used in the calibration of the PID. An accurate knowledge of the energy of the particle is crucial for determining scattering angles and for estimating the effective analysing power.

A Geant4 simulation of the detector geometry in the A2 hall [131] was used during various stages of the work on this project. The existing simulation was updated to include the new PID, polarimeter and supporting structures [132]. Geant4 is a simulation toolkit [133] based upon a collection of C++ classes that model the passage of particles through materials. As particles traverse designated detector regions in the simulation the energy deposited is calculated in a series of steps (the step interval can be adjusted) according to the cross-sections of physical processes that are databased. The input to the simulation is a phase space event file which contains the 4-vectors of the photon beam and the desired reaction products as well as the vertex of the interaction in the target. The phase space events are generated using the EdGen [134] event generator.

Chapter 6

Updated Detector Equipment for Polarimeter Measurements

This chapter outlines the design and construction of the phase-II nucleon polarimeter setup at the University of Edinburgh. This design and construction work was carried out by myself with the assistance of colleagues and technical staff. The design considerations of the polarimeter required a subsequent redesign and reconstruction of the Particle Identification Detector (PID, this variant being PID-III) as well as a new target cover. The design considerations of these three components and their construction is described in subsequent sections. Testing, carried out during construction for PID-III, is also discussed.

6.1 Design

The basic design for the phase-II polarimeter was outlined in the proposal for the experiment [135]. The design built upon the previous phase-I polarimeter that was used in an earlier experiment [26]. A Geant4 simulation of the phase-I polarimeter setup can be seen in Figure 6.1. This setup was designed to measure polarisation for protons but not neutrons. Tracking information for events in this setup was more limited due to the lack of the MWPCs. The MWPCs were not in place as the space they are usually positioned in was taken up by the graphite polarimeter.

The proposed phase-II polarimeter was designed to measure polarimetry infor-

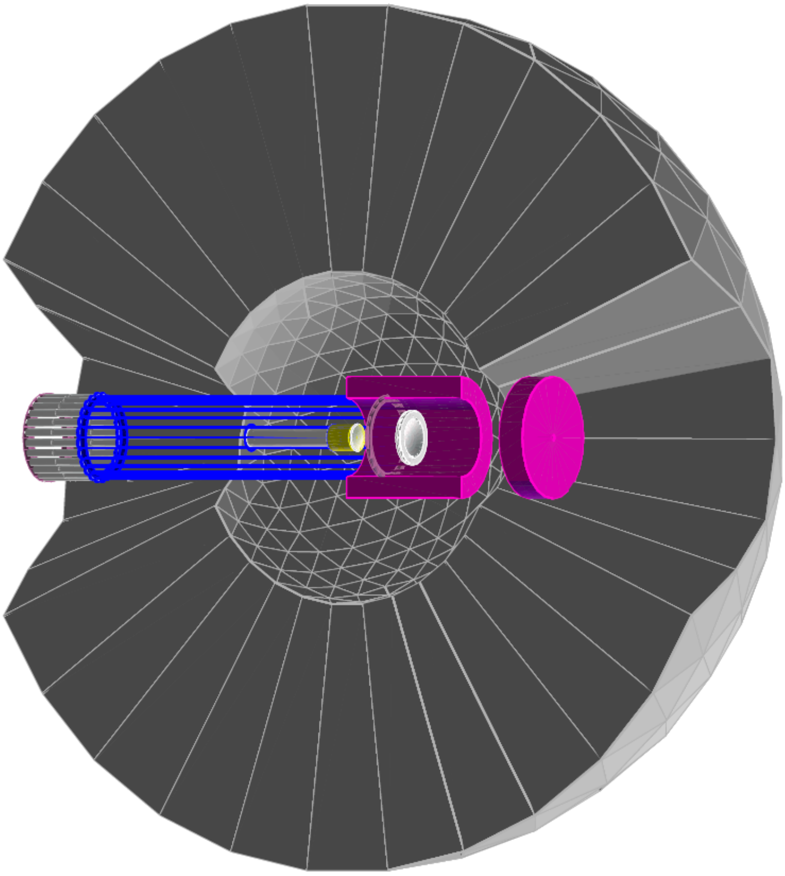

Figure 6.1 *A Geant4 simulation of the phase-I polarimeter. The PID is shown in blue, the graphite polarimeter in pink and the target in yellow [135]. Note the lack of the MWPCs. The photon beam enters from the left of this image.*

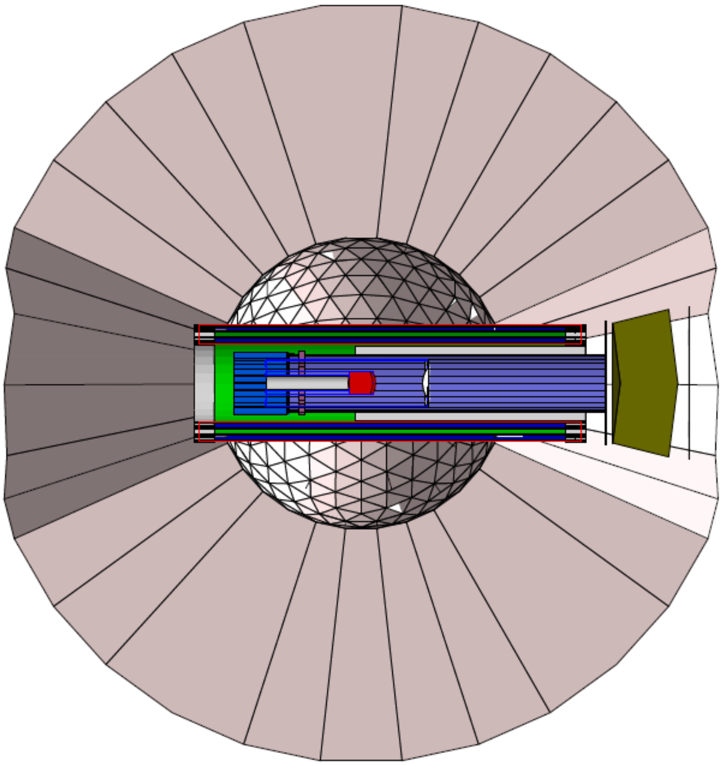

Figure 6.2 *A Geant4 simulation of the phase-II polarimeter [135]. The target is shown in red, the PID in blue and the MWPCs in red/bright green. In this design it was envisaged that there would be a 1.5 cm graphite cylinder, this is shown in grey between the PID and MWPCs. A new forward plug detector is depicted in dark green.*

mation for both protons and neutrons. The design envisaged that the phase-II would utilise both the PID and MWPCs. The design in the proposal featured a 1.5 cm thick layer of graphite between the PID and MWPCs. This design also included a new “forward plug” detector in the setup. A preliminary version of the design can be seen in Figure 6.2.

The 1.5 cm thickness of graphite in this design is less than the 2.25 cm of graphite used in the phase-I polarimeter. In the final design it was decided that the thickness of the graphite should be increased as much as possible to maximise the probability of a scattering event to occur. However, this component must sit between the PID and the MWPCs. Fitting more than 1.5 cm of material in this space was not possible without redesigning and rebuilding the PID (or MWPCs). Due to this limitation it was decided that a new smaller version of the PID would be built. Reducing the size of the PID also requires that the target cover would need to be reduced in size.

6.1.1 Polarimeter Design

Redesigning the PID and target cover allowed the polarimeter to be over 1 cm thicker than the preliminary design in the experimental proposal. The main piece of the polarimeter is a 30 cm long graphite cylinder of inner radius of 3.9 cm and an outer radius of 6.5 cm. The polarimeter also consists of a graphite end cap (situated downstream) at the end of this cylinder. This end cap is 2.6 cm thick and has a hole of 2.4 cm in radius removed from the centre to allow the beam to pass through. To allow the polarimeter to be fixed into a support structure, three shallow channels were drilled into the edge of the barrel and three holes of radius 0.33 cm were drilled into the end cap. These channels were spaced 120° apart from each other around the edge of the barrel. The holes in the cap were centred at a radius of 5.6 cm and again were spaced 120° apart from each other.

6.1.2 PID-III Design

The new PID-III was designed to have comparable performance to the existing PID-II. To achieve this, the segmentation of PID-III was kept the same as the previous iteration (24 elements). Each element would also be constructed from the same EJ204 plastic scintillator and the thickness of each element was kept at 4 mm [136]. The readout for the PID is also via the same type of photomultiplier tubes (Hamamatsu H3164-10) as used in PID-II. To reduce the PID in size the inner radius of the barrel formed by the elements was reduced to 3.3 cm. Due to this reduction in radius, the length of each PID element could be reduced from 50 cm to 30 cm whilst retaining the same angular coverage (in θ). As in the previous iteration, one long edge of each element has a side angled at 15° so that the elements can be arranged into a barrel shape.

To enable PID utilisation for events with particles going into the end cap, additional end pieces were added to one end of each PID element. These elements are again 4 mm thick pieces of EJ204. To improve light transfer from these end pieces along the length of the rest of the element, a 45° angled cut was taken from the end of each long PID element piece. The exact dimensions of these pieces and of the main part of the PID elements can be seen in Appendix A.

Scintillation light from the PID elements is channelled via lightguides to PMTs for readout. Due to the reduction in size of the PID, it would not be possible to

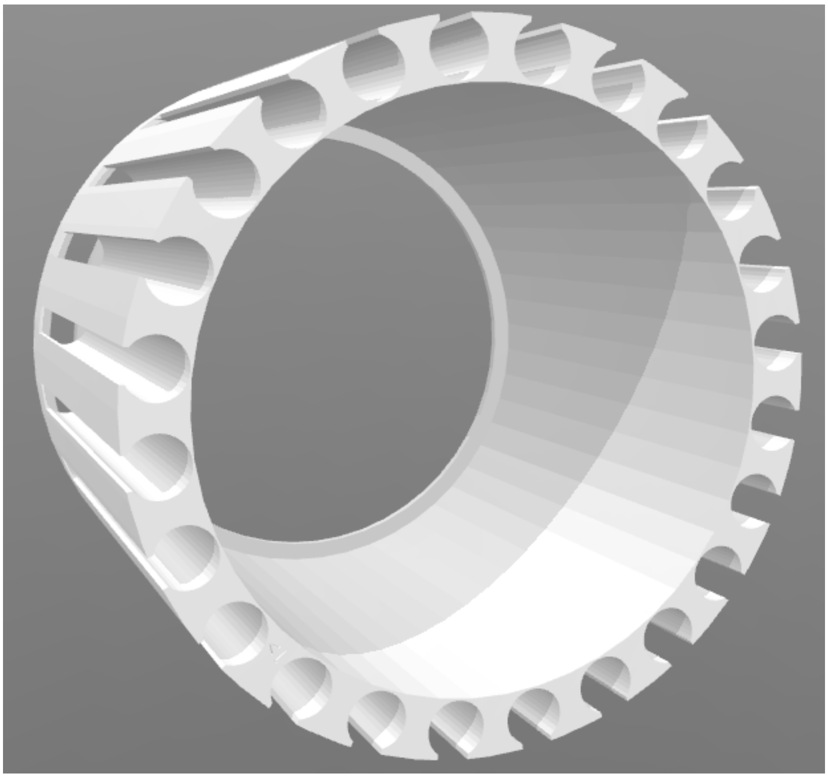

Figure 6.3 *CAD image of the PID support crown. There are 24 channels for the PMTs and a slot at one end, the light guides are inserted into this slot to couple to a PMT.*

have the PMTs at the same radius as the PID without moving the PID further forward. This is due to the way in which the target cover increases in size beyond the immediate target cell region. To keep the PID in the same position, curved perspex lightguides are used to channel the scintillator light out a further 2.2 cm in radius from the PID elements. At this point they are optically coupled to the PMTs for readout. The PID elements and PMTs require a supporting structure to keep them fixed in place. A new 3D printed "crown" was designed to support both the PID elements and PMTs simultaneously. The support crown is a cylinder with 24 channels to insert PMTs into, a CAD drawing of the crown can be seen in Figure 6.3; a full schematic diagram is available in Appendix A.

6.1.3 Target Cover Design

The hydrogen target cover also needed to be reduced in size in order to incorporate the new smaller PID and graphite polarimeter. The cover for the target was redesigned and built at the University of Edinburgh. The cover is a series of three pipes of gradually increasing diameter, the narrowest part that covers the liquid hydrogen target was the key piece to reduce in size. A new 1.5 mm thick carbon fibre tube of inner diameter 57 mm was used for this piece of the cover. New cover and window flanges; as well as two sections of aluminium pipe were also procured. Schematic diagrams are included in Appendix A.

6.2 Construction

6.2.1 Polarimeter Construction

The polarimeter barrel and end cap were machined from a graphite block by Olmec Advanced Materials [137]. The graphite was subsequently painted to reduce the spread of graphite dust. Threaded steel rods were inserted through holes in the end cap and along the channels in the graphite barrel. These were fixed in place at one end by screwing them onto a 1 cm thick aluminium ring. The rods were then fixed in place at the opposite end by an aluminium plate (again 1 cm thick) placed after the end cap. This plate is attached to an aluminium pipe that is used to position the polarimeter into the supporting "cradle" structure. An image of the polarimeter after painting and being fixed into its supports can be seen in Figure 6.4; schematic diagrams of the cradle structure can be seen in Appendix A.

The cradle is the same length as the polarimeter such that the entire graphite block can rest in the cradle before insertion. The support tube rests on two points on the cradle that can then be clamped down individually. The supporting tube was deliberately designed to be as long to be able to introduce the polarimeter into the rest of the detector setup very gradually. This is crucial due to the fragility of the MWPC and the small clearance between the components in the detector setup. The cradle is supported by two adjustable legs that are clamped to the edges of the existing Crystal Ball support structure and a third central leg that rests in place on this support structure as seen in Figure 6.5. The two legs that are clamped to the structure are individually adjustable in such a way that the cradle can be levelled to ensure that the polarimeter is inserted into the detector setup on a flat level and not at an angle.

Figure 6.4 *The painted polarimeter fixed into the support structure. The polarimeter end cap can be seen at the top right end of the support thread channel.*

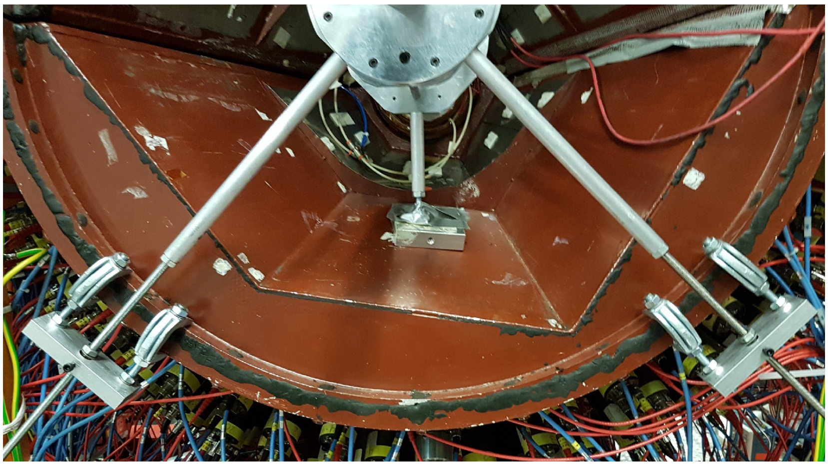

Figure 6.5 *The assembled polarimeter support cradle fixed in position on the Crystal Ball frame. The positioning of the three legs can be seen as well as the adjustable clamps to alter the level of the cradle.*

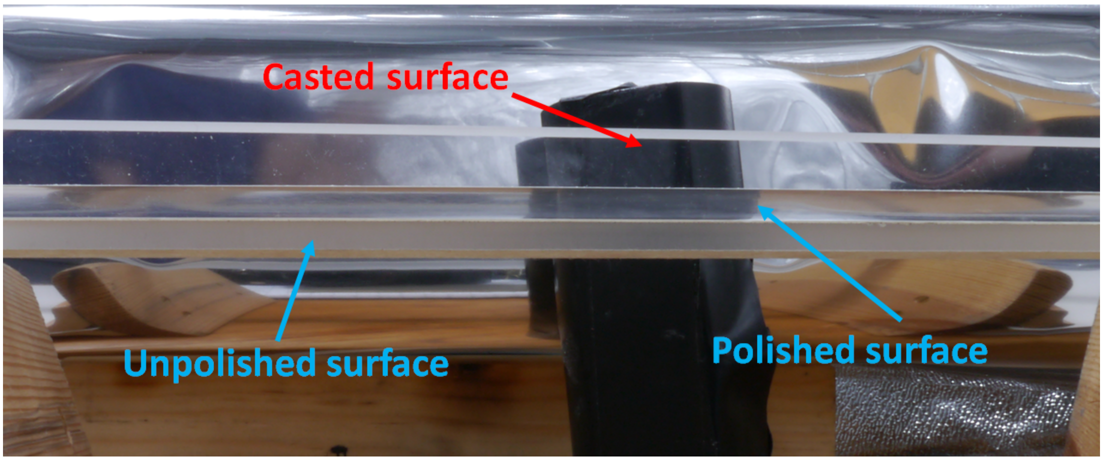

Figure 6.6 *Image showing the cut surfaces of a PID element before and after polishing compared to the cast surface.*

6.2.2 PID-III Construction

The PID elements and end pieces were cut from a cast sheet of EJ-204 by the mechanical workshop at the University of Edinburgh. Any edge that was cut in this way had a very rough surface, this is far from optimal for light transfer. The cut surfaces of the scintillator were polished. The polishing procedure involved gently sanding each edge with five successive grades (ISO grit ratings of P220, P600, P1000, P2000 and P3000 in order of coarsest to smoothest) of sand paper before applying a final polishing solution. The 321 polishing solution by Novus was used for this purpose [138]. The difference in optical quality of the surface before and after polishing can clearly be seen in Figure 6.6. After polishing the elements were thoroughly cleaned with isopropyl alcohol.

After cleaning, the end pieces were glued in place using EPO-TEK 301-2 epoxy glue [139]. After this glue cured, the elements were wrapped in 1 mil (25.4 μm) thick aluminised mylar along their length. The end pieces were painted with BC-620 reflective paint [140]. This paint was not suitable for the long, thin, nature of the main length of the scintillator elements. However, wrapping of the end pieces in mylar was deemed unsuitable due the fragility of the pieces once glued in place. The lightguides for the PID were also made by the mechanical workshop. A quick qualitative test of light transmission through the lightguides was carried out with a laser to ensure that light transmission was sufficient. As seen in Figure 6.7 the light transmission was very satisfactory. As with the PID elements, the lightguides also needed polishing, cleaning and wrapping. This was

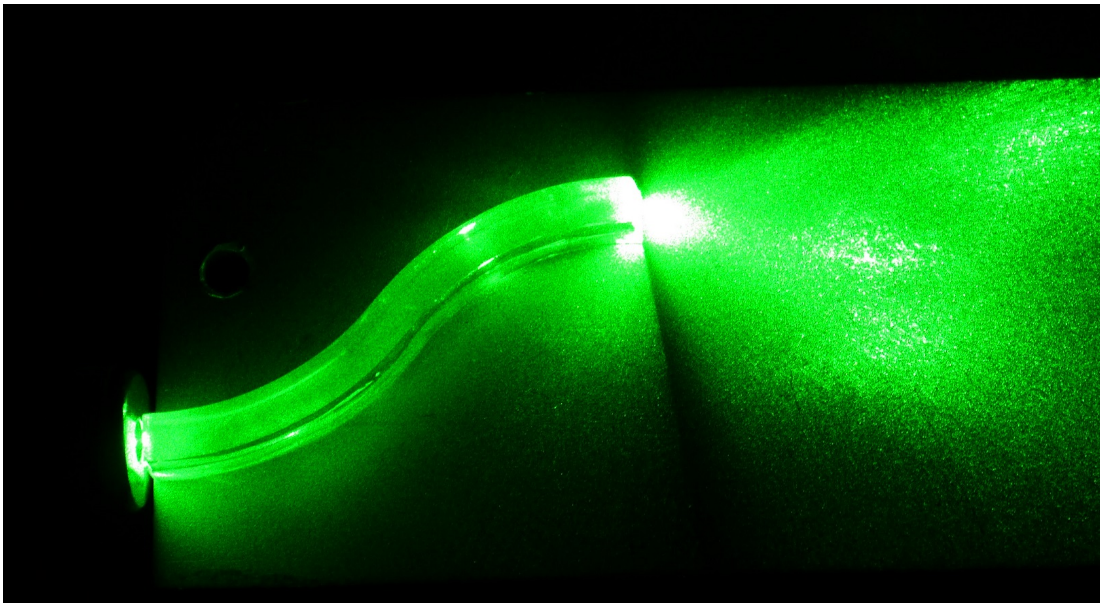

Figure 6.7 *Qualitative test of light transmission through a curved lightguide using a laser.*

achieved using the exact same method as for the PID elements. Once wrapped, the lightguides were glued onto the PID elements using the same EPO-TEK 301-2 glue as used for the end pieces.

After the lightguides were fixed in place, the PID was arranged in two halves, as shown in Figure 6.8. Each half was wrapped in an additional layer of 1 mil aluminised mylar. Following this, the lightguides from each half were slotted into position in the support crown. Once all 24 lightguides were in place, they were fixed into the support crown with silicone putty as shown in Figure 6.9. Once fixed in place, the PMT channels in the support crown were checked with an endoscope camera (see Figure 6.10). Any material blocking the lightguide surface (such as mylar foil or putty) was removed. After this all of the PID elements were wrapped in black tedlar for lightproofing. Silicone grease was applied to the PMT surface where it would interface with the lightguides and the PMTs were inserted into their channels. The support crown was subsequently wrapped in black tedlar. Black putty was inserted behind the PMTs in their channels for further lightproofing. The finished PID can be seen in Figure 6.11.

Figure 6.8 *Preliminary arrangement of half of the PID elements.*

Figure 6.9 *Lightguides being fixed into place in the support crown during construction.*

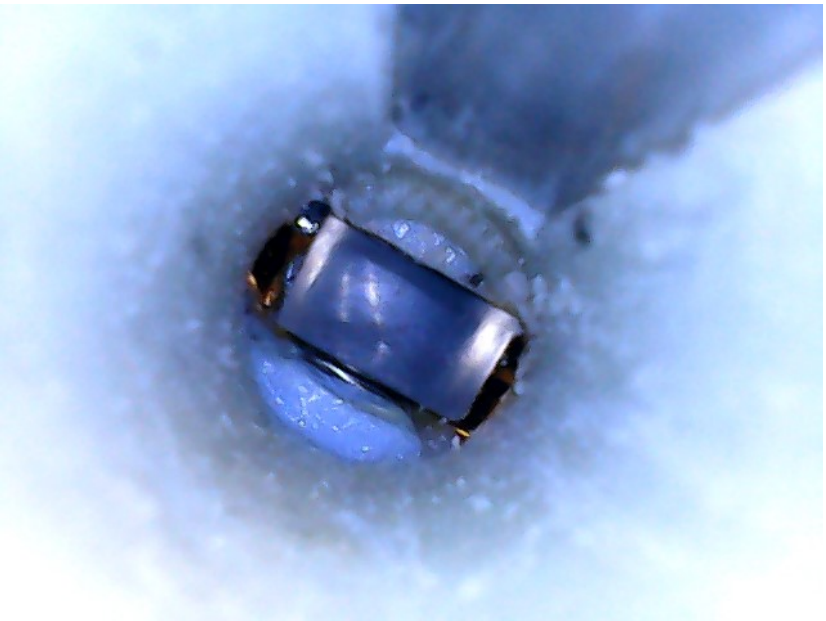

Figure 6.10 *An image from the endoscope camera used to confirm the lightguides were well situated in the support crown channels and not obscured by silicone sealant or mylar wrapping.*

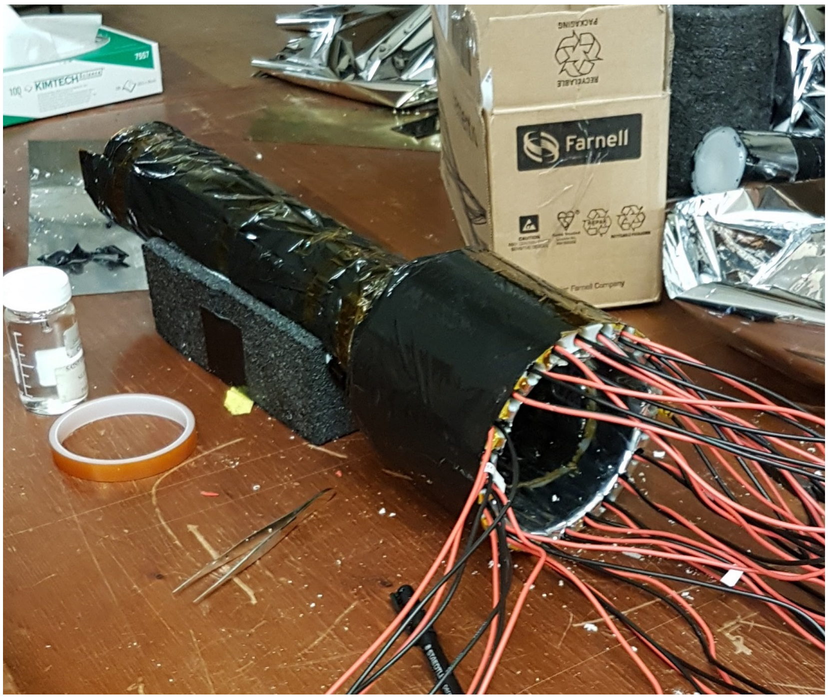

Figure 6.11 *PID-III shortly after final wrapping and construction.*

Figure 6.12 *The new target cover fully assembled prior to shipping.*

6.2.3 Target Cover Construction

The metal sections of the target cover were welded together by the mechanical workshop at the University of Edinburgh. The kapton window at the end of the cover was glued onto the flange with Torr Seal glue [141]. This flange was then glue onto the carbon fibre tube, which was in turn glued in place (again using Torr Seal) on the aluminium section. The cover was leak tested and no issues were found. The completed cover, seen in Figure 6.12, was then shipped to Mainz for installation.

6.3 Preliminary Testing on PID-III

Prior to their insertion into the crown, all of the PMTs were electronically tested. A selection of PID elements were also tested before they were fixed into the support crown. This testing examined the signal produced in a PID element from a radioactive source. A 111 kBq (at time of commission, 1995) ^{207}Bi was used for testing purposes [142]. The source was placed at various points along the PID element and the counts over 5 minutes were measured in order to examine how the signal varied as a function of distance from the PMT. This test setup can be seen in Figure 6.13. The variation in signal strength along the length of the elements was compared to the behaviour of elements used in PID-II. As can be seen in Figure 6.14, the tested PID-III elements compare favourably with those used in PID-II. This variation in signal is due to light attenuation along the length of the detector elements. This is discussed further in Chapter 7.

Once PID-III was shipped to Mainz and installed, the voltages for the PID-III PMTs were all readjusted in order to have similar signal output to the PID-II PMTs. This was carried out prior to the beamtime by examining the interaction of cosmic ray particles with the PID. The voltages used during the August 2016

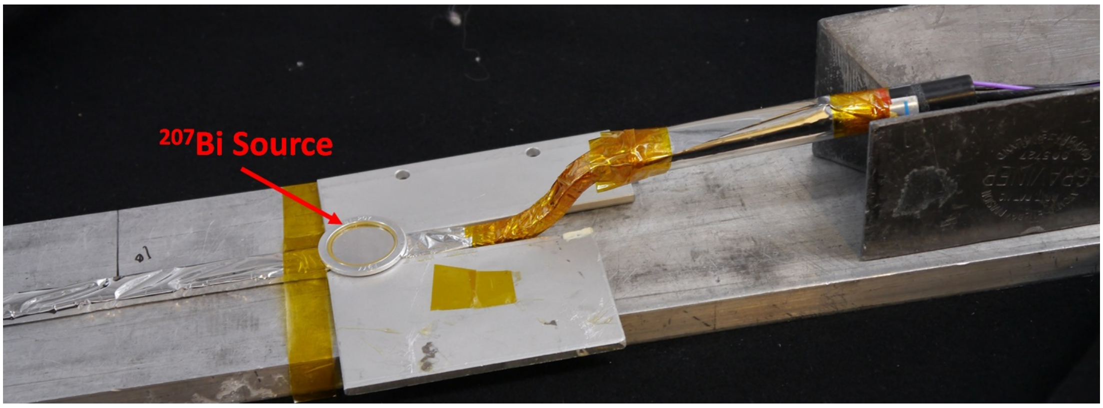

Figure 6.13 *^{207}Bi source placed on top of a test PID element as part of droop testing of the new elements.*

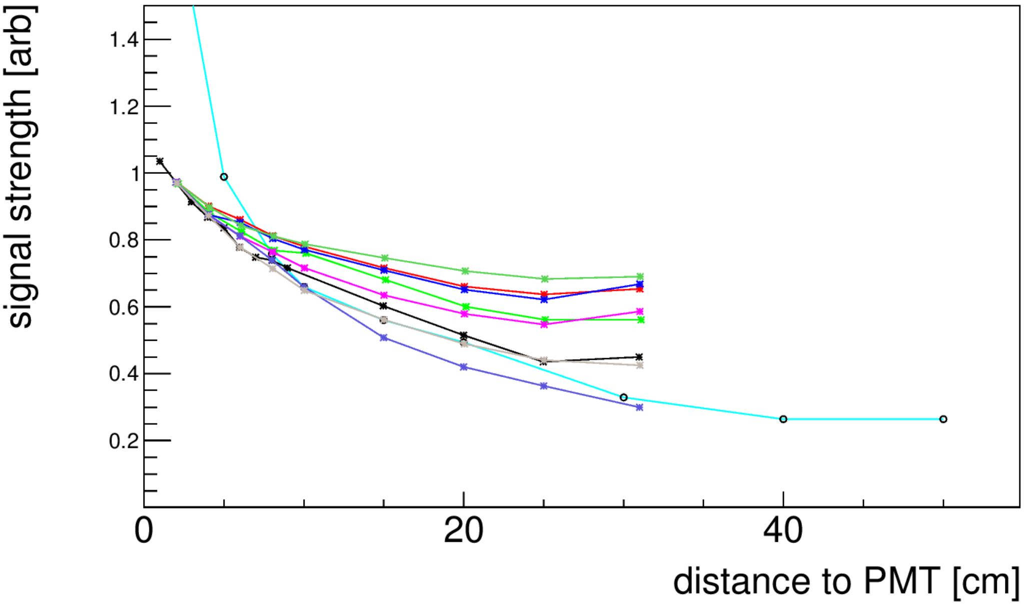

Figure 6.14 *Plot of the signal strength as a function of distance from PMT. The averaged performance of PID-II elements is illustrated in a light blue (line extending to 50 cm) and a sample of various PID-III elements are shown in various colours (lines ending at 30 cm).*

Table 6.1 *Voltages for the PID-III PMTs after adjustment*

PMT #	Voltage/V	PMT #	Voltage/V
0	850	12	1200
1	850	13	950
2	880	14	1050
3	1050	15	920
4	1130	16	850
5	950	17	830
6	1000	18	900
7	950	19	1050
8	1150	20	1150
9	900	21	1300
10	900	22	900
11	950	23	1050

beamtime for the individual PMTs after adjustment are listed in Table 6.1.

Chapter 7

Detector Calibrations

To convert the electrical signal outputs from the various detector systems into useful physical quantities detector calibration constants need to be determined. This chapter outlines the processes by which the detector systems used in the A2 hall are calibrated. Much of the calibration work on the detectors is carried out by colleagues within the A2 collaboration. Credit for each process will be explicitly outlined.

7.1 Timing Calibrations

Accurate timing calibrations are vital for background subtraction procedures (outlined in Section 8.1.1). These calibrations are also important for carrying out any analysis that looks at coincidence hits of detectors. The timing calibration procedure is outlined here and specific or additional procedures for individual detectors are described in their relevant subsections. The energy and timing calibrations for the detectors were carried out by Chris Mullen and other A2 collaboration members at the University of Glasgow unless specified otherwise.

Time to Digital converters (TDCs) provide detector hit timings, with the TDC providing a start and stop signal. The width of this signal is digitised to a discrete channel value. For a given channel, c, the physical time, t, is a function of the gain, g, and offset, o. The physical time is calculated via the relation

$$t = g(c - o). \tag{7.1}$$

The goal of a timing calibration is to determine the correct values for the constant and offset. The gain is a property that is intrinsic to the TDC and will *not* vary on an element by element basis. The offset does need to be determined on an element by element basis however. The offset can be adjusted and chosen in such a way that coincidence peaks that are used for calibration are centred on 0.

TDCs for different detectors are stopped and started in a slightly different way. The TDCs for the tagger, PID and CB are started by the trigger signal and stopped by their own signal as shown in Equation (7.2). The TDCs for the TAPS and Veto detectors are started by their own signal and stopped by the trigger signal as shown in Equation (7.3). When looking at time differences between detectors the trigger time should be made to cancel. The trigger time is affected by jittering so removing it improves the timing resolution. As such, time 'differences' are actually either a sum or a difference depending upon the detector combination.

$$t = t_{\mathrm{trig}} - t_{\mathrm{det}} \tag{7.2}$$

$$t = t_{\mathrm{det}} - t_{\mathrm{trig}} \tag{7.3}$$

To determine the timing offset for a detector element the timing spectrum of each element is fitted with a Gaussian. The mean, μ, calculated from this fit is used in conjunction with the conversion gain,g, and old offset value,o_{old}, in Equation (7.4) to determine a new value for the offset, o_{new}.

$$o_{\mathrm{new}} = o_{\mathrm{old}}\frac{\mu}{g} \tag{7.4}$$

7.1.1 Crystal Ball

The conversion gain for all Crystal Ball elements is fixed at 0.117 ns/channel [143]. As such, only the timing offsets must be determined for each element. There are three steps to this procedure. One of these steps, the time walk correction is necessary due to the fact that the NaI(Tl) crystals have a slow rise time of $\sim$ 250 ns [32]. This slow rise time means that the time at which the signal exceeds the LED threshold is strongly dependent upon the amplitude of the signal - i.e. there is an energy-dependent component to the time.

Time Prealignment

The first step to determining the correct offset is the time prealignment. The time difference, Δt, for all cluster hits combinations is determined dependent upon the central detector element hit in each case. Events examined are not dependent upon a PID coincident hit and slow charged particles are neglected. As such, the events examined are photon event clusters. The time difference distribution for each element, i, is fitted with a Gaussian. The mean value of the Gaussian for each element, μ_i, is used to determine a new offset value, o'_i, for each element. This is calculated via

$$o'_i = o_i + \frac{\mu_i}{g_i}, \tag{7.5}$$

where o_i is the initial offset and g_i is the conversion gain which is the same for each element as outlined earlier. Offsets are calculated iteratively for all elements. Once converged the mean values for all Δt distributions are centred at 0.

Time Walk Correction

The time-energy dependent component must be corrected to optimise the Crystal Ball timing resolution. To do so plots of the time as a function of the energy deposition, E_{dep}, in each element are fitted with

$$t(E_{\text{dep}}) = a + \frac{b}{(E_{\text{dep}} + c)^d}, \tag{7.6}$$

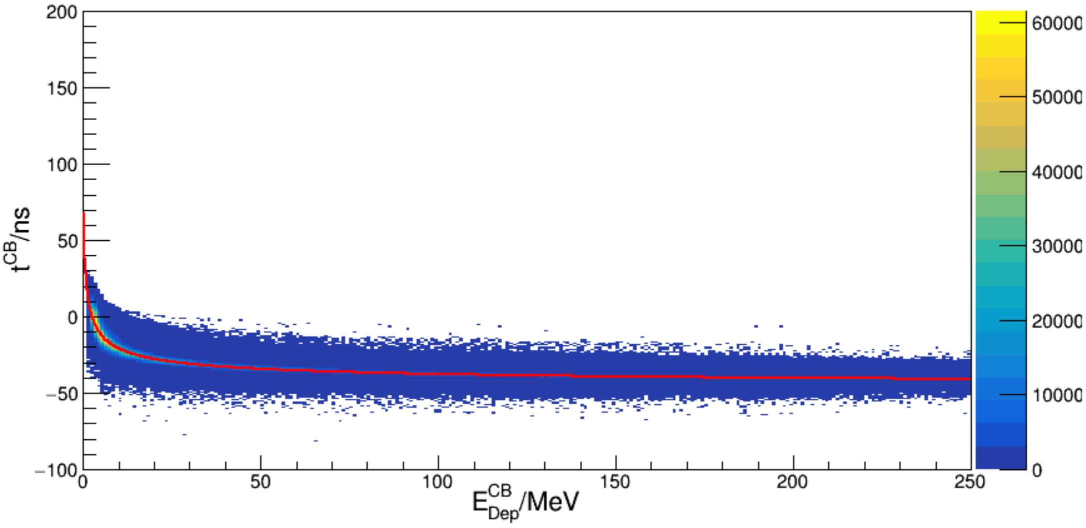

Figure 7.1 *Time in the Crystal Ball as a function of the energy deposit in the Crystal Ball showing the time walk effect [144].*

where a, b, c and d are free parameters that are determined individually for each detector element. Figures 7.1 shows an example of this fitting procedure. The result of applying the correction is clearly seen in Figure 7.2. The parameter a is the rise time parameter. For some elements, this may need to be adjusted further as discussed in the next section. This fit is applied on π^0 events that have also had missing-mass and invariant-mass cuts applied in order to have a clean signal. The relative timing of the tagger is used to calculate the time for all detector elements for the selected events. The parameters determined in Equation (7.6) are used to obtain a corrected detector time, t', via

$$t' = t - (a + \frac{b}{(E_{\text{dep}} + c)^d}). \tag{7.7}$$

Because the tagger-time difference is used to calculate the corrected parameters, the distributions of t' is automatically centred at 0 with respect to the tagger.

Final Calibrations

The fits for the time-energy dependence carried out for the time-walk correction are not particularly accurate for elements with low statistics (e.g. elements in the backwards region). This inaccuracy causes a slight shift in the relative timing between CB elements. This can be corrected by fitting the mean values of the

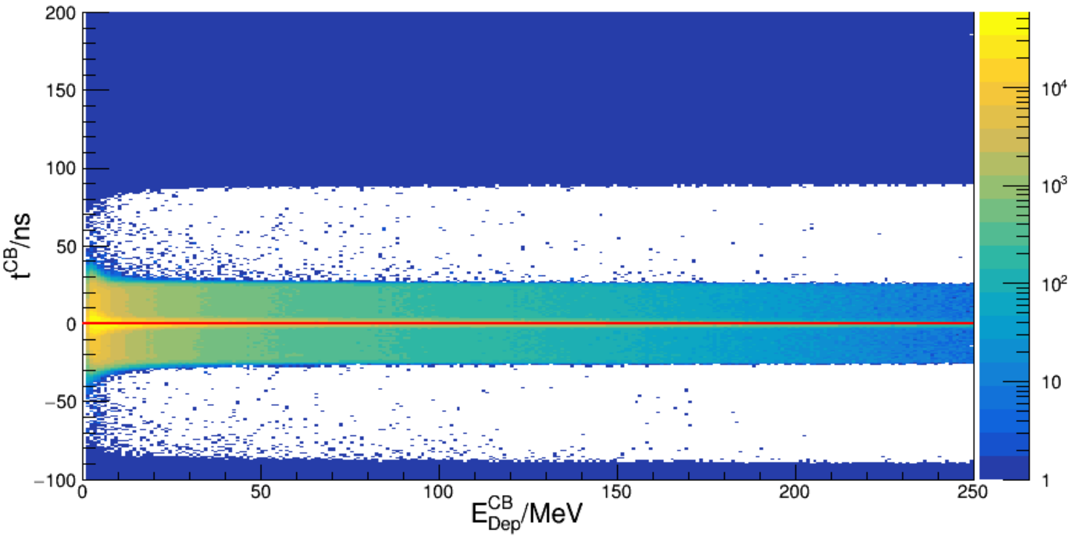

Figure 7.2 *Time in the Crystal Ball as a function of the energy deposit in the Crystal Ball after the time walk correction has been applied [144].*

relative times again after the time walk correction. These fits can be centered at 0 by adjusting the rise-time parameter, a, from Equations (7.6) and (7.7).

7.1.2 TAPS

The TDCs used for TAPS have a fixed conversion gain of 0.05 ns/channel; as such, to calibrate TAPS the TDC offsets must be optimised for each element. Unlike the Crystal Ball, the detector elements used in TAPS have a short rise time so a time-walk correction is not needed. The TDC offset values are calibrated using the same procedure as for the Crystal Ball. Time-difference spectra are created for the central element detector in each cluster for all neutral particles determined in TAPS. Using Equation (7.5) new values for the offset are calculated. Again this is an iterative procedure; once completed, the peaks for all detector elements should be aligned at 0. A good timing resolution for TAPS is essential as TAPS is utilised in the timing calibration of the Tagger. TAPS can also be used for time of flight measurements.

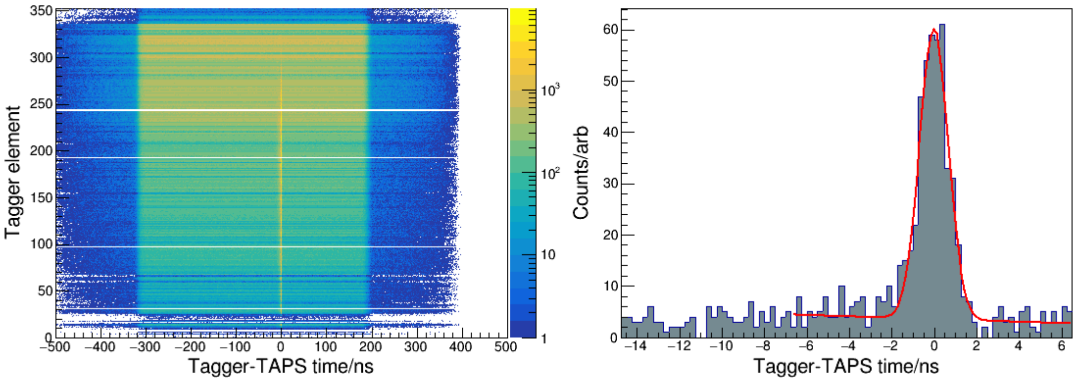

Figure 7.3 ***Left*** *: Timing spectra for all neutral particle hits in TAPS and hits in tagger.* ***Right*** *: An example fit for one tagger element [144].*

7.1.3 Tagger

As mentioned in the prior section, the timing calibration for the Tagger is dependent upon TAPS; as such, the calibration for TAPS must be carried out first. The gain of the Tagger TDCs is fixed at 0.117 ns/channel [143]; as with TAPS and the Crystal Ball, the TDC offsets must be calibrated. For the Tagger, all combinations of neutral particles in TAPS and hits in the Tagger are examined. The time difference between the TAPS elements and the tagger (for every activated tagger element) is calculated and plotted as seen in Figure 7.3. The coincidence peak is fitted with a Gaussian and Equation (7.5) is utilised once again to iteratively adjust the offset values until all timing spectra peak at 0.

7.1.4 PID

The TDCs for the PID have fixed gains of 0.117 ns/channel [143], so as with the Tagger and TAPS, the TDC offsets must be adjusted for each element. Again, this is done by fitting a Gaussian to time difference spectra and using Equation (7.5) to iteratively find new values for the offset until the peaks align at 0 in the spectra for each element. For the PID, two different charged particle hits in the PID are taken as a pair and the time difference between these is plotted as a function of detector element hit.

7.2 Energy Calibrations

Energy deposition in a scintillator is generally converted to an electrical signal (typically via a PMT). This analog electrical signal is then usually converted to a digital signal via a charge to digital converter (QDC). The digitised channel number a signal is detected in, c, can be converted to a physical energy deposition, E_{Dep}, via the relation

$$E_{\mathrm{Dep}} = g(c - p), \tag{7.8}$$

where g is the conversion gain (Energy Unit/Channel) and p is the pedestal position (channel) that represents the channel that corresponds to zero energy. The purpose of carrying out the energy calibration is to find suitable values for g and p. This conversion assumes the approximation that the produced electrical signal is linearly proportional to the energy deposited.

7.2.1 Crystal Ball

The energy calibration of the Crystal Ball must be carried out in several steps. An initial low-energy calibration is carried out that is important for the DAQ system. A second energy calibration valid for higher energies is then carried out. This is followed by a higher-order correction to counteract an overcorrection from the second step. The second and third calibrations are important for offline analysis of the data. These are described below.

Low-Energy Calibrations

The low-energy calibration for the Crystal Ball is carried out by colleagues at the Institut für Kernphysik in Mainz. To carry out the calibration a $^{241}\mathrm{Am}/^{9}\mathrm{Be}$ source is used. This source produces a 4.438 MeV monochromatic gamma ray through a series of decays

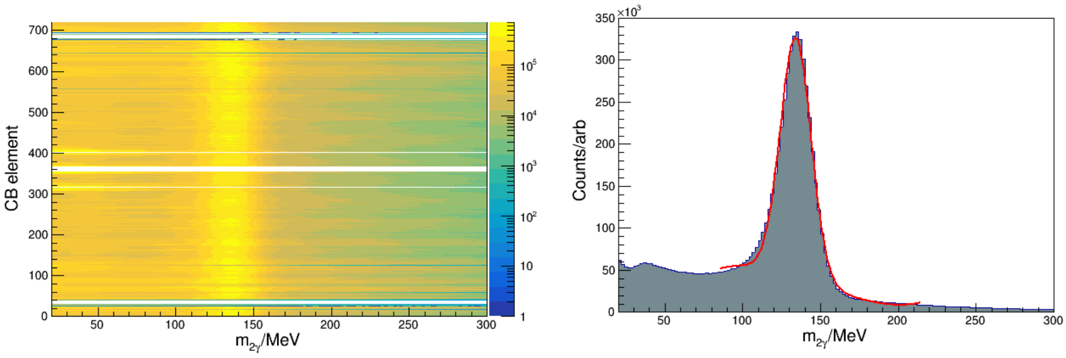

Figure 7.4 ***Left*** *: Spectrum of the invariant mass for all CB elements.* ***Right*** *: An example fit for one CB element[144].*

$$
\begin{aligned}
{}^{241}_{95}Am &\rightarrow^{237}_{93} Np + \alpha, \\
{}^{9}Be + \alpha &\rightarrow^{13} C^{*}, \\
{}^{13}C^{*} &\rightarrow^{12} C^{*} + n,
\end{aligned}
$$

where ^{12}C* subsequently decays to its groundstate via the emission of a 4.438 MeV gamma ray. This is the gamma ray that is used in this calibration. The gain for each detector element photomultiplier tube is adjusted so that the peak in the ADC spectrum from these photons occurs in the same position in this spectrum.

High-Energy Calibrations

Most events of interest in the Crystal Ball have far higher energies than the 4.438 MeV photons used for the low-energy calibration. As such, for offline analysis a higher-order energy calibration must be applied. To carry out this energy calibration photons from the decay of the neutral π^0 meson are used. The peak of the π^0 meson in the two-photon invariant mass spectrum is used as a reference point for this calibration process. The invariant mass for all neutral cluster pairs is filled in histograms depending upon the central detector element of the clusters. This calibration process must be done iteratively as the gain adjustment of a particular detector element is not independent of the gain applied to other elements. After several iterations of gain correction the peak of the π^0 should be at the correct position for all detector elements. An example of this can be seen in Figure 7.4.

Quadratic Energy Calibrations

After carrying out the calibration described in the previous section, the two-photon invariant-mass spectrum should have a peak at the position of the π^0. However, in the same spectrum the peak for the η meson is not in the correct position with respect to its real mass. This is due to an overcorrection by the energy calibration for higher energies. This overcorrection is caused by the photon energy being reduced due to detector thresholds and shower losses. The relative weight of this energy loss is smaller for higher cluster energies, hence the overcorrection for higher energies, such as photons from the η.

To adjust for this, a quadratic function is applied to the energy deposition [145]. This function takes the form

$$E' = aE + bE^2, \tag{7.9}$$

where E' and E are the corrected and uncorrected energies respectively. The constants a and b are determined such that the corrected energies result in the correct invariant masses for both the π^0 and η mesons. The two correction parameters are determined for each detector element. Further details on the high-energy calibration process can be found in Ref [146].

7.2.2 TAPS

The energy calibration for TAPS is performed in a similar manner to the Crystal Ball calibration. There is a low-energy calibration stage that must be carried out for data taking and a higher-energy calibration that is required for offline analysis. The low-energy calibration stage for TAPS is carried out using cosmic rays.

Low-Energy Calibrations - Cosmic Rays

Unlike in the CB, cosmic rays can be used to perform an energy calibration in TAPS. Due to the fact that all of the elements in TAPS are orientated

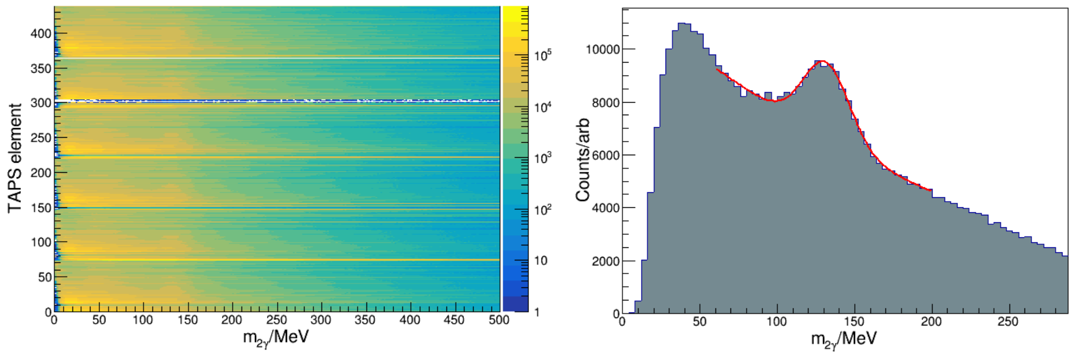

Figure 7.5 ***Left*** *: Spectrum of the invariant mass for all TAPS elements.* ***Right*** *: An example fit for one TAPS element [144].*

horizontally the distribution of cosmic ray trajectories is equivalent for all elements. A calibration using cosmic rays is generally carried out before and after a measurement.

The spectra obtained from a TAPS cosmic ray measurement is fitted with a Gaussian and an exponential background on an element by element basis. From the Gaussian peak position, the mean energy deposited by cosmic rays can be calculated. From this cosmic ray spectrum the pedestal position can be extracted; thus using Equation (7.8), the conversion gain for each element can be determined.

High-Energy Calibration

The gains for the TAPS elements are calibrated using the same process as is used for the CB. However, in the case of TAPS events where one photon is detected in the CB and one is detected in TAPS are used to carry out the calibration. This is due to the very limited statistics of π^0 decays where both photons are detected in TAPS. Figure 7.5 shows how the invariant-mass spectrum of these events appears for all elements once the process is complete. Because one of the photons must be detected in the Crystal Ball, the calibration for the Crystal Ball must be carried out before the high-energy calibration for TAPS.

Additional Calibrations

In addition to the calibrations detailed above there are also further TAPS calibrations that are applied. These calibrations are carried out in order to use

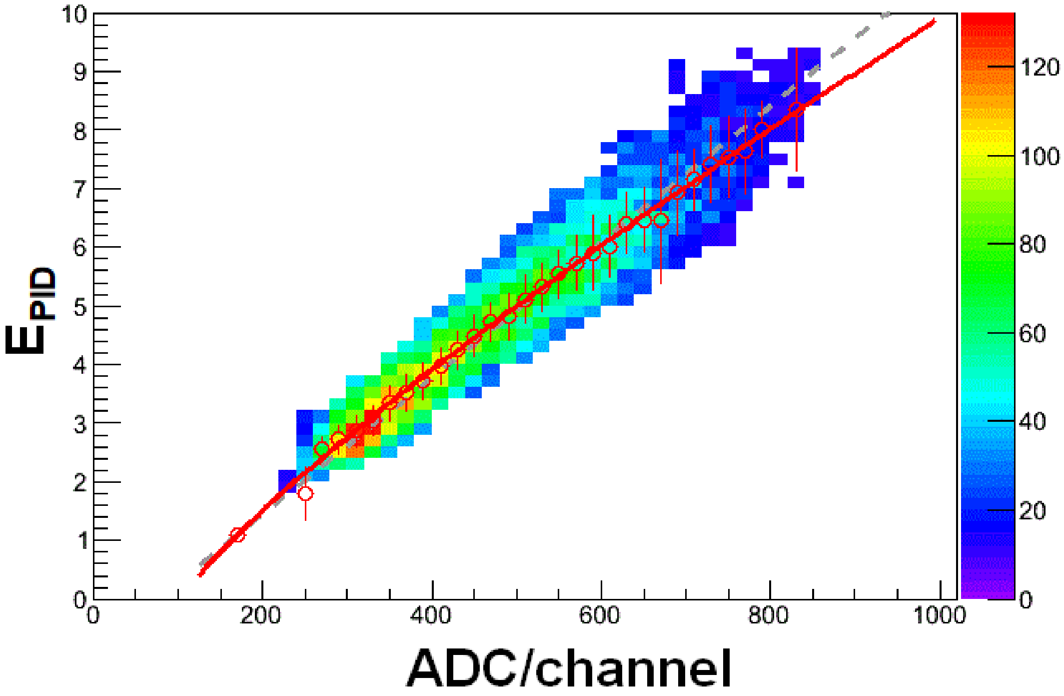

Figure 7.6 *Calculated* E_{PID} *values plotted as a function of the ADC channel number [147].*

the BaF_2 detectors for pulse shape analysis. As TAPS is not used in the analysis outlined in this thesis (beyond needing to calibrate for the tagger) this calibration will not be detailed here. The procedure for these calibrations is outlined in [146].

7.2.3 PID

To select appropriate pedestal and gain values for the PID elements, events from the reaction $\gamma n \to p\pi^-$ are examined. The selection of these events must be done without utilising the PID. In principle, any reaction that produces two particles (with at least one charged) could be used. Only events in a narrow angular range in θ of 35-45° were selected. From Monte Carlo simulations of the same reaction, the value E_{PID} for a given value of E_{CB} can be determined. This relation is then applied to determine the E_{PID} values for the real data from their real E_{CB} values. These calculated E_{PID} values are then plotted as a function of their ADC channel number. This plot is then fitted with a function of the form given in Equation (7.8) to produce a straight line. The fit parameters directly give the gain and pedestal values. An example fit of this type can been seen in Figure 7.6

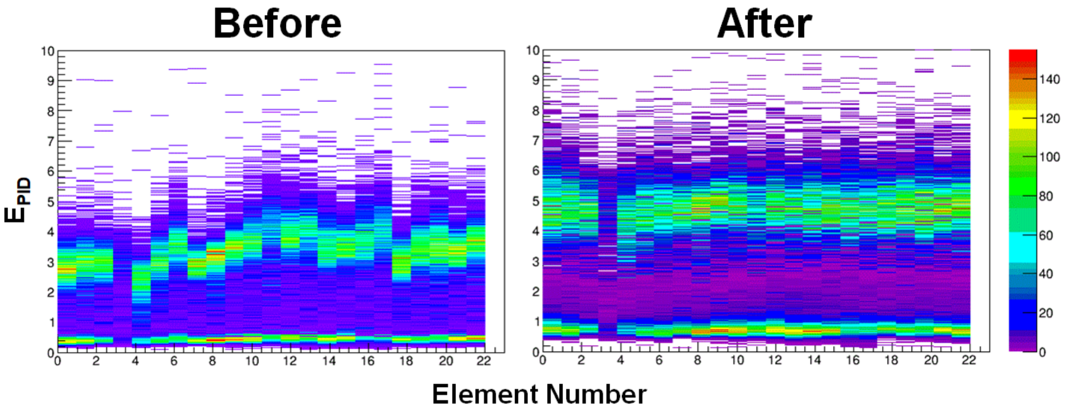

Figure 7.7 *E_{PID} for a given reference point as a function of element number before (Left) and after (Right) iteratively calibrating the PID [147].*

This procedure is done for all PID elements. Once completed, reference points in E_{CB} on a plot of E_{PID} as a function of E_{CB} (An E- ΔE plot) are taken for each element. Reference points should be taken across the full range of energy deposition values. E_{PID} at these reference points is then plotted as a function of the PID element number. If the calibration is correct, these points should all be aligned. If this is not the case the calibration procedure outlined above is repeated until the points align. An example of how such a plot may look before and after all elements are sufficiently aligned can be seen in Figure 7.7.

The energy calibration for the PID was carried out by Mikhail Bashkanov at the University of Edinburgh.

7.2.4 Tagger

The relation between the electron energy and the tagger element hit depends upon the magnetic field strength of the tagger dipole magnet and upon the energy of the electron beam. Between beamtimes the energy of the electron beam is very stable, however, from beamtime to beamtime the magnetic field strength can vary slightly. Over the course of a single beamtime the field is usually stable. The calibration of the tagger energy is carried out using the ugcalv2ua [106] program. The magnetic field map and the electron beam energy are fed into this program. The program then associates electron energies with tagger channels. The calibration can be tested by changing the electron beam energy and feeding this electron beam into the tagger magnet with a very low intensity. If this is done without a radiator present then the beam should feed directly into the focal plane detector, if the calibration is correct then the element that will trigger should correspond with the energy of the beam provided.

7.3 Other Calibrations

7.3.1 PID Light Attenuation

The PID elements are relatively long, thin pieces of plastic scintillator. The readout of each element is carried out via a PMT at one end of the element, light is attenuated as it travels along the element to the PMT. Because of this, a particle of a given energy that is incident upon the PID will produce a different signal depending upon the position along the length of an element that the particle hits. To correct for this, a light-attenuation correction (referred to in the A2 collaboration as a "droop" correction) must be applied.

To carry out this correction individual protons incident upon the PID are selected across a range of angles. For a given angle an E-ΔE plot is created. This plot is fitted with the $E_{\mathrm{PID}} = f(E_{\mathrm{CB}})$ curve determined from Monte Carlo simulations of protons incident upon the PID and CB. The quantity $\frac{E_{PID}}{f(E_{CB})}$ is determined and plotted as a function of the hit position of the particle along the PID, L. L is a function of the polar angle, θ, the distance to the target centre from the lightguide, T_0, the inner radius of the PID, R_0, and the position of the event vertex (along the z-axis) in the target, V_0. From these quantities L is defined via

$$L = T_0 + V_0 + \frac{R_0}{\tan\theta}. \tag{7.10}$$

The plot of $\frac{E_{PID}}{f(E_{CB})}$ as a function of L is fitted with a straight line to parametrise the droop as seen in Figure 7.8. The values of the light attenuation constants are tabulated in Appendix D.

This correction for the PID was carried out by Mikhail Bashkanov at the University of Edinburgh.

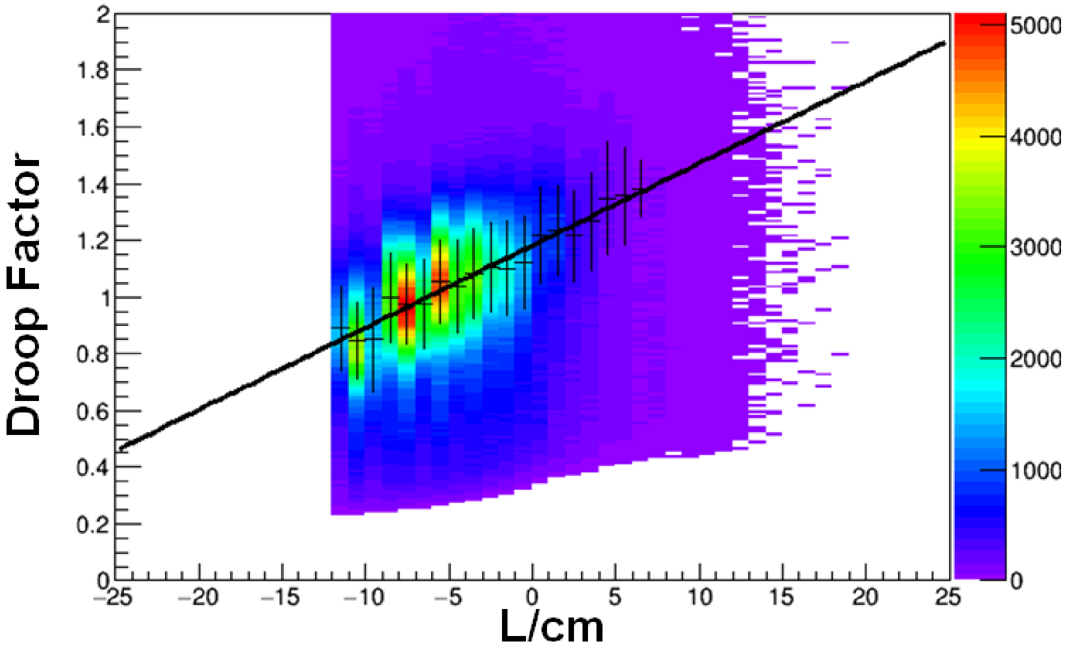

Figure 7.8 $\frac{E_{PID}}{f(E_{CB})}$ *as a function of L with a fit to parametrise the light attenuation factor [147].*

7.3.2 PID Azimuthal Angle Calibration

The PID is moved in and out of the Crystal Ball on a fairly regular basis. For example, the PID needs to be removed if any work needs to be carried out on the MWPC or the target. When it is replaced the correlation of PID element to azimuthal angle, ϕ, may be different. To correct for this, events with exactly one hit in the PID and one hit in the CB are examined. The ϕ distribution in the Crystal Ball is examined and the coincidence peak is found. In addition to the clear coincidence peak, there is also a smaller peak 180° separated from this. This peak is due to reactions that have produced a charged and a neutral particle back to back. Reactions where this occurs and the charged particle is not detected in the CB, but is detected in the PID (and vice versa for the neutral particle), produce a “false” coincidence peak. To reduce systematic uncertainties, the PID element numbers are plotted as a function of ϕ and a linear function is fitted to this distribution. From the fit, the angular position of each individual element can be determined. This correction for the PID was carried out by Chris Mullen and other A2 collaboration members at the University of Glasgow.

Chapter 8

Event Selection and Discussion of Systematic Uncertainties

8.1 Event Selection

The procedure used to identify events of interest for the determination of the observables Σ and $C_{x'}$ is outlined in the following subsections. After the selection cuts detailed in Sections 8.1.2 and 8.1.3 are applied to the data, a background subtraction procedure is applied to remove contributions from random events. The procedure and purpose of this subtraction is detailed in Section 8.1.1.

The analysis of experimental data is carried out using various pieces of code based upon the CERN ROOT language [148] and is a multi-step process. The first step is to read and sort the raw data files. This is done by the AcquRoot software developed by the A2 collaboration [149]. The output of Acqu provides information on an event-by-event basis. This output is then processed further using the A2GoAT software [150]. This software allows for particle reconstruction and further data sorting into new analysis trees. A2GoAT can then be used again to carry out further physics analysis of the initial output [151]. These physics files can then be analysed further using CERN ROOT macros [152]. This chapter outlines the various cuts and event selection procedures that are applied to the data in the second and third (A2GoAT) stages, as well as the fitting procedures used in the final stage to extract quantities of interest.

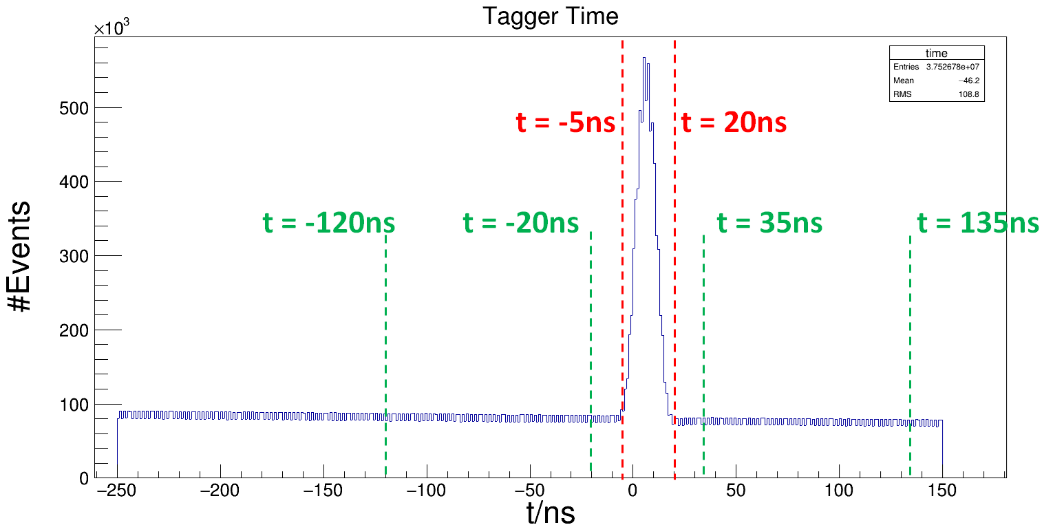

Figure 8.1 *Tagger timing distribution with the prompt peak clearly present. The prompt (red) and random (green) windows used are illustrated on the plot.*

8.1.1 Random Subtraction

This section discusses the random subtraction method employed in the analysis. Within the timing coincidence window for an event, numerous electrons will be detected in the focal plane of the tagger. Only one of these electrons will be responsible for producing the bremsstrahlung photon that reacted with the target to cause the detected event. Photons associated with other tagged electrons within the event timing window may have been absorbed in the collimator or simply not have interacted with the target. Knowing which electron produced the event photon is vital for calculating any information that is dependent upon the photon energy. It is impossible to determine exactly which electron is responsible for the event photon. Instead, a random subtraction can be applied to the data to remove the contribution of any ‘random’ photons. A timing coincidence is used whereby tagger hits recorded within a 25 ns window of the event are classified as ‘prompt’. Any events outside this window are ‘random’ events. As can be seen in Figure 8.1 there is a clear peak in the prompt region and a relatively flat background of random events outside this. Some random events also occur within the prompt region, these events must be subtracted.

To subtract the contribution of random events in the prompt peak, events are sampled from three regions, the prompt peak, a random window to the left of the prompt peak and a random window to the right of the prompt peak. The width of these regions is used to determine the prompt versus random ratio (R_w) using the relation

$$R_w = \frac{P}{R_{\text{Low}} + R_{\text{High}}}, \tag{8.1}$$

where P, R_{Low} and R_{High} represent the widths of the prompt and random windows. In the analysis detailed in this chapter P has a width of 25 ns (-5 - 20 ns) and the two random windows were each of width 100 ns (R_{Low} = -120 - -20 ns and R_{High} = 35 - 135 ns), giving a R_w value of 0.125. Data analysis is conducted for all photons tagged in an event. The random events are used in combination with R_w to re-scale the prompt events via

$$N_t = N_{\text{p}} - N_r R_w, \tag{8.2}$$

to remove the contributions of random events. In Equation (8.2), N_{p} is the number of prompt events, N_r is the number of random events, R_w is as defined above and N_t is the 'true' number of prompt events after random subtraction. This random subtraction procedure is carried out at the end of the A2GoAT physics stage of the analysis for all events. This process is crucial to accurately determine parameters that are strongly dependent upon the incident photon energy. The missing mass (discussed further in Section 8.1.2) is one such example, as can be seen in Figure 8.2.

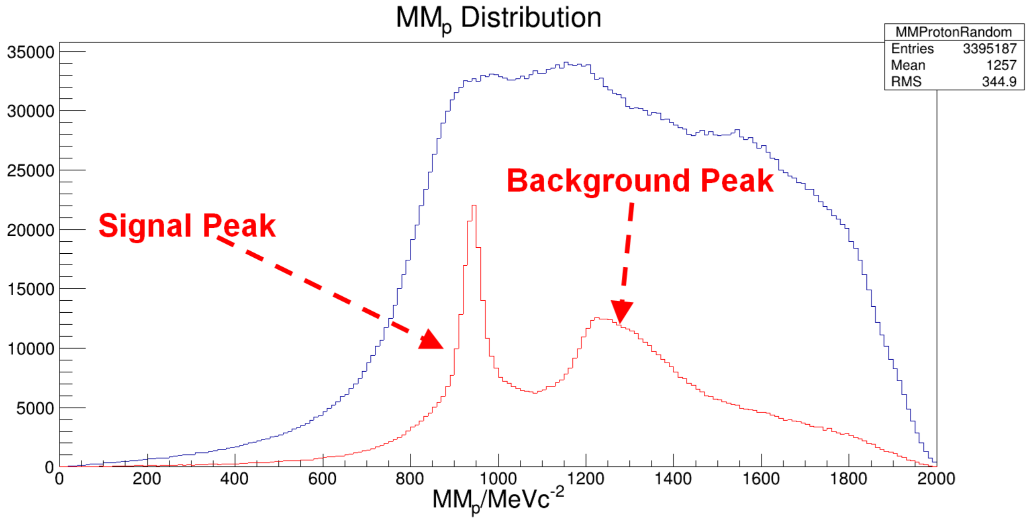

Figure 8.2 *An example missing mass distribution for prompt (red) and random (blue) photons. As discussed in Section 8.1.2, events of interest should show a peak at* $MM_{\mathrm{p}} \approx 940$ *MeV. This peak and a peak at higher missing mass (background contribution) can clearly be seen in the prompt spectrum. Random events are smeared over a range of missing mass values.*

8.1.2 Analysis of Σ

As discussed in Chapter 3 the beam asymmetry observable, Σ, is a single polarisation observable that is dependent upon the linear polarisation of the incident photon beam. This single polarisation observable quantity is not dependent upon the proton or neutron from the photodisintegration reaction scattering in the polarimeter. As such, to extract Σ from the data, any $\vec{\gamma}d \to pn$ events can be analysed. Events where both the proton and neutron are not scattered in the polarimeter were analysed to extract Σ. A cut that ensures the reaction products are coplanar in ϕ can be utilised to ensure the detected tracks were not scattered by the polarimeter.

Σ Selection Cuts

Initial event selection is applied at the first stage of the GoAT analysis. Here there is a requirement that events have two particles detected in the CB and that their total energy is above 100 MeV. Particle assignment is carried out in the physics analysis stage of GoAT. The first requirement is that of the two particles detected, one is charged and the other is neutral. This determination is based upon the detectors that register a hit for this particular particle track. A particle is taken to be charged if it registers a hit in the PID, MWPC and CB detectors. A particle is taken to be neutral if it only registers a hit in the CB. At this stage the charged track is assigned to be a 'proton' and the neutral track is a 'neutron'.

The next selection cut that is applied is a cut on the vertex position along the z–axis for the 'proton' track. Any tracks with the proton vertex position outside of -60 mm to 60 mm are removed (see Figure 8.3). The target cell is 100 mm long and is centred at 0 in the analysed distributions, the cut is slightly broader than this to allow for uncertainties in the reconstruction of the vertex. This cut ensures that only events that originate from within the target cell are retained.

Due to the kinematics of the reaction, the two particles produced should be coplanar in ϕ. A cut is applied that removes any events where the difference in ϕ between the two tracks is outside of $(180\pm15)^\circ$ (see Figure 8.4). Again this cut is deliberately slightly broad to compensate for any uncertainty in the measured ϕ values of the tracks.

To clean the event sample further, a graphical cut is applied to a plot of $dE_{\mathrm{p}}(E_{\mathrm{p}})$.

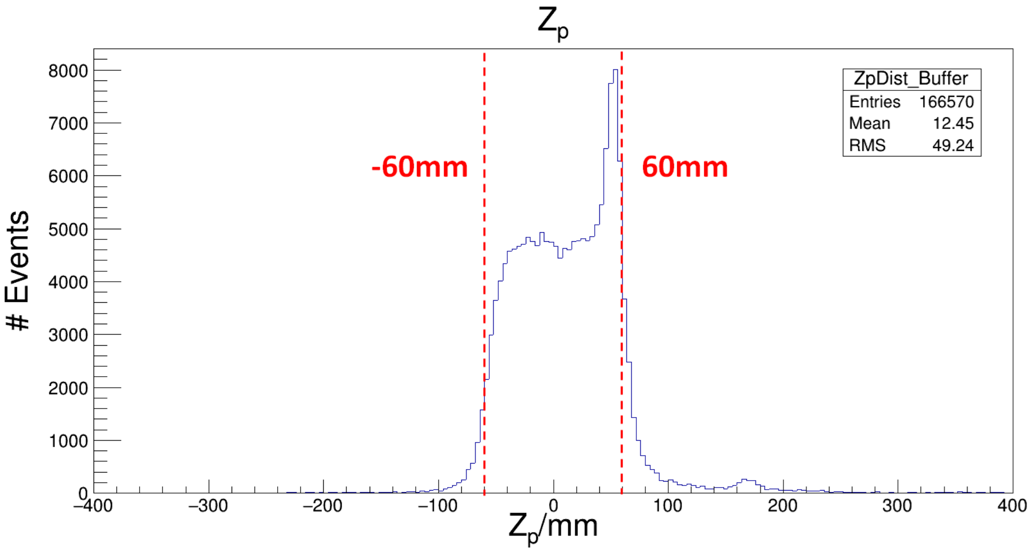

Figure 8.3 *Z vertex distribution for proton tracks, Z_{p}, with the cut region on -60 mm to 60 mm shown.*

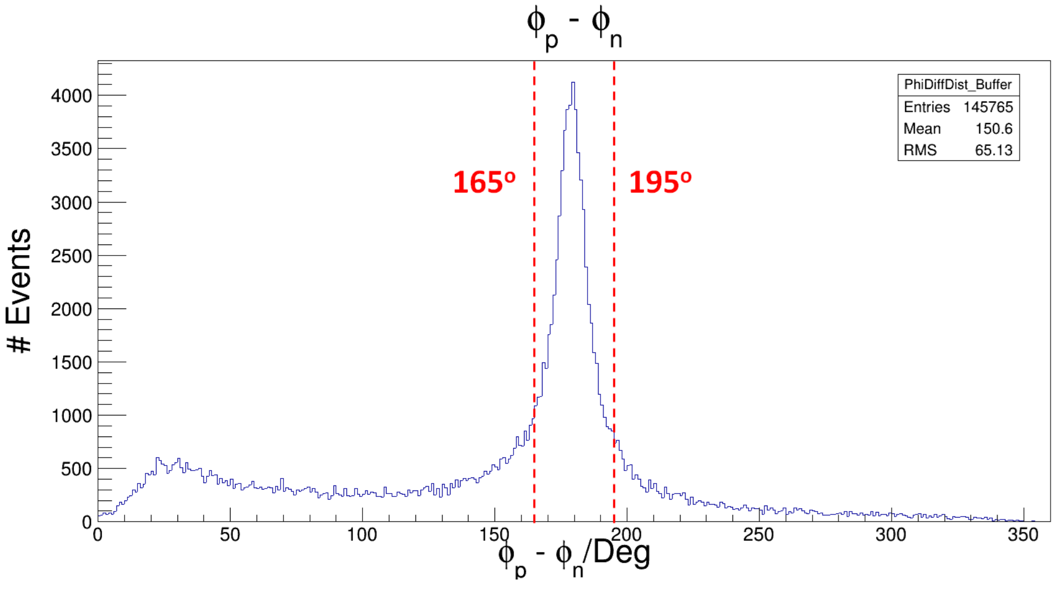

Figure 8.4 *Distribution of $\Delta\phi$ between the proton and neutron tracks with the $(180\pm15)^{\circ}$ cut region illustrated. A small peak between 0-50° can be observed in the plot, this is likely due to the contribution of background reactions where more than two particles have been produced.*

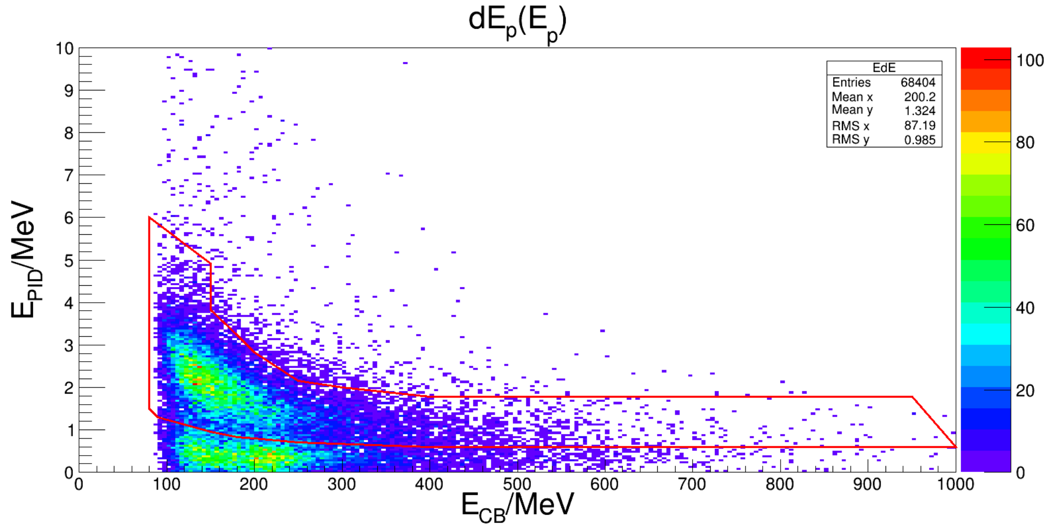

Figure 8.5 *Plot of the energy deposited in the Crystal Ball, E_{CB}, as a function of the energy deposited in the PID, E_{PID}, for the proton tracks. The graphical cut region that is selected out is outlined in red.*

This is a plot of the energy deposit for the proton track in the PID (dE_{p}) as a function of its energy deposit in the CB (E_{p}). As described in Chapter 5, different types of charged particles leave deposits in different regions of this plot that are characteristic of the type of particle produced. The graphical cut applied selects out the proton region and removes any events where the charged track lies outside of this region as shown in Figure 8.5. As can be observed, this cut removes pions from $\vec{\gamma}p \rightarrow n\pi^+$ reactions, which also produce coplanar neutral and charged tracks. The points on the cut were chosen by fitting a Gaussian to the projection of the 2-D distribution onto the y-axis and taking the mean minus 2σ of this fit for the lower level of the cut. This was done in roughly 50 MeV slices for the region 100-300 MeV. In this region, the cut was also adjusted to be σ on the lower level if 2σ was within one σ of a similar fit for the pion band. The upper level of the band was taken to be $\mu + 2\sigma$.

After these initial data cuts, the remaining events are analysed in more detail and many new quantities are calculated before further cuts are applied. Many of these quantities are dependent upon the incident photon energy. These quantities must be calculated for every photon associated with the event (see Section 8.1.1 for more on this). One of the first quantities to be calculated is the kinetic energy of the proton based upon the event kinematics. Knowing the energy of the photon beam, the mass of the target and produced particles, along with the proton polar angle, θ, the proton kinetic energy can be calculated from the event kinematics.

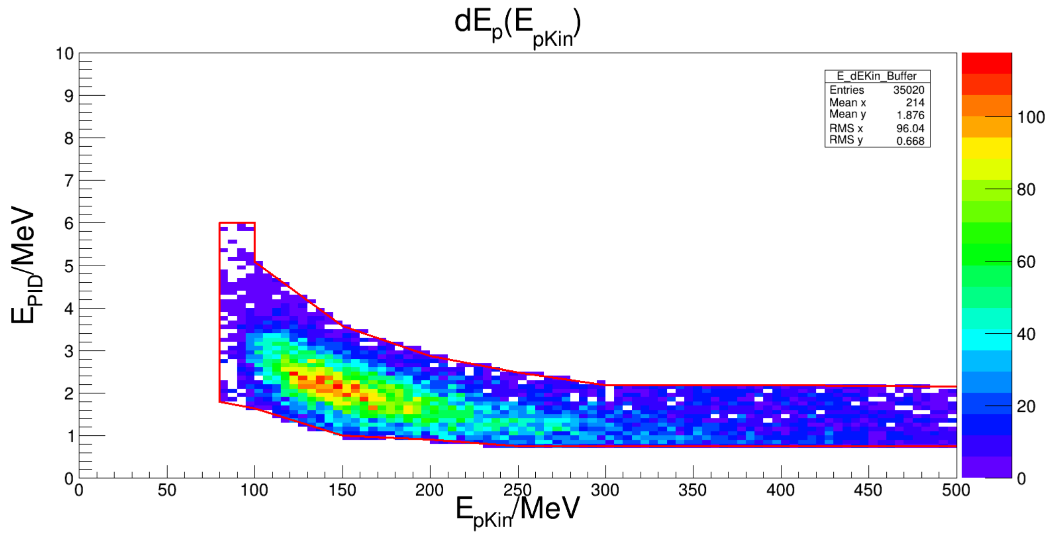

Figure 8.6 *Plot of the calculated kinetic energy, E_{pKin}, as a function of the energy deposited in the PID, E_{PID}, for the proton tracks after the selection cut has been applied. The graphical cut region that is selected out is outlined in red.*

This energy, E_{Kin}, is utilised in a further cut in combination with the PID energy. This is plotted as $dE_{\mathrm{p}}(E_{\mathrm{Kin}})$ and a further graphical cut is used to check that the proton is within the expected region of the plot based upon its expected energy from the kinematics. Any events with proton tracks outside of this graphical cut are removed (Figure 8.6). The shape of this fit was chosen by carrying out a similar procedure to the initial E_{CB}-dE_{PID} cut.

Assuming that the information on the proton track is correct, the neutron track can also be 'reconstructed' by utilising four-momenta conservation. If the target is taken to be at rest and the photon beam is assumed to carry momentum only along the z–axis, then the four-vector of the neutron, $\underline{n}_{\mathrm{rec}}$ is given by

$$\underline{n}_{\mathrm{rec}} = (\underline{d} + \underline{\gamma}) - \underline{p}, \tag{8.3}$$

where $\underline{d}$ and $\underline{\gamma}$ are taken to be

$$\underline{d} = (0, 0, 0, m_{\mathrm{d}}) \tag{8.4}$$

$$\underline{\gamma} = (0, 0, E_\gamma, E_\gamma), \tag{8.5}$$

with $m_{\mathrm{d}} = 1875.613$ MeVc^{-2} and $\underline{p}$ being the four-vector of the detected (unscattered) proton. From this four-vector, quantities for the 'reconstructed' track can be calculated. Crucially the 'mass' of this particle can be determined from this reconstructed particle. This is the 'missing mass' of the reaction had only the proton been detected. As this reconstructed track is expected to be a neutron, a cut is applied on this missing mass quantity. A broad cut of any events with missing mass outside of 800-1300 MeVc^{-2} is applied initially. Cuts are then applied to the missing mass based upon the incident photon energy, E_γ. This is due to the increasing broadening of the missing mass peak and the increasing background contribution (which also broadens) as E_γ increases (see Figure 8.8). From this figure it is clear that due to the broadening of the background peak at high E_γ, some background events may be leaking into the "signal" event peak. The contribution of this background and how to subtract it correctly should be investigated further as a potential source of systematic uncertainty. In the region of E_γ = 200-800 MeV a variable cut on the missing mass is applied. Gaussians were fitted to the missing mass distributions (without a cut) for 10 E_γ bins in the range specified above (see Figure 8.7). The mean, μ and standard deviation, σ, from these fits were used to apply a cut on any events outside of $(\mu \pm 2\sigma)$ MeVc^{-2} in each energy bin. For any events outside of this 200-800 MeV photon-energy range, a cut of $(\mu \pm 2\sigma)$ MeVc^{-2} was applied based upon μ and σ from a Gaussian fit of the missing mass distribution for events of all photon energies.

Another quantity that can be determined from $\underline{\mathrm{n}}_{\mathrm{rec}}$ is the reconstructed θ angle, θ_{nrec}, for the track. This angle is calculated assuming that the vertex position of the neutron track is equal to that of the measured proton. Because the events analysed for the determination of Σ are expected to be events without any scattering events in the polarimeter, θ_{nrec} should be equal to θ_{nmeas}. In the calculation of θ_{nmeas} the vertex position is assumed to be (0, 0, 0). Due to the angular resolution of the detectors and the potential for elastic scattering in the polarimeter or detectors these two quantities are unlikely to be exactly equal. Nonetheless, they should be very similar and a cut can be imposed upon the difference between θ_{nrec} and θ_{nmeas} to refine the event selection. In the case of

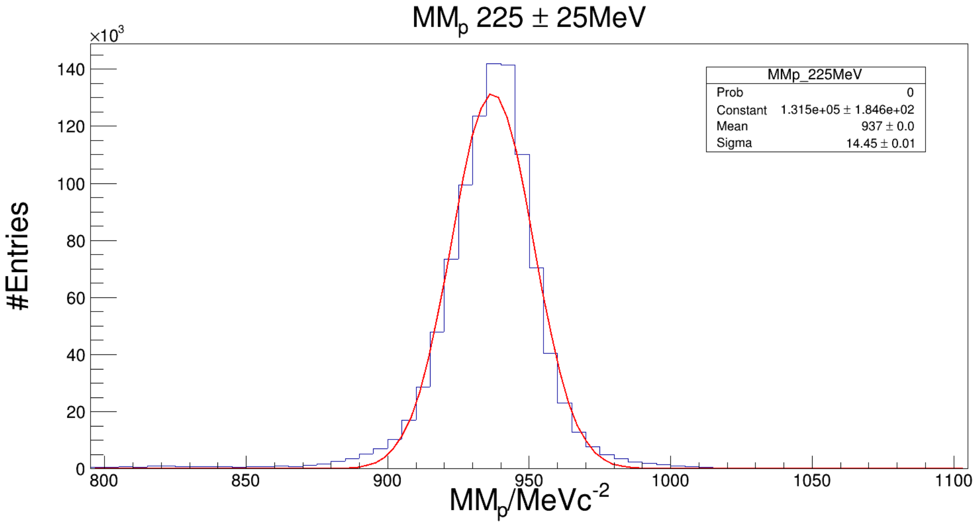

Figure 8.7 *The missing mass calculated from the proton track vector,* $MM_{\rm p}$*, for* E_γ *= 225±25 MeV with a Guassian fit applied to the peak.*

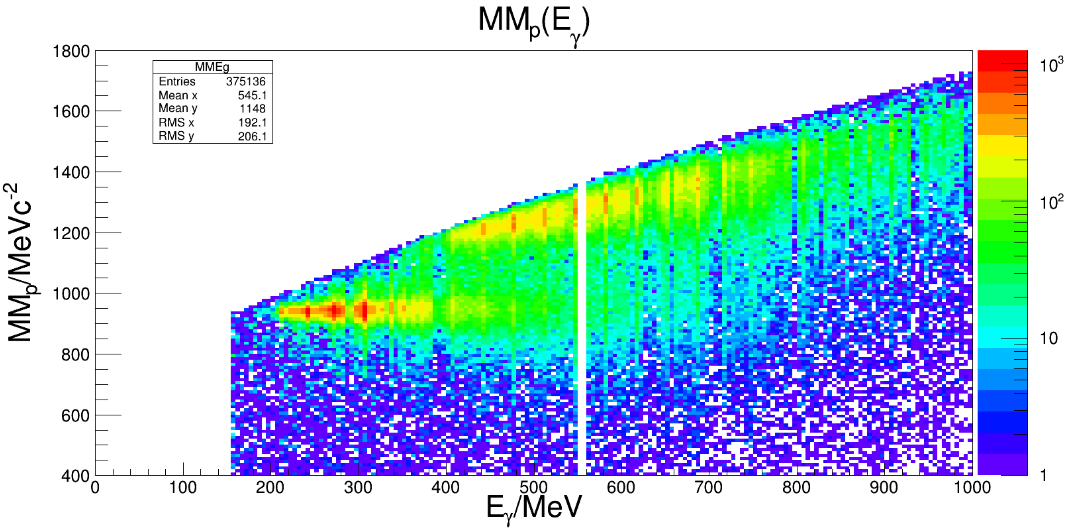

Figure 8.8 *The missing mass calculated from the proton track vector as a function of the incident photon energy,* E_γ*. The ∼940 MeV signal peak broadens as* E_γ *increases. A background peak begins to appear at* $E_\gamma \sim$ *350 MeV. Note that the z-axis of this figure is in a logarithmic scale.*

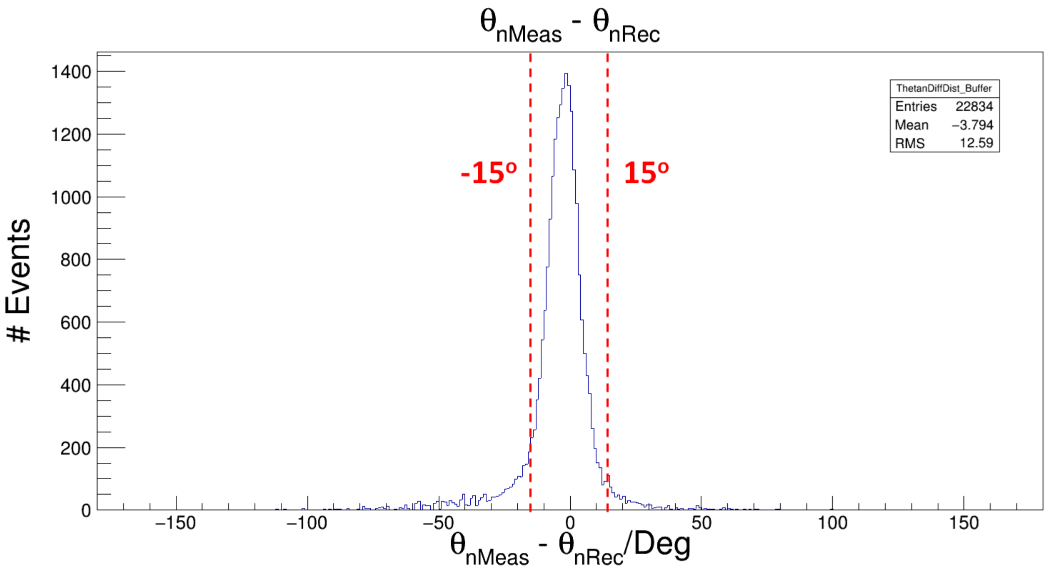

Figure 8.9 *The difference between the θ values for the measured and reconstructed neutron tracks illustrating the $\Delta\theta \pm 15^\circ$ region cut on the data.*

this work, any events with $\theta_{\text{nmeas}} - \theta_{\text{nrec}}$ greater than ± 15° were excluded (see Figure 8.9).

8.1.3 Analysis of $C_{x'}$

The observable $C_{x'}$ is the components of the recoil polarisation in the x' plane. The extraction of this observables requires the analysis of recoil particles from scattering events in the polarimeter. Compared to the analysis of Σ, the selection procedure is more involved and the available statistics are smaller. The selection cuts used to identify events of interest are outlined in the following section.

$C_{x'}$ Selection Cuts

The initial event selection is again applied at the first stage of the A2GoAT analysis. The requirement at this stage is for two particles to be detected in the CB with a total energy sum of over 100 MeV. Particle assignment is again applied at the physics analysis stage of A2GoAT, but it is here that the analysis method diverges significantly from the Σ analysis.

For $\gamma d \rightarrow pn$ events with a subsequent charge-exchange scattering reaction in the

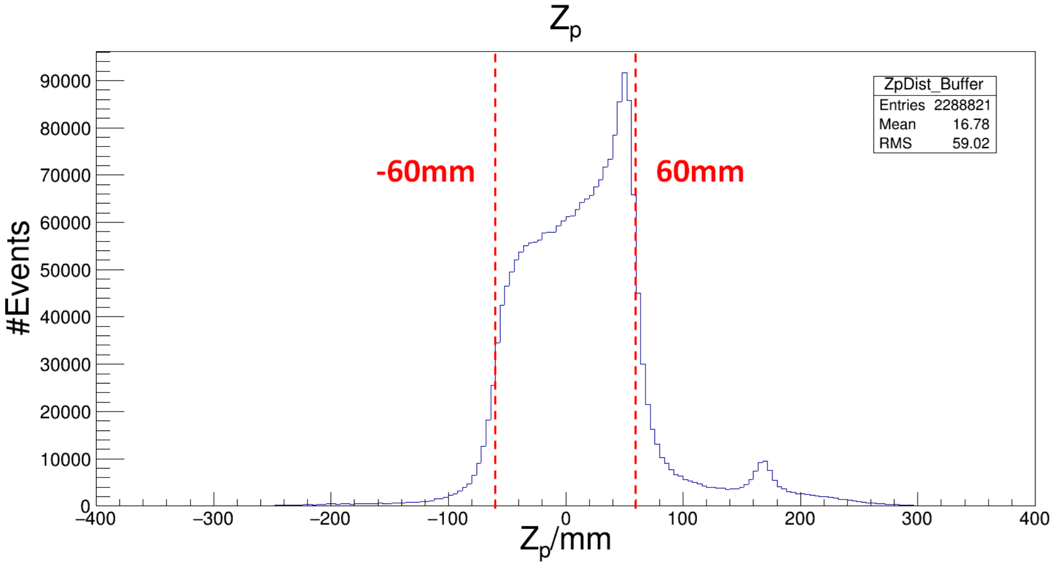

Figure 8.10 *$Z_{\rm p}$ distribution for proton tracks with the -60 mm to 60 mm cut region shown. The window of the target cell can clearly be seen in this distribution as the small peak centred at ∼170 mm.*

polarimeter, two tracks should be observed. One of these should be an unscattered proton and the other should be a proton from the charge-exchange reaction. For the track of the unscattered proton, hits should be registered in the PID, MWPC and CB detectors. For the charge-exchange proton, hits should only be detected in the MWPC and CB. This is due to the positioning of the graphite polarimeter relative to the PID and MWPC detectors. As the polarimeter is placed after the PID, the neutron should not undergo a scattering interaction until after it traverses the PID. Any events where the two tracks do not have these detector hit combinations are removed. This selection process can easily be understood by referring to Figure 5.17 in Chapter 5.

The tracks are assigned to be the proton and 'neutron' track. Following this assignment a cut on the Z vertex position, $Z_{\rm p}$ of the proton track is imposed. As this track is expected to be from an unscattered proton, it should have a vertex within the target cell. The same cut as for the analysis in Section 8.1.2 is applied and any events with $Z_{\rm p}$ outside of -60 mm to 60 mm are removed (see Figure 8.10). After this, a graphical cut is applied on a plot of $dE_{\rm p}(E_{\rm p})$. This is again done in the same manner as for the Σ analysis (see Figure 8.11). As the $C_{x'}$ analysis extends to higher photon energies than the Σ analysis, the PID cut was loosened above 300 MeV to ensure higher energy photons were not lost.

Following the preliminary cuts detailed above, the events are analysed on a

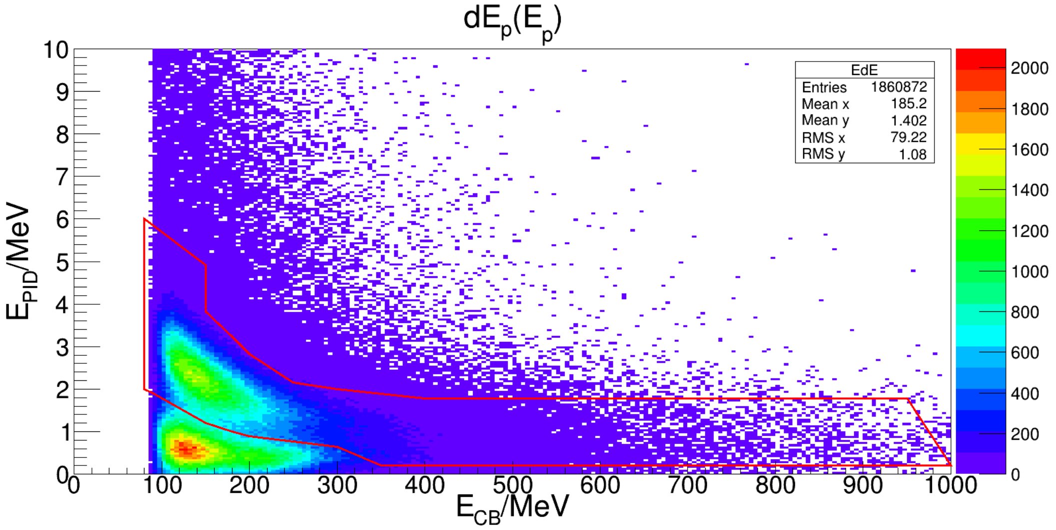

Figure 8.11 *Plot of the energy deposited in the Crystal Ball, E_{CB}, as a function of the energy deposited in the PID, E_{PID}, for the proton tracks. The graphical cut region that is selected out is outlined in red.*

photon by photon basis. The missing mass is calculated as outlined in Section 8.1.2. Again a rough cut on 800-1300 MeVc^{-2} is applied. This is followed by energy dependent missing mass cuts (as detailed in Section 8.1.2) based upon Gaussian fits to the missing mass distributions in bins of 50 MeV (see Figure 8.12). However, due to a lack of statistics in the higher energy range (above 500 MeV) Gaussian fitting could not be performed accurately. A cut of $(\mu \pm 2\sigma)$ MeVc^{-2} based upon a fit to the missing mass distribution across all E_γ was used for any events outside of this E_γ = 200 - 500 MeV range.

To ensure that the scattering event occurs inside the polarimeter, a cut is applied based upon the 'Point of Closest Approach' (POCA) of the scattered proton track and the reconstructed neutron track from four-momenta conservation. Considering two tracks and defining the point, $\underline{x}_i$, as a point along the track, $\hat{\underline{u}}_i$ as the initial unit vector of track i, $\underline{v}_i$ as the initial vertex of track i and t_i as a scalar constant for track i then $\underline{x}_i$ can be defined as

$$\underline{x}_i = \underline{v}_i + t_i \hat{\underline{u}}_i. \tag{8.6}$$

The 'Distance of Closest Approach' (DOCA) occurs at the point where the distance between the two tracks,

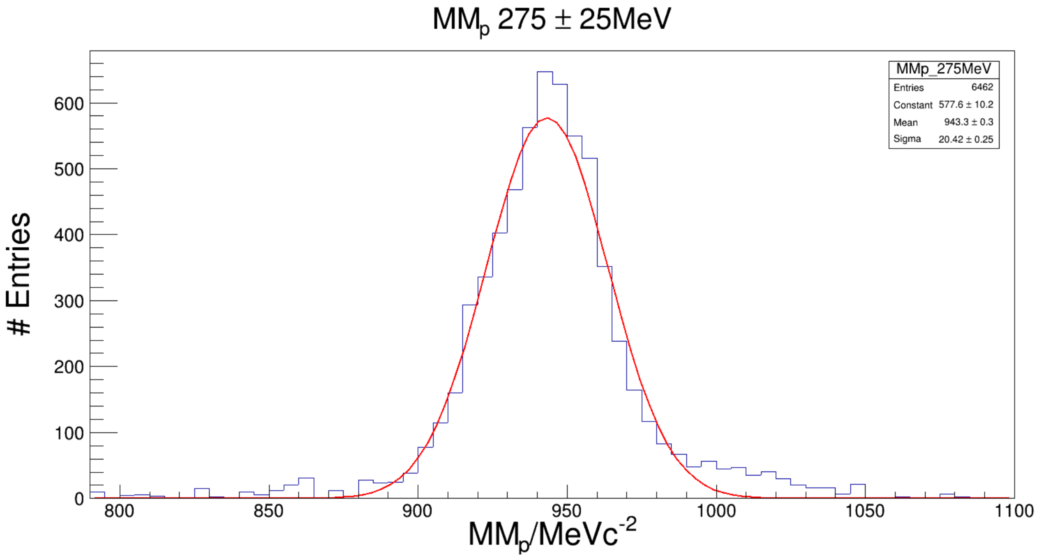

Figure 8.12 *The missing mass calculated from the proton track vector,* MM_p*, for* E_γ *= 275±25 MeV with a Guassian fit applied to the peak.*

$$\Delta\underline{x} \equiv \underline{x}_1 - \underline{x}_2, \tag{8.7}$$

is minimised. For this value to be minimised (at the point of closest approach) the following condition is imposed

$$\underline{\hat{u}}_i \cdot \Delta\underline{x} = 0. \tag{8.8}$$

From this requirement a system of two equations with two unknowns, t_1 and t_2, can be constructed. Solving for t_1 and t_2 yields

$$t_1 = \frac{\Delta\underline{v} \cdot [\underline{\hat{u}}_1 - \underline{\hat{u}}_2(\underline{\hat{u}}_1 \cdot \underline{\hat{u}}_2)]}{(\underline{\hat{u}}_1 \cdot \underline{\hat{u}}_2)^2 - 1} \text{and} \tag{8.9}$$

$$t_2 = \frac{\Delta\underline{v} \cdot [\underline{\hat{u}}_1(\underline{\hat{u}}_1 \cdot \underline{\hat{u}}_2) - \underline{\hat{u}}_2]}{(\underline{\hat{u}}_1 \cdot \underline{\hat{u}}_2)^2 - 1}, \tag{8.10}$$

where the term $\Delta\underline{v}$ is given by

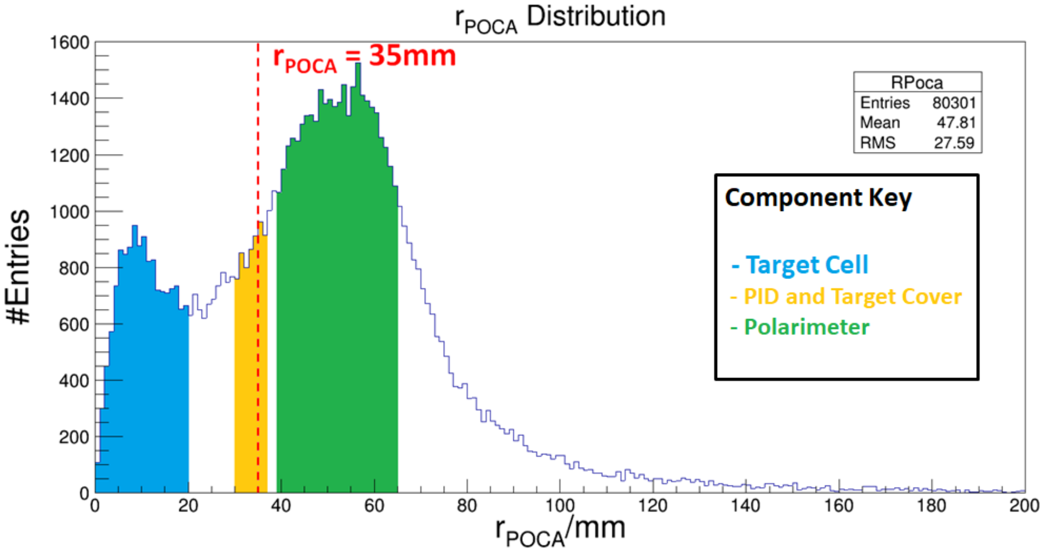

Figure 8.13 r_{POCA} *distribution with the 35 mm cut point marked. Also shown are the regions corresponding to different detector components with a colour key provided.*

$$\Delta \underline{v} = \underline{v}_1 - \underline{v}_2. \tag{8.11}$$

With the calculated values for t_1 and t_2 the point of closest approach can be determined from the midpoint between the two points $\underline{x}_1$ and $\underline{x}_2$ calculated from Equation (8.6). Events of interest should have a reconstructed scattering point (POCA) within the volume of the polarimeter. A selection cut is imposed upon the radius of this scattering point,

$$r_{\mathrm{POCA}} = \sqrt{x^2_{\mathrm{POCA}} + y^2_{\mathrm{POCA}}}, \tag{8.12}$$

with any events yielding r_{POCA} less than 35 mm removed (see Figure 8.13). The positions of various detector components are coloured in this figure. Shown in Figures 8.14 and 8.15 are the distribution of DOCA values and the values as a function of r_{POCA} respectively. As can be seen in these figures the DOCA value is peaked at 0 with some width due to the vertex resolution, this implies that the remaining tracks intersect and a further cut on the DOCA values is not necessary.

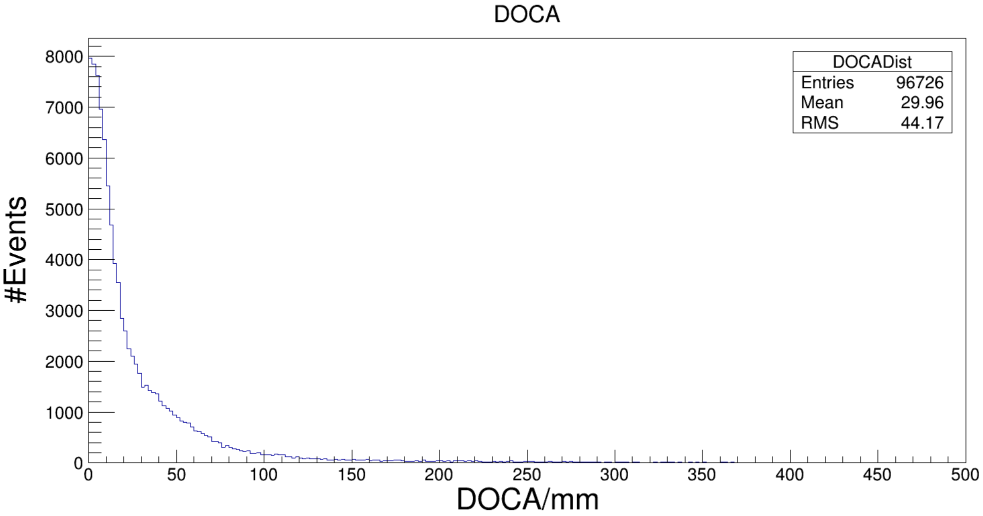

Figure 8.14 *DOCA distribution showing a clear peak at 0 with some width due to the resolution of the vertex determination and track reconstruction.*

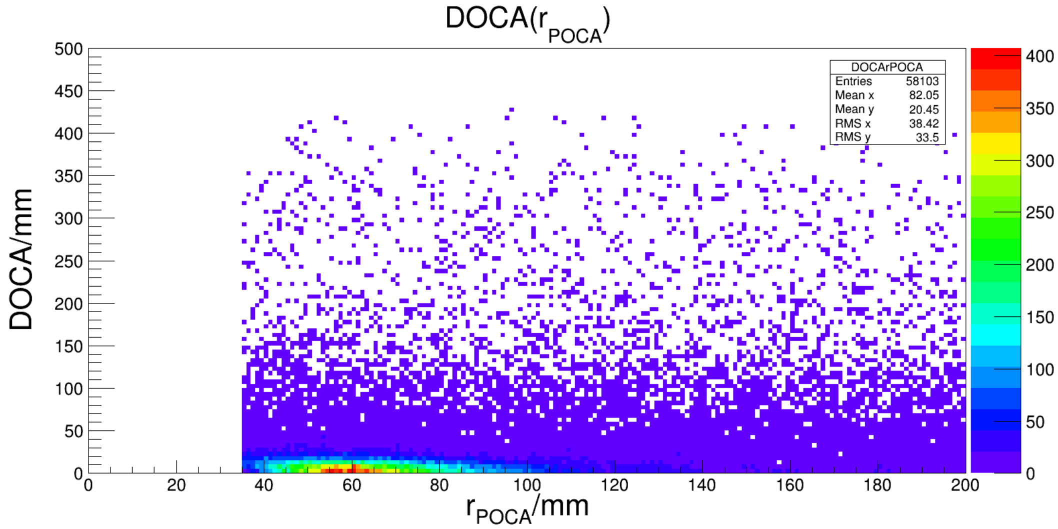

Figure 8.15 *DOCA as a function of* r_{POCA} *distribution after the cut on* r_{POCA}*. A clear band at low DOCA is apparent.*

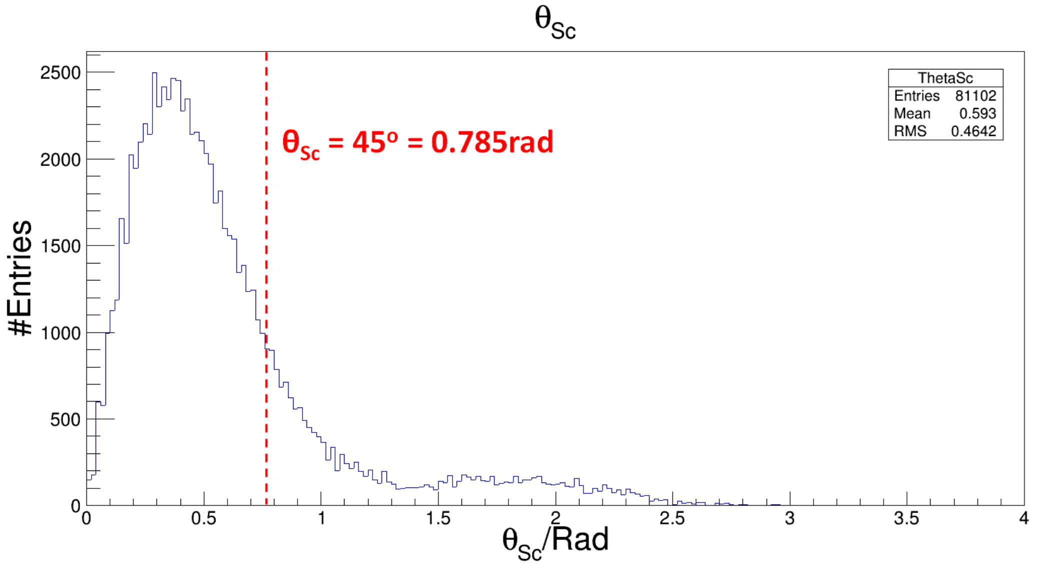

Figure 8.16 *θ_{Sc} distribution of scattered neutrons with the 45° ($\frac{\pi}{4}$ rad) cut point marked.*

A selection cut is applied on the polar scattering angle, θ_{Sc}, of the neutron. This is the angle θ of the recoil particle in the (x',y',z') plane as defined and shown in Section 3.1. Any events with θ_{Sc} greater than 45° are removed (see Figure 8.16). The purpose and reasoning for this cut on θ_{Sc} are discussed in Section 8.2.2. The azimuthal angle in the scattered frame, ϕ_{Sc}, is also calculated at this point. No cuts are imposed on ϕ_{Sc} as it is required to extract the desired observables, the distribution of ϕ_{Sc} for each beam helicity integrated across the full range of E_γ can be seen in Figure 8.17.

For analysing the neutron scatter events in the polarimeter a final E-dE style cut is implemented. For this the MWPCs are utilised as the 'dE' component. For a 'hit' to be registered in the MWPCs for a given track, a minimum of one of the chambers was required to register a hit. Each chamber has a detection efficiency of roughly 70% for protons. The total signal in the MWPCs is calculated separately for the case of one chamber or two chamber hits. The total MWPC signal is calculated for each track and a path length correction is applied by multiplying the total energy deposit by $\sin\theta$.

For the proton track the sample of events is already very clean after the application of the PID E-dE cut. However for the 'neutron' track there is a small narrow band of events present on E-dE plots derived using the MWPC and CB information as can be seen in Figure 8.18. A projection of the 2-D

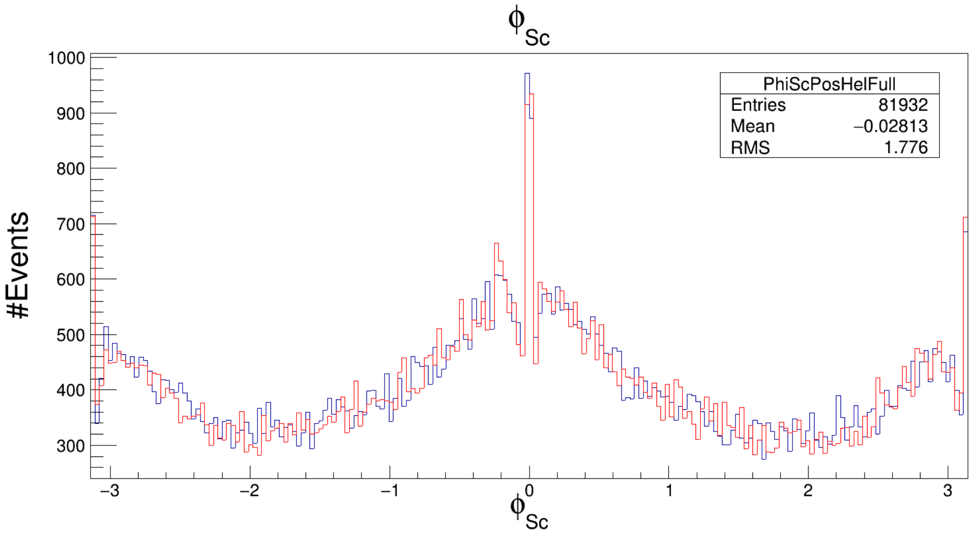

Figure 8.17 ϕ_{Sc} *distribution of scattered neutrons for positive (blue) and negative (red) photon beam helicities. These distributions are integrated over all photon energies, small deviations between the two distributions are observed but further binning is required to form useful asymmetries.*

distribution onto the y-axis was taken for this plot and the narrow band was fitted with a Gaussian. This fit was used to set a lower limit (taken as $\mu + 2\sigma$) for the acceptable minimum MWPC energy deposition. This process was applied separately for events with one or two chambers registering hits.

8.1.4 Summary

The effect of each selection cut on the analysis of the data is evaluated in Table 8.1. This tables presents the number of *remaining* (i.e. after the previous cut has been applied) events removed by each selection cut. This is presented for the Σ analysis and the $C_{x'}$ analysis. The total number of events remaining after all selection cuts and random subtraction procedures is tabulated in Table 8.2.

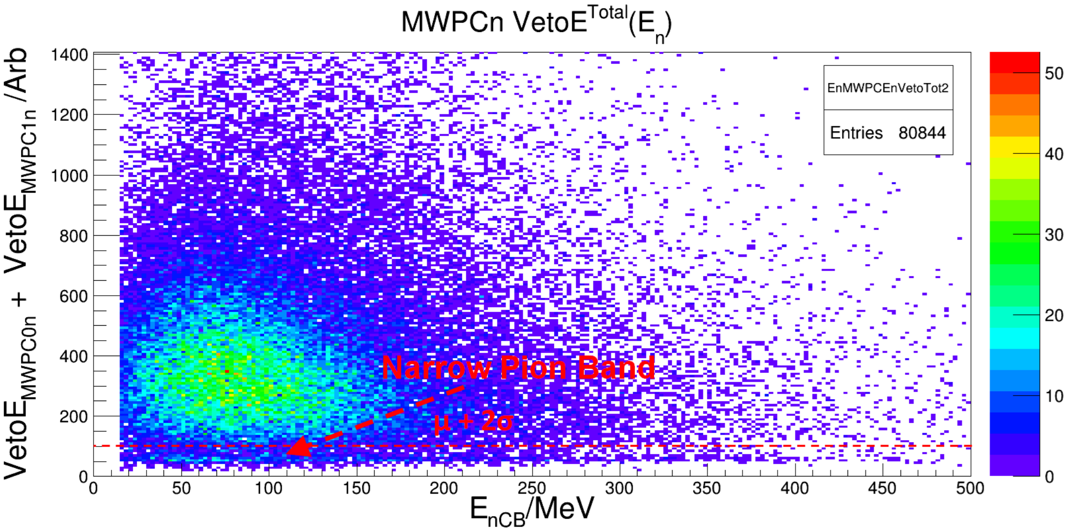

Figure 8.18 *The total signal (adjusted for path length), effectively an uncalibrated energy, in the MWPCs as a function of the energy deposition in the Crystal Ball. This plot is for events where the scattered proton has produced a signal in both MWPCs. A line illustrating roughly where the cut is applied is also shown.*

Table 8.1 *The percentage of* remaining *events removed by each selection cut for the analysis of Σ and $C_{x'}$. I.e. for Σ after the track selection cut, the Z_{p} cut removes 11.3% of the events that remained after the cut on track selection.*

Σ Analysis Cut	% Remaining Events Removed by Cut	$C_{x'}$ Analysis Cut	% Remaining Events Removed by Cut
Track Selection	91.5	Track Selection	98.5
Z_{p}	11.3	Z_{p}	17.7
$\Delta\phi$	53.5	E-dE	50.45
E-dE	38.4	MM_{p}	71.6
$E_{\mathrm{Kin}} - dE$	10.5	r_{POCA}	69
MM_{p}	50.6	θ_{Sc}	29.3
$\Delta\theta_{\mathrm{n}}$	9.5	MWPC E-dE	3.54

Table 8.2 *Overall number of events integrated across all energy bins for each analysis*

# Events Σ Analysis	# Events $C_{x'}$ Analysis
5200192	455567

8.2 Observable Extraction

8.2.1 Overview of Σ Extraction

After the event selection procedure detailed in Section 8.1.2 is carried out the remaining events are used to fill various histograms. As discussed in Section 3.3, Σ can be determined experimentally by taking the ratio

$$\frac{N^{\parallel}(\phi_{\mathrm{p}}) - N^{\perp}(\phi_{\mathrm{p}})}{N^{\parallel}(\phi_{\mathrm{p}}) + N^{\perp}(\phi_{\mathrm{p}})} = p_{\gamma}^{\mathrm{lin}} \Sigma \cos(2\beta), \tag{8.13}$$

where ϕ_{p} refers to ϕ of the measured proton track in the lab frame. β is given by $\phi_{\mathrm{p}} + \frac{\pi}{4}$. This is due to the fact that the two polarisations measured in the experiment are not actually exactly parallel and perpendicular to the laboratory frame. Rather they are at ±45°, as such the value of ϕ_0 is $\frac{\pi}{4}$. Histograms of the asymmetry (left hand expression of Equation (8.13)) as a function of ϕ_{p} were constructed from the data. These were obtained for bins of E_{γ} and $\cos\theta_{\mathrm{CM}}$. There are 21 E_{γ} bins, each 10 MeV wide ranging from 410 to 620 MeV. This is the range of E_{γ} over which the beam has appreciable linear polarisation (∼0.1–0.47). For each E_{γ} bin there are 20 bins in $\cos\theta_{\mathrm{CM}}$ between -1 to 1.

As outlined in Section 3.3, Σ can be determined by fitting the histograms with a function of the form

$$f(\phi_{\mathrm{p}}) = \mathrm{P}_0(\cos(2\phi_{\mathrm{p}} + \frac{\pi}{2})), \tag{8.14}$$

where the fit parameter P_0 is the value $p_{\gamma}^{\mathrm{lin}}\Sigma$ directly. The parameter from this fit is extracted and divided by the linear polarisation value (taken at the center of the energy bin analysed) to calculate a value for Σ. These values are then plotted as a function of $\cos\theta_{\mathrm{CM}}$ for each E_{γ} bin.

8.2.2 Overview of $C_{x'}$ Extraction

As discussed in Section 3.4, $C_{x'}$ and p_y can in theory be extracted simultaneously from the data by examining the asymmetry defined by

$$\frac{N^{-}(\phi_{\text{Sc}}) - N^{+}(\phi_{\text{Sc}})}{N^{-}(\phi_{\text{Sc}}) + N^{+}(\phi_{\text{Sc}})} = \frac{A_{\text{Eff}} p_{\gamma}^{\odot} C_{x'} \sin\phi_{\text{Sc}}}{1 + A_{\text{Eff}} p_y \cos\phi_{\text{Sc}}}, \tag{8.15}$$

where $N^{\pm}$ refer to the number of scattered events (as a function of ϕ_{Sc}) for events with positive and negative photon beam helicity respectively. As discussed in Section 5.2.2, $p_{\gamma}^{\odot}$ is the degree of circular polarisation of the photon beam and is given by [113]

$$p_{\gamma}^{\odot} = \frac{p_{e^-}^{\odot} \times E_{\gamma} \times (E_{e^-} + \frac{1}{3}(E_{e^-} - E_{\gamma}))}{E_{e^-}^2 + (E_{e^-} - E_{\gamma})^2 - \frac{2}{3}E_{e^-} \times (E_{e^-} - E_{\gamma})}, \tag{8.16}$$

with the terms in this equation as defined in the earlier section. The term A_{Eff} in Equation (8.15) is the effective analysing power of the scattering charge exchange reaction between the neutron and carbon polarimeter. A_{Eff} was determined on a bin-by-bin basis as discussed in Section 3.4.1. The resulting values of A_{Eff} for each energy and angular bin are shown in Figure 8.19.

The reasoning for the cut on θ_{Sc} is related to the variation of A_y (see Figure 3.3). At $\theta_{\text{Sc}} \sim 45^{\circ}$ A_y changes sign, including data from both sides of this line would effectively ‘dilute’ the effective analysing power of the data sample.

To evaluate the values of $C_{x'}$ and p_y the ϕ_{Sc} values of any events remaining after selection cuts are used to fill a collection of histograms. Histograms are filled independently for each helicity and are binned in E_{γ} and $\cos\theta_{\text{CM}}$. Due to the more limited statistics available for the scattered data there are only eight 100 MeV wide E_{γ} bins in the range 200-1000 MeV used in the analysis of the data. For each energy bin there are five bins in $\cos\theta_{\text{CM}}$ between -1 and -1. The analysis was also repeated with three bins in $\cos\theta_{\text{CM}}$ between -1 and -1.

Histograms of the asymmetry (defined by the left hand side of Equation (8.15))

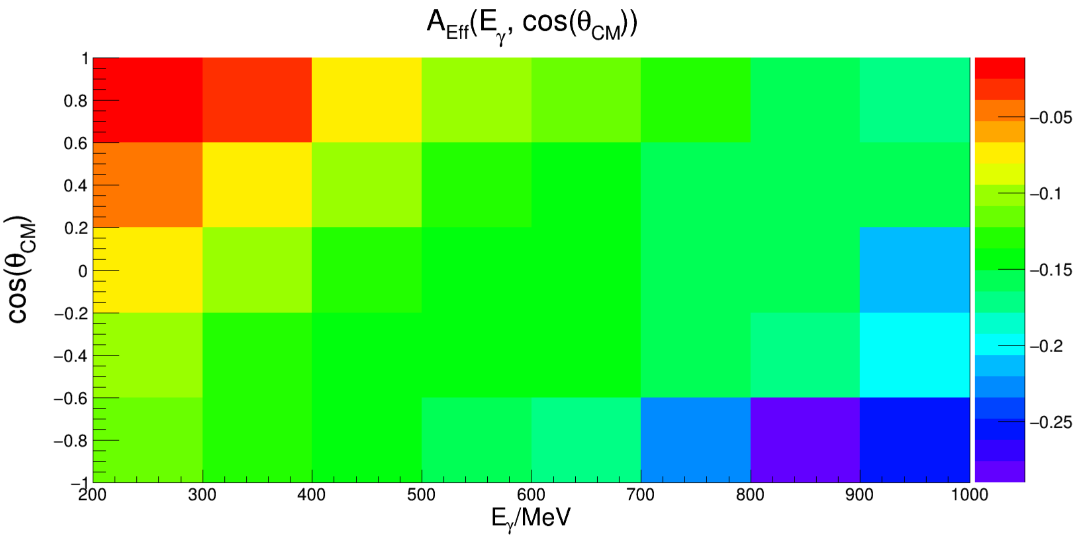

Figure 8.19 *A_{Eff} used to determine $C_{x'}$ for each energy and angular bin examined. The value of A_{Eff} is represented by the colour scale included.*

binned in E_γ and $\cos\theta_{\text{CM}}$ are constructed. The resulting asymmetry histograms are fitted with a function of the form

$$f(\phi_{\text{Sc}}) = \frac{P_1 \sin\phi_{\text{Sc}}}{1 + P_2 \cos\phi_{\text{Sc}}}, \tag{8.17}$$

where the parameters P_1 and P_2 can used to extract $C_{x'}$ and p_y respectively. This is done by dividing the respective fit parameter with $A_{\text{Eff}} p_\gamma^\odot$ (P_1) or A_{Eff} (P_2). Due to the available statistics, it was not possible to accurately extract both parameters simultaneously. As such, P_2 was fixed in order to extract $C_{x'}$. The value that P_2 should be fixed at was examined and is discussed further in Section 9.2. By carrying out a Taylor expansion of Equation (8.17) with respect to $P_2 \cos\phi_{\text{Sc}}$ it can be shown that this term should have a very small effect on the determination of P_1.

For the analysis of $C_{x'}$, it is not only the events from production runs using the amorphous moeller radiator that can be used. During linearly polarised photon production runs using the diamond radiator the helicity of the electron beam is still being flipped. By combining the two opposite linear polarisations (after scaling to ensure there an equal number of events from each) an effective "unpolarised" (in a linear polarisation sense) set of events can be recovered. These can be analysed to extract $C_{x'}$.

8.3 Systematic Uncertainties

This section discusses potential sources of systematic uncertainties that may affect the final results. Potential sources of systematic errors are considered for the analysis of Σ and the analysis of $C_{x'}$. Some potential uncertainties are shared between the two analyses but will need to be assessed individually in each case.

For the analysis of Σ there are several potential sources of systematic uncertainty that can be introduced when experimentally determining the observable. Some of these sources were briefly discussed in Section 3.3. As mentioned in this previous section, the fit that is used to determine Σ is a function that is constructed based upon several assumptions. The assumption that the polarisation in the parallel and perpendicular case is equal ($p_\gamma^{\parallel} = p_\gamma^{\perp} = p_\gamma$) can introduce a systematic uncertainty if this is not true. The value of the ϕ offset, ϕ_0, also has the potential to induce systematic errors in the value of Σ.

Another assumption was that the acceptance would be constant within each ϕ bin. If this is not true then the choice of the ϕ bin width can potentially impact the value of Σ. Additionally, as discussed in [30] a correction factor due to the ϕ bin width can be approximated to be $\frac{\Delta\phi}{\sin[\Delta\phi]}$. With 20 bins in ϕ this yields a correction factor of 1.017, a very small effect.

For the experimental extraction of $C_{x'}$, there are also several potential sources of systematic errors. As in the Σ case, the various acceptances are a potential source. The assumption that the polarisation of each helicity is equal is a further consideration. However, potentially the largest source of systematic errors for the analysis of $C_{x'}$ is the value of A_{Eff} that is used in the analysis. The value used to extract $C_{x'}$ is based upon averaging over a relatively broad angular and energy bin. This value is also chosen under the assumption that the reaction can be treated as an interaction with a quasi-free n,p interaction with a proton in the graphite polarimeter. As discussed in Section 3.4.1 the analysing power for quasi-elastic processes can differ significantly from the analysing power for elastic scattering processes. The deviation of the value used from the “true” quasi-elastic analysing power should be analysed further as a potential source of systematic uncertainty.

Both analysis threads share one large potential source of systematic uncertainties, event selection cuts. The width, shape and choice of the selection cuts utilised may all induce a systematic uncertainty in the final results. Some of the selection cuts are also correlated (e.g. missing mass and the $\Delta\phi$ cut). Ideally the effect of all uncorrelated selection cuts should be studied prior to publication of the results. The contribution of physics background events should also be studied. Due to time constraints only an assessment of one selection cut, the missing mass, was analysed for the Σ analysis. Assessment of the effects of the other selection cuts is in progress.

To assess the impact of systematic uncertainties introduced due to the choice of the missing mass selection cut, the analysis was carried out utilising two different cuts on the missing mass. These two cuts correspond to $\mu \pm \sigma$ and $\mu \pm 2\sigma$ for the missing mass (see Section 8.2.1). Due to the increase in statistics in the $\mu \pm 2\sigma$ data this cut was used in the final analysis. To produce an estimate of the systematic uncertainty from this choice of missing mass cut, the difference between the values of Σ using different cut widths was investigated. The differences are presented in Figure 8.23. The mean and root mean squared (RMS) values of these plots are taken to be an estimate of the systematic error for the illustrated E_γ bin.

As outlined in Section 8.2.2 asymmetries between the yields from the two photon-beam helicities are used to extract $C_{x'}$. The limited statistics available for constraining this function (Equation (8.17)) meant that a simultaneous extraction of $C_{x'}$ and p_y was not possible with this first data set. Because of this the p_y component was fixed in order to extract $C_{x'}$. To assess possible systematics in using this method, p_y was fixed to be either 0 or an estimated value based on p_y extracted from a parallel unpolarised beam method [147]. The data used a fitted function as employed in [101]. The fit was also carried out with p_y free to vary but constrained to within the physical range. An example of the fits resulting from these three different methods of constraining p_y is presented in Figure 8.20.

Values of $C_{x'}$ were extracted from these fits and plotted as a function of E_γ and as a function of $\cos\theta_{\mathrm{CM}}$. The resulting values using all three fit methods as a function of E_γ for the three and five $\cos\theta_{\mathrm{CM}}$ bin cases can be seen in Figures 8.21 and 8.22 respectively. As can be observed in these figures, the method of constraining p_y does not generally have a significant impact on the resulting value of $C_{x'}$.

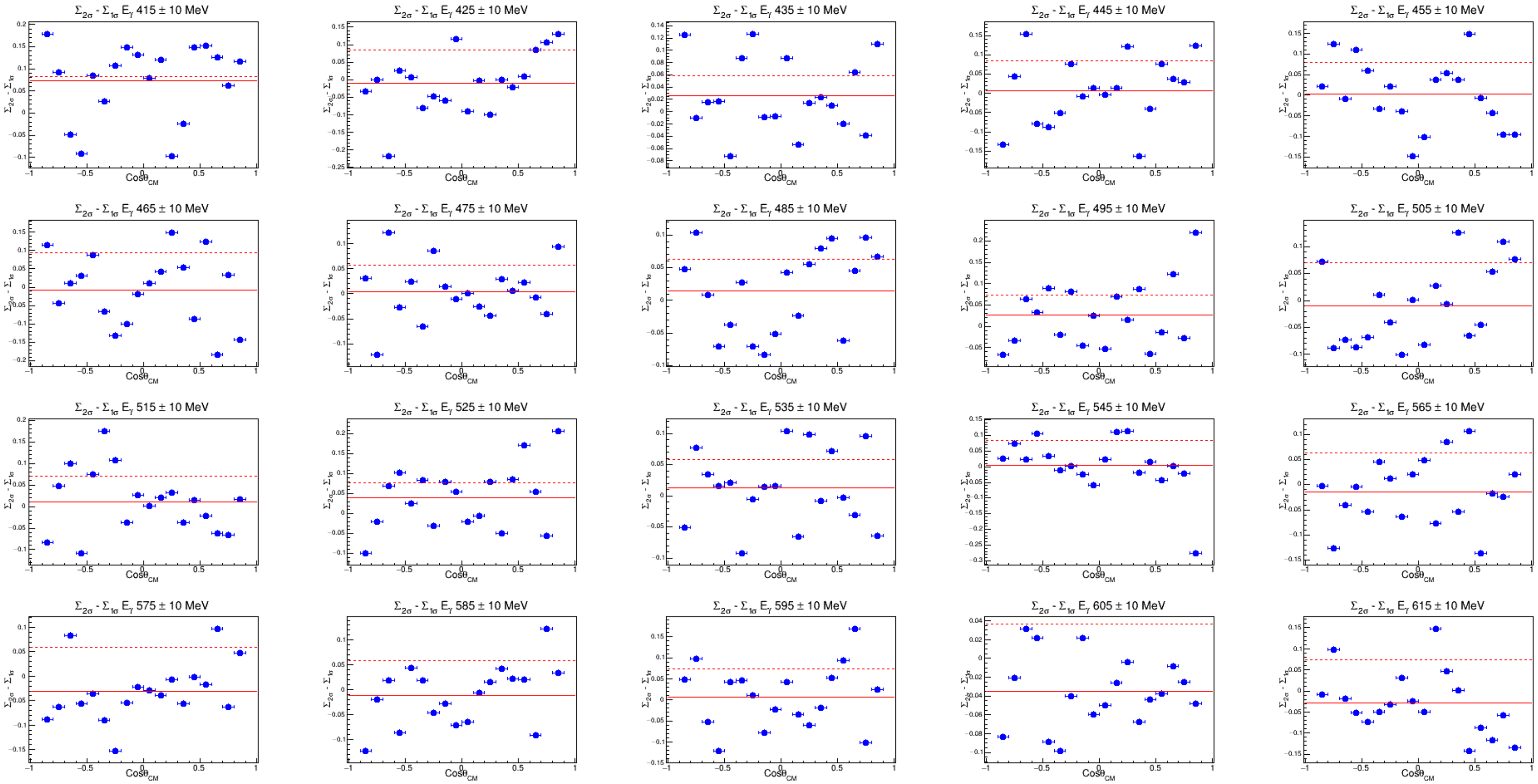

Figure 8.20 *The difference between the values of* Σ *from the analysis with missing mass cuts of* $\mu \pm \sigma$ *and* $\mu \pm 2\sigma$*. The red solid line demonstrates the mean of the data points. The dashed red line is the RMS value of the points. The sum of the mean and RMS values is taken to be an upper limit for the systematic error in the illustrated* E_γ *bin.*

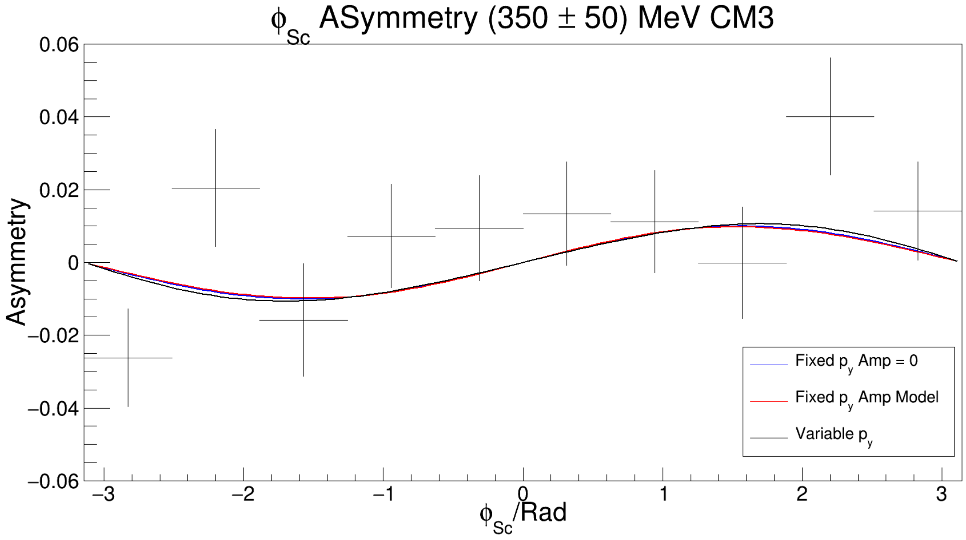

Figure 8.21 *Asymmetry in ϕ_{Sc} between the two photon beam helicities for scattered neutrons in one 100 MeV wide E_γ bin. Demonstrated on the plot are three fits to the data with differing values for the second parameter (that relates to p_y) either fixed or limited respectively.*

Potential sources of systematic errors that should be considered and assessed prior to publication of the data are listed in Table 8.3 for the Σ analysis and Table 8.4 for the $C_{x'}$ analysis. The current status of the assessment of each source is also listed in these tables.

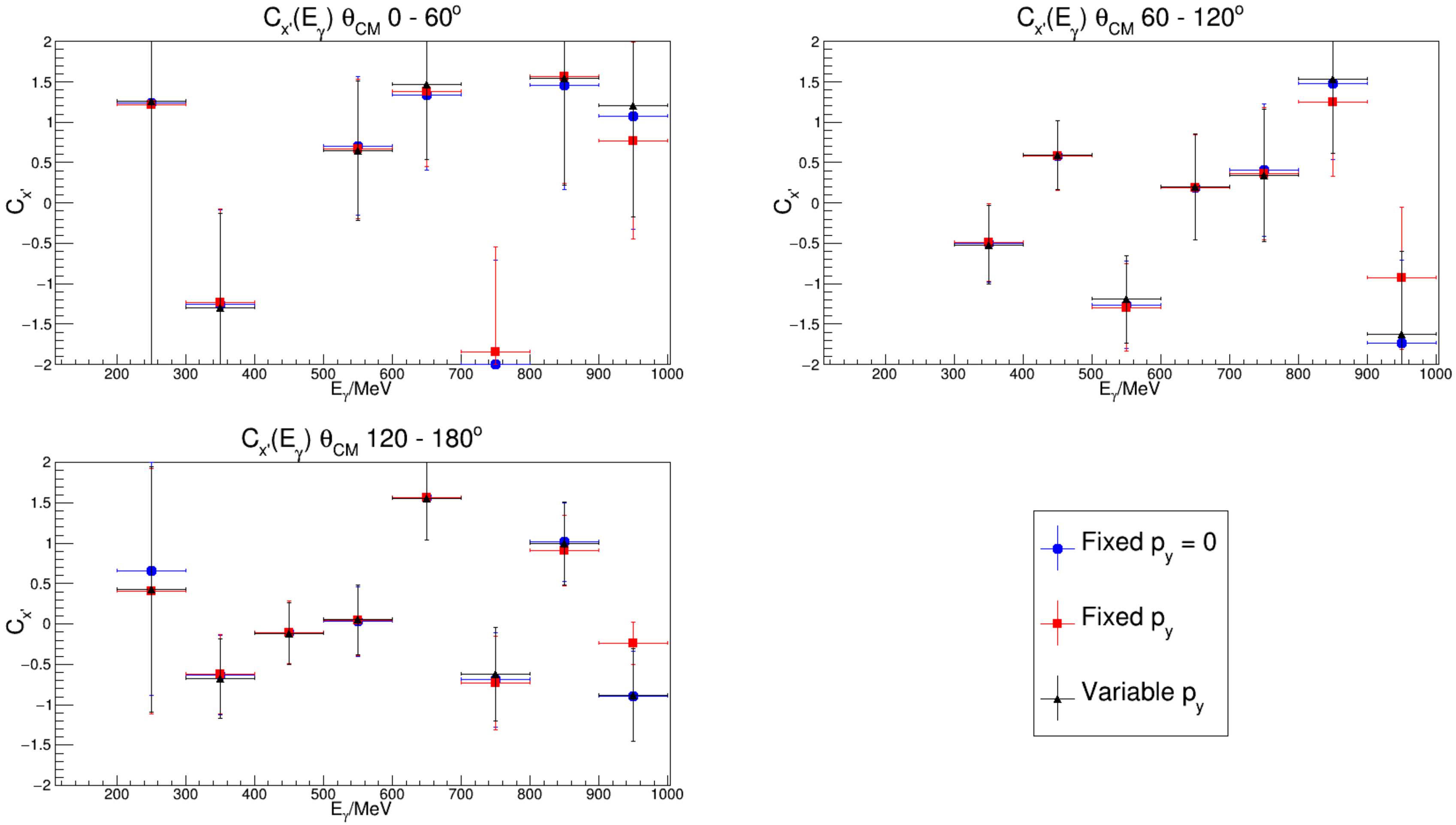

Figure 8.22 *Results obtained for $C_{x'}$ plotted as a function of E_γ across three angular bins in $\cos\theta_{\mathrm{CM}}$. Results for the three different fitting methods are shown as outlined in the provided legend.*

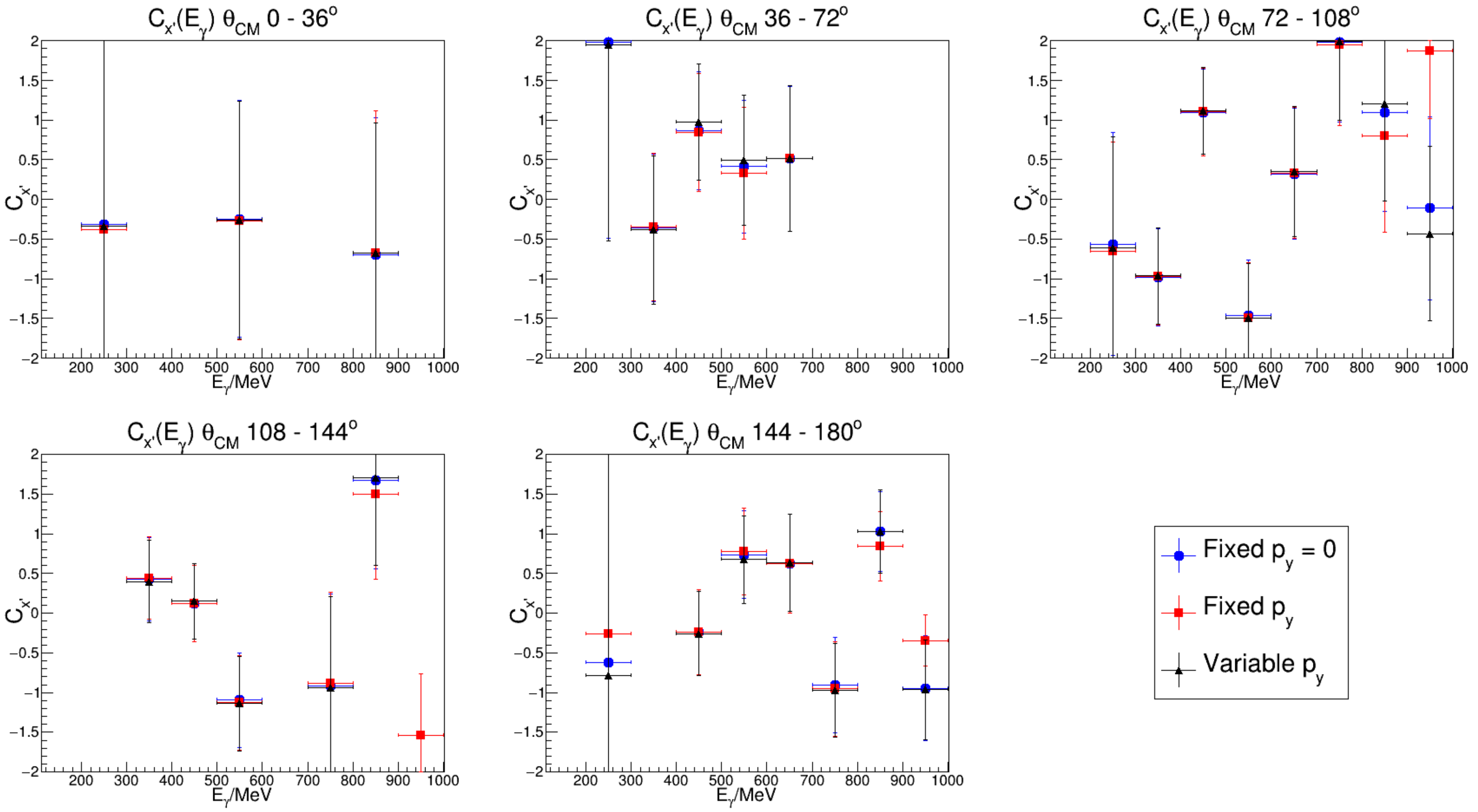

Figure 8.23 *Results obtained for $C_{x'}$ plotted as a function of E_γ across five angular bins in $\cos\theta_{\rm CM}$. Results for the three different fitting methods are shown as outlined in the provided legend.*

Table 8.3 *Potential sources of systematic uncertainties on Σ that should be considered and the status of their analysis.*

Source of Systematic Uncertainty	Status
Track Selection	To be analysed
Z_{p} Cut	To be analysed
E-dE Cut	To be analysed
E_{Kin}-dE Cut	To be analysed
$MM/\Delta\phi/\Delta\theta_{\mathrm{n}}$ Cut	Analysed
ϕ Binning	To be analysed
Fit method	To be analysed
Flux normalisation	To be analysed
Acceptance	To be analysed
ϕ_0 Fit offset	To be analysed
Photon Polarisation	To be analysed
Background subtraction	To be analysed

Table 8.4 *Potential sources of systematic uncertainties on $C_{x'}$ that should be considered and the status of their analysis.*

Source of Systematic Uncertainty	Status
Track Selection	To be analysed
Z_{p} Cut	To be analysed
E-dE Cut	To be analysed
MM Cut	To be analysed
r_{POCA} Cut	To be analysed
θ_{Sc} Cut	To be analysed
MWPC E-dE Cut	To be analysed
ϕ_{Sc} Binning	To be analysed
p_y Value	Analysed
Fit method	To be analysed
Acceptance	To be analysed
Photon Polarisation	To be analysed
Analysing power	To be analysed
Background subtraction	To be analysed

Chapter 9

Results

The results for Σ and $\mathrm{C}_{x'}$ are presented in this chapter. The results obtained and outlined in this section are tabulated in Appendix E.

9.1 Σ Results

As discussed in Section 8.2.1, asymmetries between the yields for the two linear polarisations were produced and fitted with a $\cos 2\phi$ asymmetry to extract Σ. An example fit of the form defined by Equation (8.14) can be seen in Figure 9.1. Due to the presence of a dead tagger channel, the E_γ bin centred at 555 MeV did not contain any data. As such it was excluded from further analysis. Extracted values for Σ are shown for the twenty remaining E_γ bins in Figures 9.2 - 9.6.

The systematic error (estimated from the difference between the missing mass cuts as discussed in Section 8.3) is shown as a solid band at the bottom of each plot. The magnitude of the difference between -1 and the top of each bar represents the value of the systematic error. The error bars on the points on these plots indicate statistical uncertainty in Σ, σ_Σ, due to the uncertainty in the fit parameter, σ_{P_0}, and the uncertainty in the linear polarisation of the beam, $\sigma_{p_\gamma^{\mathrm{lin}}}$. σ_Σ is given by

$$\sigma_\Sigma = \sqrt{\left[\left(\frac{\sigma_{P_0}}{p_\gamma^{\mathrm{lin}}}\right)^2 + \left(\frac{P_0 \sigma_{p_\gamma^{\mathrm{lin}}}}{(p_\gamma^{\mathrm{lin}})^2}\right)^2\right]}, \tag{9.1}$$

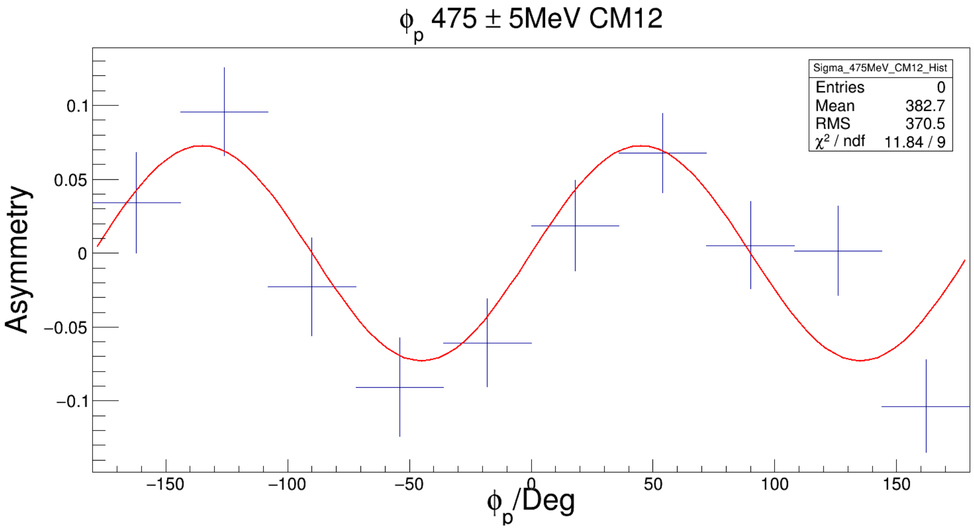

Figure 9.1 *Example fit of* $\mathrm{P}_0(\cos(2\phi + \frac{\pi}{2}))$ *to the asymmetry between* $N^{\parallel}(\phi_{\mathrm{p}})$ *and* $N^{\perp}(\phi_{\mathrm{p}})$ *for the extraction of* Σ*. This is one 10 MeV wide bin in* E_γ *for* $\cos\theta_{\mathrm{CM}}$ *= -0.2 - -0.3. Fit parameters are included in the top right.*

where $\sigma_{p_\gamma^{\mathrm{lin}}}$ has been determined to be 3 % [153]. However it is worth noting that σ_Σ is generally dominated by the impact of the value of σ_{P_0}.

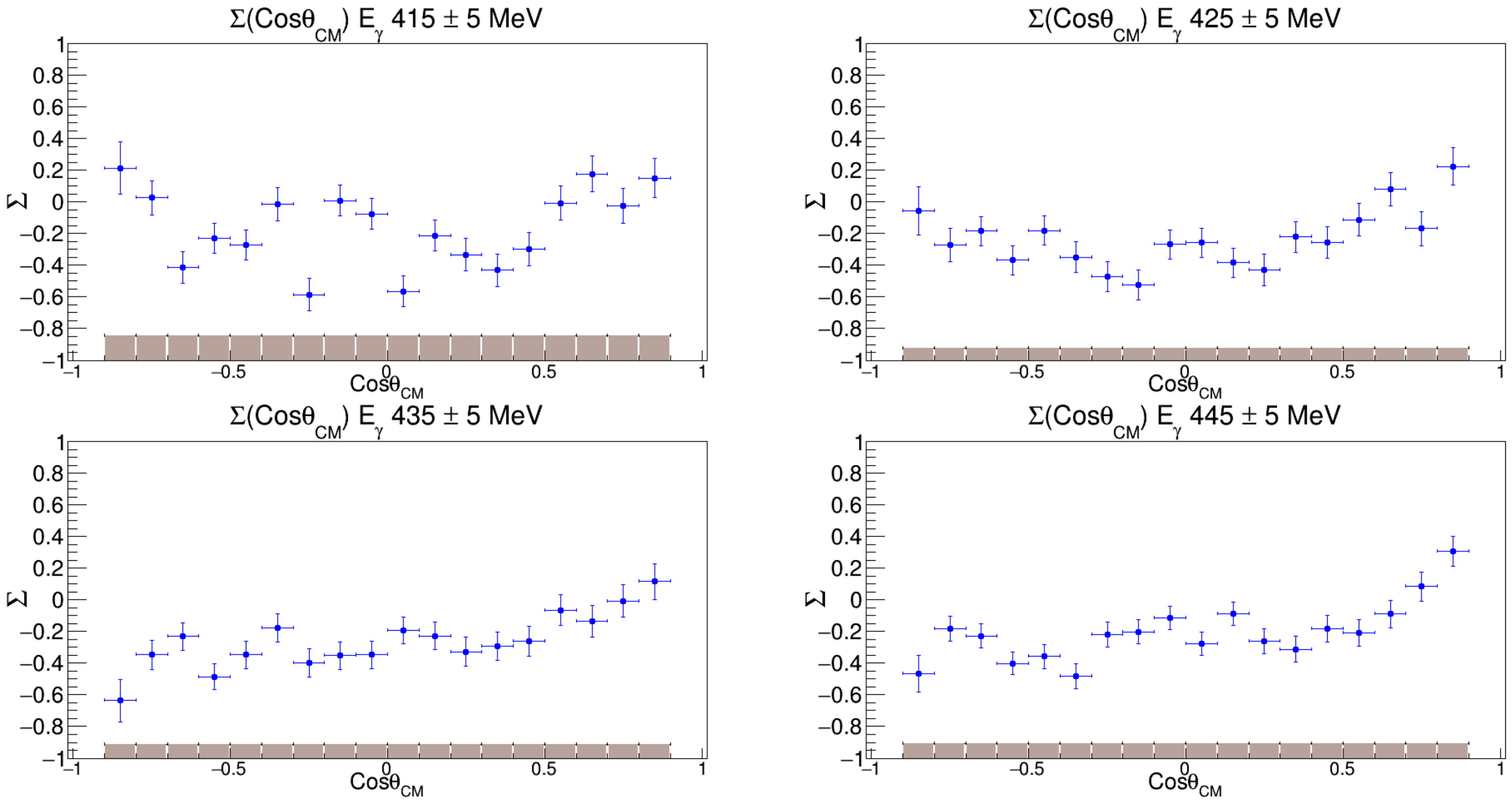

Figure 9.2 $\Sigma(\cos\theta_{\mathrm{CM}})$ *across four* E_γ *bins of width 10 MeV each. The systematic error is shown as a solid band at the bottom of each plot.*

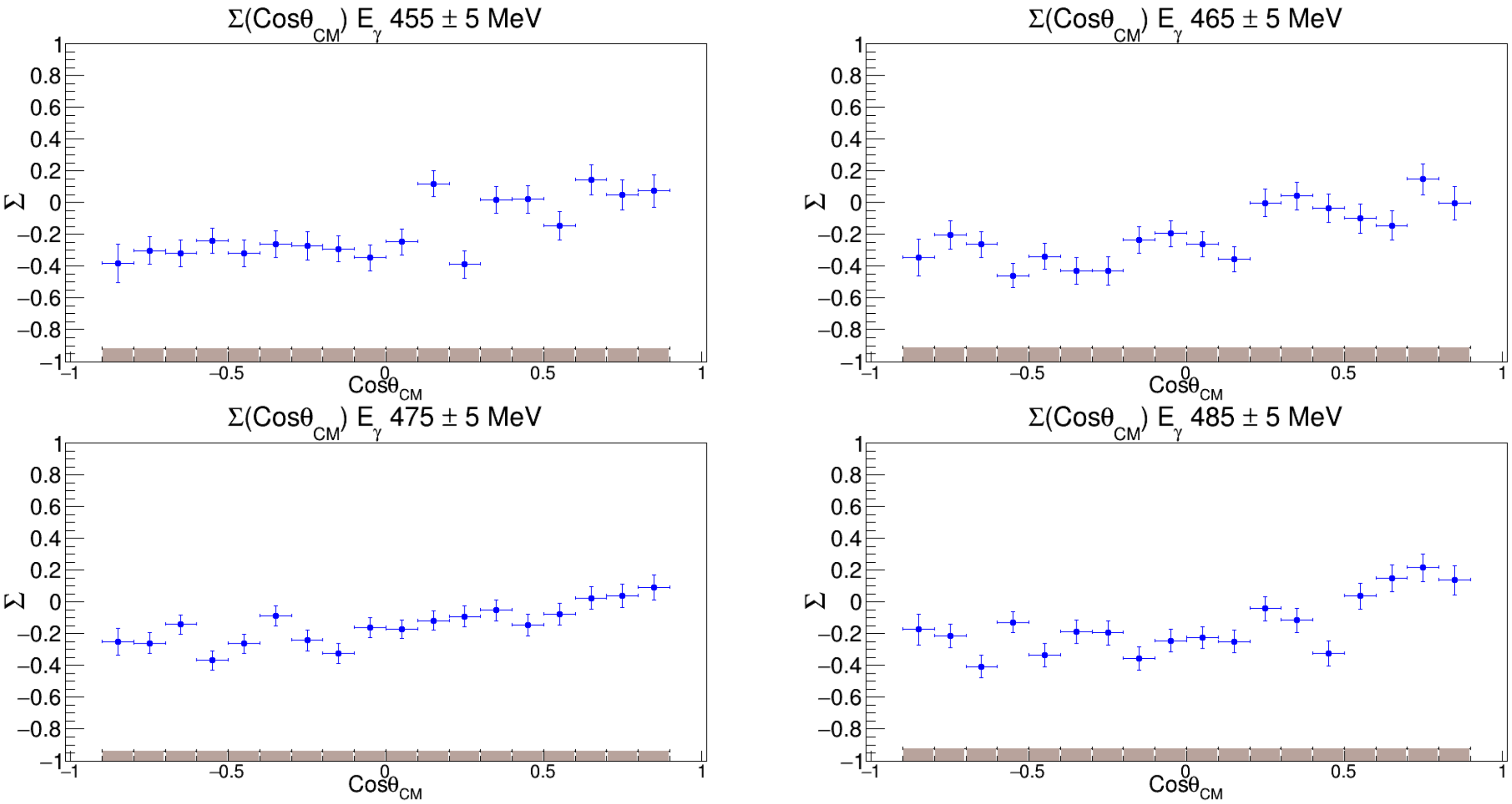

Figure 9.3 $\Sigma(\cos\theta_{\mathrm{CM}})$ *across four* E_γ *bins of width 10 MeV each. The systematic error is shown as a solid band at the bottom of each plot.*

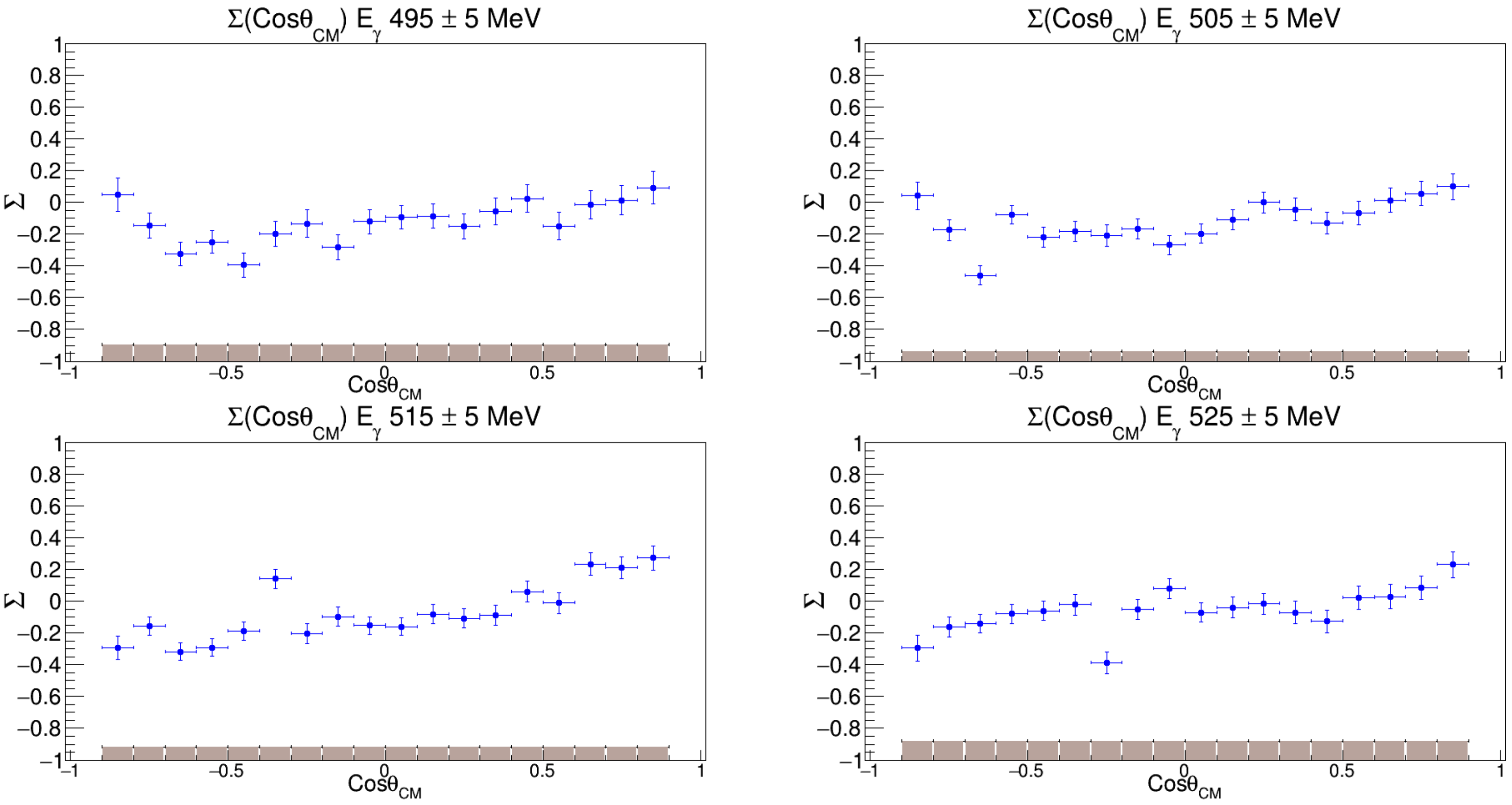

Figure 9.4 *$\Sigma(\cos\theta_{\mathrm{CM}})$ across four E_γ bins of width 10 MeV each. The systematic error is shown as a solid band at the bottom of each plot.*

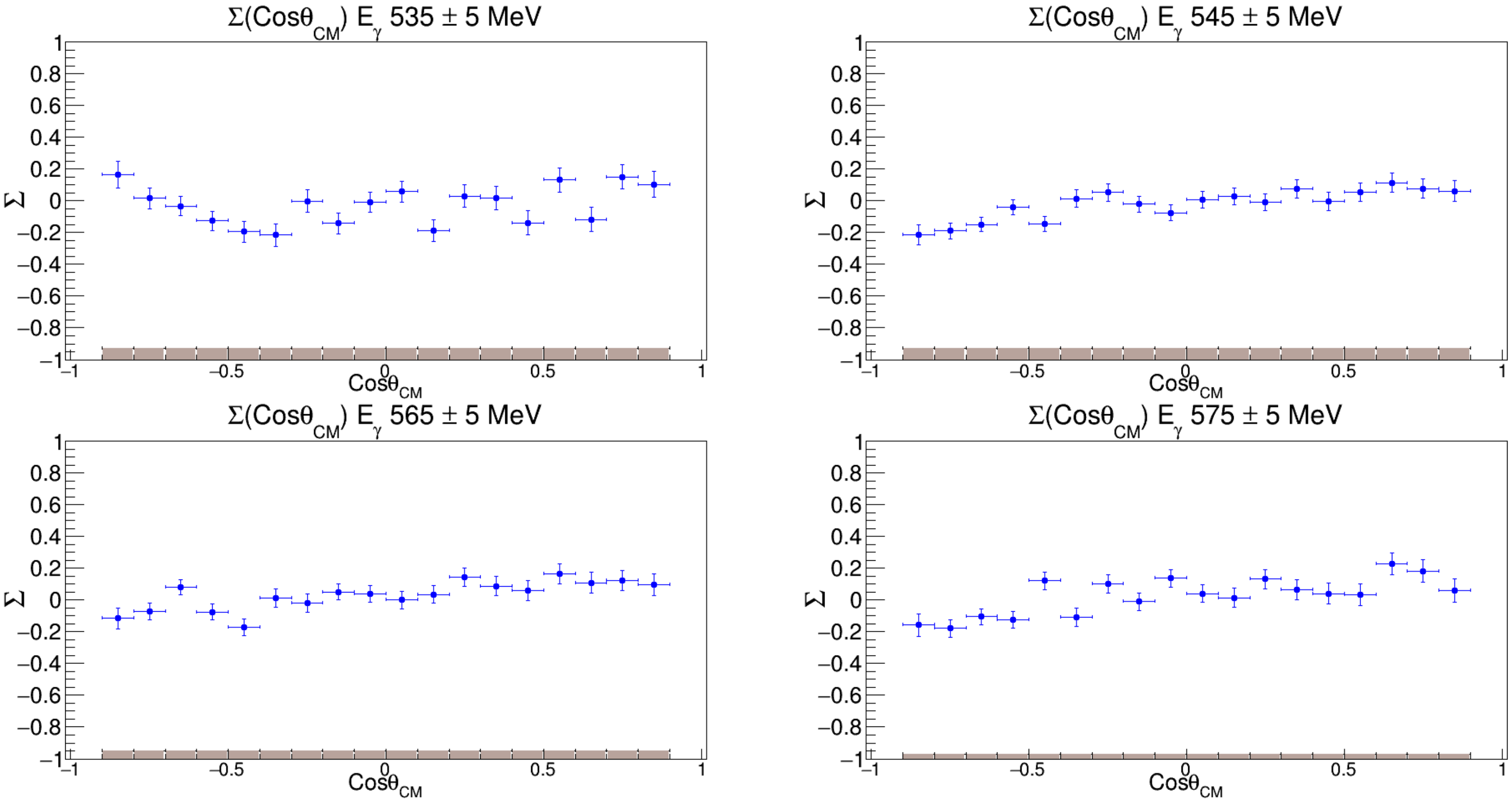

Figure 9.5 *$\Sigma(\cos\theta_{\mathrm{CM}})$ across four E_γ bins of width 10 MeV each. The systematic error is shown as a solid band at the bottom of each plot.*

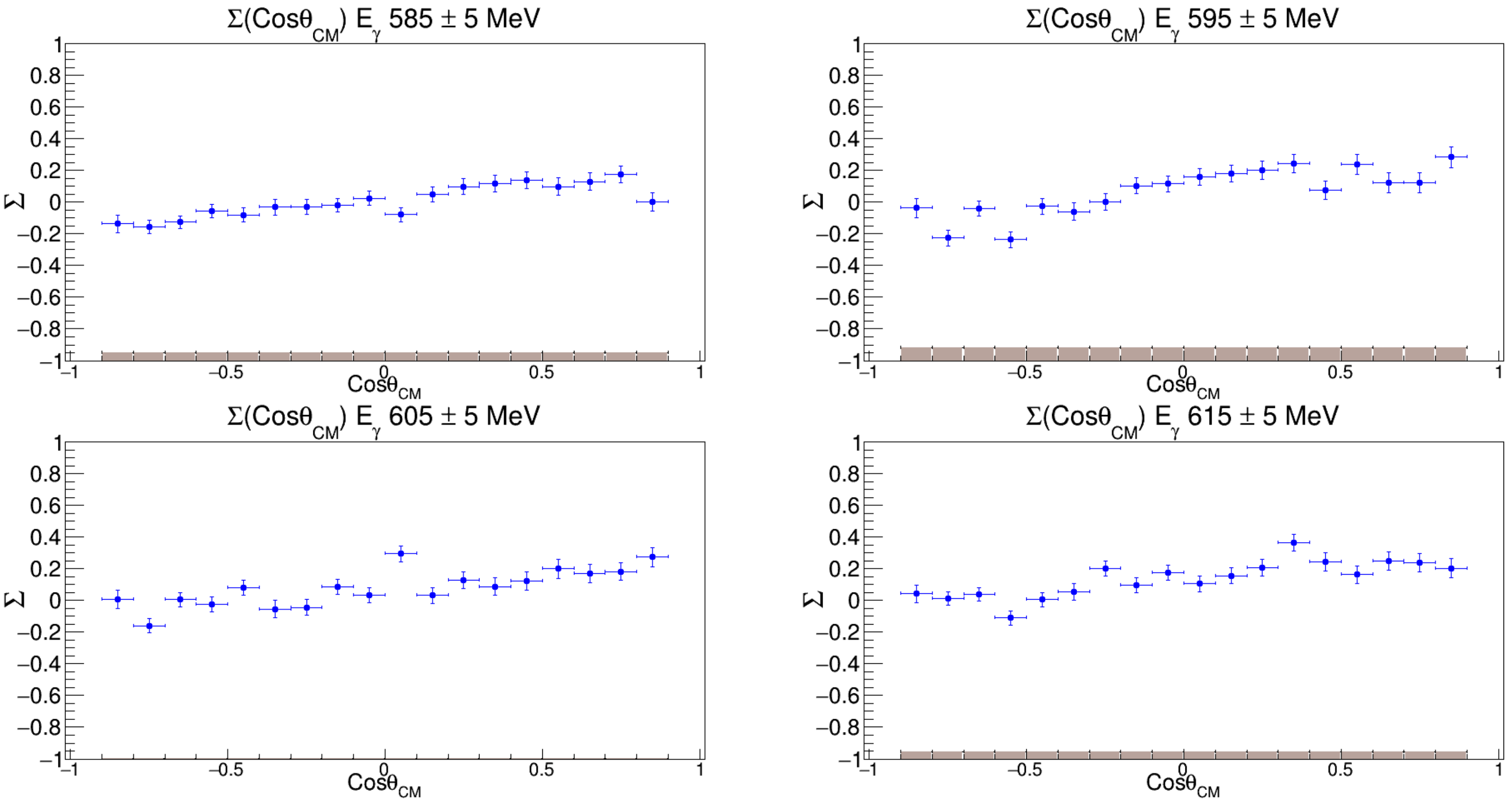

Figure 9.6 $\Sigma(\cos\theta_{\mathrm{CM}})$ *across four* E_γ *bins of width 10 MeV each. The systematic error is shown as a solid band at the bottom of each plot.*

As a cross check, Σ was also calculated for data in which an (n,p) scatter is observed in the nucleon polarimeter. In the analysis of the scattered data it is assumed that the proton from the photodisintegration reaction does not scatter in the polarimeter. If this assumption is correct, protons from the scattered data should also be analysable to extract Σ. This analysis provides a further test of the results and serves as a check on the quality of the event selection procedure for the scattered events. Due to the reduced statistics available, the number of angular bins was reduced by a factor of four and the number of photon-energy bins by two.

The results are superimposed as shown in Figure 9.7. Due to the halving of the number of E_γ bins in the scattered event analysis, each set of scattered results is presented in comparison to two consecutive E_γ bins for the non-scattered analysis. Overall the two sets of results are generally in good agreement. The results for the scattered event analysis clearly have a larger uncertainty but this is to be expected from the considerable reduction in available statistics. This concurrence of the results provides validation of the selection procedure for the scattered events.

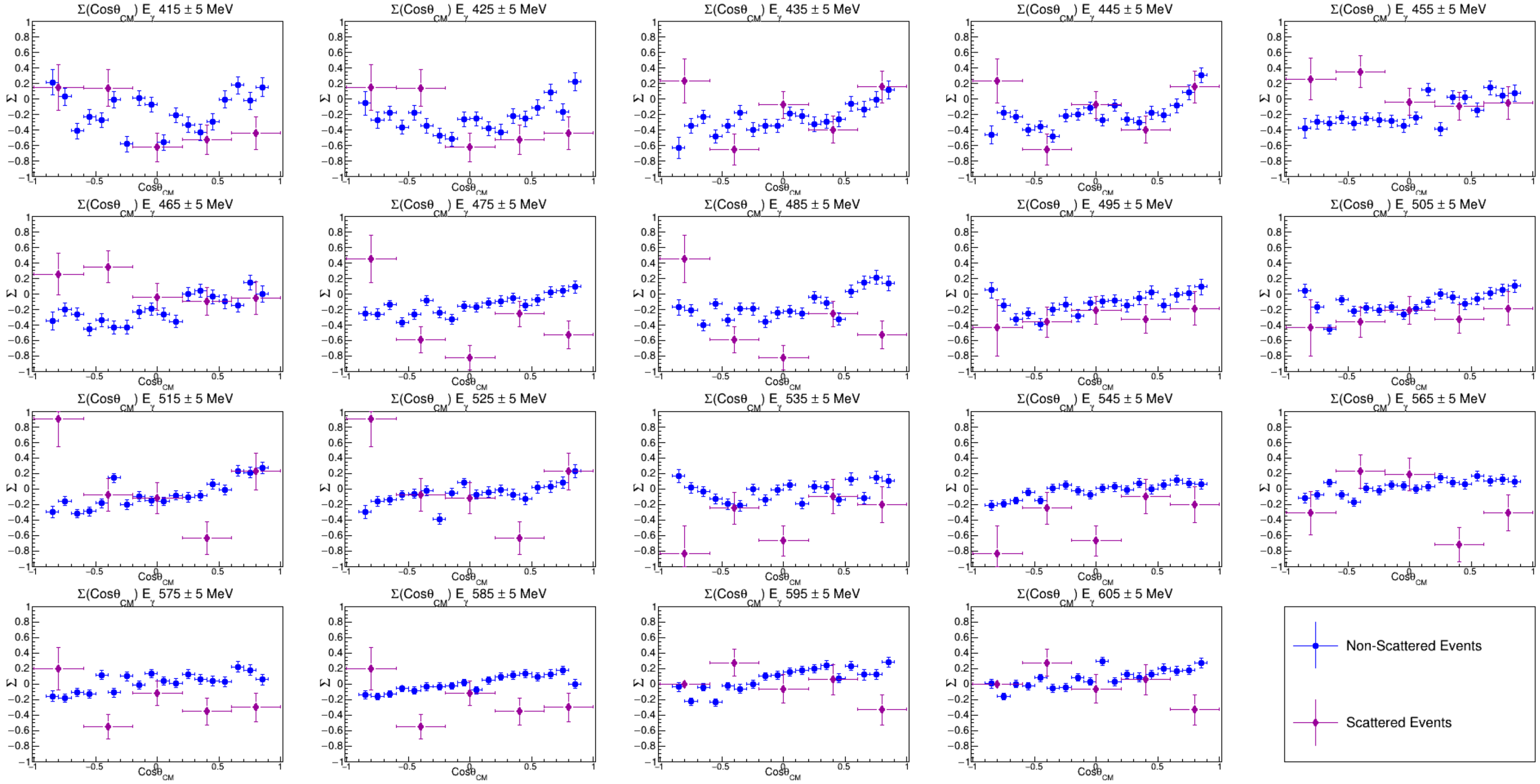

Figure 9.7 Σ $(\cos\theta_{\mathrm{CM}})$ *across several* E_γ *bins of width 10 MeV each.* Σ *values calculated from the analysis of scattered events is also plotted, note that the* E_γ *bins for this data are 20 MeV wide so are plotted on both of the corresponding non-scattered bins.*

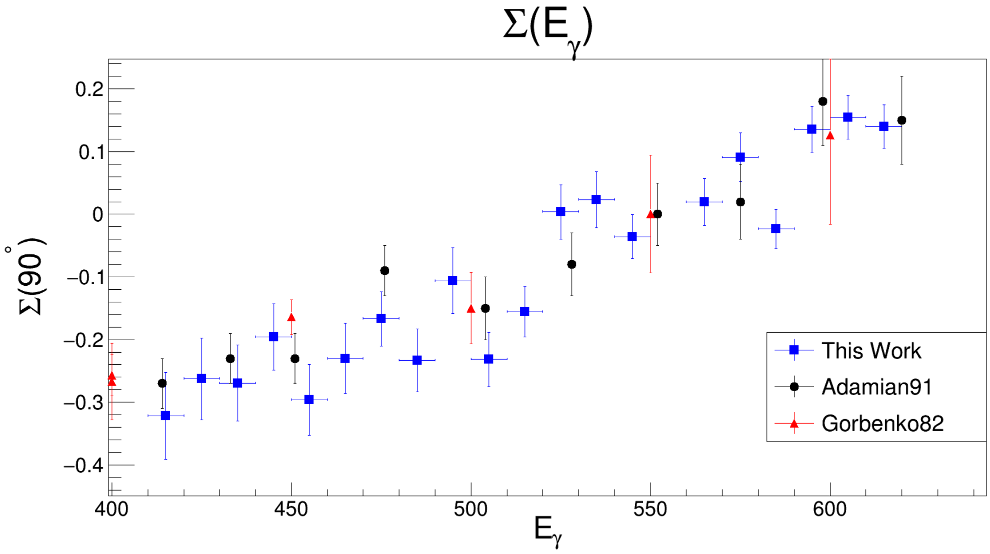

Figure 9.8 Σ *at* $\theta_{\mathrm{CM}} = 90°$. *Results from this work are presented alongside results (multiplied by -1) from work by Adamian [154] and Gorbenko [155]*

There are a limited number of previous data points available from measurements of Σ within this energy range from work by Adamian and Gorbenko [154, 155]. The data points from Adamian are superimposed on the results from this work in Figures 9.9 - 9.11. The values for Σ at $\theta_{\mathrm{CM}} = 90°$ are presented in Figure 9.8. Note that there is no bin at this angle in this analysis. The value plotted is a weighted average from the bin either side of this point. Because of a different convention used in calculating the asymmetry for the previous data ($N^{\perp} - N^{\parallel}$), these data have been multiplied by -1 to compare with the new data. The previous data points are in excellent agreement with the results from this analysis. However, this new data provides a far more comprehensive measurement of Σ across the energy range of interest.

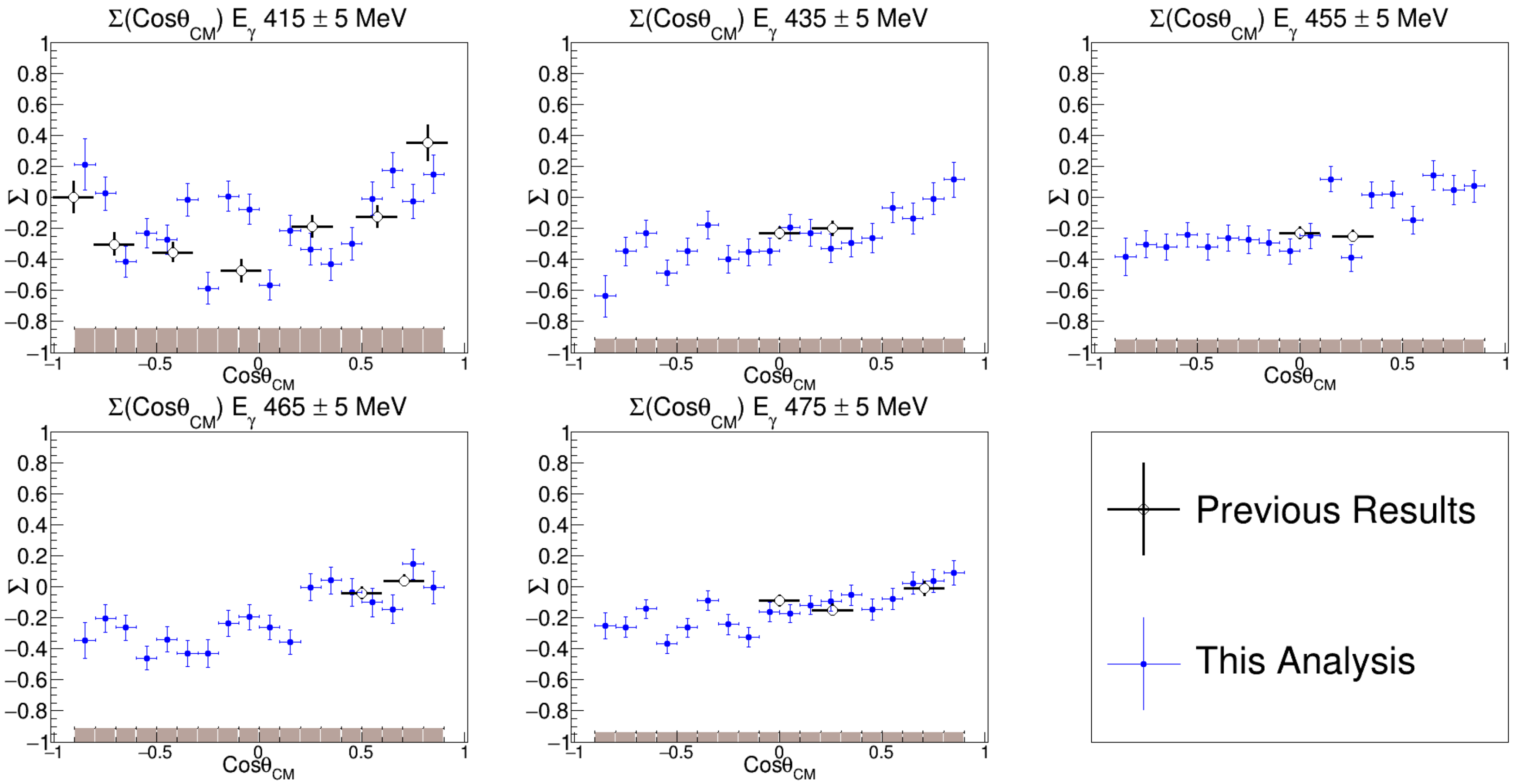

Figure 9.9 $\Sigma(\cos\theta_{\mathrm{CM}})$ *across five* E_γ *bins of width 10 MeV each. Previous data points (multiplied by -1) are indicated in black [154]. Systematic errors are included as solid bars along the bottom of each plot.*

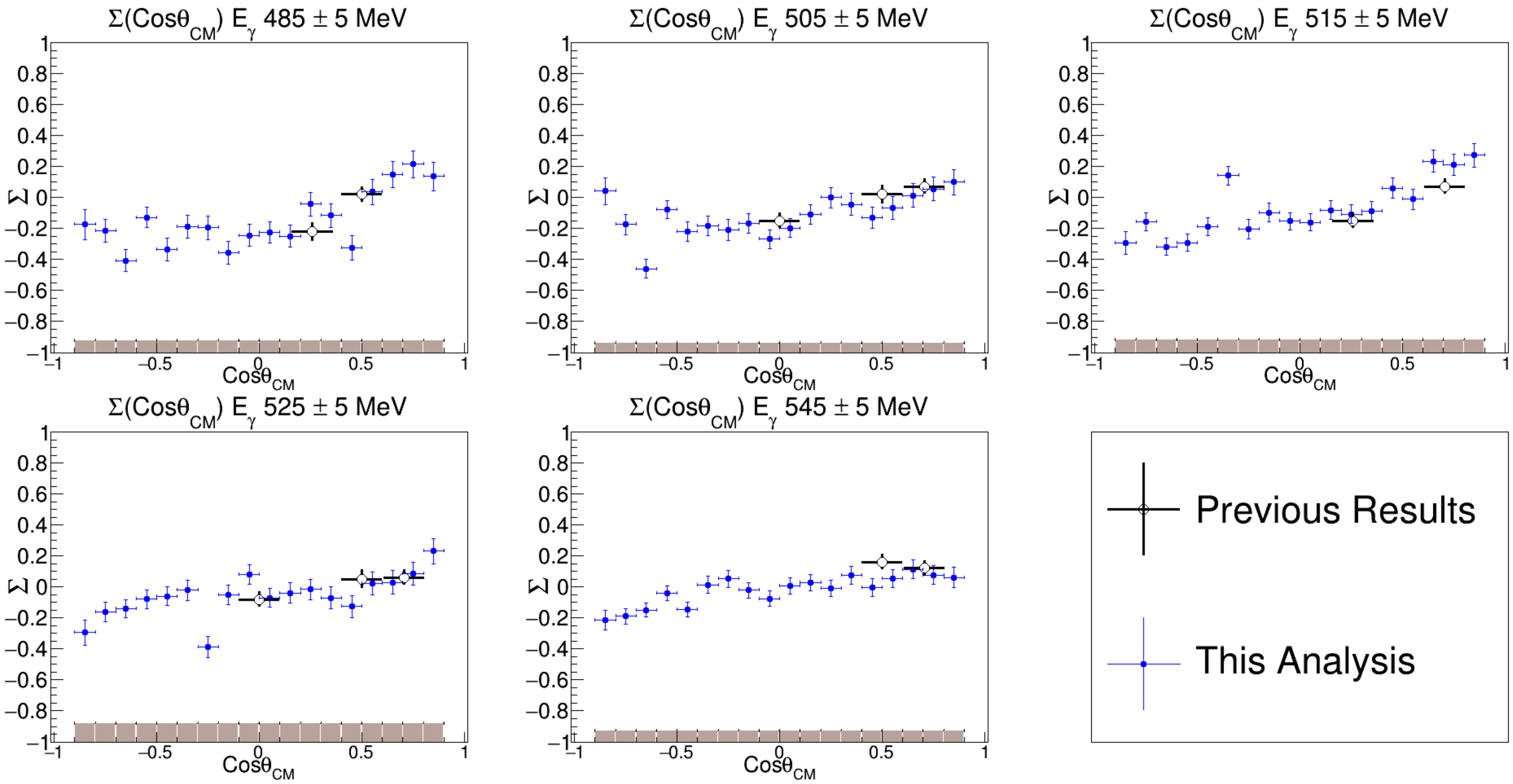

Figure 9.10 $\Sigma(\cos\theta_{\text{CM}})$ *across five* E_γ *bins of width 10 MeV each. Previous data points (multiplied by -1) are indicated in black [154]. Systematic errors are included as solid bars along the bottom of each plot.*

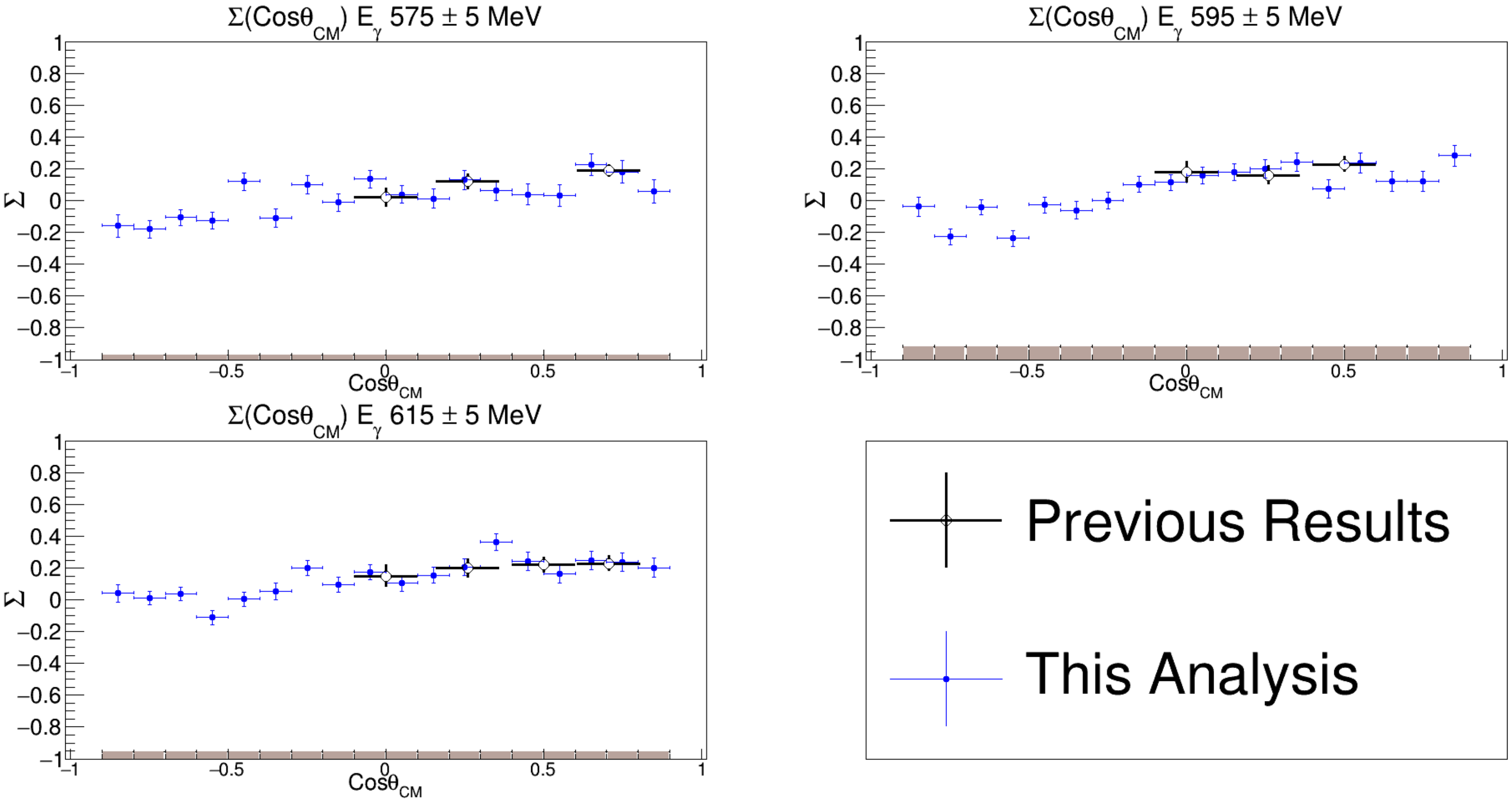

Figure 9.11 $\Sigma(\cos\theta_{\mathrm{CM}})$ *across three* E_γ *bins of width 10 MeV each. Previous data points (multiplied by -1) are indicated in black [154]. Systematic errors are included as solid bars along the bottom of each plot.*

9.2 $C_{x'}$ Results

As discussed in Section 8.3 the choice of value for p_y (and therefore P_2) in Equation (8.17) does not have a large impact upon the determined values of the fit parameter P_1. P_1 is utilised to determine $C_{x'}$. $C_{x'}$ was determined separately using each fit method outlined in the previous section. The resulting values using all three fit methods as a function of E_γ for the three and five $\cos\theta_{\mathrm{CM}}$ bin cases were presented previously. These values are presented again here for completeness and can be seen in Figures 9.12 and 9.13 respectively. The extracted $C_{x'}$ as a function of $\cos\theta_{\mathrm{CM}}$ is presented in Figure 9.14. For clarity only the fixed $p_y = 0$ fit method is presented in Figure 9.14.

Although the statistical accuracy is poor in certain kinematic regions, the new data gives first indications of the trends in $C_{x'}$ for deuteron photodisintegration at low photon energies. This is the first examination of $C_{x'}$ for the final state neutron in this reaction. When presented as a function of E_γ (as in Figure 9.13) the most statistically well defined bin is the 108-144° bin. For the most backward angular bin (144-180°) there are signs that $C_{x'}$ may be negative in the region of the Δ. When presented as a function of $\cos\theta_{\mathrm{CM}}$ (Figure 9.14) at low photon energies (in the region of the Δ) there are indications that $C_{x'}$ is largely negative but with hints of more positive values at extreme forward and backward angles. Similar behaviour is also observed in the higher photon energy bin which covers the region of the d*(2380) (500-600 MeV). For the three highest energy E_γ bins there are very limited statistics but there may be signs of a very rapid change in $C_{x'}$.

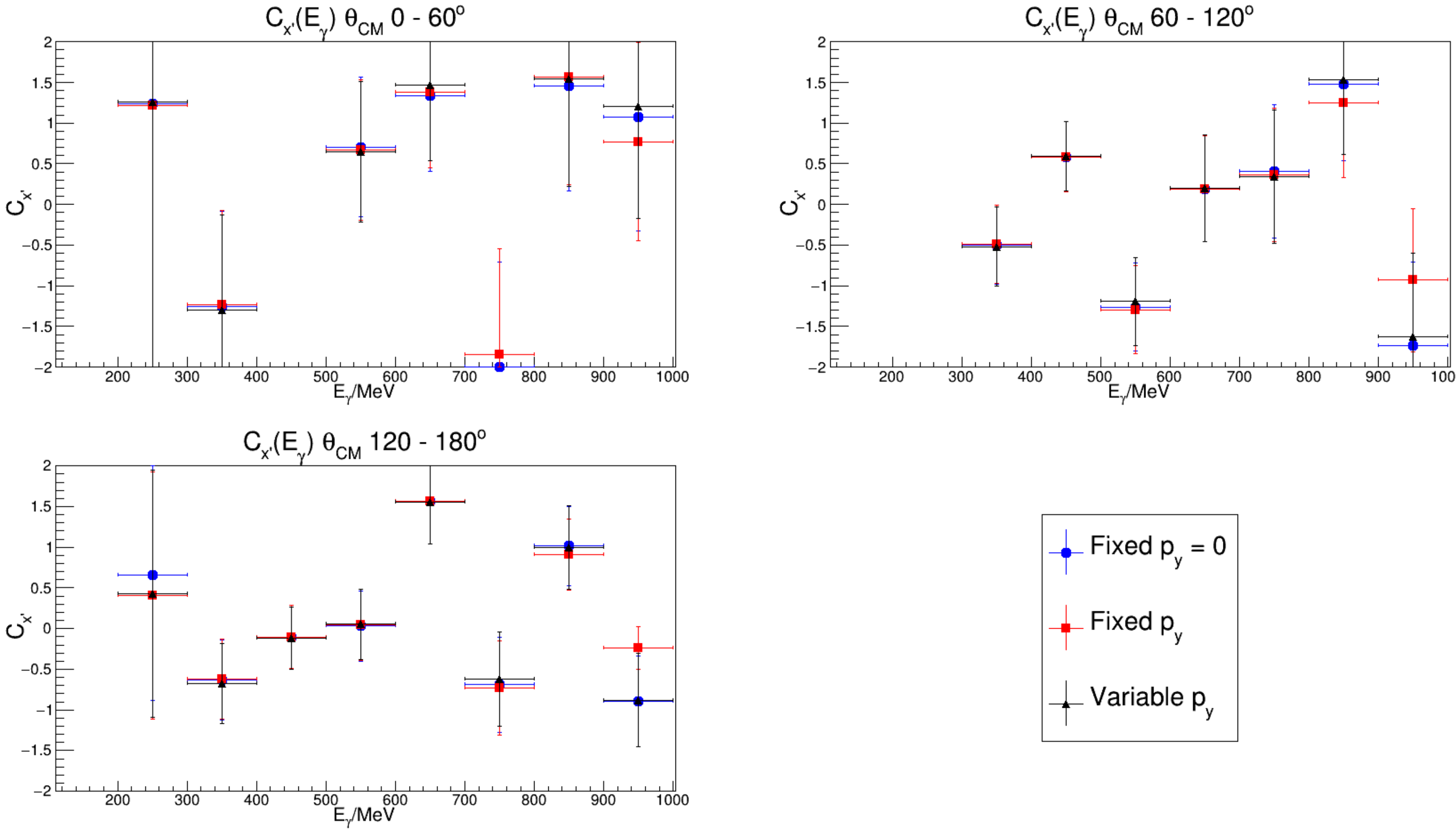

Figure 9.12 *Results obtained for $C_{x'}$ plotted as a function of E_γ across three angular bins in $\cos\theta_{\mathrm{CM}}$. Results for the three different fitting methods are shown as outlined in the provided legend.*

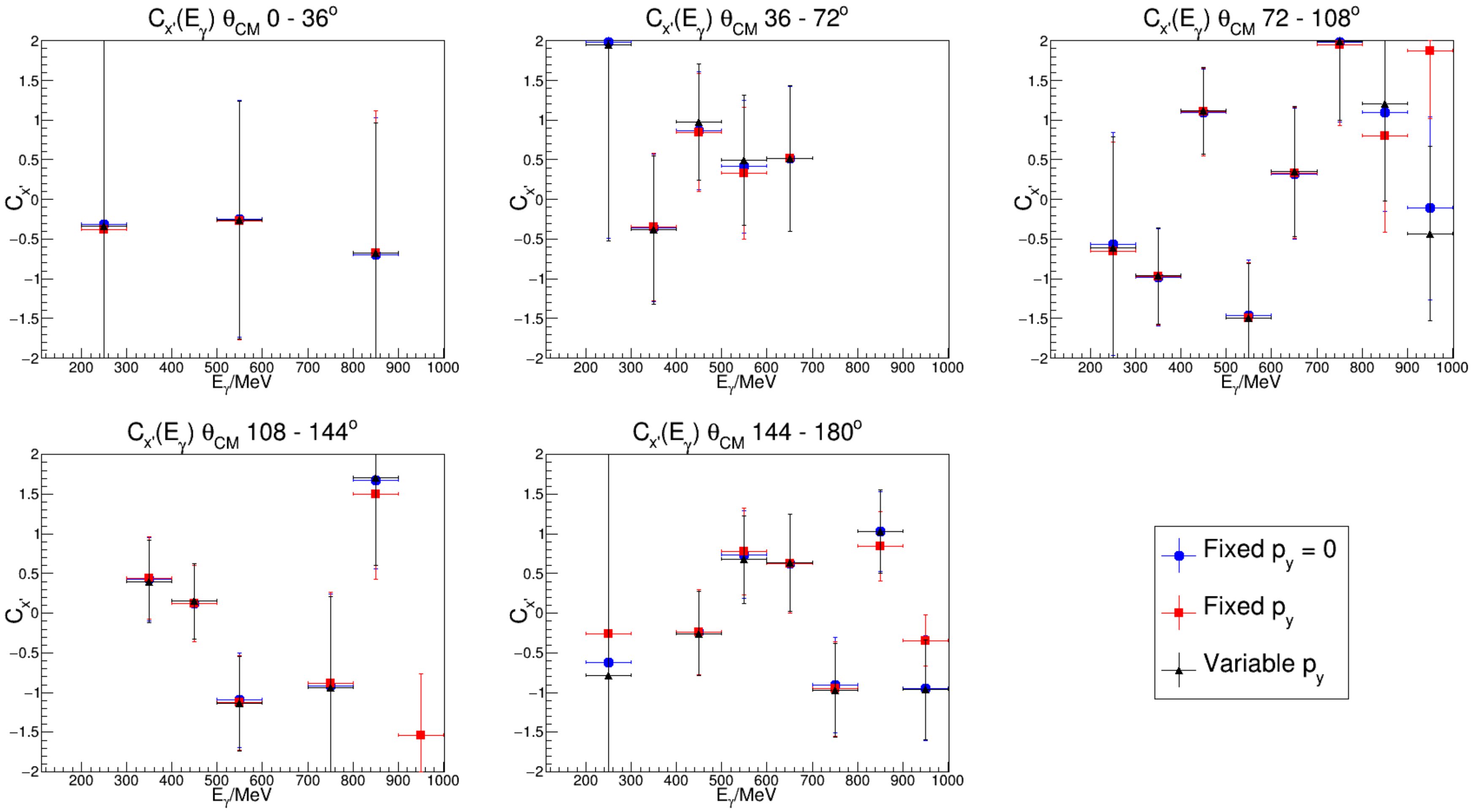

Figure 9.13 *Results obtained for $C_{x'}$ plotted as a function of E_γ across five angular bins in $\cos\theta_{\rm CM}$. Results for the three different fitting methods are shown as outlined in the provided legend.*

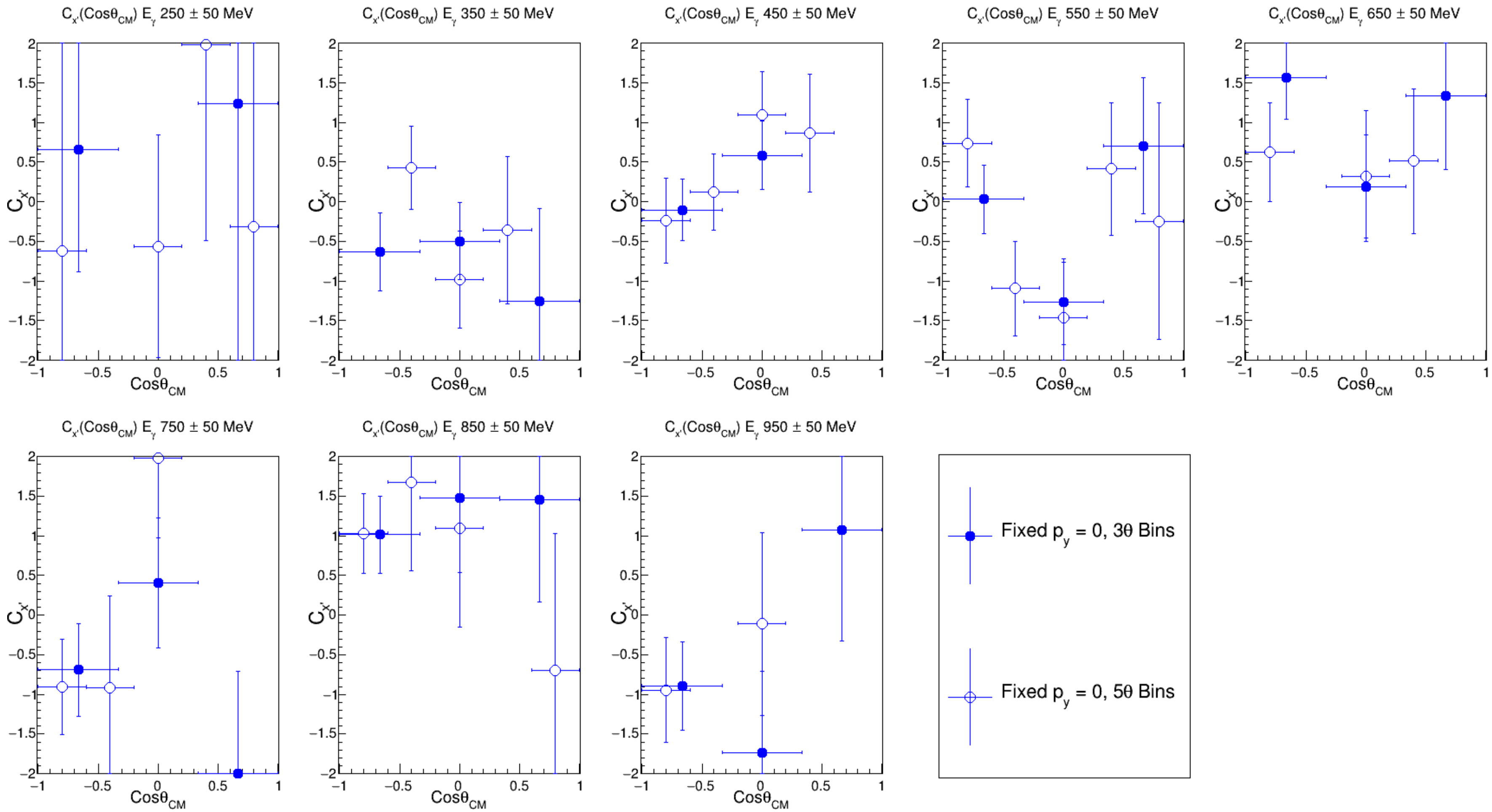

Figure 9.14 *Obtained values for $C_{x'}$ plotted as a function of $\cos\theta_{\rm CM}$ across the full energy range examined. Only points obtained from the analysis with p_y = 0 are plotted to improve the clarity of the plot.*

Chapter 10

Interpretation of Results and Discussion

This chapter introduces a preliminary interpretation of the results for Σ. This is followed by a discussion on the potential consequences of these results and further avenues for future investigation.

10.1 Interpretation of Σ Results

An initial attempt to examine the angular dependence of the measured values of Σ was undertaken. The polarisation observable terms in the polarised differential cross section expression given in Equation (3.4) can be decomposed in terms of associated Legendre functions [156]. The angular distribution of the Σ observable can be expressed as the function

$$\begin{aligned} f(x) = (1-x^2)\Bigg(&3P_0 + 15xP_1 + \frac{15}{2}P_2(7x^2-1) + \frac{105}{2}P_3(3x^3-x) + \\ &\frac{105}{8}P_4(33x^4-18x^2+1) + \frac{63}{8}P_5(143x^5-110x^3+15x) \\ &+\frac{315}{16}P_6(143x^6-143x^4+33x^2) + \frac{495}{16}P_7(221x^7-273x^5+91x^3-7x)\Bigg), \end{aligned} \tag{10.1}$$

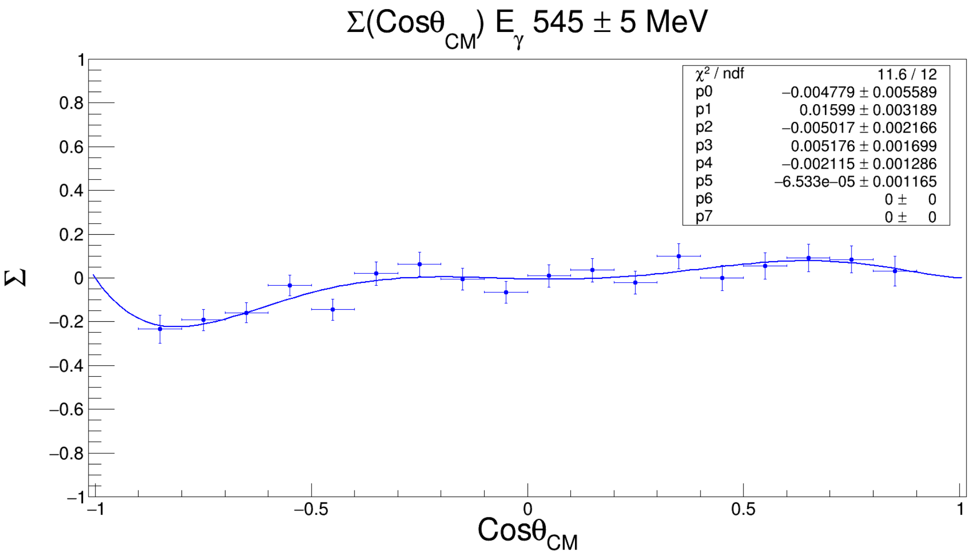

Figure 10.1 *$\Sigma(\cos\theta_{\text{CM}})$ in one 10 MeV wide E_γ bin. The solid line represents the fit defined by Equation (10.1) to the data, fit parameters are included in the top right.*

where $x = \cos\theta_{\text{CM}}$. An example fit to the data is presented in Figure 10.1. The fit parameters, P_0-P_7, are relabelled to be the parameters P^2_{n+2} where n is the initial parameter number in the fit, i.e. $P_0 = P^2_2, P_1 = P^2_3$ and so on. As can be seen from the resultant fit parameters (inset on figure) in Figure 10.1 the 7th (P^2_8) and 8th (P^2_9) parameters of this fit are fixed. With these parameters not fixed, the plot has too many free variables to fit satisfactorily. The values of these parameters would also be expected to be very small, as observed in the parameters that are measured, the values reduce in magnitude from P^2_2–P^2_7. This function was fitted to the results for Σ in all of the analysed angular and energy bins as shown in Figures 10.2 - 10.6.

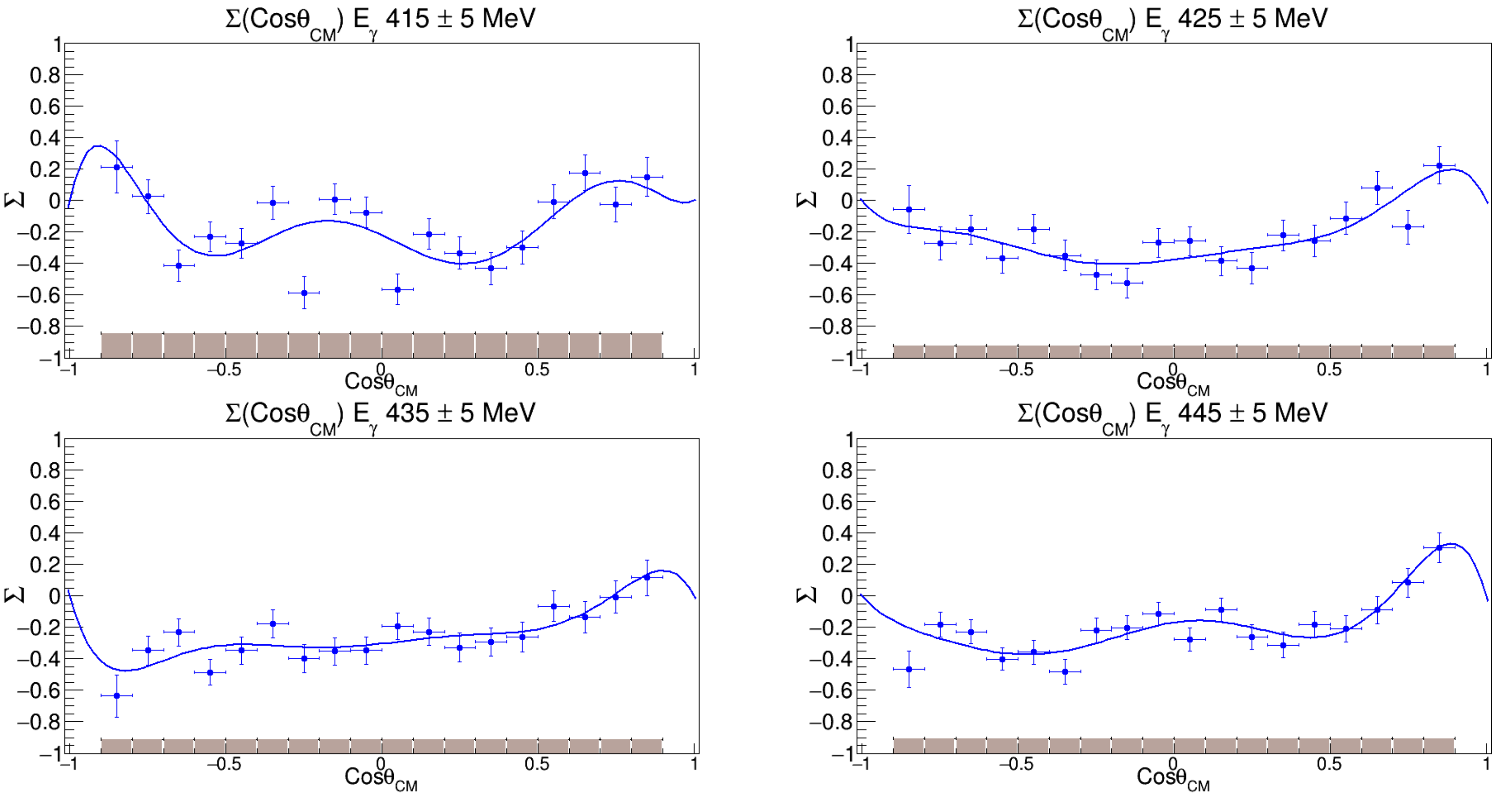

Figure 10.2 $\Sigma(\cos\theta_{\mathrm{CM}})$ *across four* E_γ *bins of width 10 MeV each. Solid blue line represents fit of Equation (10.1) to the data. Systematic errors are included as solid bars along the bottom of each plot.*

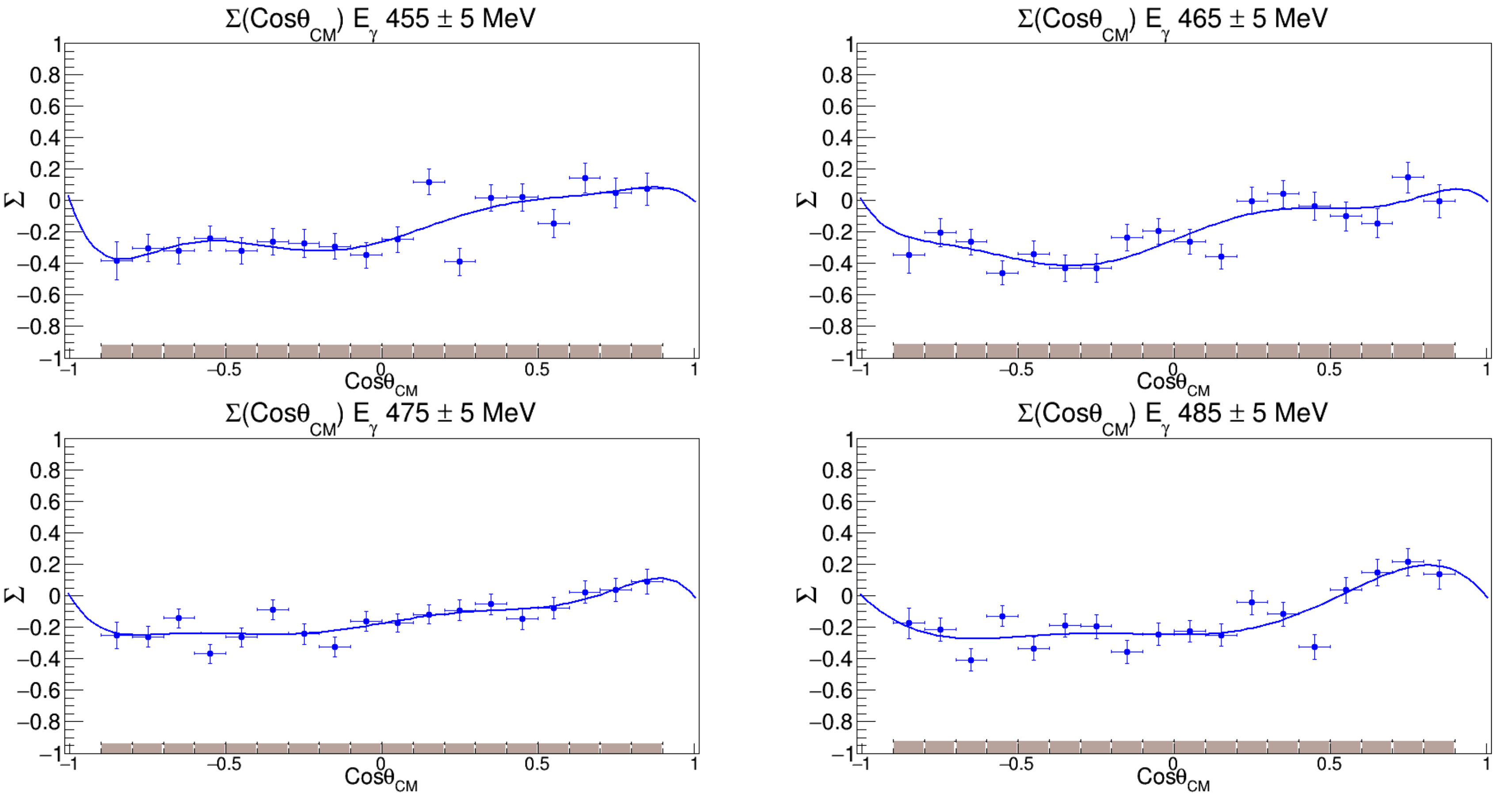

Figure 10.3 *$\Sigma(\cos\theta_{\mathrm{CM}})$ across four E_γ bins of width 10 MeV each. Solid blue line represents fit of Equation (10.1) to the data. Systematic errors are included as solid bars along the bottom of each plot.*

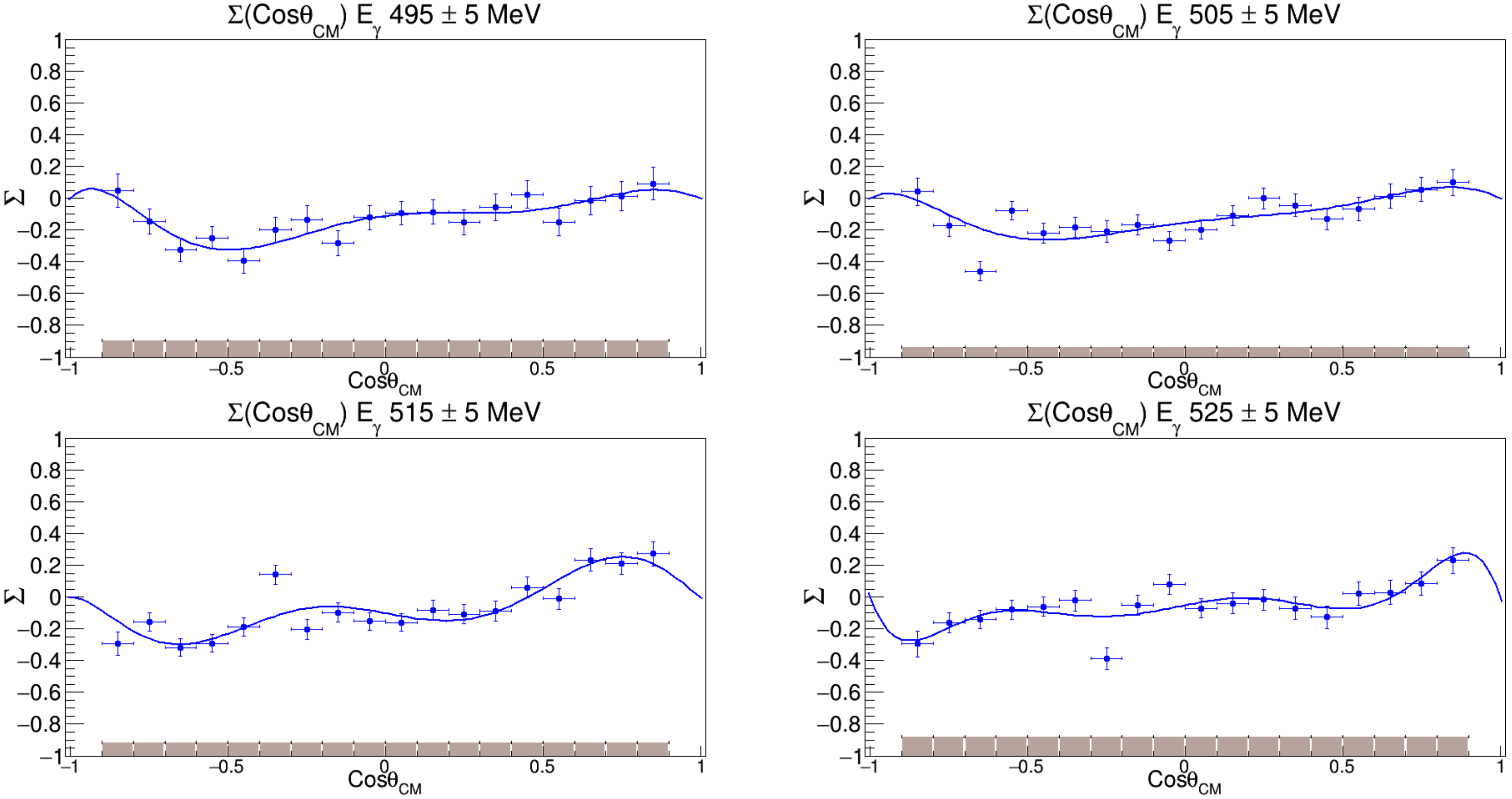

Figure 10.4 $\Sigma(\cos\theta_{\mathrm{CM}})$ *across four* E_γ *bins of width 10 MeV each. Solid blue line represents fit of Equation (10.1) to the data. Systematic errors are included as solid bars along the bottom of each plot.*

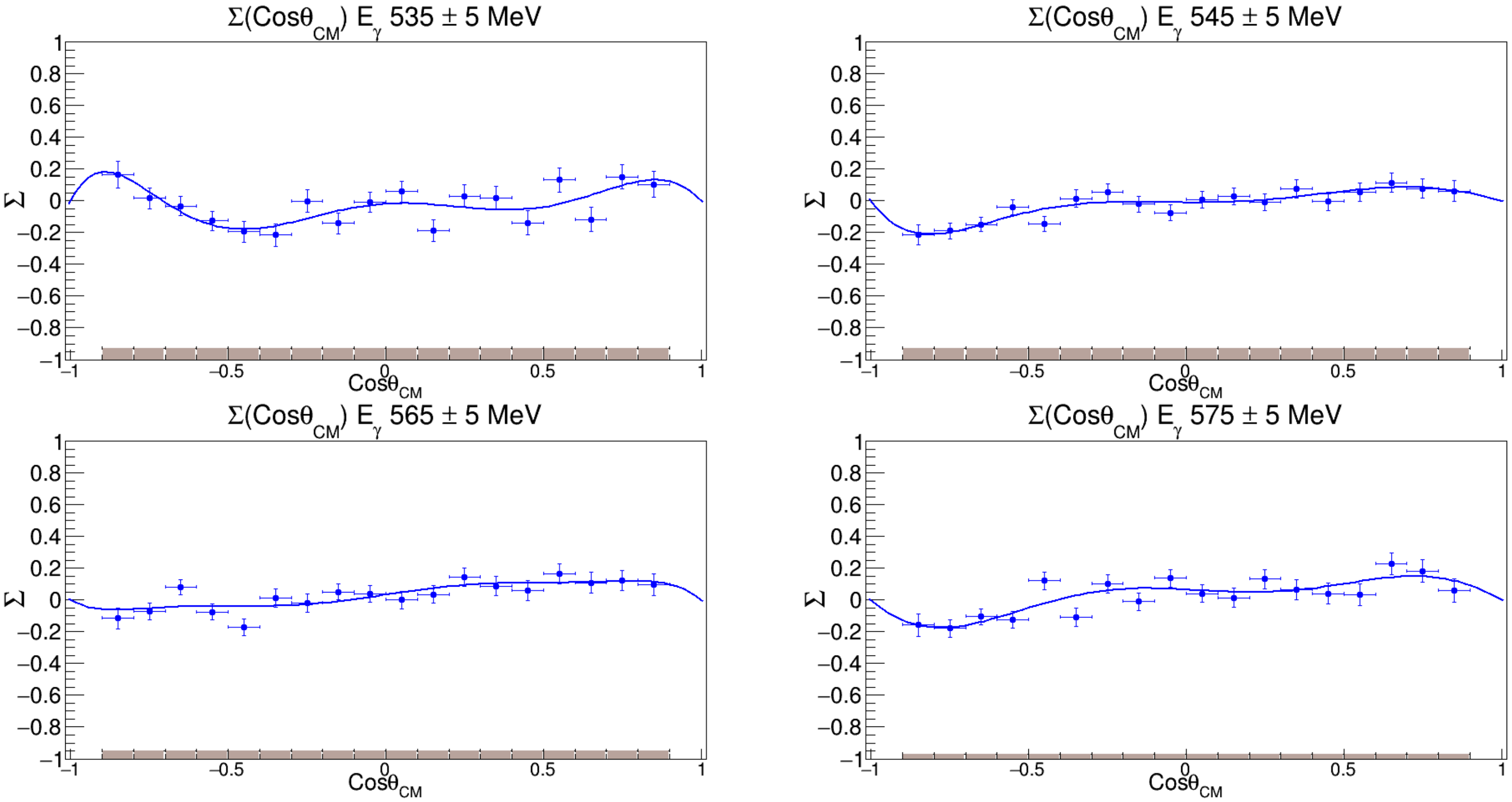

Figure 10.5 $\Sigma(\cos\theta_{\mathrm{CM}})$ *across four* E_γ *bins of width 10 MeV each. Solid blue line represents fit of Equation (10.1) to the data. Systematic errors are included as solid bars along the bottom of each plot.*

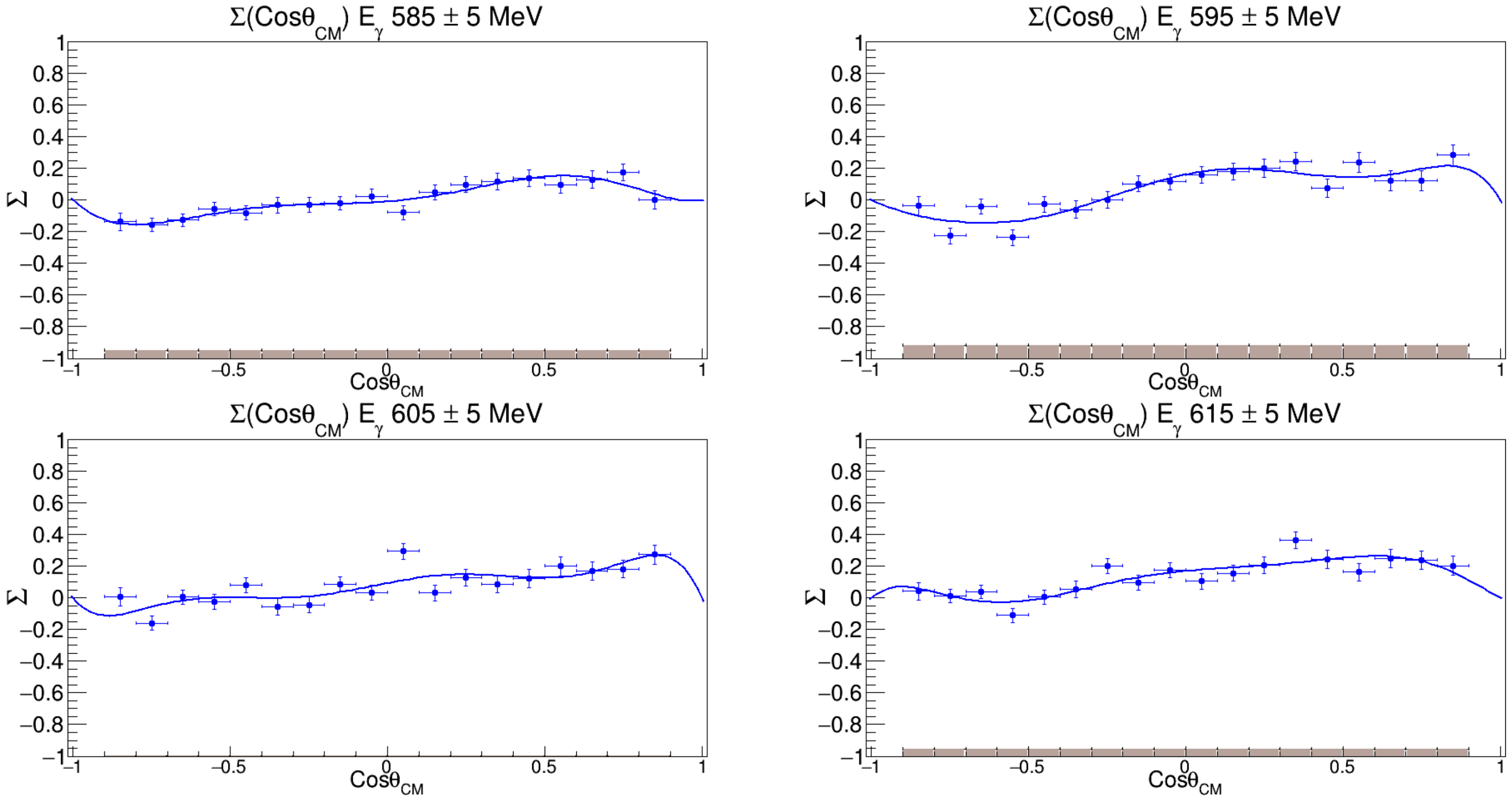

Figure 10.6 $\Sigma(\cos\theta_{\mathrm{CM}})$ *across four* E_γ *bins of width 10 MeV each. Solid blue line represents fit of Equation (10.1) to the data. Systematic errors are included as solid bars along the bottom of each plot.*

The values of the fit parameters, P^2_{2-7}, were extracted for each E_γ bin. The values of these parameters as a function of E_γ are presented in Figure 10.7. The variation of these parameters as a function of the energy will need further theoretical work to be interpreted further. A brief examination of the energy dependence using a simplistic model is included in Appendix G.

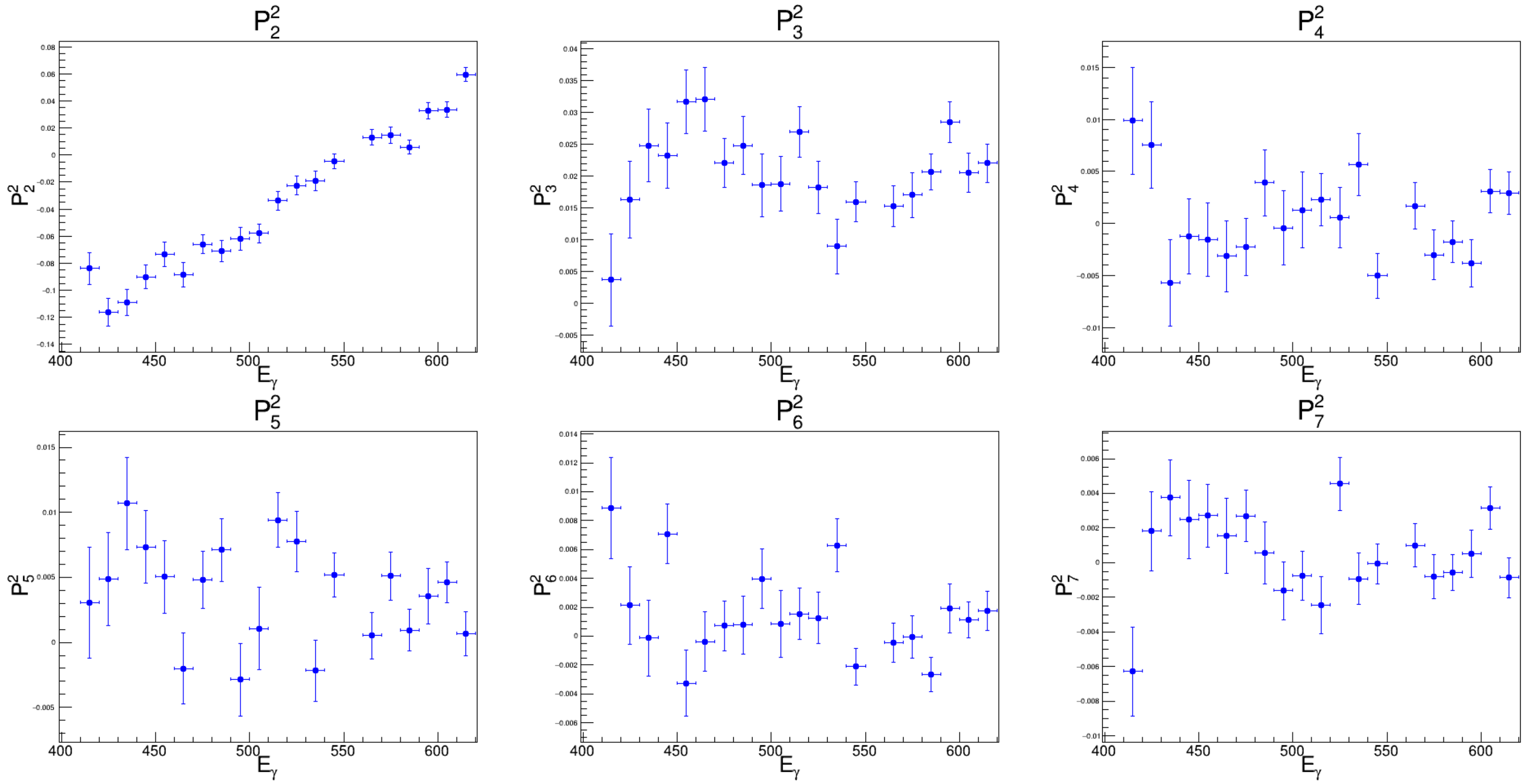

Figure 10.7 *Fit parameters of the function given by Equation (10.1), P^2_{2-7}, as a function of E_γ.*

10.2 Discussion and Conclusions

This section will present a first discussion of the results obtained and indicate a pathway for future analysis to constrain the role of the d*(2380) to the data.

10.2.1 Discussion of Σ Results

The obtained results for the beam asymmetry, Σ, are in good agreement with the previous measurements of this observable, while significantly increasing the statistical accuracy and kinematic coverage. The fits discussed in Section 10.1 appear to provide a good description of the data. The analysis presented in this thesis is just a first step to obtaining sensitivity and constraining the d*(2380) parameters. In the future, model predictions developed can be compared to the experimental data and the results of this first associated Legendre function analysis.

In the past, beam asymmetry data has been invaluable in constraining the properties of resonant states. For example a multipole analysis has been undertaken to obtain the E2/M1 transition ratio in the $\gamma N \to \Delta(1232)$ reaction [157]. It would be interesting to explore the use of the new beam asymmetry (Σ) data with other available measurements (e.g. cross section) in order to ascertain whether sensitivity to the different EM transitions to the d*(2380) can be extracted. Such transition ratios can in turn be used to extract other parameters. In the analysis of the $\Delta(1232)$ the quadrupole electric transition moment, $\langle Q_{zz} \rangle$, and transition magnetic moment, $\mu_{N\Delta}$, were calculated via

$$\frac{E2}{M1} = \frac{1}{2} k M_N \frac{\langle Q_{zz} \rangle_{N\Delta}}{\mu_{N\Delta}}, \tag{10.2}$$

where M_N is the mass of nucleon and k is the photon momentum [158]. In the reaction $\gamma d \to d^*(2380)$ it is expected that the transition could proceed via an E2(2^+), M3(3^+) or E4(4^+) transition. By drawing analogy to the previous work it is possible that with further analysis the ratio of these transitions could be determined for this reaction. From this, further properties of the state could be determined.

10.2.2 The way forward to improved $C_{x'}$ data

The measured values of $C_{x'}$ present a first look at this observable in a previously unexamined energy range. However, this experiment was a proof of principle measurement to prove the technique ready for larger beamtimes in the future. Although the results have large statistical uncertainties the feasibility of the measurement has been proved and the analysis gives a solid base to plan future measurements. It should be noted that the achieved statistical accuracy was consistent with the expected estimates in the proposal (Appendix F).

With the limited beamtime of the experiment it was decided to focus on achieving a high degree of linear polarisation in the beamtime available. This meant using a high electron beam energy to achieve the highest degree of polarisation. This comes at the cost of reducing the degree of circular polarisation for photon energies in the region relevant to the d*(2380). To improve $C_{x'}$ in the future it may be advisable to use a lower beam energy.

The observed asymmetries in the region examined are expected to be very small due to the low (as low as 10% in the lowest energy bins) degree of circular polarisation of the photon beam. It should also be noted that the cross section for deuteron photodisintegration also falls off rapidly as E_γ rises beyond 300 MeV [159]. A longer beamtime would help to improve the available statistics. The combination of the two data sets should be possible if care is taken to reproduce close to exact experimental conditions as in the current data. Uncertainties in the target position, shifts in the PID or MWPC and the polarimeter itself could all introduce systematic uncertainties into the analysis. There is also the potential that in future runs the photon beam intensity could be increased. This is due to the recent installation of the newly upgraded photon tagger at MAMI that is capable of handling higher rates of events [160].

A significant factor impacting the available statistics for the scattered data is the efficiency of the MWPC detectors. The efficiency of each chamber for proton detection is only 70% at most. As such, imposing any conditions where both chambers produce a signal (which improves the accuracy of the vertex determination) immediately removes a large fraction of events. If the MWPC efficiency could be improved in some way, then the vertex determination could be improved and the number of events retained could be increased.

10.2.3 Conclusions

This work presented in this thesis outlines the design and construction of a new recoil polarimeter, which was utilised in a measurement of polarisation observables in deuteron photodisintegration. This polarimeter includes a newly built particle identification detector, PID-III. The polarimeter had its first commissioning experiment in the A2 hall at MAMI in August 2016 and operated successfully providing polarisation information on final-state neutrons over a wide kinematic range and with good acceptance. This creates a new experimental capability for the A2 collaboration at MAMI.

The linearly polarised photon beam asymmetry, Σ, has been measured in the $\vec{\gamma}d \rightarrow pn$ reaction in the photon energy range of 410–620 MeV and across a very wide kinematic range. The Σ data are in excellent agreement with the sparse previous data in this region. This new measurement of Σ has expanded the data set for deuteron photodisintegration considerably and will be a valuable resource for theoretical studies. Analysis of the E_γ and angular dependencies of the new Σ data was undertaken, guided by previous theoretical works. Constraining the d*(2380) resonance from the new data appears possible with further theoretical studies.

The recoil polarisation observable, $C_{x'}$, was also measured in the $\vec{\gamma}\mathrm{d}\rightarrow\mathrm{p}\vec{n}$ reaction for photon energies in the range 200-1000 MeV. This is the first measurement of $C_{x'}$ for the final state neutron. Although the $C_{x'}$ data has a modest statistical accuracy, it offers a first glimpse of this observable across the energy range relevant to the d*(2380) resonance. These measurements provide a proof of principle for the experimental method to extract neutron polarisation observables.

This thesis provides valuable new constraints on the photodisintegration of the deuteron. As well as constraining our general theoretical understanding of the process, the data indicate sensitivity to the role of the d*(2380) may be evident in the data. This is important as it would be the first observation of the d*(2380) with an electromagnetic probe. EM probes are the key to establishing the nature of the d*(2380) in the future, particularly to validate its potential hexaquark nature.

Appendix A

Phase-II Polarimeter Schematic Diagrams

Measurements on schematics are in mm unless stated otherwise.

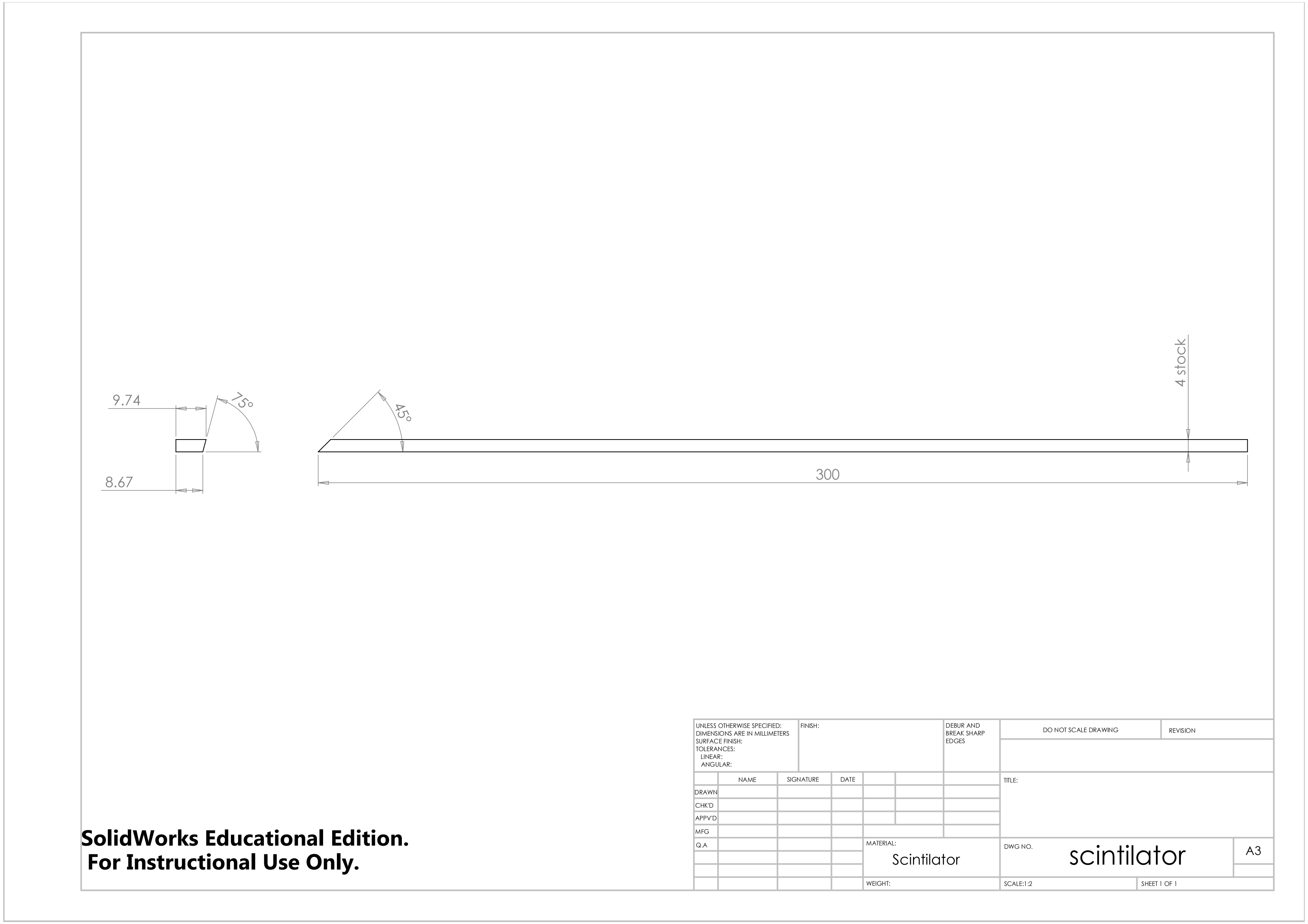

Figure A.1 *Schematic drawing of PID-III detector element*

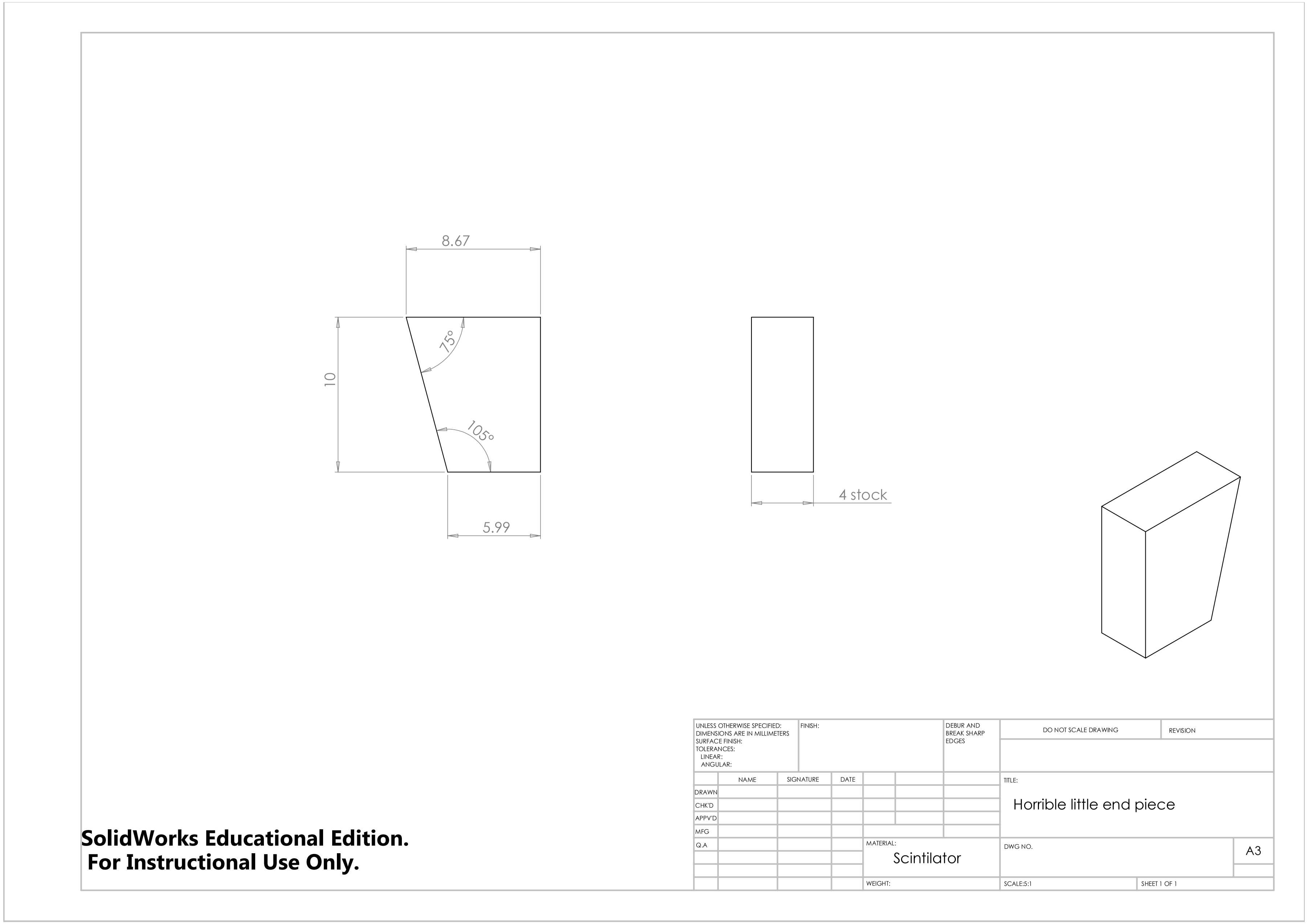

Figure A.2 *Schematic drawing of end piece for PID-III*

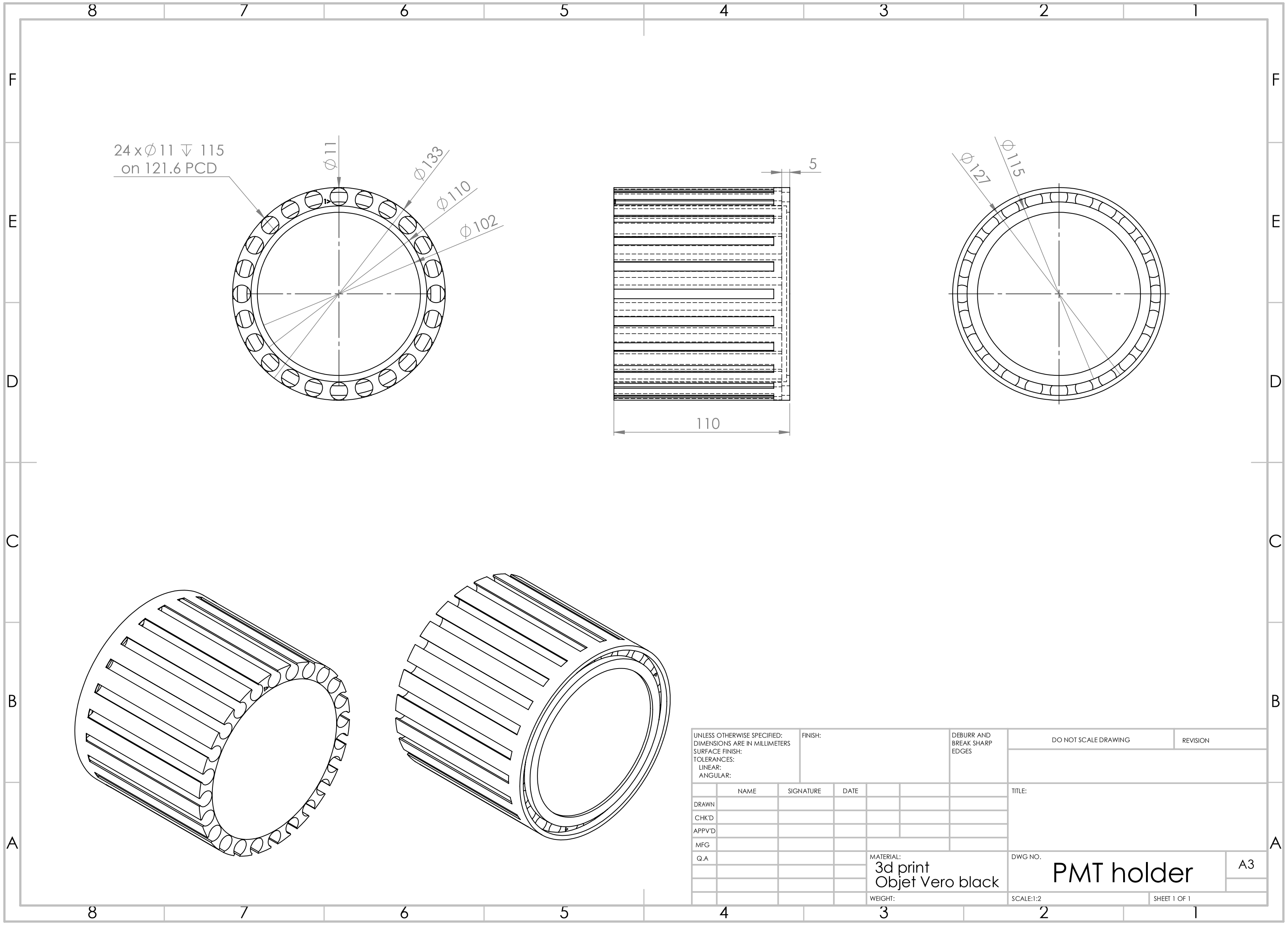

Figure A.3 *Schematic drawing of PMT support structure for PID-III. This is the PMT support "crown".*

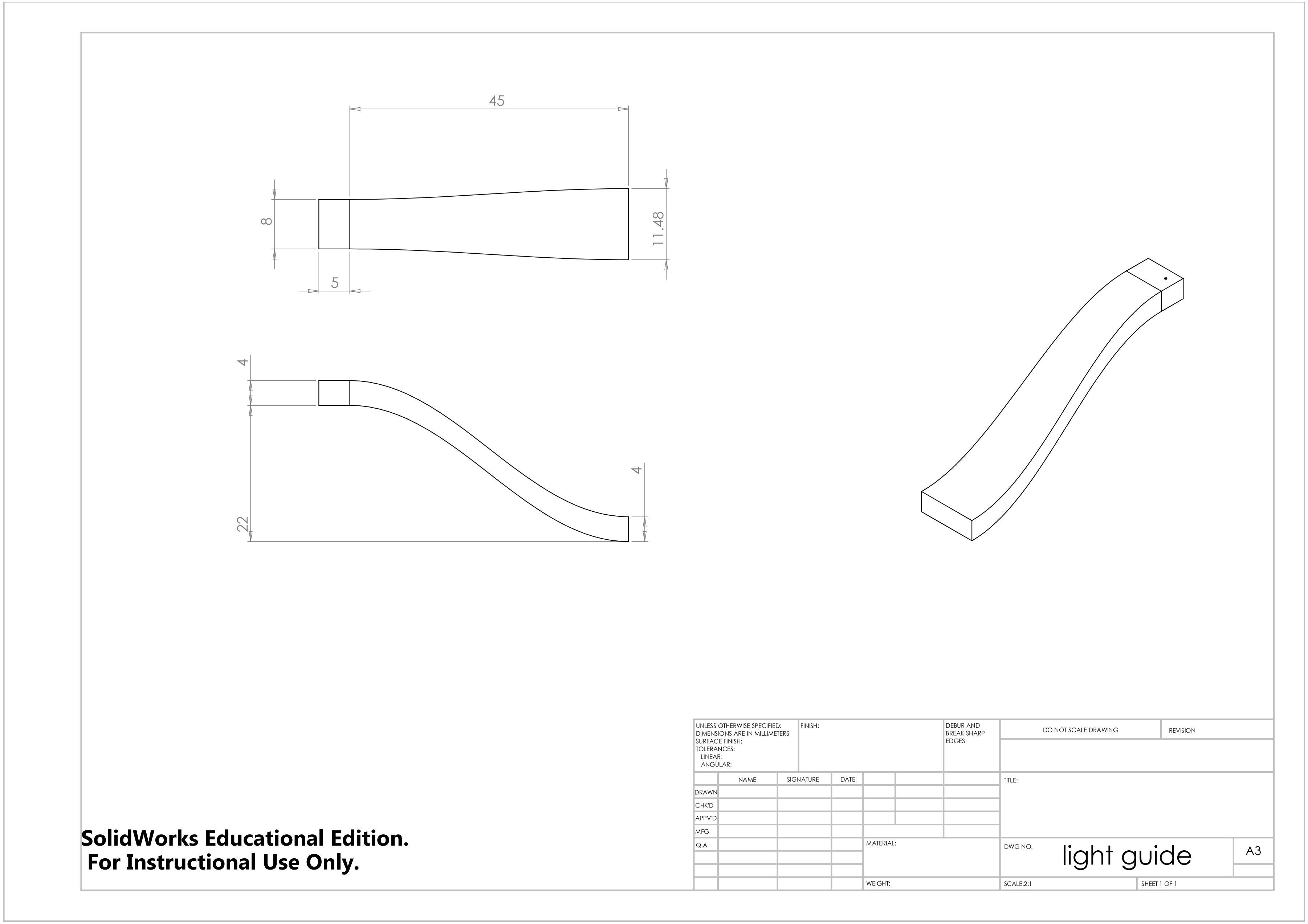

Figure A.4 *Schematic drawing of new lightguide for PID-III*

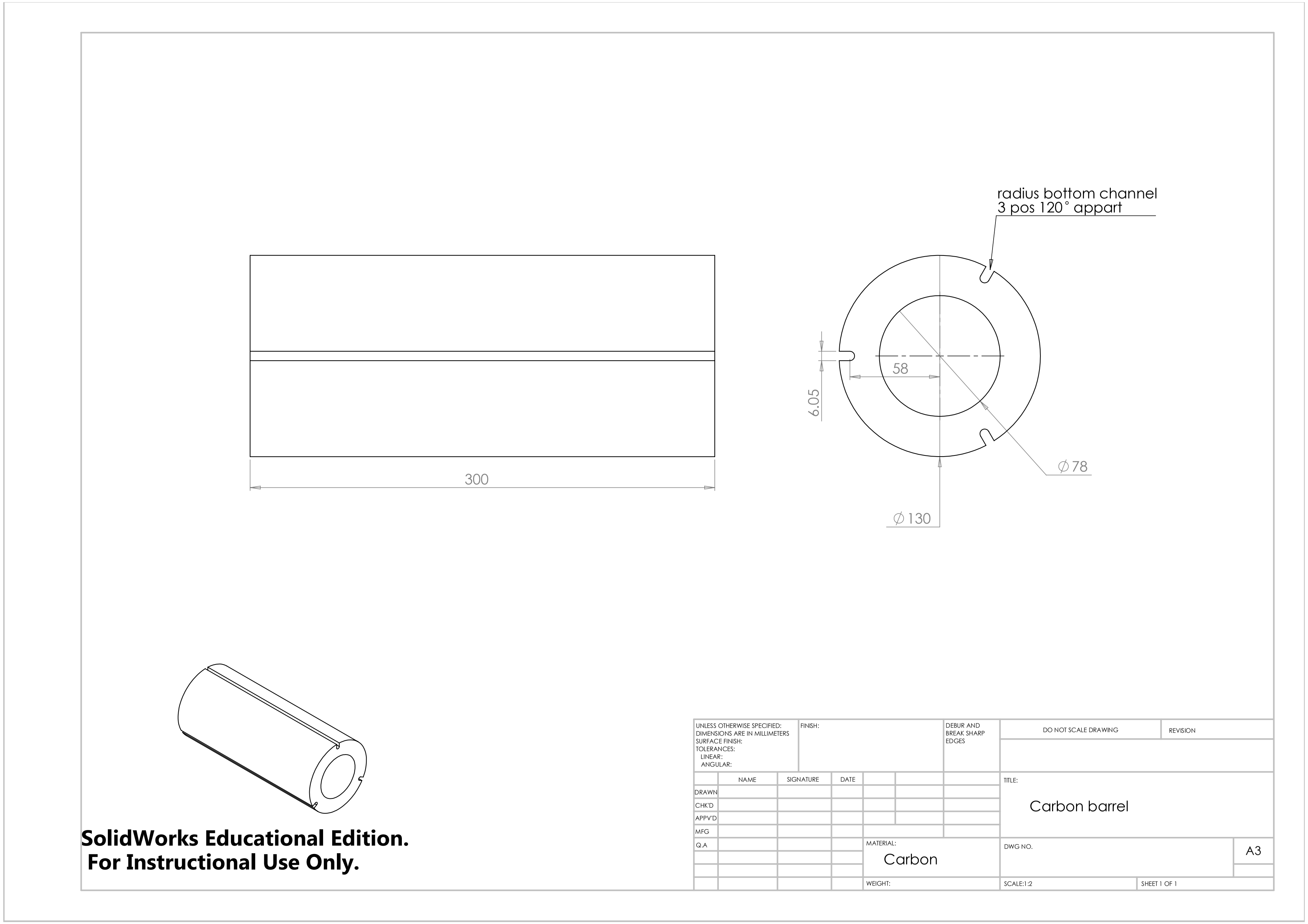

Figure A.5 *Schematic drawing of polarimeter barrel*

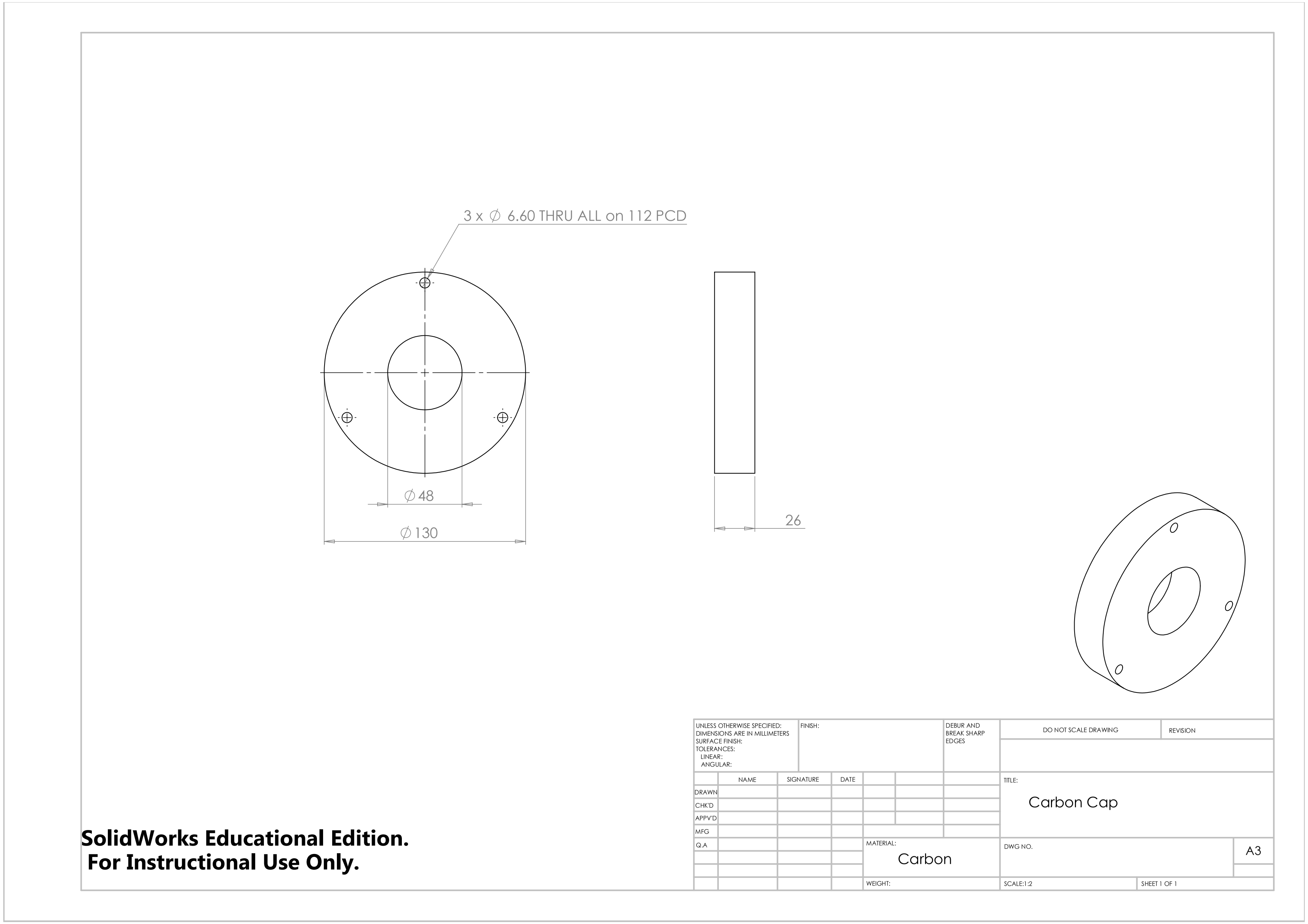

Figure A.6 *Schematic drawing of polarimeter end cap*

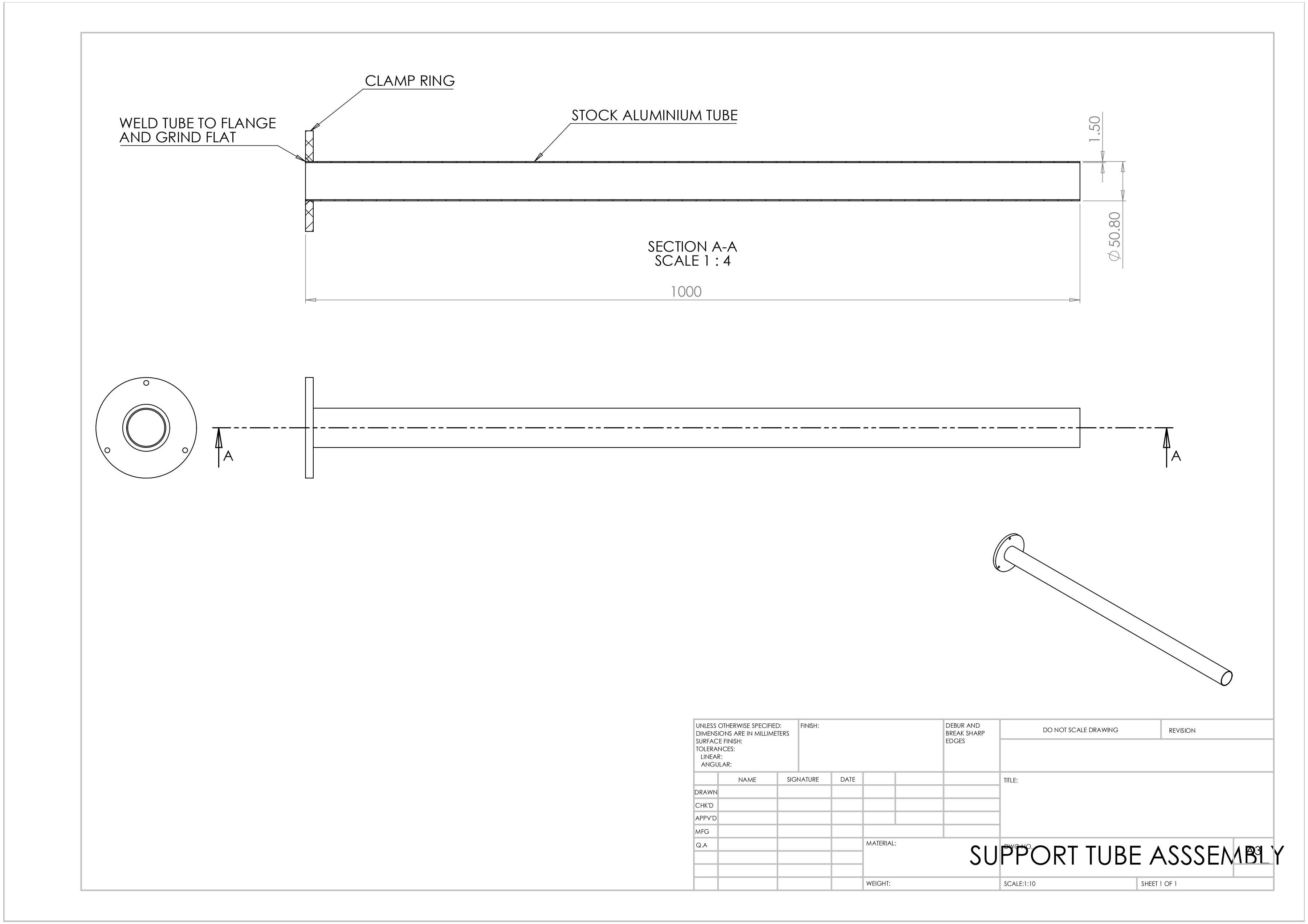

Figure A.7 *Schematic drawing of polarimeter support pipe*

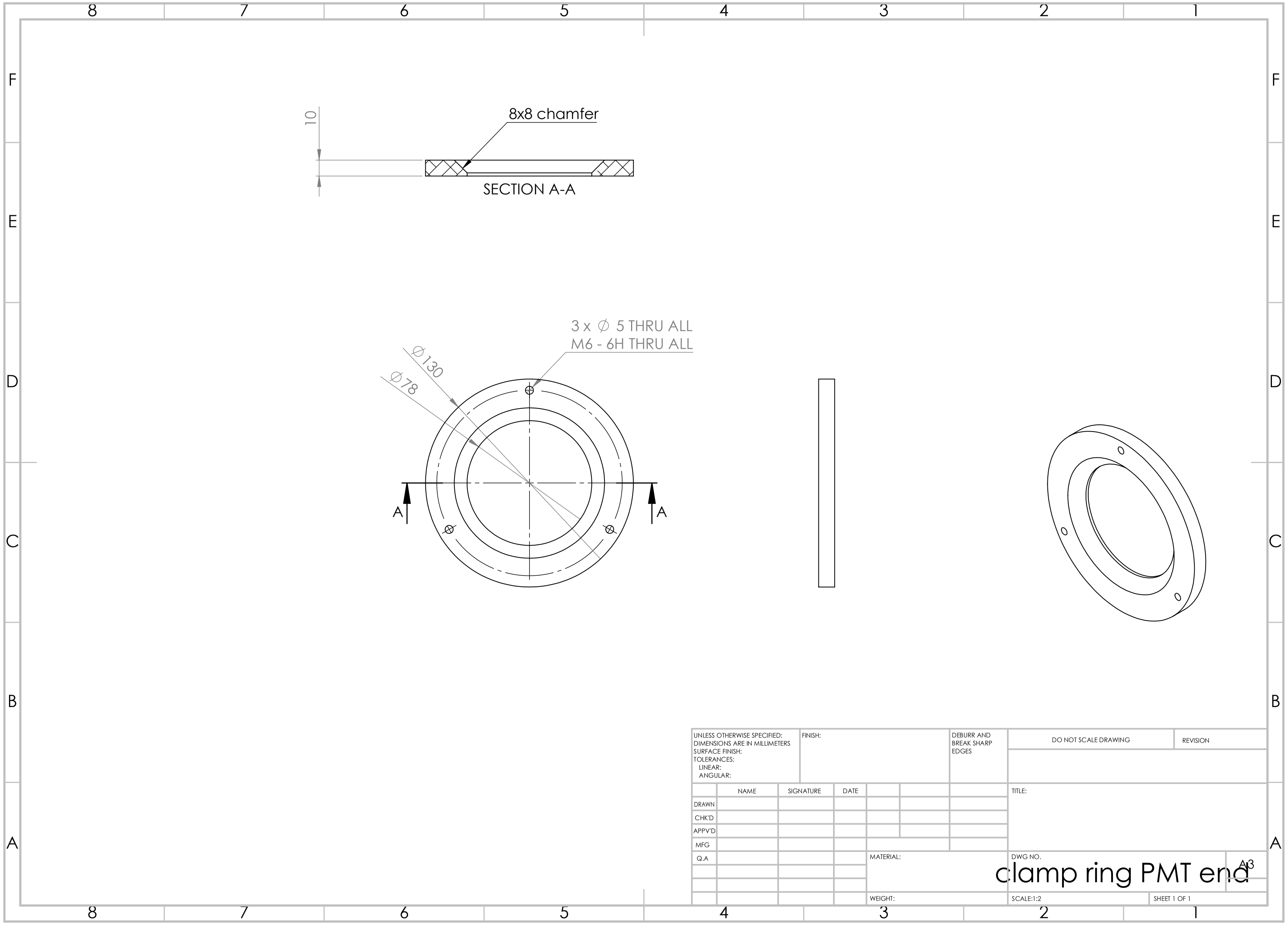

Figure A.8 *Schematic drawing of polarimeter support ring for the PMT end*

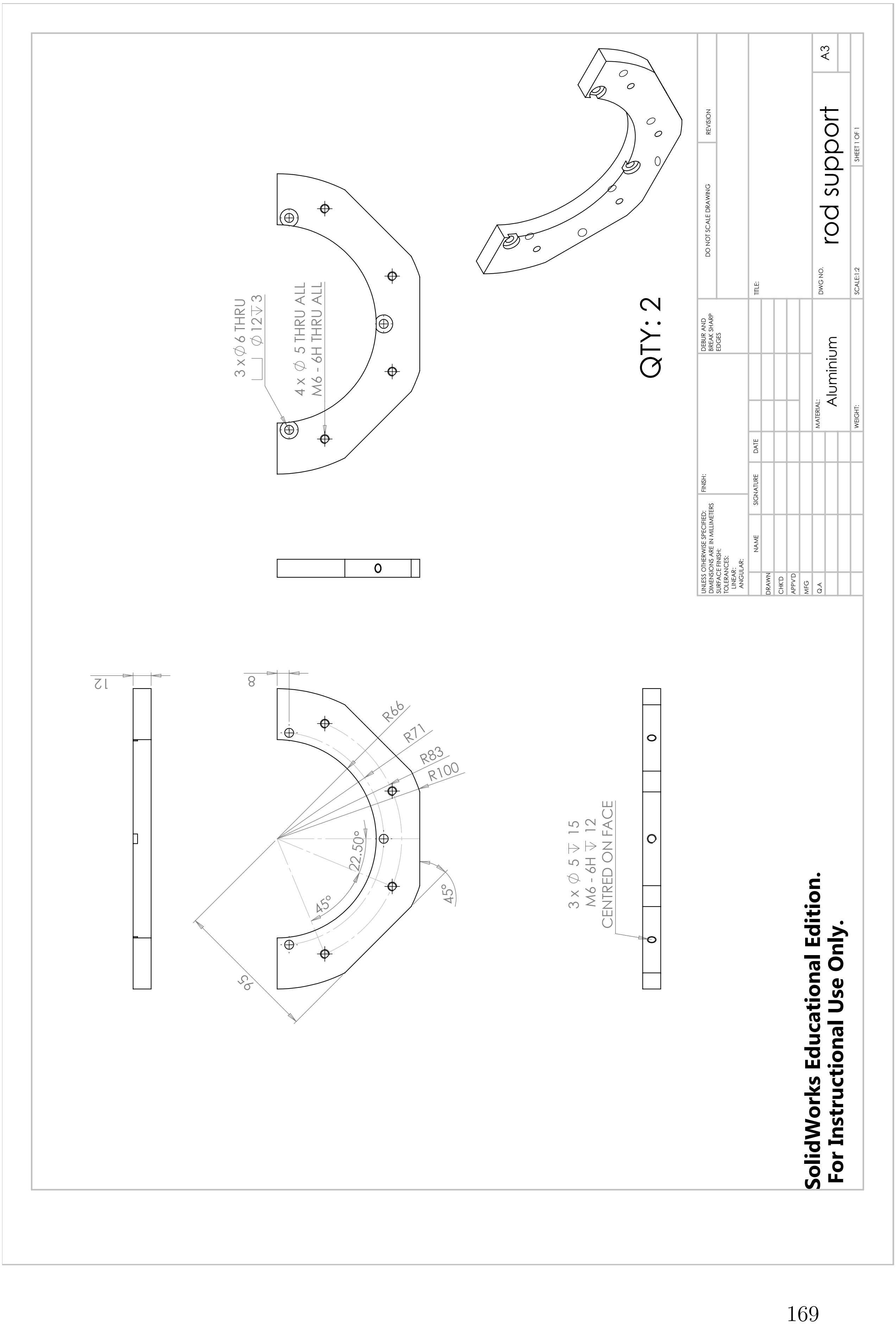

Figure A.9 *Schematic drawing of polarimeter support cradle part*

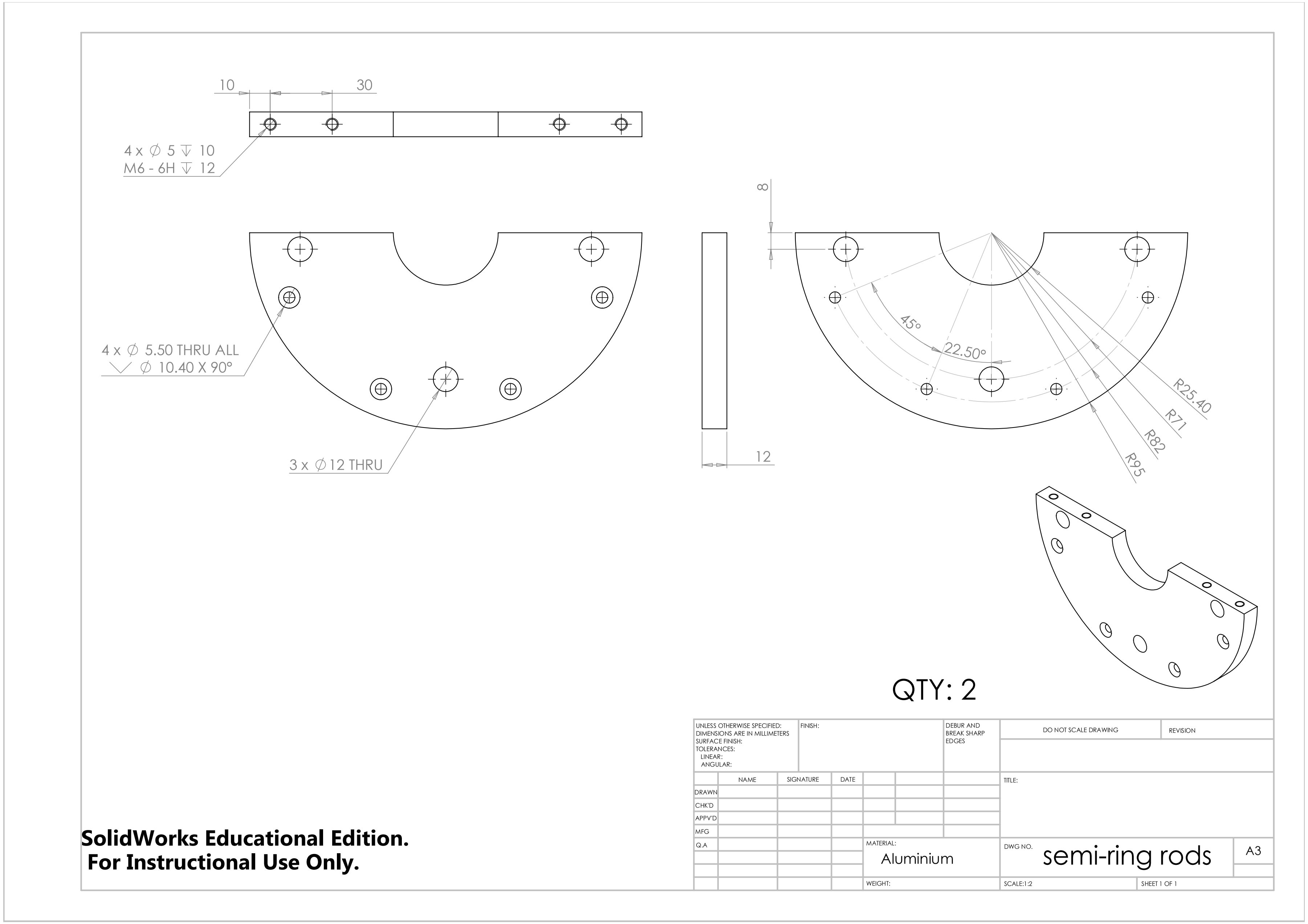

Figure A.10 *Schematic drawing of polarimeter support cradle part*

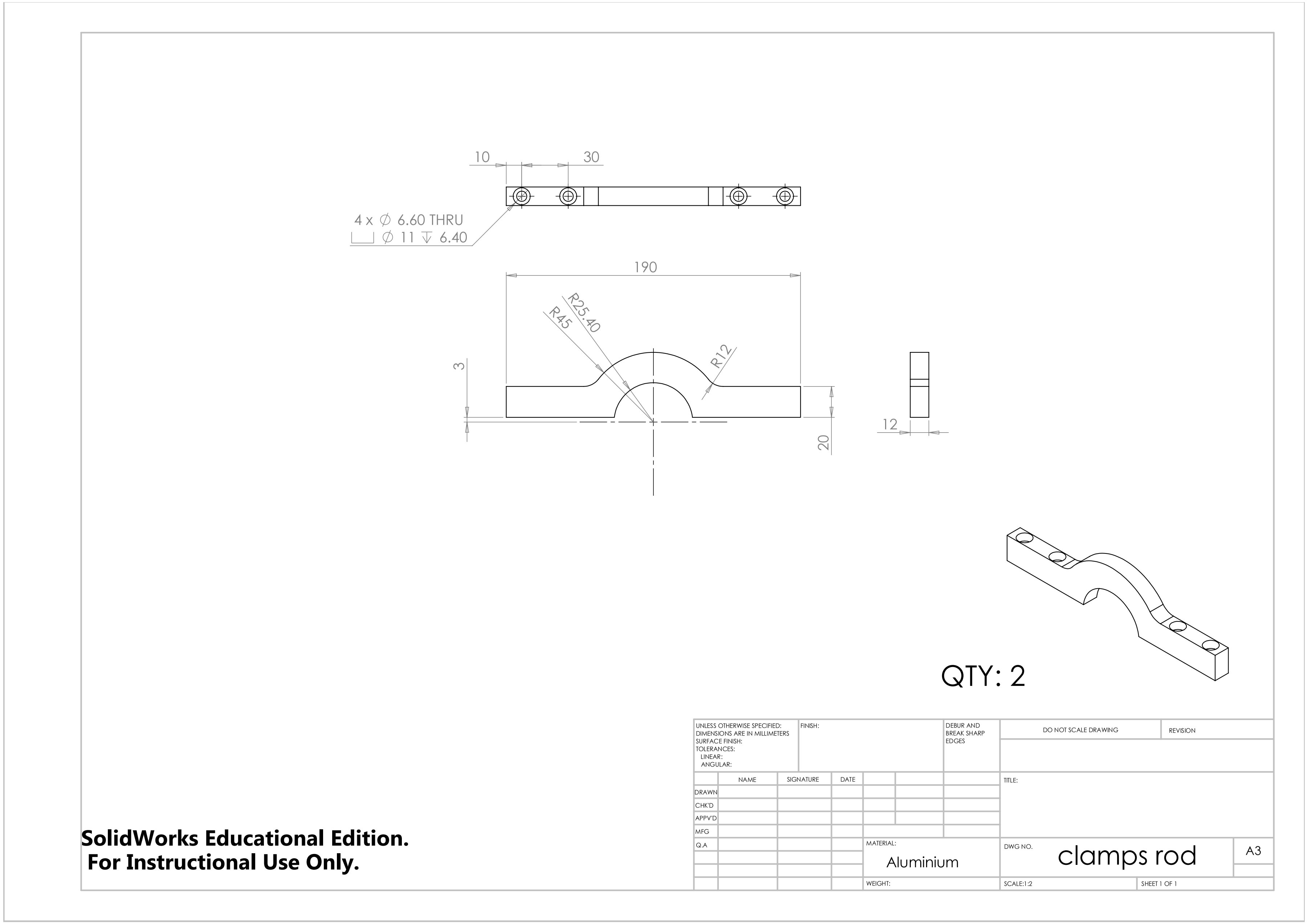

Figure A.11 *Schematic drawing of polarimeter support cradle part, this is the top clamp that fixes the support pipe in place*

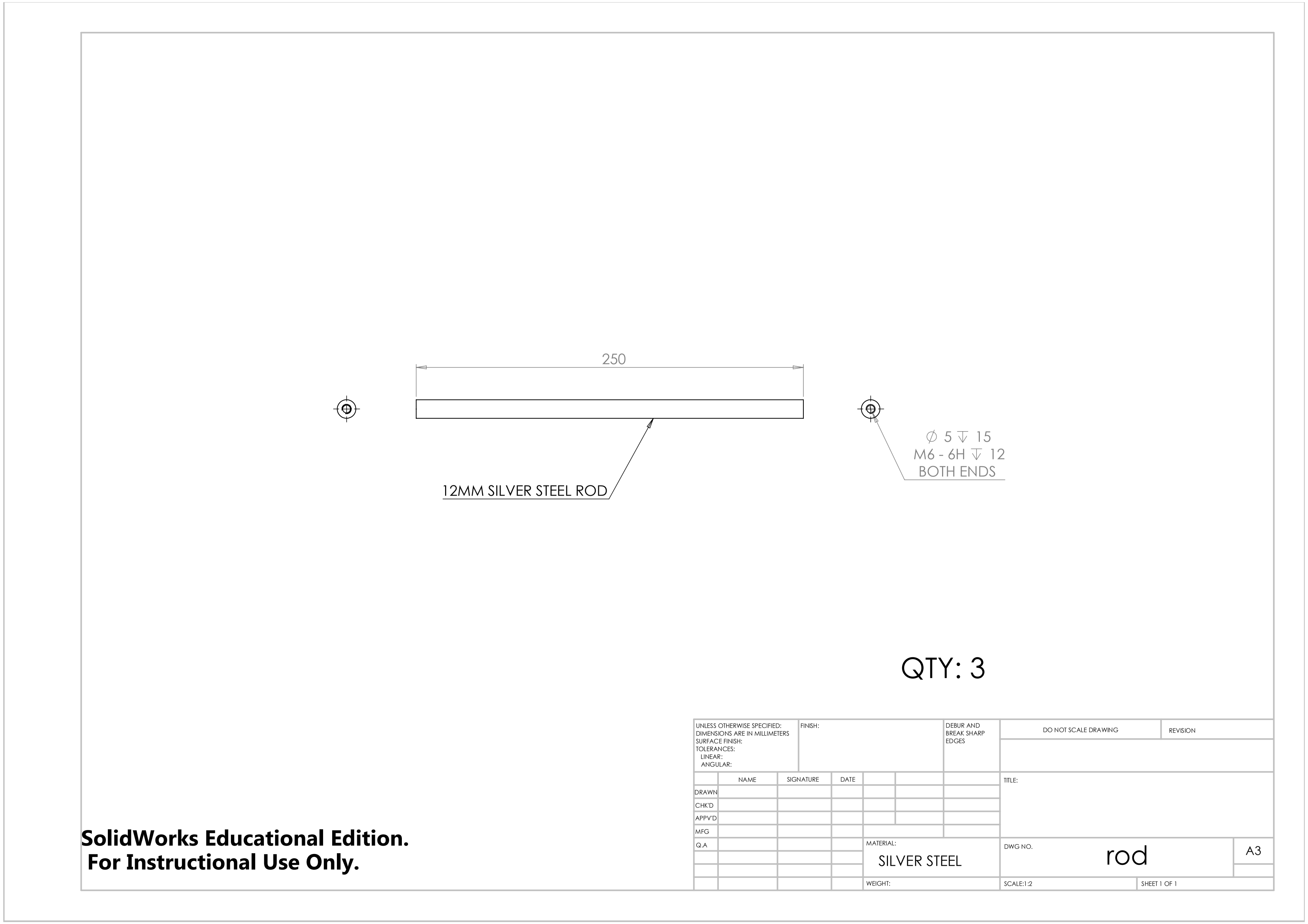

Figure A.12 *Schematic drawing of polarimeter support cradle part, this is the rod that fixes the two sides of the cradle together*

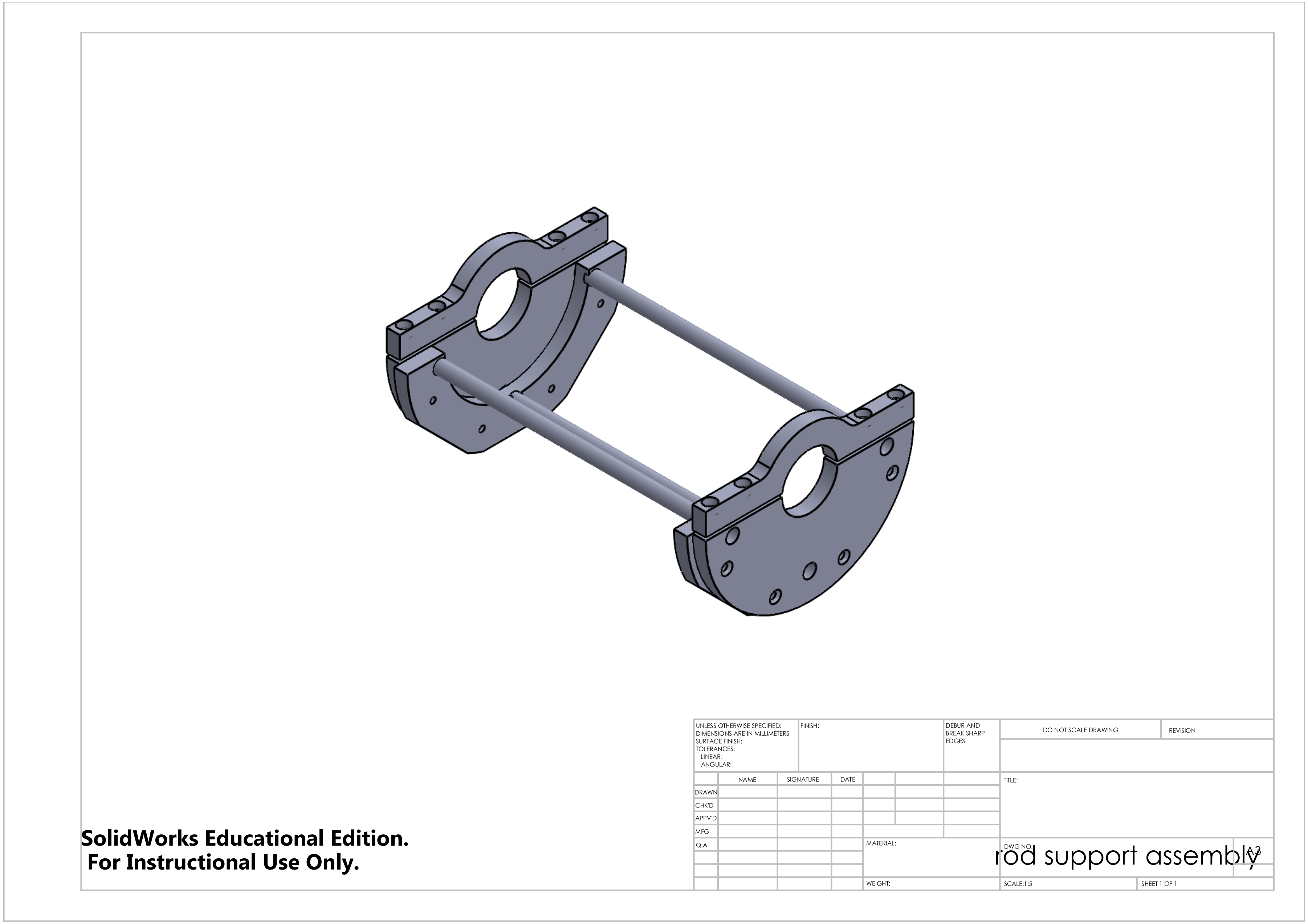

Figure A.13 *Schematic drawing of the completed polarimeter support cradle*

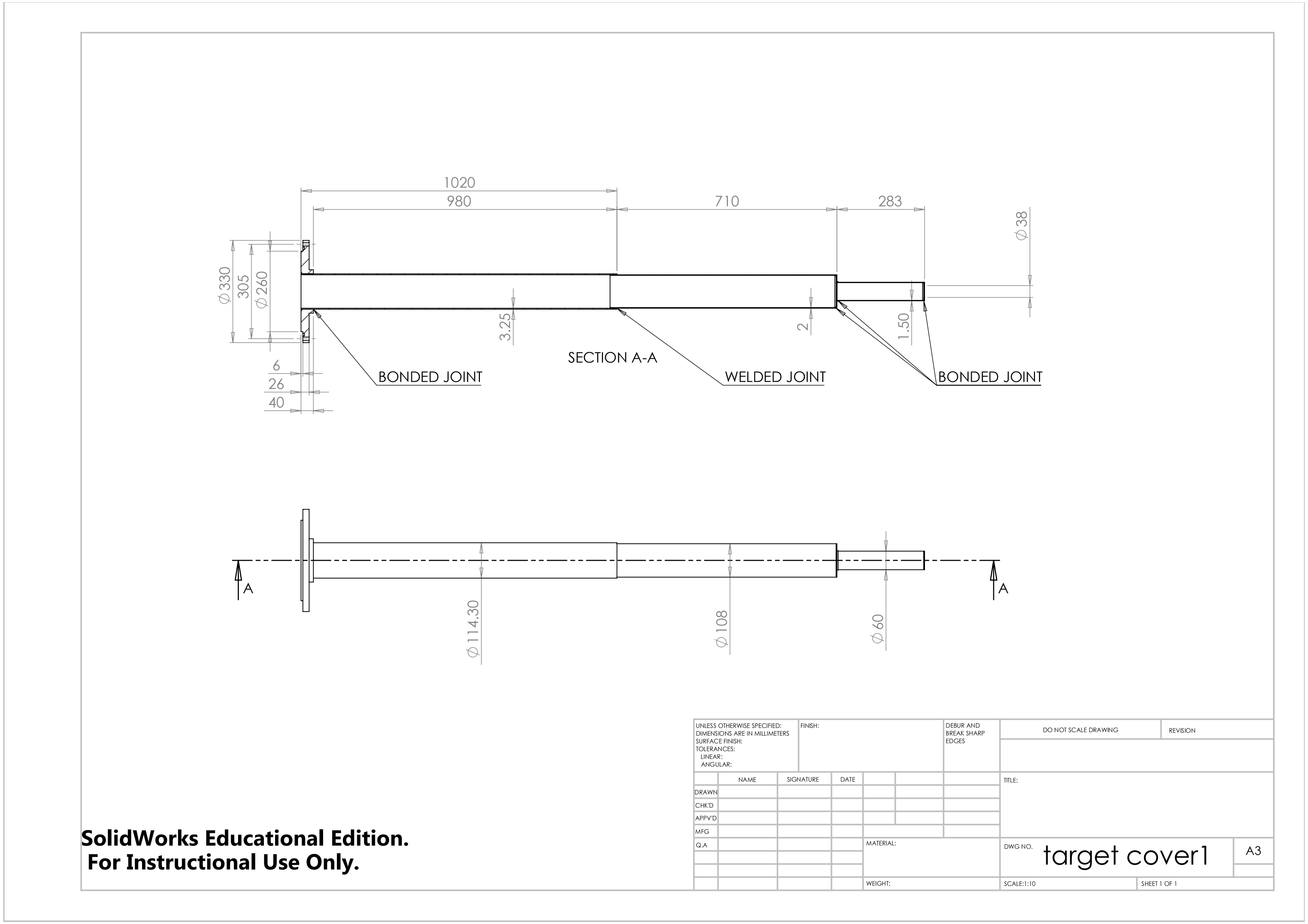

Figure A.14 *Schematic drawing of the new target cover showing the interface flange and the three distinct sections of pipe*

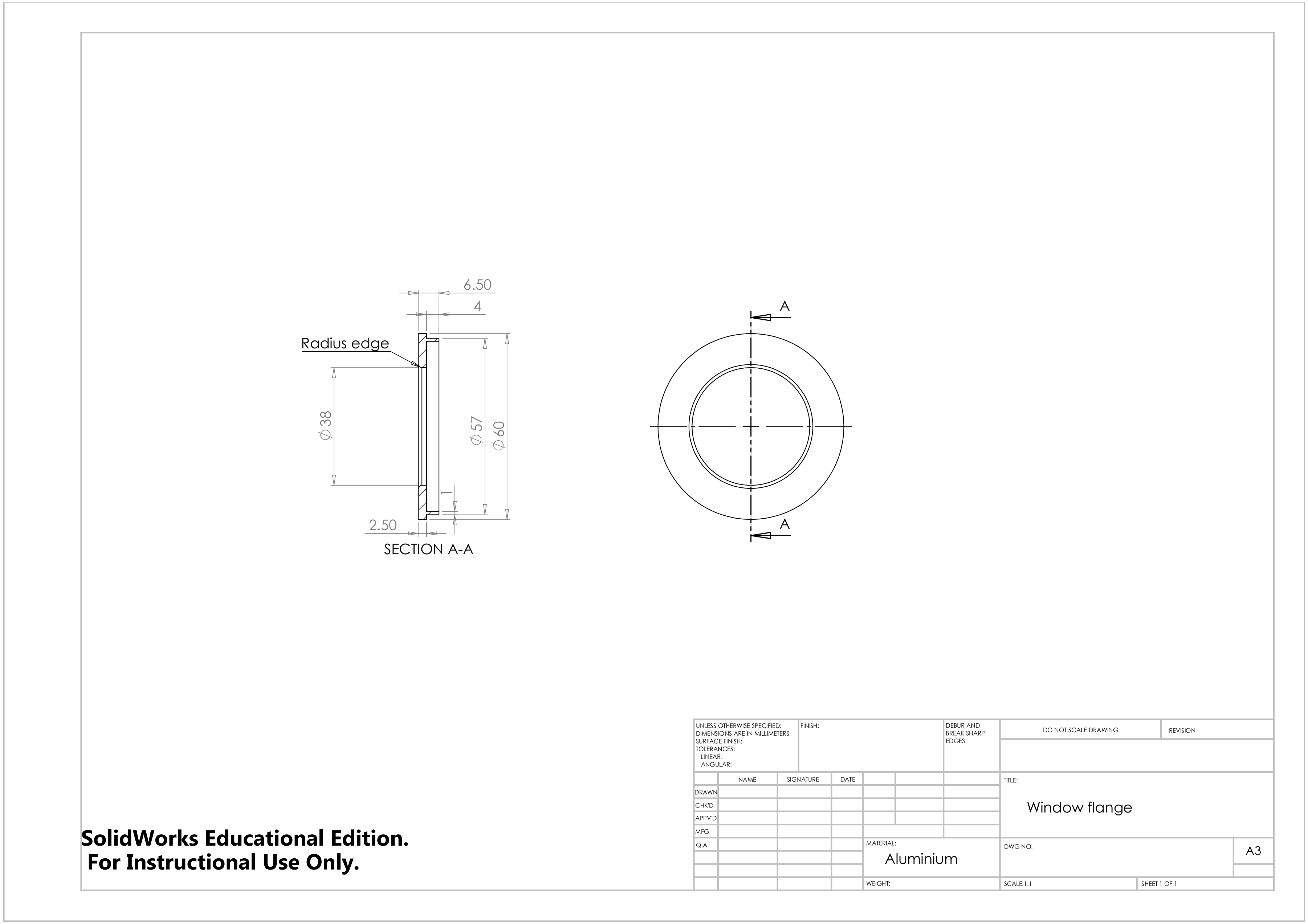

Figure A.15 *Schematic drawing of the window flange for the new target cover.*

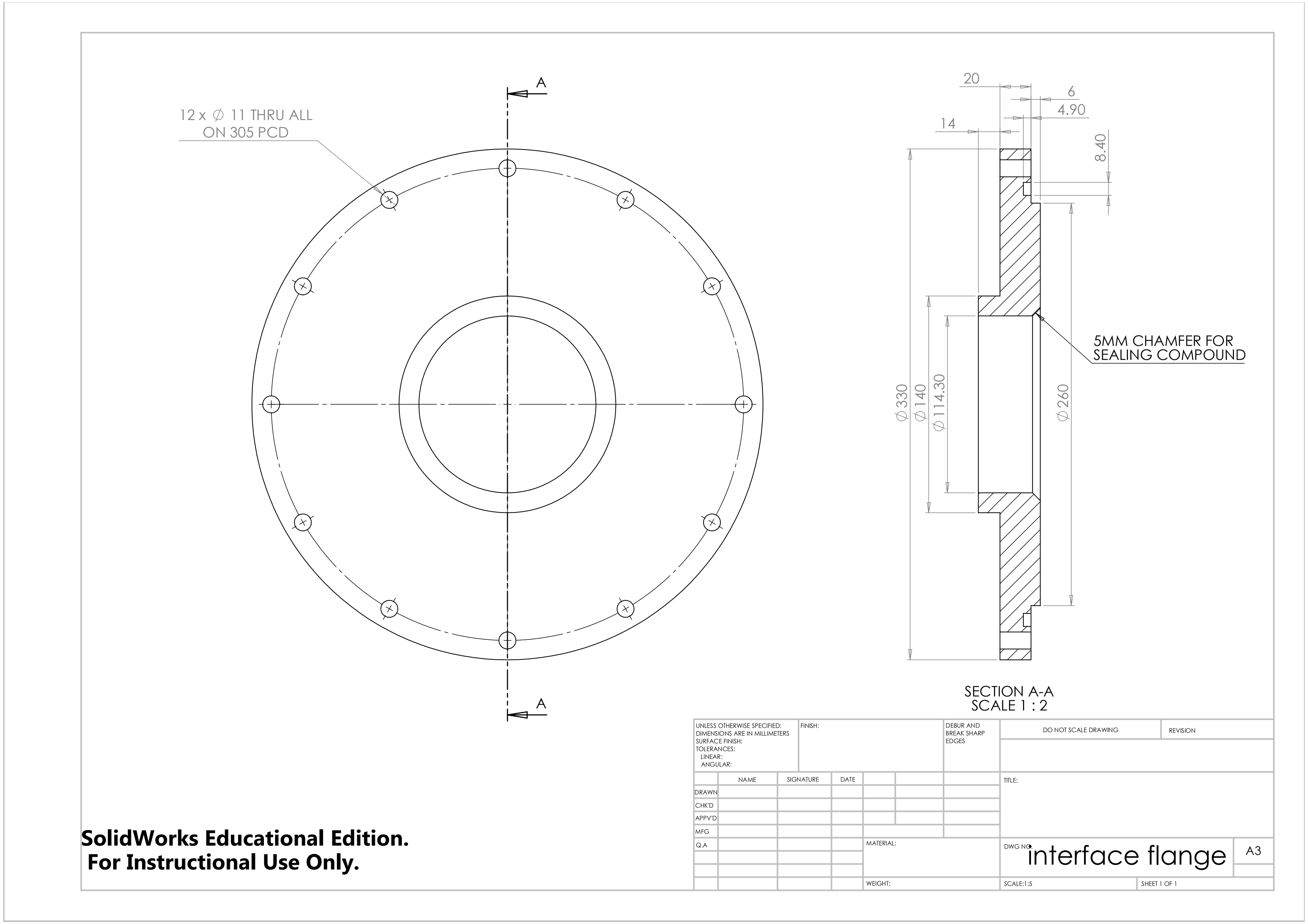

Figure A.16 *Schematic drawing of the interface flange for the new target cover.*

Appendix B

Mandlestam Variables

Processes of two particles going to two particles are often discussed in terms of the Lorentz-invariant Mandlestam variable quantities s, t and u. These quantities are defined via the following relations where $\underline{p}_i$ is the four momenta of particle i,

$$s = (\underline{p}_1 + \underline{p}_2)^2 = (\underline{p}_3 + \underline{p}_4)^2, \tag{B.1}$$

$$t = (\underline{p}_1 - \underline{p}_3)^2 = (\underline{p}_4 - \underline{p}_2)^2, \tag{B.2}$$

$$u = (\underline{p}_1 - \underline{p}_4)^2 = (\underline{p}_3 - \underline{p}_2)^2. \tag{B.3}$$

The sum of the three quantities can be shown to be given by

$$s + t + u = m_1^2 + m_2^2 + m_3^2 + m_4^2. \tag{B.4}$$

s, t and u are also often used to describe reaction channels. These channels correspond to different Feynman diagrams for the scattering process. The exchange particle involved in the process has four momenta squared is equal to the Mandlestam variable corresponding to the channel of the process. Feynman diagrams for the three channels are shown in Figure B.1.

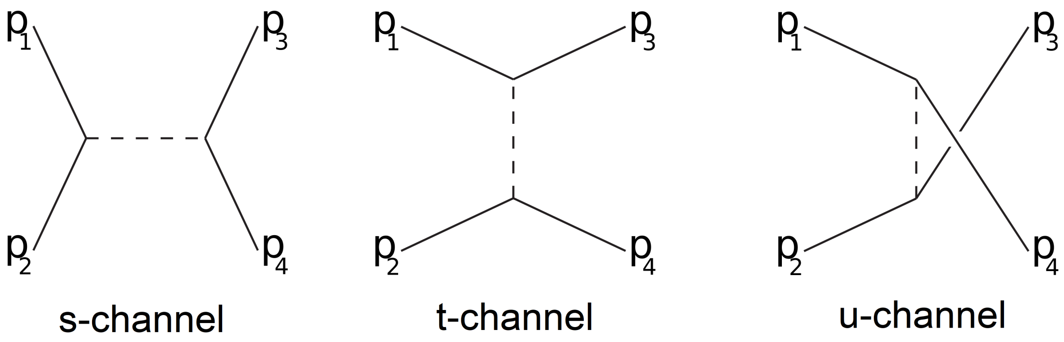

Figure B.1 *Feynman diagrams representing s, t and u channels respectively [161–163].*

Appendix C

Polarisation Observables in γN Reactions

Analytical calculations of s-channel photon nucleon (γN) processes are often discussed in terms of s-channel helicity amplitudes. If we consider γN interactions the γ and N each have two helicity states. As such we have four helicity amplitudes for helicity transitions in the interaction. These four amplitudes correspond to single helicity flipping (S_1 and S_2), double helicity flipping (D) and no helicity flipping (N). These helicity amplitudes relate to a set of transversity amplitudes via the set of relations [164] given by Equations (C.1 - C.4). Note that these transversity amplitudes are complex quantities.

$$b_1 = \frac{1}{2}[(S_1 + S_2) + i(N - D)] \tag{C.1}$$

$$b_2 = \frac{1}{2}[(S_1 + S_2) - i(N - D)] \tag{C.2}$$

$$b_3 = \frac{1}{2}[(S_1 - S_2) - i(N + D)] \tag{C.3}$$

$$b_4 = \frac{1}{2}[(S_1 - S_2) + i(N + D)] \tag{C.4}$$

Taking bilnear combinations of these four transversity amplitudes produces 16 real quantities. These real quantities are measurable and are referred to as polarisation observables. These 16 observables are summarised in Table C.1. Measurements of these observables may require complex combinations of

Table C.1 *Polarisation Observables*

Typical Symbol	Helicity Representation	Transversity Representation	Measurement Needed
σ/t	$\|N\|^2+\|S_1\|^2+\|S_2\|^2+\|D\|^2$	$\|b_1\|^2+\|b_2\|^2+\|b_3\|^2+\|b_4\|^2$	$\{$—;—;—$\}$
Σ	$2\Re(S_1^*S_2 - ND^*)$	$\|b_1\|^2+\|b_2\|^2-\|b_3\|^2-\|b_4\|^2$	$\{L(\frac{\pi}{2},0)$;—;—$\}$ $\{$—$;y';y\}$
T	$2\Im(S_1N^* - S_2D^*)$	$\|b_1\|^2-\|b_2\|^2-\|b_3\|^2+\|b_4\|^2$	$\{$—$;y;$—$\}$ $\{L(\frac{\pi}{2},0)$; —$;y\}$
P	$2\Im(S_2N^* - S_1D^*)$	$\|b_1\|^2-\|b_2\|^2+\|b_3\|^2-\|b_4\|^2$	$\{$—;—$;y\}$ $\{L(\frac{\pi}{2},0);y;$—$\}$
G	$-2\Im(S_1S_2^* + ND^*)$	$2\Im(b_1b_3^* + b_2b_4^*)$	$\{L(\pm\frac{\pi}{4},0);z;$—$\}$
H	$-2\Im(S_1D^* + S_2N^*)$	$-2\Re(b_1b_3^* - b_2b_4^*)$	$\{L(\pm\frac{\pi}{4},0);x;$—$\}$
E	$\|S_2\|^2-\|S_1\|^2-\|D\|^2+\|N\|^2$	$-2\Re(b_1b_3^* + b_2b_4^*)$	$\{c;z;$—$\}$
F	$2\Re(S_2D^* + S_1N^*)$	$2\Im(b_1b_3^* - b_2b_4^*)$	$\{c;x;$—$\}$
O$_x$	$-2\Im(S_2D_2^* + S_1N^*)$	$-2\Re(b_1b_4^* - b_2b_3^*)$	$\{L(\pm\frac{\pi}{4},0)$;—$;x'\}$
O$_z$	$-2\Im(S_2S_1^* + ND^*)$	$-2\Im(b_1b_4^* + b_2b_3^*)$	$\{L(\pm\frac{\pi}{4},0)$;—$;z'\}$
C$_x$	$-2\Re(S_2N^* + S_1D^*)$	$2\Im(b_1b_4^* - b_2b_3^*)$	$\{c;$—$;x'\}$
C$_z$	$\|S_2\|^2-\|S_1\|^2-\|N\|^2+\|D\|^2$	$-2\Re(b_1b_4^* - b_2b_3^*)$	$\{c;$—$;z'\}$
T$_x$	$2\Re(S_1S_2^* + ND^*)$	$2\Re(b_1b_2^* - b_3b_4^*)$	$\{$—$;x;x'\}$
T$_z$	$2\Re(S_1N^* + S_2D^*)$	$2\Im(b_1b_2^* - b_3b_4^*)$	$\{$—$;x;z'\}$
L$_x$	$2\Re(S_2N^* - S_1D^*)$	$2\Im(b_1b_2^* + b_3b_4^*)$	$\{$—$;z;x'\}$
L$_Z$	$\|S_1\|^2+\|S_2\|^2-\|N\|^2-\|D\|^2$	$2\Re(b_1b_2^* - b_3b_4^*)$	$\{$—$;z;z'\}$

Modified format from [164].
Notation in the "Measurement Needed" column is $\{P_\gamma$, P$_T$, P$_R\}$ where:
P_γ = Beam Polarisation, L (θ) = linearly polarised at θ to scattering plane, C = circularly polarised
P$_T$ = Direction of target polarisation
P$_R$ = Direction of recoil polarisation measured

polarised beams and targets or the study of recoil particle polarisations.

Appendix D

PID Light Attenuation Constants

Values for the PID-III light attenuation constants are included in Tables D.1 and D.2.

Table D.1 *Light Attenuation constant values for the PID-III elements as a function of the distance along the element in mm (Part I)*

Element #	Light Attenuation Constant at Distance D/mm															
	0	10	20	30	40	50	60	70	80	90	100	110	120	130	140	150
1	2.17	1.98	1.81	1.66	1.52	1.40	1.29	1.20	1.11	1.04	0.97	0.91	0.86	0.81	0.77	0.73
2	2.08	2.58	2.32	2.08	1.88	1.69	1.53	1.38	1.25	1.14	1.03	0.94	0.86	0.79	0.72	0.67
3	1.61	1.46	1.34	1.23	1.13	1.05	0.97	0.91	0.85	0.80	0.75	0.71	0.68	0.65	0.62	0.60
4	1.43	1.32	1.23	1.14	1.07	1.01	0.95	0.90	0.86	0.82	0.78	0.75	0.73	0.70	0.68	0.67
5	3.47	3.06	2.71	2.40	2.13	1.90	1.70	1.53	1.38	1.25	1.14	1.04	0.96	0.89	0.82	0.77
6	1.62	1.46	1.32	1.21	1.11	1.03	0.96	0.90	0.85	0.81	0.77	0.74	0.72	0.70	0.68	0.67
7	2.18	1.95	1.75	1.59	1.44	1.31	1.20	1.11	1.03	0.96	0.90	0.84	0.80	0.76	0.73	0.70
8	1.62	1.51	1.40	1.31	1.23	1.15	1.08	1.02	0.96	0.91	0.87	0.83	0.79	0.76	0.73	0.70
9	2.69	2.42	2.19	1.98	1.80	1.63	1.48	1.35	1.24	1.13	1.04	0.96	0.88	0.82	0.76	0.71
10	2.09	1.88	1.70	1.54	1.40	1.28	1.17	1.08	1.00	0.93	0.87	0.82	0.78	0.74	0.70	0.67
11	2.32	2.15	1.99	1.85	1.71	1.59	1.48	1.37	1.27	1.18	1.10	1.02	0.95	0.88	0.82	0.76
12	1.71	1.57	1.45	1.35	1.25	1.16	1.09	1.02	0.96	0.91	0.86	0.81	0.77	0.74	0.71	0.68
13	1.70	1.55	1.42	1.30	1.20	1.11	1.03	0.96	0.91	0.85	0.81	0.77	0.73	0.70	0.68	0.66
14	1.61	1.46	1.34	1.23	1.13	1.05	0.98	0.92	0.87	0.82	0.78	0.75	0.72	0.69	0.67	0.65
15	1.31	1.21	1.13	1.06	1.00	0.94	0.89	0.85	0.81	0.77	0.75	0.72	0.70	0.68	0.66	0.64
16	1.97	1.83	1.70	1.58	1.47	1.37	1.28	1.19	1.11	1.04	0.97	0.91	0.85	0.79	0.74	0.70
17	1.45	1.33	1.22	1.13	1.05	0.98	0.92	0.87	0.83	0.79	0.76	0.73	0.70	0.68	0.66	0.65
18	1.31	1.21	1.12	1.04	0.97	0.92	0.87	0.82	0.79	0.75	0.73	0.70	0.68	0.67	0.65	0.64
19	1.27	1.17	1.08	1.01	0.94	0.89	0.84	0.80	0.76	0.73	0.70	0.68	0.66	0.64	0.63	0.62
20	1.41	1.26	1.14	1.03	0.95	0.88	0.83	0.78	0.74	0.71	0.69	0.67	0.65	0.64	0.63	0.62
21	1.57	1.44	1.33	1.23	1.14	1.06	0.99	0.92	0.87	0.82	0.78	0.74	0.71	0.68	0.65	0.63
22	2.17	1.97	1.79	1.63	1.49	1.36	1.24	1.14	1.05	0.97	0.89	0.83	0.77	0.72	0.67	0.63
23	1.68	1.56	1.45	1.35	1.26	1.18	1.11	1.04	0.98	0.93	0.88	0.84	0.80	0.77	0.74	0.71
24	1.46	1.34	1.23	1.14	1.06	0.98	0.92	0.87	0.82	0.78	0.74	0.71	0.69	0.66	0.64	0.62

Table D.2 *Light Attenuation constant values for the PID-III elements as a function of the distance along the element in mm (Part II)*

Element #	Light Attenuation Constant at Distance D/mm														
	160	170	180	190	200	210	220	230	240	250	260	270	280	290	300
1	0.70	0.67	0.64	0.62	0.60	0.58	0.56	0.55	0.54	0.52	0.51	0.50	0.50	0.49	0.48
2	0.62	0.57	0.53	0.49	0.46	0.43	0.41	0.39	0.37	0.35	0.33	0.32	0.31	0.29	0.28
3	0.58	0.56	0.55	0.54	0.52	0.51	0.50	0.50	0.49	0.48	0.48	0.47	0.47	0.46	0.46
4	0.65	0.64	0.62	0.61	0.60	0.60	0.59	0.58	0.58	0.57	0.57	0.56	0.56	0.56	0.55
5	0.72	0.68	0.65	0.62	0.59	0.57	0.55	0.53	0.52	0.50	0.49	0.48	0.47	0.47	0.46
6	0.65	0.64	0.64	0.63	0.62	0.62	0.61	0.61	0.61	0.60	0.60	0.60	0.60	0.60	0.59
7	0.67	0.65	0.63	0.62	0.60	0.59	0.58	0.57	0.56	0.56	0.55	0.54	0.54	0.54	0.53
8	0.67	0.65	0.63	0.62	0.60	0.58	0.57	0.56	0.55	0.54	0.53	0.52	0.52	0.51	0.50
9	0.66	0.62	0.59	0.55	0.53	0.50	0.48	0.46	0.44	0.42	0.41	0.39	0.38	0.37	0.36
10	0.64	0.62	0.60	0.58	0.57	0.56	0.54	0.53	0.53	0.52	0.51	0.51	0.50	0.50	0.49
11	0.71	0.66	0.61	0.57	0.53	0.50	0.47	0.44	0.41	0.38	0.36	0.33	0.31	0.29	0.28
12	0.66	0.64	0.62	0.60	0.58	0.57	0.56	0.55	0.54	0.53	0.52	0.51	0.51	0.50	0.50
13	0.64	0.62	0.60	0.59	0.58	0.57	0.56	0.55	0.54	0.54	0.53	0.53	0.53	0.52	0.52
14	0.63	0.62	0.61	0.60	0.59	0.58	0.57	0.56	0.56	0.55	0.55	0.55	0.54	0.54	0.54
15	0.63	0.62	0.61	0.60	0.59	0.58	0.57	0.57	0.56	0.56	0.55	0.55	0.55	0.55	0.54
16	0.66	0.62	0.58	0.55	0.52	0.49	0.46	0.44	0.41	0.39	0.37	0.35	0.34	0.32	0.31
17	0.63	0.62	0.61	0.60	0.60	0.59	0.58	0.58	0.58	0.57	0.57	0.57	0.56	0.56	0.56
18	0.63	0.62	0.61	0.60	0.59	0.59	0.58	0.58	0.58	0.57	0.57	0.57	0.57	0.57	0.56
19	0.61	0.60	0.59	0.58	0.57	0.57	0.56	0.56	0.56	0.55	0.55	0.55	0.55	0.55	0.54
20	0.61	0.60	0.60	0.59	0.59	0.59	0.58	0.58	0.58	0.58	0.58	0.58	0.58	0.58	0.58
21	0.61	0.59	0.58	0.56	0.55	0.54	0.53	0.52	0.51	0.51	0.50	0.50	0.49	0.49	0.48
22	0.59	0.56	0.53	0.50	0.47	0.45	0.43	0.42	0.40	0.39	0.37	0.36	0.35	0.34	0.34
23	0.69	0.66	0.64	0.63	0.61	0.59	0.58	0.57	0.56	0.55	0.54	0.53	0.53	0.52	0.51
24	0.61	0.59	0.58	0.57	0.56	0.56	0.55	0.54	0.54	0.53	0.53	0.53	0.52	0.52	0.52

Appendix E

Tabulated Results

Values for the observables Σ and $C_{x'}$ obtained in the experiment outlined in this thesis are tabulated in this Appendix for completeness.

E.1 Σ Results

The results for Σ obtained from the analysis of the unscattered data with the 2σ missing mass cut applied are tabulated in Tables E.1 - E.3. The photon energy point listed, E_γ, refers to the centre of the 10 MeV wide energy bins used. Similarly, the $\cos\theta_{\mathrm{CM}}$ point refers to the centre of the angular bin, each angular bin has a width of 0.1. Errors quoted are statistical errors. Note that as discussed in the main text the 555 MeV point is empty due to a dead tagger channel at this point.

Table E.1 Σ *values for the reaction* $\gamma d \rightarrow np$ *at the specified* $\cos\theta_{\mathrm{CM}}$ *points (Part I)*

E_γ/MeV	$\cos\theta_{\mathrm{CM}}$					
	0.85	0.75	0.65	0.55	0.45	0.35
415	0.147 ± 0.126	0.017 ± 0.114	0.143 ± 0.113	-0.008 ± 0.110	-0.346 ± 0.107	-0.418 ± 0.104
425	0.209 ± 0.120	-0.149 ± 0.110	0.073 ± 0.107	-0.119 ± 0.102	-0.245 ± 0.101	-0.247 ± 0.098
435	0.123 ± 0.114	0.038 ± 0.101	-0.120 ± 0.100	-0.081 ± 0.096	-0.262 ± 0.095	-0.307 ± 0.091
445	0.292 ± 0.098	0.088 ± 0.091	-0.109 ± 0.087	-0.213 ± 0.086	-0.166 ± 0.084	-0.279 ± 0.080
455	0.093 ± 0.103	0.027 ± 0.096	0.169 ± 0.094	-0.145 ± 0.091	0.011 ± 0.089	0.005 ± 0.085
465	-0.040 ± 0.106	0.109 ± 0.097	-0.136 ± 0.094	-0.093 ± 0.091	-0.028 ± 0.090	0.064 ± 0.086
475	0.120 ± 0.082	0.024 ± 0.073	0.047 ± 0.073	-0.096 ± 0.070	-0.173 ± 0.069	-0.078 ± 0.066
485	0.138 ± 0.096	0.189 ± 0.087	0.106 ± 0.084	0.026 ± 0.082	-0.314 ± 0.080	-0.122 ± 0.078
495	0.042 ± 0.104	0.001 ± 0.091	-0.013 ± 0.091	-0.139 ± 0.088	0.017 ± 0.085	-0.067 ± 0.084
505	0.069 ± 0.082	0.071 ± 0.077	0.017 ± 0.076	-0.049 ± 0.072	-0.131 ± 0.070	-0.057 ± 0.069
515	0.259 ± 0.076	0.207 ± 0.070	0.222 ± 0.071	-0.002 ± 0.066	0.041 ± 0.066	-0.114 ± 0.065
525	0.245 ± 0.082	0.119 ± 0.075	0.041 ± 0.077	0.043 ± 0.073	-0.090 ± 0.071	-0.068 ± 0.072
535	0.106 ± 0.084	0.154 ± 0.078	-0.115 ± 0.078	0.121 ± 0.078	-0.126 ± 0.077	0.034 ± 0.074
545	0.031 ± 0.068	0.085 ± 0.062	0.091 ± 0.062	0.055 ± 0.060	-0.000 ± 0.058	0.100 ± 0.058
555	N/a	N/a	N/a	N/a	N/a	N/a
565	0.071 ± 0.069	0.123 ± 0.064	0.102 ± 0.065	0.159 ± 0.063	0.072 ± 0.062	0.092 ± 0.062
575	0.031 ± 0.074	0.194 ± 0.070	0.200 ± 0.069	0.036 ± 0.068	0.035 ± 0.067	0.070 ± 0.064
585	-0.008 ± 0.059	0.139 ± 0.054	0.142 ± 0.055	0.103 ± 0.054	0.175 ± 0.052	0.110 ± 0.052
595	0.273 ± 0.067	0.132 ± 0.063	0.152 ± 0.064	0.241 ± 0.063	0.094 ± 0.058	0.235 ± 0.059
605	0.270 ± 0.062	0.197 ± 0.058	0.183 ± 0.059	0.184 ± 0.060	0.125 ± 0.059	0.090 ± 0.056
615	0.219 ± 0.060	0.243 ± 0.057	0.260 ± 0.057	0.147 ± 0.058	0.257 ± 0.057	0.339 ± 0.053

Table E.2 *Σ values for the reaction $\gamma d \rightarrow np$ at the specified $\cos\theta_{\mathrm{CM}}$ points (Part II)*

E_γ/MeV	$\cos\theta_{\mathrm{CM}}$					
	0.25	0.15	0.05	-0.05	-0.15	-0.25
415	-0.332 ± 0.102	-0.172 ± 0.096	-0.576 ± 0.098	-0.055 ± 0.099	0.003 ± 0.098	-0.609 ± 0.102
425	-0.451 ± 0.098	-0.375 ± 0.090	-0.265 ± 0.091	-0.266 ± 0.093	-0.539 ± 0.093	-0.442 ± 0.094
435	-0.322 ± 0.093	-0.204 ± 0.085	-0.174 ± 0.085	-0.322 ± 0.087	-0.355 ± 0.087	-0.397 ± 0.091
445	-0.270 ± 0.081	-0.083 ± 0.075	-0.273 ± 0.074	-0.137 ± 0.075	-0.195 ± 0.076	-0.206 ± 0.079
455	-0.380 ± 0.088	0.121 ± 0.082	-0.255 ± 0.080	-0.334 ± 0.082	-0.244 ± 0.083	-0.283 ± 0.087
465	-0.003 ± 0.086	-0.336 ± 0.080	-0.260 ± 0.078	-0.191 ± 0.082	-0.251 ± 0.083	-0.422 ± 0.087
475	-0.089 ± 0.066	-0.086 ± 0.061	-0.171 ± 0.060	-0.171 ± 0.063	-0.334 ± 0.063	-0.255 ± 0.067
485	-0.039 ± 0.076	-0.244 ± 0.073	-0.216 ± 0.070	-0.193 ± 0.072	-0.381 ± 0.074	-0.191 ± 0.078
495	-0.151 ± 0.082	-0.099 ± 0.078	-0.108 ± 0.074	-0.146 ± 0.076	-0.283 ± 0.077	-0.165 ± 0.085
505	0.008 ± 0.066	-0.138 ± 0.064	-0.206 ± 0.061	-0.279 ± 0.062	-0.172 ± 0.064	-0.188 ± 0.068
515	-0.109 ± 0.061	-0.063 ± 0.060	-0.166 ± 0.057	-0.141 ± 0.056	-0.104 ± 0.061	-0.203 ± 0.062
525	-0.005 ± 0.066	-0.043 ± 0.066	-0.081 ± 0.062	0.080 ± 0.062	-0.053 ± 0.064	-0.394 ± 0.069
535	0.014 ± 0.070	-0.187 ± 0.068	0.064 ± 0.064	-0.006 ± 0.064	-0.110 ± 0.066	-0.038 ± 0.070
545	-0.021 ± 0.053	0.036 ± 0.054	0.010 ± 0.051	-0.065 ± 0.049	-0.005 ± 0.050	0.064 ± 0.055
555	N/a	N/a	N/a	N/a	N/a	N/a
565	0.148 ± 0.057	0.028 ± 0.057	-0.004 ± 0.054	0.010 ± 0.052	0.037 ± 0.052	-0.014 ± 0.057
575	0.118 ± 0.061	0.033 ± 0.060	0.034 ± 0.057	0.125 ± 0.054	-0.003 ± 0.054	0.096 ± 0.059
585	0.119 ± 0.048	0.053 ± 0.047	-0.074 ± 0.046	0.019 ± 0.043	-0.009 ± 0.044	-0.029 ± 0.047
595	0.208 ± 0.058	0.165 ± 0.054	0.151 ± 0.053	0.116 ± 0.050	0.102 ± 0.050	-0.010 ± 0.054
605	0.174 ± 0.055	0.023 ± 0.052	0.286 ± 0.051	0.047 ± 0.048	0.060 ± 0.048	-0.035 ± 0.050
615	0.230 ± 0.053	0.181 ± 0.050	0.098 ± 0.049	0.188 ± 0.049	0.088 ± 0.046	0.215 ± 0.049

Table E.3 *Σ values for the reaction $\gamma d \rightarrow np$ at the specified $\cos\theta_{\mathrm{CM}}$ points (Part III)*

E_γ/MeV	$\cos\theta_{\mathrm{CM}}$					
	-0.35	-0.45	-0.55	-0.65	-0.75	-0.8
415	-0.021 ± 0.104	-0.283 ± 0.095	-0.211 ± 0.095	-0.408 ± 0.098	0.020 ± 0.109	0.148 ± 0.166
425	-0.354 ± 0.098	-0.209 ± 0.091	-0.378 ± 0.091	-0.177 ± 0.092	-0.286 ± 0.103	-0.060 ± 0.152
435	-0.186 ± 0.090	-0.344 ± 0.085	-0.483 ± 0.082	-0.224 ± 0.086	-0.337 ± 0.093	-0.629 ± 0.134
445	-0.486 ± 0.079	-0.343 ± 0.076	-0.419 ± 0.072	-0.238 ± 0.075	-0.165 ± 0.081	-0.460 ± 0.114
455	-0.268 ± 0.084	-0.321 ± 0.084	-0.216 ± 0.078	-0.300 ± 0.082	-0.325 ± 0.088	-0.381 ± 0.122
465	-0.408 ± 0.084	-0.365 ± 0.082	-0.451 ± 0.076	-0.284 ± 0.079	-0.203 ± 0.088	-0.332 ± 0.117
475	-0.096 ± 0.064	-0.260 ± 0.062	-0.367 ± 0.059	-0.144 ± 0.060	-0.274 ± 0.066	-0.265 ± 0.085
485	-0.175 ± 0.074	-0.335 ± 0.072	-0.131 ± 0.067	-0.387 ± 0.070	-0.208 ± 0.074	-0.199 ± 0.097
495	-0.210 ± 0.079	-0.406 ± 0.076	-0.260 ± 0.071	-0.313 ± 0.073	-0.122 ± 0.078	0.060 ± 0.104
505	-0.202 ± 0.065	-0.218 ± 0.063	-0.080 ± 0.059	-0.437 ± 0.062	-0.208 ± 0.065	0.037 ± 0.087
515	0.145 ± 0.060	-0.160 ± 0.057	-0.269 ± 0.055	-0.337 ± 0.055	-0.155 ± 0.058	-0.291 ± 0.075
525	-0.005 ± 0.067	-0.066 ± 0.061	-0.084 ± 0.059	-0.122 ± 0.058	-0.141 ± 0.064	-0.284 ± 0.082
535	-0.222 ± 0.070	-0.210 ± 0.065	-0.119 ± 0.061	-0.035 ± 0.060	-0.001 ± 0.064	0.167 ± 0.085
545	0.020 ± 0.054	-0.145 ± 0.048	-0.035 ± 0.047	-0.159 ± 0.046	-0.192 ± 0.049	-0.234 ± 0.063
555	N/a	N/a	N/a	N/a	N/a	N/a
565	0.022 ± 0.059	-0.178 ± 0.052	-0.058 ± 0.051	0.083 ± 0.048	-0.065 ± 0.052	-0.116 ± 0.064
575	-0.092 ± 0.060	0.100 ± 0.054	-0.152 ± 0.053	-0.106 ± 0.050	-0.150 ± 0.053	-0.149 ± 0.068
585	-0.036 ± 0.049	-0.099 ± 0.043	-0.052 ± 0.041	-0.133 ± 0.039	-0.148 ± 0.042	-0.128 ± 0.053
595	-0.030 ± 0.055	0.002 ± 0.050	-0.231 ± 0.049	-0.050 ± 0.046	-0.259 ± 0.048	-0.030 ± 0.060
605	-0.042 ± 0.054	0.085 ± 0.048	-0.026 ± 0.046	0.012 ± 0.044	-0.177 ± 0.046	0.005 ± 0.058
615	0.077 ± 0.051	0.014 ± 0.045	-0.098 ± 0.044	0.021 ± 0.042	-0.000 ± 0.043	0.035 ± 0.056

E.2 $C_{x'}$ Results

The results for $C_{x'}$ obtained from the analysis of the scattered data with three and five $\cos\theta_{\mathrm{CM}}$ bins are tabulated in Tables E.4 and E.5 respectively. The photon energy point listed, E_γ, refers to the centre of the 100 MeV wide energy bins used. Similarly, the $\cos\theta$CM point refers to the centre of the angular bin. Errors quoted are statistical errors.

Table E.4 *$C_{x'}$ values for the reaction $\gamma d \rightarrow np$ at the specified $\cos\theta_{\mathrm{CM}}$ points. Values of p_y are fixed as those listed in the table to extract $C_{x'}$ as described in the main body of the Thesis.*

E_γ/MeV	$\cos\theta_{\mathrm{CM}}$					
	$\frac{2}{3}$		0		$-\frac{2}{3}$	
	p_y	$C_{x'}$	p_y	$C_{x'}$	p_y	$C_{x'}$
250 ± 50	0	1.243 ± 3.780	0	-2.181 ± 1.115	0	0.653 ± 1.532
350 ± 50	0	-1.252 ± 1.167	0	-0.498 ± 0.484	0	-0.633 ± 0.492
450 ± 50	0	2.176 ± 0.827	0	0.587 ± 0.433	0	-0.103 ± 0.389
550 ± 50	0	0.707 ± 0.861	0	-1.262 ± 0.544	0	0.030 ± 0.435
650 ± 50	0	1.335 ± 0.926	0	0.191 ± 0.653	0	1.566 ± 0.525
750 ± 50	0	-1.996 ± 1.293	0	0.406 ± 0.821	0	-0.689 ± 0.587
850 ± 50	0	1.457 ± 1.291	0	1.475 ± 0.942	0	1.017 ± 0.486
950 ± 50	0	1.075 ± 1.400	0	-1.734 ± 1.029	0	-0.892 ± 0.561
250 ± 50	-0.027	1.218 ± 3.772	-0.075	-2.164 ± 1.110	-0.113	0.403 ± 1.517
350 ± 50	-0.017	-1.236 ± 1.166	-0.031	-0.489 ± 0.484	-0.039	-0.620 ± 0.491
450 ± 50	0.006	2.172 ± 0.828	0.009	0.586 ± 0.433	0.01	-0.104 ± 0.389
550 ± 50	0.078	0.668 ± 0.863	0.097	-1.293 ± 0.544	0.104	0.045 ± 0.433
650 ± 50	0.042	1.382 ± 0.929	0.046	0.193 ± 0.654	0.051	1.567 ± 0.524
750 ± 50	0.095	-1.849 ± 1.306	0.102	0.363 ± 0.821	0.13	-0.726 ± 0.580
850 ± 50	0.264	1.565 ± 1.317	0.267	1.247 ± 0.921	0.428	0.912 ± 0.438
950 ± 50	0.593	0.770 ± 1.221	0.644	-0.930 ± 0.881	0.914	-0.238 ± 0.261
250 ± 50	-1	1.264 ± 3.786	-1	-2.185 ± 1.115	1	0.428 ± 1.519
350 ± 50	-1	-1.301 ± 1.170	-1	-0.520 ± 0.484	-1	-0.672 ± 0.491
450 ± 50	1	2.222 ± 0.819	1	0.594 ± 0.427	-1	-0.116 ± 0.386
550 ± 50	-1	0.647 ± 0.863	1	-1.194 ± 0.536	-1	0.054 ± 0.431
650 ± 50	-1	1.471 ± 0.931	-1	0.200 ± 0.652	-1	1.558 ± 0.519
750 ± 50	1	-2.149 ± 1.253	-1	0.339 ± 0.818	1	-0.619 ± 0.583
850 ± 50	-1	1.540 ± 1.316	1	1.537 ± 0.927	-0.756	0.994 ± 0.514
950 ± 50	1	1.208 ± 1.377	-1	-1.628 ± 1.029	-0.57	-0.879 ± 0.576

Table E.5 *$C_{x'}$ values for the reaction $\gamma d \rightarrow np$ at the specified $\cos\theta_{\mathrm{CM}}$ points. Values of p_y are fixed as those listed in the table to extract $C_{x'}$ as described in the main body of the Thesis.*

E_γ/MeV	$\cos\theta$CM									
	$\frac{4}{5}$		$\frac{2}{5}$		0		$-\frac{2}{5}$		$-\frac{4}{5}$	
	p_y	$C_{x'}$	p_y	$C_{x'}$	p_y	$C_{x'}$	p_y	$C_{x'}$	p_y	$C_{x'}$
250 ± 50	0	-0.313 ± 12.623	0	1.979 ± 2.468	0	-0.562 ± 1.406	0	-3.667 ± 1.285	0	-0.625 ± 4.755
350 ± 50	0	-3.118 ± 2.515	0	-0.361 ± 0.931	0	-0.977 ± 0.612	0	0.431 ± 0.523	0	-2.444 ± 0.822
450 ± 50	0	2.386 ± 1.523	0	0.861 ± 0.744	0	1.100 ± 0.548	0	0.126 ± 0.482	0	-0.235 ± 0.535
550 ± 50	0	-0.247 ± 1.491	0	0.413 ± 0.834	0	-1.461 ± 0.694	0	-1.091 ± 0.596	0	0.739 ± 0.554
650 ± 50	0	3.163 ± 1.467	0	0.512 ± 0.913	0	0.325 ± 0.823	0	2.386 ± 0.816	0	0.625 ± 0.624
750 ± 50	0	-2.947 ± 1.928	0	-2.662 ± 1.308	0	1.982 ± 1.011	0	-0.914 ± 1.161	0	-0.904 ± 0.602
850 ± 50	0	-0.693 ± 1.723	0	2.359 ± 1.555	0	1.096 ± 1.242	0	1.676 ± 1.111	0	1.028 ± 0.505
950 ± 50	0	10.998 ± 1.281	0	-2.130 ± 1.784	0	-0.111 ± 1.150	0	-3.006 ± 0.992	0	-0.945 ± 0.659
250 ± 50	-0.012	-0.383 ± 12.574	-0.044	2.054 ± 2.444	-0.075	-0.658 ± 1.386	-0.106	-3.825 ± 1.262	-0.127	-0.263 ± 4.669
350 ± 50	-0.012	-3.043 ± 2.509	-0.023	-0.344 ± 0.929	-0.031	-0.973 ± 0.610	-0.037	0.443 ± 0.521	-0.04	-2.408 ± 0.821
450 ± 50	0.005	2.385 ± 1.524	0.007	0.848 ± 0.744	0.009	1.102 ± 0.548	0.01	0.125 ± 0.482	0.01	-0.237 ± 0.535
550 ± 50	0.067	-0.266 ± 1.498	0.087	0.330 ± 0.834	0.097	-1.490 ± 0.693	0.102	-1.125 ± 0.597	0.106	0.780 ± 0.550
650 ± 50	0.038	3.245 ± 1.474	0.045	0.514 ± 0.917	0.046	0.335 ± 0.824	0.047	2.415 ± 0.816	0.053	0.630 ± 0.622
750 ± 50	0.088	-2.776 ± 1.969	0.101	-2.626 ± 1.314	0.101	1.943 ± 1.011	0.105	-0.887 ± 1.156	0.147	-0.952 ± 0.594
850 ± 50	0.264	-0.675 ± 1.792	0.268	2.583 ± 1.563	0.261	0.802 ± 1.217	0.28	1.500 ± 1.067	0.481	0.844 ± 0.441
950 ± 50	0.608	6.741 ± 1.298	0.532	-2.345 ± 1.655	0.769	1.876 ± 0.855	0.709	-1.534 ± 0.769	0.899	-0.346 ± 0.323
250 ± 50	1	-0.336 ± 12.613	-1	1.945 ± 2.471	1	-0.608 ± 1.401	1	-3.763 ± 1.277	-1	-0.786 ± 4.741
350 ± 50	-1	-3.218 ± 2.522	-1	-0.386 ± 0.933	1	-0.965 ± 0.607	-1	0.401 ± 0.522	1	-2.337 ± 0.815
450 ± 50	1	2.386 ± 1.510	1	0.977 ± 0.735	-1	1.116 ± 0.547	1	0.151 ± 0.474	-1	-0.259 ± 0.530
550 ± 50	-1	-0.263 ± 1.498	1	0.493 ± 0.822	-1	-1.494 ± 0.692	-1	-1.136 ± 0.595	1	0.676 ± 0.553
650 ± 50	-1	3.329 ± 1.476	-1	0.516 ± 0.917	-1	0.355 ± 0.821	-1	2.460 ± 0.812	-1	0.632 ± 0.613
750 ± 50	1	-3.051 ± 1.854	1	-2.627 ± 1.276	1	1.996 ± 0.995	1	-0.936 ± 1.150	-1	-0.971 ± 0.586
850 ± 50	1	-0.676 ± 1.639	-1	2.514 ± 1.573	1	1.205 ± 1.219	1	1.712 ± 1.104	0.913	1.029 ± 0.521
950 ± 50	1	11.109 ± 1.191	-1	-2.248 ± 1.784	1	-0.430 ± 1.099	1	-3.198 ± 0.971	-1	-0.964 ± 0.627

Appendix F

Comparison of $C_{x'}$ results to proposal estimates

$C_{x'}$ was calculated in relatively wide angular and energy bins. Both of these issues are due to the large reduction in available statistics for the case of the scattered data. This is in part due to the relatively low probability of scattering in the polarimeter but also due to the fact that results were measured over a shorter beamtime than initially requested in the experiment proposal [135]. With the number of scattered particles observed, errors on the values of $C_{x'}$ are roughly in line with the values expected from the experimental proposal. The absolute range of the error in $C_{x'}$, $\Delta C_{x'}$, is given in the proposal as

$$\Delta C_{x'} = \sqrt{\frac{2}{A^2 N}}, \tag{F.1}$$

where A is the product of the beam polarisation and the effective analysing power and N is the number of scattered events. Considering the bin centred at 350 MeV and 0 in $\cos\theta_{CM}$ as an example there are roughly 40000 events in this bin. The effective analysing power and polarisation in this bin are both ~ 0.1. Using these values in Equation (F.1) yields $\Delta C_{x'} = 0.707$. The observed error in this bin from the fit to the data was ± 0.5, i.e. $\Delta C_{x'} \approx 1$.

Appendix G

Energy Dependence of Σ Legendre Fits

To further examine the data for Σ, the energy dependence of the parameters of the Legendre fit (defined by Equation (10.1)) was examined. To assesses this energy dependence, the parameters, P^2_{2-7}, were plotted as a function of E_γ and were fitted with a function consisting of three Gaussians and a Breit-Wigner function. This function is chosen in order to attempt to provide a smooth, continuous function to fit the data. The Gaussians were centred at 420 MeV, 520 MeV and 620 MeV respectively in order to cover the full energy range; the Breit-Wigner was centred at 570 MeV ($\sqrt{s}$ = 2378 MeV) with a width of 70 MeV in order to assess the potential impact of the d*(2380) resonance. The free parameters in this fit were the amplitudes of each component. These fits were carried out simultaneously on the parameters P^2_{2-7} using the MINUIT minimisation tool [165]. The fit for each parameter can be seen as a solid line in Figure G.1 where the errors on the fit are also illustrated as a shaded red area. The fit without the Breit-Wigner (three Gaussians only) component is also shown in this figure as a dashed line, the Breit-Wigner component of the fit appears to have a relatively large effect on the P^2_3, P^2_4 and P^2_6 components.

The parameters from the energy dependent fits can be used to produce the second order Legendre Polynomial parameters, P^2_{2-7}, for a given energy. These Legendre Polynomials can then be fitted to the data for Σ as a function of $\cos\theta_{\mathrm{CM}}$. An example of such a fit for both the three Gaussian and Breit-Wigner case (and a fit based upon fitting seven Gaussians) compared to the original energy-independent fit can be seen in Figure G.2. The three fits are generally in very good agreement with each other with some slight deviations at the edges. This pattern is observed across the full energy range as can be seen in Figure G.3.

This fitting and analysis is *not* a definitive fit of the data. It is merely an attempt to begin to try and examine the energy dependence of the extracted fit parameters. A full theoretical assessment is required to make any firm conclusions about the potential impact of the d*(2380) resonance on the energy dependence of these parameters.

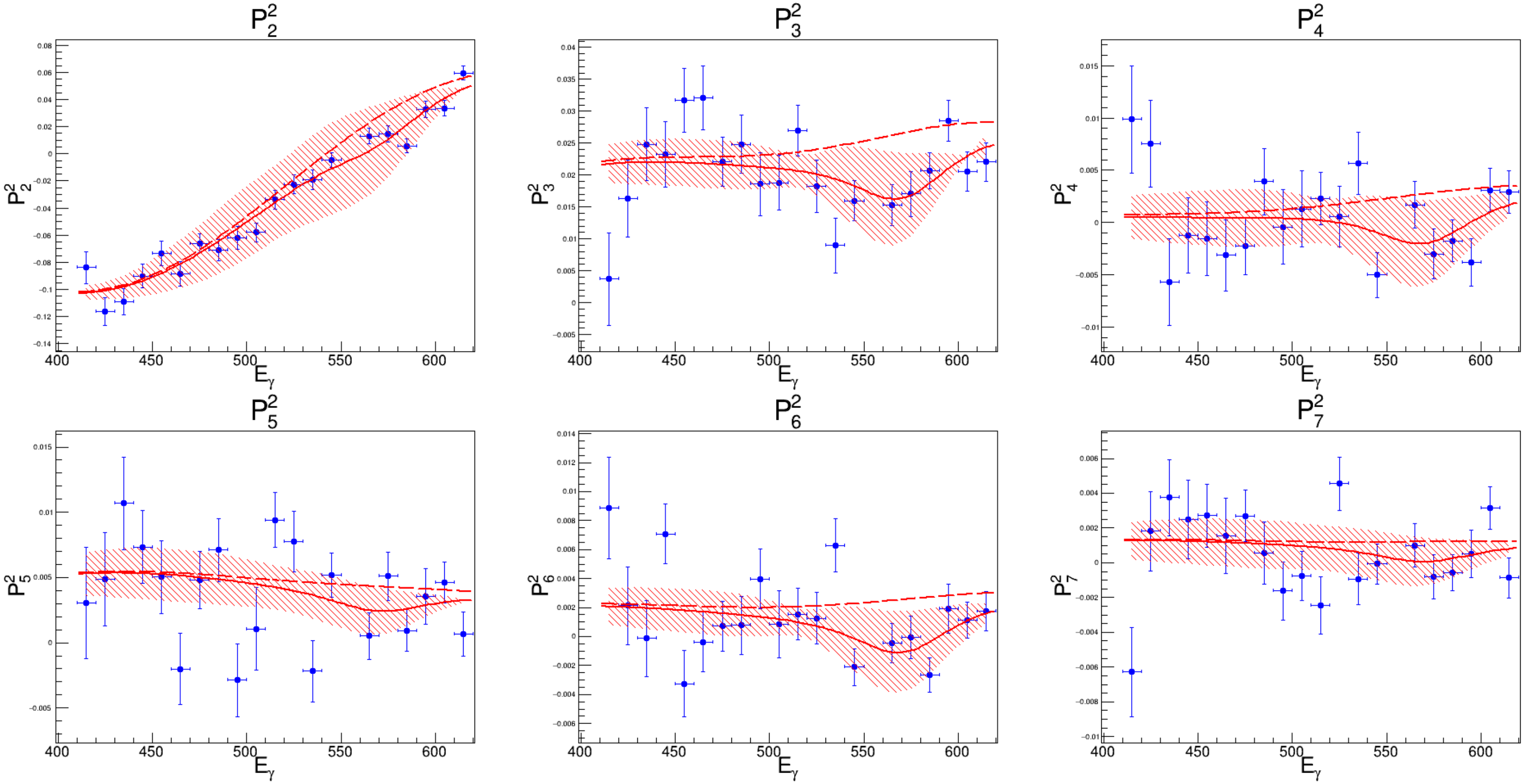

Figure G.1 *Fit parameters P^2_{2-7} fitted with a function formed of three Gaussian fits and a Breit-Wigner represented with a solid red line to characterise their energy dependence. The red band on the fit demonstrates the error range. The dashed line represents a fit to the parameters with three Gaussian fits only to demonstrate the effect of the additional Breit-Wigner component.*

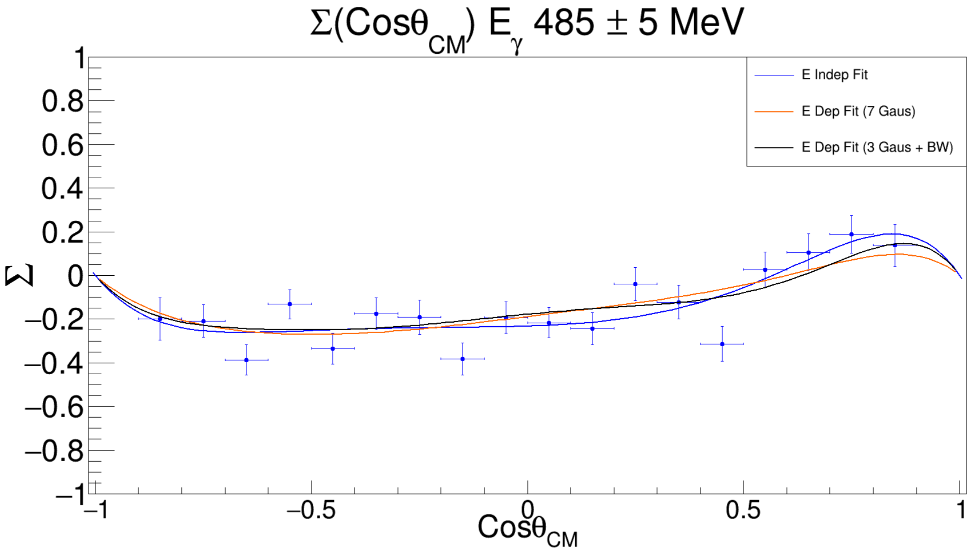

Figure G.2 *$\Sigma(\cos\theta_{\mathrm{CM}})$ in one 10 MeV wide E_γ bin. Demonstrated on the plot are three fits, the original energy independent and two further fits. The parameters for these fits were set based upon energy dependent fits (using three Gaussians and a Breit-Wigner or seven Gaussians) to the parameters P^2_{2-7} as a function of E_γ.*

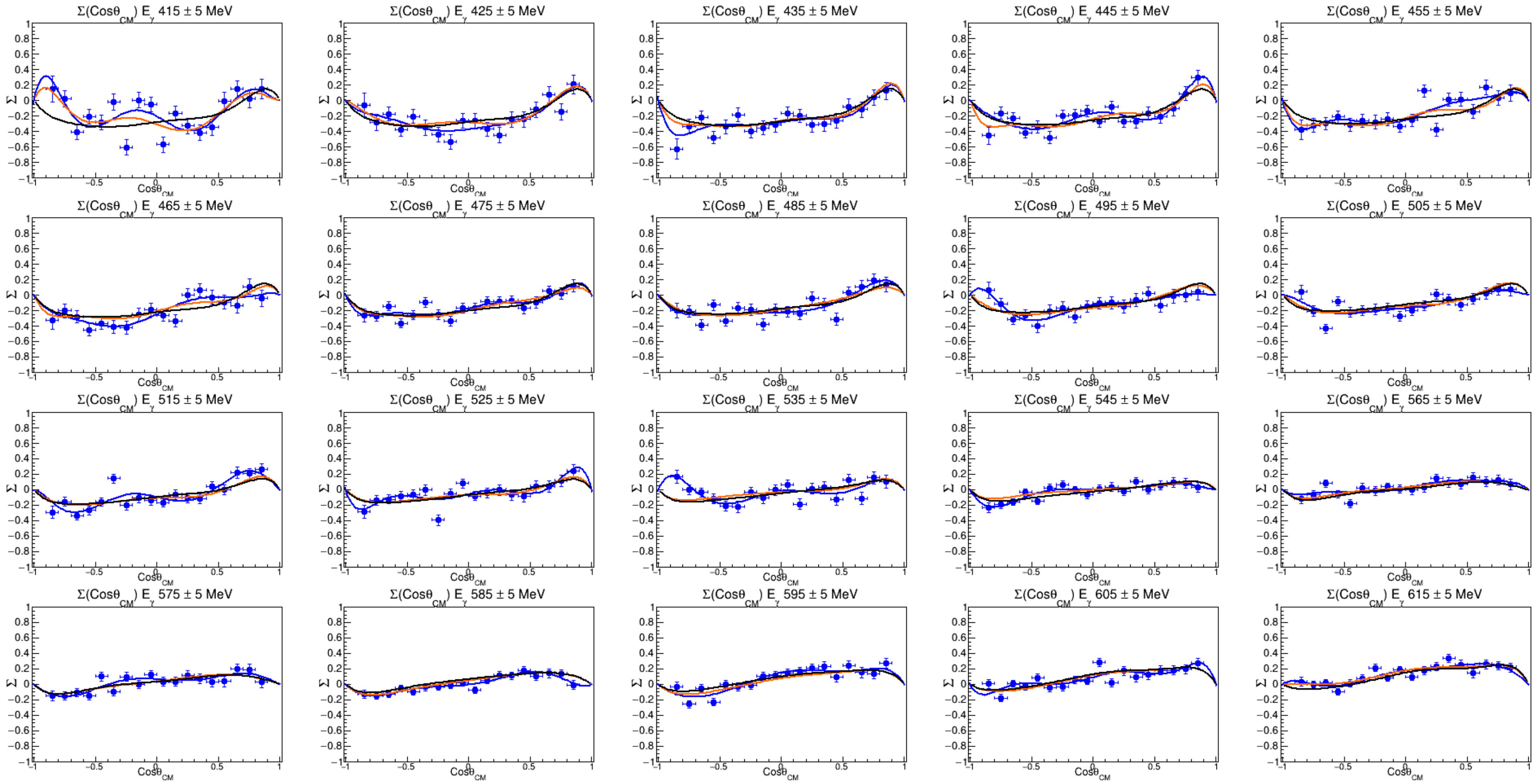

Figure G.3 Σ $(\cos\theta_{\mathrm{CM}})$ *across 20* E_γ *bins of width 10 MeV each. Shown for each* E_γ *bin are the three different fits to the data. The colouring of these lines is as defined in Figure G.2.*

Bibliography

[1] M. B. Hecht et. al. Nucleon Mass and pion loops. *Physical Review C*, 65:055204, 2002.

[2] N. Brambilla et. al. QCD and strongly coupled gauge theories: challenges and perspectives. *European Physical Journal C*, 74(10):2981, 2014.

[3] R. Gilman and Franz Gross. Electromagnetic structure of the deuteron. *Journal of Physics G: Nuclear and Particle Physics*, 28(4):R37–R116, 2002.

[4] H. J. Arrends. The Institute for Nuclear Physics at the University of Mainz. *Nuclear Physics News*, 18(2):5–11, 2008.

[5] A. Starostin et. al. Measurement of $K^-p \rightarrow \eta\Lambda$ near threshold. *Physical Review C*, 64:055205, 2001.

[6] R. Novotny. The BaF_2 Photon Spectrometer TAPS. *IEEE Transactions on Nuclear Science*, 38(2):379385, 1991.

[7] A.R.Gabler et. al. Response of TAPS to monochromatic photons with energies between 45 and 790 MeV. *Nuclear Instruments and Methods in Physics Research Section A*, 346:168–176, 1994.

[8] E. D. Bloom et. al. High-Energy Inelastic e-p Scattering at 6° and 10°. *Physical Review Letters*, 23(16):930–934, 1969.

[9] E. D. Bloom et. al. Observed Behaviour of Highly Inelastic Electron-Proton Scattering. *Physical Review Letters*, 23(16):934–939, 1969.

[10] Anthony W. Thomas, Wolfram Weise. *The Structure of the Nucelon.* Wiley, Berlin, 2005.

[11] H.J. Lipkin. Quark Models and Quark Phenomenology. *ArXiv High Energy Physics - Phenomenology e-prints*, 1993.

[12] M.Gell-Mann. A Schematic Model of Baryons and Mesons. *Physics Letters*, 8(3):214–215, 1964.

[13] G .Zweig. An SU_3 model for strong interaction symmetry and its breaking; Version 1. (CERN-8182/TH.401), 1964.

[14] G .Zweig. An SU_3 model for strong interaction symmetry and its breaking; Version 2. (CERN-8419/TH.412), 1964.

[15] `https://en.wikipedia.org/wiki/File:Baryon-octet-small.svg`. Wikimedia Commons, Accessed 05/05/18.

[16] `https://en.wikipedia.org/wiki/File:Baryon-decuplet-small.svg`. Wikimedia Commons, Accessed 05/05/18.

[17] V. E. Barnes et. al. Observations of a Hyperon with Strangeness Minus Three. *Physical Review Letters*, 12(8):204–206, 1964.

[18] O. W. Greenberg. Spin and Unitary-Spin Independence in a Paraquark Model of Baryons and Mesons. *Physical Review Letters*, 13(20):598–602, 1964.

[19] S. J. Brodsky et. al. Nonperturbative QCD coupling and its β function from light-front holography. *Physical Review D*, 81:096010, 2010.

[20] V. Bernard and U. G. Meißner. Chiral Perturbation Theory. *Annual Review of Nuclear and Particle Science*, 57(1):33–60, 2007.

[21] K. G. Wilson. Confinement of Quarks. *Physical Review D*, 10(8):2445–2459, 1974.

[22] S. Dürr et. al. Ab Initio Determination of Light Hadron Masses. *Science*, 322(5905):1224–1227, 2008.

[23] J. J. Dudek et. al. Isoscalar meson spectroscopy from lattice QCD. *Physical Review D*, 83:111502, 2011.

[24] R. G. Edwards et. al. Excited state baryon spectroscopy from lattice QCD. *Physical Review D*, 84:074508, 2011.

[25] Greig Cowan and Tim Gershon. *Tetraquarks and Pentaquarks*. 2399-2891. IOP Publishing, 2018.

[26] D. I. Glazier et. al. M. H. Sikora, D. P. Watts. Measurement of the ${}^1\mathrm{H}(\overrightarrow{\gamma}, \overrightarrow{p})\pi^0$ Reaction Using a Novel Nucleon Spin Polarimeter. *Physical Review Letters*, 112:022501, Jan 2014.

[27] N. Zachariou. *Determination of the Azimuthal Asymmetry of Deuteron Photodisintegration in the Energy Region* $E_\gamma = 1.1 - 2.3$ *GeV*. PhD thesis, George Washington University, 2012.

[28] `https://en.wikipedia.org/wiki/Spherical_coordinate_system#/media/File:3D_Spherical.svg`. Wikimedia Commons, Accessed 01/08/18.

[29] V. P. Barannik et. al. Proton Polarization in Deuteron Photodisintegration by Linearly Polarized Photons and Dibaryon Resonances. *Nuclear Physics A*, 451:761–767, 1986.

[30] N. Zachariou and Y. Ilieva. Determination of the Beam-Spin Asymmetry using the ϕ-bin method. *CLAS-NOTE*, 011, 2012.

[31] K. Wijesooriya et. al. Polarization measurements in neutral pion photproduction. *Physical Review C*, 66:034614, 2002.

[32] M. Sikora. *Recoil Polarimetery in Meson Photoproduction Reactions.* PhD thesis, University of Edinburgh, 2011.

[33] Kenneth S. Krane. *Introductory Nuclear Physics.* John Wiley and Sons, 1988.

[34] E. Aprile-Giboni. et. al. Proton-carbon effective analysing power between 95 and 570 MeV. *Nuclear Instrumentation Methods A*, 215:147–157, 1983.

[35] INS Data Analysis Center. SAID. `http://gwdac.phys.gwu.edu/analysis/nn_analysis.html`. Accessed 17//05/2018.

[36] D. Glazier. *Measurement of the Neutron Electric Form Factor at* $Q^2 = 0.8\left(\frac{GeV}{c}\right)^2$. PhD thesis, University of Glasgow, 2003.

[37] R. L. Jaffe. Multiquark hadrons I. Phenomenology of $\mathrm{Q}^2\overline{\mathrm{Q}}^2$ mesons*. *Physical Review D*, 15(1):267–281, 1977.

[38] D. Strottman. Multiquark baryons and the MIT bag model. *Physical Review D*, 20(3):748–767, 1979.

[39] R. L. Jaffe. Multiquark hadrons. II . Methods. *Physical Review D*, 15(1):281–289, 1977.

[40] F. J. Dyson and Nguyen-Huu Xuong. Y = 2 States in SU(6) Theory. *Physical Review Letters*, 13(26):815–817, 1964.

[41] R. L. Jaffe. Perhaps a Stable Hihyperon. *Physical Review Letters*, 38(5):195–198, 1977.

[42] T. Goldman et. al. "Inevitable" nonstrange dibaryon. *Physical Review C*, 39(5):1889–1895, 1989.

[43] H. Fritzsch and P. Minkowski. ψ-resonances, gluons and the Zweig rule. *Il Nuovo Cimenta A*, 30:393–429, 1975.

[44] V. Matheiu, N. Kochelev and V. Vento. The Physics of Glueballs. *Internation Journal of Modern Physics E*, 18:1–49, 2009.

[45] C. Bernard. Exotic mesons in quenched lattice QCD. *Physical Review D*, 56(11):7039–7051, 1997.

[46] H. Clement. On the history of dibaryons and their final observation. *Progress in Particle and Nuclear Physics*, 93:195–242, 2017.

[47] Harry. J. Lipkin. New possibilities for exotic hadrons - anticharmed strange baryons. *Physics Letters B*, 195(3):484–488, 1987.

[48] Kenneth. H. Hicks. Experimental Search for Pentaquarks. *Progress in Particle and Nuclear Physics*, 55:647–676, 2005.

[49] Kenneth. H. Hicks. On the conundrum of the pentaquark. *European Physical Journal H*, 37:1–31, 2012.

[50] M. Bashkanov et. al. Exclusive measurements of $pd \rightarrow^{3} He\pi\pi$: The ABC effect revisited. *Physics Letters B*, 637:223–228, 2006.

[51] M. Bashkanov et. al. Double-Pionic Fusion of Nuclear Systems and the "ABC" Effect: Approaching a Puzzle by Exclusive and Kinematically Complete Measurements. *Physical Review Letters*, 102:052301, 2009.

[52] S. K. Choi et. al. Observation of a Resonancelike Structure in the $\pi^{+-}\psi'$ Mass Distribution in Exclusive $B \rightarrow K\pi^{+-}\psi$ Decays. *Physical Review Letters*, 100:142001, 2008.

[53] R.Aaij. et. al. Observation of the Resonant Character of the Z(4430)$^{-}$ State. *Physical Review Letters*, 112:222002, 2014.

[54] T. Aaltonen et. al. Evidence for a Narrow Near-Threshold Structure in the $J/\psi\phi$ Mass Spectrum in $B^{+} \rightarrow J/\psi\phi K^{+}$ Decays. *Physical Review Letters*, 102:242002, 2009.

[55] R.Aaij. et. al. Observation of $J/\psi\phi$ Structures Consistent with Exotic States from Amplitude Analysis of $B^{+} \rightarrow J/\psi\phi K^{+}$ Decays. *Physical Review Letters*, 118:022003, 2017.

[56] R.Aaij. et. al. Amplitude analysis of $B^{+} \rightarrow J/\psi\phi K^{+}$ decays. *Physical Review D*, 95:012002, 2017.

[57] Fl Stancu. Can Y(4140) be a $c\bar{c}s\bar{s}$ tetraquark? *Journal of Physics G*, 37:075017, 2010.

[58] R.Aaij. et. al. Observation of $J/\psi p$ Resonances Consistent wiith Pentaquark States in $\Lambda_b^0 \rightarrow J\psi K^{-}p$ Decays. *Physical Review Letters*, 115:072001, 2015.

[59] R.Aaij. et. al. Model-Independent Evidence of $J/\psi p$ Contributions to $\Lambda^0 b \rightarrow J/\psi K^{-}$ Decays. *Physical Review Letters*, 115:082002, 2016.

[60] R.Aaij. et. al. Evidence for Exotic Hadron Contributions $J/\psi p$ Contributions to $\Lambda^0 b \rightarrow J/\psi K^{-}$ Decays. *Physical Review Letters*, 115:082003, 2016.

[61] Hua-Xing Chen et. al. Towards Exotic Hidden-Charm Pentaquarks in QCD. *Physical Review Letters*, 115:172001, 2015.

[62] L. Roca, J. Nieves and E. Oset. LHCb pentaquark as a $\overline{D} * \Sigma_c - \overline{D} * \Sigma *_c$ molecular state. *Physical Review D*, 92:094003, 2015.

[63] L. Maiani, A.D. Polosa and V. Riquer. The new pentaquarks in the diquark model. *Physics Letters B*, 749:289–291, 2015.

[64] Richard F. Lebed. The pentaquark candidates in the dynamical diquark picture. *Physics Letters B*, 749:454–457, 2015.

[65] Qian Wang, Xiao-Hai Liue and Qiang Zhao. Photoproduction of hidden charm pentaquark states $P_{\mathrm{c}}^{+}(4380)$ and $P_{\mathrm{c}}^{+}(4450)$. *Physical Review D*, 92:034022, 2015.

[66] V. Kubarovsky and M. B. Voloshin. Formation of hidden-charm pentaquarks in photon-nucleon collisions. *Physical Review D*, 92:031502, 2015.

[67] M. Karliner and J. L. Rosner. Photoproduction of exotic baryon resonances. *Physics Letters B*, 752:329–332, 2016.

[68] A. Abashian, N. E. Booth, K. M. Crowe. Possible Anomaly in Meson Production in p + d Collisions. *Physical Review Letters*, 5(6):258–260, 1960.

[69] N. E. Booth, A. Abashian, K. M. Crowe. Anomaly in Meson Production in p + d Collisions. *Physical Review Letters*, 7(1):35–39, 1961.

[70] R.J. Homer et. al. Evidence for an Anomaly in Two Pion Production. *Physis Letters*, 9(1):72–75, 1964.

[71] J.H. Hall, T.A. Murray and L. Riddiford. Evidence for a Low Energy S-Wave π - π Interaction and Possible Doubly Charged Dibaryon Enhancement. *Nuclear Physics B*, 12:573–585, 1969.

[72] T. Risser, M.D. Shuster. Anomalous Enhancements in Multiple-Pion Production with Deuterons. *Physis Letters B*, 43(1):68–72, 1973.

[73] C. A. Mosbacher and F. Osterfeld. Double $\Delta(1232)$ excitation and the ABC effect in the reaction n + p $\rightarrow^2 H(\pi\pi)$. *ArXiv Nuclear Theory e-prints*, 1999.

[74] J. Ping, H. Pang, F. Wang, T. Goldman. d* dibaryon in the extended quark-delocalization, color screening model. *Physical Review C*, 65:044003, 2002.

[75] T. Barnes, S. Capstick, M.D. Kovarik, E.S. Swanson. NN core interactions and differential cross sections from one gluon exchange. *Physical Review C*, 48(2):539–552, 1993.

[76] T. Kamae and T.Fujita. Possible Existence of a Deeply Bound Δ - Δ System. *Physical Review Letters*, 38(9):471–475, 1977.

[77] J. Ping, H.X. Huang, H.R. Pang, F. Wang and C.W. Wong. Quark models of dibaryon resonances in nucleon-nucleon scattering. *Physical Review C*, 79:024001, 2009.

[78] P. Adlarson et. al. Abashian-Booth-Crowe Effect in Basic Double-Pionic Fusion: A New Resonance? *Physical Review Letters*, 106:242302, 2011.

[79] P. Adlarson et. al. Isospin decomposition of the basic double-pionic fusion in the region of the ABC effect. *Physics Letters B*, 721:229–236, 2013.

[80] P. Adlarson et. al. Measurement of the pn $\rightarrow$ pp$\pi^0\pi^0$ reaction in search for the recently observed resonance structure in d$\pi^0\pi^0$ and d$\pi^+\pi^-$ systems. *Physical Review C*, 88:055208, 2013.

[81] P. Adlarson et al. (WASA at COSY Collaboration). Measurement of the np $\rightarrow$ np$\pi^0\pi^0$ reaction in search for the recently observed d(2380) resonance. *Physics Letters B*, 743:325, 2015.

[82] H. Clement, M. Bashkanov and T. Skorodko. From CELSIUS to COSY: on the observation of a dibaryon resonance. *Physica Scripta*, 2015(T166), 2015.

[83] P. Adlarson et al. (WASA-at COSY Collaboration SAID Data Analysis Center). Neutron-proton scattering in the context of the d*(2380) resonance. *Physical Review C*, 90:035204, 2014.

[84] P.Adlarson et. al. Evidence for a New Resonance from Polarized Neutron-Proton Scattering. *Physical Review Letters*, 112:202301, 2014.

[85] R.A. Arndt, W.J. Briscoe, I.I. Starkovsky and R.K. Workman. Updated analysis of NN elastic scattering to 3 GeV. *Physical Review C*, 76:025209, 2007.

[86] R.K. Workman, W.J. Briscoe and I.I. Starkovsky. Sensitivity of the COSY dibaryon candidate to np elastic scattering measurements. *Physical Review C*, 93:045201, 2016.

[87] P. Adlarson et. al. Abashian-Booth-Crowe resonance structure in the double pionic fusion to ^{4}He. *Physical Review C*, 86:032201, 2012.

[88] P. Adlarson et. al. ABC effect and resonance structure in the double-pionic fusion to ^{3}He. *Physical Review C*, 91:015201, 2015.

[89] F. Huang, Z.Y. Zhang, P.N. Shen, W.L. Wang. Is d* a candidate for a hexaquark-dominated exotic state? *Chinese Physics C*, 39(7):071001, 2015.

[90] M. Bashkanov, H. Clement and T. Skorodko. Branching Ratios for the decaay of d*(2380). *European Physical Journal A*, 51:87, 2015.

[91] Z. Zhang Y. Dong, P. Shen. On the form factors of $d^*(2380)$. *ArXiv e-prints*, 2018.

[92] T. Kamae et. al. Observation of an Anomalous Structure in Proton Polarization from Deuteron Photodisintegration. *Physical Review Letters*, 38(9):468–471, 1977.

[93] F. F. Liu, D. E. Lundquist and B. H. Wiik. Measurements of the Polarization of Protons from Deuteron Photodisintegration*. *Physical Review*, 165:1478, 1968.

[94] R. Kose et. al. Measurements of the Polarization of Protons from Deuteron Photodisintegration for Photon Energies between 282 and 405 MeV*. *Zeitschrift für Physik*, 220:305–320, 1969.

[95] N. Austern. Isobar Role in Two-Nucleon Processes: Deuteron Photoeffect*. *Physical Review*, 100:1522–1529, 1955.

[96] H. Ikeda et al. Angular Dependence of Proton Polarization in the Reaction γd $\to$ pn and a Partial-Wave Analysis of Possible Dibaryon Resonances. *Physical Review Letters*, 42:1321, 1979.

[97] H. Ikeda et. al. Further Measurement of Proton Polarizatin in Deuteron Photodisintegration at Photon Energies Between 400 and 650 MeV; Possible Evidence for Dibaryon Resonances. *Nuclear Physics B*, 172:509–533, 1980.

[98] A.S. Bratashevsky et. al. Energy dependence of proton polarization in the $\gamma d \to np$ reaction at angles of 43, 78 and 120°. *JETP Letters*, 31(5):270–272, 1980.

[99] A.S. Bratashevsky, A.A. Zybalov, S.P. Karasev, O.G. Konovalov, P.V. Sorokin, Yu.O. Storozhenko, A.E. Tenishev. Polarization of Protons in Reaction $\gamma d \to pn$ at E_γ = 0.7 - 1 GeV for θ(p) = 90-degrees C.M. *Yadernaya Fizika*, 44(4):960–964, 1986.

[100] V.B. Ganenko et. al. Polarization observables Σ, P_y T_1 in the reaction $\overrightarrow{\gamma}d \to \overrightarrow{p}$ at photon energies between 200 and 600 MeV and dibaryon resonances. *Zeitschrift für Physik A*, 341:205–216, 1992.

[101] K. Wijesooriya et. al. Polarization Measurements in High-Energy Deuteron Photodisintegration. *Physical Review Letters*, 86(14):2975–2979, 2001.

[102] D. Drechsel, S. S. Kamalov and L. Tiator. Unitary isobar Model – MAID2007. *European Physical Journal A*, 34:69–97, 2007.

[103] C. Bignamini et. al. Is the X(3872) Production Cross Section at $\sqrt{s}$=1.96 TeV Compatible with a Hadron Molecule Interpretation? *Physical Review Letters*, 103:162001, 2009.

[104] W. Luo et. al. Polarization Components in π^0 Photoproduction at Photon Energies of up to 5.6 GeV. *Physical Review Letters*, 108:222004, 2012.

[105] R. Beck S. J. Hall, G. J. Miller and P. Jennewein. A focal plane system for the 855 MeV tagged photon spectrometer at MAMI-B. *Nuclear Instruments and Methods in Physics Research Section A*, 368:698–708, 1996.

[106] J. C. McGeorge et. al. Upgrade of the Glasgow photon tagging spectrometer for Mainz MAMI-C. *European Journal of Physics A*, 37:129–137, 2008.

[107] A. Jankowiak. The Mainz Microtron MAMI - Past and future. *European Physical Journal A*, 28:149–160, 2006.

[108] J. Alyea et. al. Neutrons and the Crystal Ball experiments, 1997.

[109] M. Martemianov et. al. A new measurement of the neutron detection efficiency for the NaI Crystal Ball detector. *Journal of Instrumentation*, 10(4):T04001, 2015.

[110] H. Herminghaus et. al. The design of a cascaded 800 MeV normal conducting C.W. Race Track Microtron. *Nuclear Instruments and Methods*, 138:1–12, 1976.

[111] K. Aulenbacher et. al. The MAMI source of polarised electrons. *Nuclear Instruments and Methods in Physics Research Section A*, 391:498–506, 1997.

[112] K. H. Kaiser et. al. The 1.5 GeV harmonic double-sided microtron at Mainz University. *Nuclear Instruments and Methods in Physics Research Section A*, 593:159–170, 2008.

[113] Haakon Olsen and L.C. Maximon. Electron and Photon Polarization in Bremsstrahlung and Pair Production. *Physical Review*, 110:589–590, 1958.

[114] K. Aulenbacher V. Tioukine and E. Riehn. A Mott polarimeter operating at MeV electron beam energies. *Review of Scientific Instruments*, 82:033303, 2011.

[115] K. Livingston. The Stonehenge technique. A method for aligning coherent bremsstrahlung radiators. *Nuclear Instruments and Methods in Physics Research Section A*, 603:205–213, 2009.

[116] F. Rambo et. al. Enhancement of the linear polarization of coherent bremsstrahlung by collimation of the photon beam. *Physical Review C*, 58:489–501, 1998.

[117] R. Macrae. Linear polarisation enhancement and degree of polarisation plot. `http://nuclear.gla.ac.uk/~roddym/Enhancements/Enh_amo1160_perp1159_650MeV.gif`. Accessed 30/07/2018.

[118] M. Oreglia et. al. Study of the reaction $\psi' \rightarrow \gamma\gamma J/\psi$. *Physical Review D*, 25(9):2259–2277, 1982.

[119] Elliott D. Bloom and Charles W. Peck. Physics With the Crystal Ball Detector. *Annual Review of Nuclear and Particle Science*, 33:143–197, 1983.

[120] B. M. Schwarzschild. Crystal Ball to move from SLAC to DESY. *Physics Today*, 35(1):21, 1982.

[121] W. J. Briscoe et. al. Results from the analysis of Crystal Ball meson production at BNL. *International Journal of Modern Physics A*, 22(02n03):349, 2007.

[122] S. Prakhov et. al. Measurement of the slope parameter α for the $\eta \rightarrow 3\pi^0$ decay with the Crystal Ball detector at the Mainz Microtron (MAMI-C). *Physical Review C*, 79:035204, 2009.

[123] R. Novotny et. al. Scintillators for photon detection at medium energiesa comparative study of BaF_2, CeF_3 and $PbWO_4$. *Nuclear Instruments and Methods in Physics Research Section A*, 486:131–135, 2002.

[124] `https://wwwa2.kph.uni-mainz.de/intern/daqwiki/_media/experiment/detectors/taps/taps2009_from_target.png?cache=`. Internal publication, A2 access required, Accessed 25/03/2018.

[125] D. Watts (Crystal Ball at MAMI Collaboration and A2 Collaboration). The Crystal Ball and TAPS Detectors at the MAMI Electron Beam Facility. In *Calorimetry in Particle Physics: Proceedings of the 11th International Conference, Perugia, Italy, 2004*.

[126] D. P. Watts. New particle ID Detector for Crystal Balll at MAMI-C. `http://www2.ph.ed.ac.uk/nuclear/PID/PID.pdf`, 2009. Accessed 25/03/2018.

[127] G. Audit et. al. DAPHNE: a large-acceptance tracking detector for the study of photoreactions at intermediate energies. *Nuclear Instruments and Methods in Physics Research Section A*, 301:473–481, 1991.

[128] J. Albert. Test Measurements for the Crystal Ball Detector at MAMI. Universität Mainz, Diplom Thesis, 2003.

[129] G. Braun et. al. TDC Chip and Readout Driver Developments for COMPASS and LHC-Experiments. `https://arxiv.org/pdf/hep-ex/9810048.pdf`.

[130] P. Drexler et. al. The New Readout Electronics for the BaF_2 Calorimeter TAPS. *IEEE Transactions on Nuclear Science*, 50:969–973, 2003.

[131] University of Edinburgh for the A2 Collaboration. The Edinburgh G4 simulation of the Crystal Ball detector. `http://www2.ph.ed.ac.uk/nuclear/G4/`. Accessed 18/05/2018.

[132] Stephen Kay for the A2 Collaboration. `https://github.com/sjdkay/a2geant/tree/GEANT4.10_Polarimeter`. Accessed 26/03/2018.

[133] S. Agostinelli et. al. Geant4 – A Simulation Toolkit. *Nuclear Instruments and Methods in Physics Research Section A*, 506:250–303, 2003.

[134] University of Edinburgh for A2 Collaboration. Edinburgh Phase Space Generator for the A2 collaboration. `http://www.ph.ed.ac.uk/nuclear-physics/research-activities/nuclear-and-hadron-physics/edgen-event-generator`. Accessed 31/05/2018.

[135] Dan Watts, Derek Glazier, John Annand. Proposal for Experiment : Polarisation observables using the Nucleon polarimeter with the Crystal Ball at MAMI. Internal Publication.

[136] Eljen Technology. General Purpose Plastic Scintillator EJ-200, EJ-204, EJ-208, EJ-212. `https://eljentechnology.com/images/products/data_sheets/EJ-200_EJ-204_EJ-208_EJ-212.pdf`. Accessed 27/03/2018.

[137] Olmec Advanced Materials. Olmec. `http://www.olmec.co.uk/`. Accessed 04//04/2018.

[138] Novus. Novus plastic polish. `https://www.novuspolish.com/index.html`. Accessed 27/03/2018.

[139] Epoxy Technology. EPO-TEK 301-2 Technical Data Sheet. `http://www.epotek.com/site/administrator/components/com_products/assets/files/Style_Uploads/301-2RevXII.pdf`. Accessed 27/03/2018.

[140] Saint Gobain Crystals. BC-620 Reflector Paint for Plastic Scintillators. `https://www.crystals.saint-gobain.com/sites/imdf.crystals.com/files/documents/sgc-bc620-data-sheet_69725.pdf`. Accessed 05/04/2018.

[141] Kurt J. Lesker Company. Torr Seal Specifications. `https://www.lesker.com/newweb/fluids/pdf/torrsealspecifications.pdf`. Accessed 05/04/2018.

[142] F. G. Kondev and S. Lalkovski. Nuclear Data Sheets for A = 207*. *Nuclear Data Sheets*, 112:707–853, 2011.

[143] P. Martel. *Measuring Proton Spin Polarizabilities With Polarized Compton Scattering*. PhD thesis, University of Massachusetts Amherst, 2013.

[144] Chris Mullen. University of Glasgow, Private Communication, 2018.

[145] M. Pfieffer. *Photoproduction of* η *mesons from* ^{3}*He*. PhD thesis, Universität Giessen, 2002.

[146] D. Werthmüller. *Experimental study of nucleon resonance contributions to* η*-photoproduction on the neutron*. PhD thesis, University of Basel, 2014.

[147] Mikhail Bashkanov. University of Edinburgh, Private Communication, 2018.

[148] CERN. ROOT Data Analysis Framework. `https://root.cern.ch/`. Accessed 08/04/2018.

[149] A2 Collaboration. The a2 acqu ecosystem. `https://github.com/A2-Collaboration-dev/acqu`. Accessed 08/04/2018.

[150] A2 Collaboration. Generation of analysis trees. `https://github.com/A2-Collaboration-dev/a2GoAT`. Accessed 08/04/2018.

[151] Stephen Kay. `https://github.com/sjdkay/a2GoAT/blob/NewGoATWork/src/PNeutPol.cc`. Accessed 08/04/2018.

[152] Stephen Kay. `https://github.com/sjdkay/a2GoAT/tree/NewGoATWork/Analysis_Macros`. Accessed 08/04/2018.

[153] C. Collicott. *Probing Proton Structure Through Single Polarisation Observables of Compton Scattering and π^0 Photoproduction Within The Δ(1232) Region*. PhD thesis, Dalhousie University, 2015.

[154] F. V. Adamian et. al. Deuteron photodisintegration by linearly polarized photons in the energy region 0.3-1.0 GeV. *Journal of Physics G: Nuclear and Particle Physics*, 17(8):1189, 1991.

[155] V.G. Gorbenko et. al. Cross-section Asymmetry in the Photodisintegration of the Deuteron by Polarized Photons. *Nuclear Physics A*, 381:330–342, 1982.

[156] P. Ricci A. Cambi, B. Mosconi. Cross section and polarization in deuteron photodisintegration: General formulas. *Physical Review C*, 26(2358), 1982.

[157] R. Beck. et. al. Determination of the E2/M1 ratio in the $\gamma\overrightarrow{N} \rightarrow \Delta(1232)$ transition from a simulatenous measurement of $p(\overrightarrow{\gamma}, p)\pi^0$ and $p(\overrightarrow{\gamma}, \pi^+)n$. *Physical Review C*, 61:035204, 2000.

[158] T. Watabe, Chr. V. Christov and K. Goeke. E2/M1 ratio for the $\gamma N \rightarrow \Delta$ transition in the chiral quark soliton model. *Physics Letters B*, 349:197–203, 1995.

[159] R. Crawford et. al. Two-body photodisintegration of the deuteron from 100 to 800 MeV. *Nuclear Physics A*, 603:303–325, 1996.

[160] P. Drexler et. al. Status of the new FPD detector. `https://wwwa2.kph.uni-mainz.de/intern/daqwiki/_media/meetings/collaboration_meetings/2018_04/a2_2018-04_drexler.pdf`. Accessed 01/06/2018, Internal Access Required.

[161] `https://en.wikipedia.org/wiki/File:S-channel.svg`. Wikimedia Commons, Accessed 05/05/18.

[162] `https://en.wikipedia.org/wiki/File:T-channel.svg`. Wikimedia Commons, Accessed 05/05/18.

[163] `https://en.wikipedia.org/wiki/File:U-channel.svg`. Wikimedia Commons, Accessed 05/05/18.

[164] I. S. Barker, A. Donnachie and J.K. Storrow. Complete Experiments in Pseudoscalar Photoproduction. *Nuclear Physics B*, 95:347–356, 1975.

[165] CERN. MINUIT Function Minimization and Error Analysis. /`https://root.cern.ch/download/minuit.pdf`. Accessed 31/05/2018.